Continuous and Wet-Chemical Synthesis of Micro- and Nanoparticles in a Microreactor

Tin(IV) Oxide, Cesium Dihydrogen Phosphate and Organically Modified Silica

Christina
Odenwald

Continuous and Wet-Chemical Synthesis of Micro- and Nanoparticles in a Microreactor:

Tin(IV) Oxide, Cesium Dihydrogen Phosphate and Organically Modified Silica

DISSERTATION

Zur Erlangung des Grades

des Doktors der Naturwissenschaften

der Naturwissenschaftlich-Technischen Fakultät

der Universität des Saarlandes

von

CHRISTINA ODENWALD

Saarbrücken

2020

Tag des Kolloquiums: 02. Juli 2021

Dekan: Prof. Dr. Jörn Eric Walter

Berichterstatter: Prof. Dr. Guido Kickelbick

Priv.-Doz. Dr.-Ing. Guido Falk

Vorsitz: Prof. Dr. Marc Schneider

Akademischer Mitarbeiter: Dr. Andreas Rammo

DANKSAGUNG

Ich möchte allen danken die mich während meiner Promotion unterstützt, beraten und begleitet haben.

Zuallererst danke ich Prof. Guido Kickelbick dafür, dass ich die Arbeit in seiner Forschungsgruppe anfertigen konnte und für die Freiheit, das gegebene Thema in verschiedene Richtungen entwickeln zu können. Des Weiteren danke ich ihm für die wissenschaftliche Unterstützung durch Einbringen von vielen neuen Ideen und dem Diskutieren der Ergebnisse sowie für sein Engagement meinen Forschungsaufenthalt in Kanada zu ermöglichen.

Bei Dr. Guido Falk möchte ich mich für die wissenschaftliche Begleitung und Begutachtung dieser Arbeit bedanken.

Weiterhin danke ich der gesamten Forschungsgruppe für das sehr gute Arbeitsklima, die wissenschaftliche Hilfe in den verschiedensten Bereichen sowie die interessanten und freundschaftlichen Gespräche. Ich hoffe, dass die Kontakte möglichst lange bestehen bleiben.

In besonderem Maße bedanke ich mich bei meiner Laborpartnerin Sandra. Danke für deine wissenschaftliche Hilfe und Diskussionsbereitschaft, deine ehrliche Meinung, die vielen Gespräche über alles und nichts und deine Freundschaft. Außerdem möchte ich mich bei all meinen anderen Mit-Doktorand*innen bedanken, namentlich: bei Nils für seine pragmatische Art, die unterhaltsamen Mensa-Besuche und die – obwohl erfolglos gebliebenen – lustigen „Ententreffen“, bei meinem Büronachbar Dennis für seine besonnene Art und die Hilfe bei diversen Softwareproblemen, bei Achim für die abwechslungsreichen Busfahrten und die Einführung und Überwachung der Lösemittelvorratsliste, bei Nadja für die guten Essensempfehlungen, die Mitfinanzierung unserer Kaffeemaschine und den Bau des „chemist tree“. Weiterhin danke ich Dennis für die nie langweiligen Gespräche und Filmempfehlungen, Jessica für ihre liebenswerte Art und Hilfsbereitschaft, Thomas, Bastian und Max für das Schaffen lustiger Momente im Laboralltag. Außerdem danke ich meiner thematischen Nachfolgerin Mana für ihre stets gute Laune und das, während der Übergangszeit, unkomplizierte Arbeiten am gleichen Laborplatz.

Des Weiteren möchte ich mich bei meinen damaligen Bachelorstudenten Mike und Lucas für ihre Arbeit im Labor bedanken. Ralf und seiner gesamten Gruppe danke ich für ihren „analytischen Blick“ auf die Seminarvorträge und die gute Koordination des Praktikums, Patrick für seine fortwährende Hilfsbereitschaft bei verschiedensten Problemen. Robert danke ich für seine große Unterstützung bei der Aufnahme und Auswertung der Röntgendiffraktogramme, seinen Einfallsreichtum bei neuen Fragestellungen und das sich Zeitnehmen, selbst für Proben die ihn aufgrund ihrer geringen Kristallinität wohl kaum in helle Freude versetzt haben dürften. Außerdem danke ich ihm für seine Hilfe am REM. Ebenfalls danke an Thomas, Dennis und Jessica für das Aufnehmen der Röntgendiffraktogramme. Jörg danke ich für die Einarbeitung am REM sowie die schnelle und fachkundige Hilfe bei Problemen. Nadja und Thomas danke ich für das Aufnehmen der TEM-Bilder, Michael für die Festkörper-NMR-Messungen und Susanne für die Elementanalysen und die Unterstützung im Labor.

Einen besonderen Dank auch an Stefan für seine Hilfe bei „elektronischen Problemen“ sowie an Sylvia und Hermann von der anorganischen Werkstatt für ihre unglaublich schnelle und kompetente Hilfe bei Umbauten, Reparaturen und Wartungen im Labor sowie zahlreichen Sonderanfertigungen. Ich habe das Motto „Geht nicht, gibt's nicht“ nie besser umgesetzt gesehen. Außerdem danke ich Rudi von der Werkstatt der physikalischen Chemie für seine Hilfe. Susanne danke ich besonders für die schnelle und unkomplizierte Unterstützung bei allen bürokratischen und organisatorischen Dingen.

Des Weiteren möchte ich allen Kooperationspartnern danken:

Prof. Volker Presser und seiner Forschungsgruppe danke ich für die gute Zusammenarbeit, die Ideen sowie für die schnelle Überarbeitung von Manuskripten und Posterentwürfen. Besondern Dank auch an Benjamin für die interessanten wissenschaftlichen Diskussionen und das Vorantreiben unserer gemeinsamen Studien. Es hat mir sehr viel Spaß gemacht mit dir zusammenzuarbeiten.

Dr. Tilman Sauerwald und seiner Gruppe danke ich sehr für ihre Offenheit und ihr Interesse daran, die hergestellten Partikel in ihren Messaufbauten zu testen.

Des Weiteren bedanke ich mich bei Dr. Felix Lohmann-Richters, Dr. Aron Varga und Prof. Bernd Abel für die gute Zusammenarbeit. Vor allem danke ich Felix für die Möglichkeit an diesem spannenden Thema mitzuarbeiten und die gute Kommunikation.

Abschließend möchte ich mich bei meiner guten Freundin Christina und der ganzen Familie Maus für viele abwechslungsreiche Tage, gutes Essen und Gespräche über Themen fern vom Laboralltag bedanken. Ganz besonders danke ich jedoch meiner Familie, die mich immer unterstützt, mir den Rücken freigehalten und mich nie eingeengt hat. Meinem Freund Daniel danke ich für die Unterstützung und das gemeinsame Pläne schmieden, sodass Dinge die zu Anfang noch völlig abstrakt und konfus waren, Gestalt annahmen und Realität wurden.

Vielen Dank!

KURZFASSUNG

Der MicroJet-Reaktor stellt eine Weiterentwicklung der herkömmlichen T- und Prallstromreaktoren dar und ist insbesondere für die Herstellung von nanoskaligen Präzipitaten geeignet. Ziel dieser Arbeit ist es die Stärken als auch die Restriktionen der Methode für die Synthese von anorganischen und hybriden Partikeln zu evaluieren und die Eigenschaften der Partikel hinsichtlich ihrer vorgesehenen Anwendung zu optimieren. Dazu werden im ersten Teil Zinn(IV)-oxid-Partikel aus Zinn(IV)-chlorid-Pentahydrat oder Zinn(IV)-*t*-butoxid hergestellt. Die gleichen Reaktionen werden als Becherglassynthesen, teils ultraschallunterstützt, durchgeführt um die Ergebnisse mit denen des kontinuierlichen Prozesses zu vergleichen. Im zweiten Teil wird der Einfluss der Mischeffizienz auf die Synthese von Cäsiumdihydrogenphosphatpartikeln untersucht. Der dritte Teil befasst sich mit der Synthese von organisch modifizierten Silica- (ORMOSIL-) Partikeln. Durch eine Vorhydrolyse der Alkoxysilanedukte gelingt es, die Reaktionsgeschwindigkeit an den schnellen MicroJet-Reaktor-Prozess anzupassen und ein breites Spektrum an sphärischen ORMOSILen, in großer Menge, kontinuierlich zu produzieren (bis 23 g/min). Die Partikel können danach in Siliziumoxykarbide oder karbidabgeleitete Kohlenstoffe überführt werden. Es stellt sich heraus, dass die Eigenschaften dieser Energiespeichermaterialien maßgeblich von der Art und Menge der organischen Gruppen der Vorstufenpartikel bestimmt werden.

ABSTRACT

The MicroJet reactor is an improvement of traditional T-shape and impinging jet reactors and is particularly suitable for the production of nanoscale precipitates. The aim of this work is to evaluate the strengths as well as the limitations of this method for the synthesis of inorganic and hybrid particles and to optimize the properties of the particles regarding to their intended application. In the first part tin(IV) oxide particles are produced continuously by applying tin(IV) chloride pentahydrate or tin(IV) *t*-butoxide as precursors. The same reactions are accomplished as beaker syntheses, some of them ultrasonic-assisted, to compare the results with those from the continuous process. In the second part, the influence of the mixing efficiency on the synthesis of cesium dihydrogen phosphate particles is investigated. The third part is about the synthesis of organically modified silica (ORMOSIL) particles. A prehydrolyzation of the alkoxysilane precursors turns out as a solution to adjust their reaction velocity to the fast MicroJet reactor process and to produce a broad variety of spherical ORMOSIL particles continuously in large scale (23 g/min). The particles can then be converted into silicon oxycarbides or carbide-derived carbons. It becomes apparent that the properties of these energy storage materials highly depend on the kind and amount of the organic groups of the precursor particles.

ABBREVIATIONS

ATR	attenuated total reflection
CDC	carbide-derived carbon
CHN	carbon, hydrogen, nitrogen elemental analysis
CIJR	confined impinging jets reactor
CP-MAS	cross polarization magic angle spinning
ETMS	ethyltrimethoxysilane
FT-IR	Fourier-transform infrared (spectroscopy)
HPMCP	hydroxypropyl methyl cellulose phthalate
MTES, MTMS	methyltriethoxysilane, methyltrimethoxysilane
NMR	nuclear magnetic resonance
ORMOSIL	organically modified silica
PAPTMS	(3-(phenylamino)propyl)-trimethoxysilane
PDC	polymer-derived ceramic
PhTES, PhTMS	phenyltriethoxysilane, phenyltrimethoxysilane
PLGA	poly(lactic-co-glycolic) acid
POSS	polyhedral oligomeric silsesquioxane
PTES	*n*-propyltriethoxysilane
SAFC	solid acid fuel cell
SEM	scanning electron microscopy
SiOC	silicon oxycarbide
SPE-MAS	single-pulse excitation magic angle spinning
SSA	specific surface area
TEM	transmission electron microscopy
TEOS	tetraethyl orthosilicate
TGA	thermogravimetric analysis
$\mathbf{T_m}$	melting temperature
VTMS	vinyltrimethoxysilane
XPS	X-ray photoelectron spectroscopy

TABLE OF CONTENTS

1 INTRODUCTION 1

1.1 Continuous synthesis processes for inorganic and hybrid particles 1

1.1.1 Overview 1

1.1.2 T-mixers and confined impinging jets reactors 3

1.1.3 MicroJet reactor 5

1.1.4 Fluid conditions and mixing efficiency characterization in micromixers 7

1.2 Nanoparticle production by precipitation and sol-gel methods 10

1.2.1 Precipitation method 10

1.2.2 Sol-gel method 12

1.3 Tin(IV) oxide nanoparticles 17

1.3.1 Properties and applications 17

1.3.2 Crystallography 17

1.3.3 Precursors and synthesis routes 19

1.4 Cesium dihydrogen phosphate particles 19

1.4.1 Structure and properties 19

1.4.2 Synthesis 20

1.4.3 Applications 21

1.5 Organically modified silica (ORMOSIL) particles 22

1.5.1 Definitions, synthesis methods and properties 22

1.5.2 ORMOSILs as precursors for silicon oxycarbides (SiOCs) and carbide-derived carbons (CDCs) 25

2 AIMS AND SCOPE 27

3 RESULTS AND DISCUSSION 29

3.1 Tin(IV) oxide particles 29

3.1.1 Continuous and batch synthesis of nanocrystalline tin oxide by sol-gel method and precipitation 29

3.2 Cesium dihydrogen phosphate particles 50

3.2.1 Facile and scalable synthesis of sub-micrometer electrolyte particles for solid acid fuel cells 50

3.3 ORMOSIL particles 64

3.3.1 Additive-free continuous synthesis of silica and ORMOSIL micro- and nanoparticles applying a MicroJet reactor 64

3.3.2 Carbide-derived carbon beads with tunable nanopores from continuously produced polysilsesquioxanes for supercapacitor electrodes....86

3.3.3 Influence of nitrogen-doping for carbide-derived carbons on the supercapacitor performance in an organic electrolyte and an ionic liquid 105

3.3.4 Silicon oxycarbide beads from continuously produced polysilsesquioxane as stable anode material for lithium-ion batteries.... 126

4 SUMMARY AND OUTLOOK 141

5 REFERENCES 145

1 INTRODUCTION

Continuous production means the synthesis of a material without an interruption whereby the starting materials are constantly introduced and the product is constantly discharged during the process. Whereas this proceeding is standard in industry for many liquid and organic molecules, for solids and especially nanoparticle production only a few continuous methods are established.

The drawbacks of continuous reactors are that they are not this flexible usable for various products as batch reactors are, the high initial costs for special reactor designs and the lack of experience with these techniques. On the other hand, continuous reaction pathways offer high production rates through low downtimes, the avoidance of a batch-to-batch reproducibility and an increased operating flexibility and safety.[1-4] The operating flexibility results from the opportunity to change the reaction parameters during the running process: a change of the temperature allows a variation of the particle size within a short time interval. Often an increased control over the reaction conditions is observed, which is caused by the relatively lower volume of the reacting material per area and the resulting faster response time. These specifications promote narrow size distributions in particle syntheses. The locally lower volume and the local separation of reaction educts, intermediates and products can prevent or reduce an accumulation of harmful products and waste. Also, thermal runaways can be prevented, making the process safer.[1-4] All these advantages speak for an enhanced integration of continuous-working reactors in the area of nanoparticle production. The gap of knowledge, which hinders this development, should be reduced by the results of this thesis.

1.1 Continuous synthesis processes for inorganic and hybrid particles

1.1.1 Overview

There are different possibilities to divide continuous synthesis methods for particles into categories. In this thesis, the methods are classified based on the reaction media, the reactor principle and the flow conditions (**Figure 1**).

Particles are mostly produced by gas or liquid phase syntheses. Gas phase syntheses can roughly be divided into gas-to-particle and droplet-to-particle methods (**Figure 1**, left-hand side). The gas-to-particle technique starts from atoms or molecules in a gas phase.[5] The most widely used reactors for the commercial and large-scale production of nanoparticles that work on this principle are (vapor-fed aerosol) flame reactors[5-6]. Substances like carbon blacks, fumed silica, alumina or pigmentary titania are prominent examples: Precursors like oils, $SiCl_4$, $AlCl_3$ or $TiCl_4$ are vaporized and hydrolyzed in the flame[7-8]. The advantages of this pathway are a high product purity and crystallinity, a short process chain and low costs[5-6, 8-9]. The disadvantage is that due to the high temperatures, usually highly agglomerated or aggregated particles are obtained[10]. Other gas-to-particle reactors are furnace, hot wall, plasma and laser reactors[5]. In a droplet-to-particle process, liquids are suspended in a gas and after evaporating the solvent, solid particles remain. Continuous techniques that apply this principle are flame spray pyrolysis and electro sprayings. This route benefits from its simplicity, less aggregation and the option to form multicomponent or porous particles. However, the morphology and the distribution of the formed particles are always determined by the spread and the size of the droplets.[5, 7]

Liquid phase chemical preparation methods offer advantages such as a low particle aggregation due to low process temperatures and the possibility to attach surface modifying additives.[11-12] Furthermore, a high product variety is possible, such as noble metal[13], metal oxide[14], carbonate[15], phosphate[16-17], semiconductor[18], polymer[19], or hybrid particles[20]. Continuous, liquid phase syntheses of particles can be applied in conventional, continuous stirred-tank reactors (and cascades)[21] or flow tube reactors[22] (**Figure 1**, right-hand side). A novel, promising technique in this field came up during the recent decades: the application of micro- and microstructured reactors and mixers[23-26]. Many of these devices can be regarded as miniaturized versions of conventional flow reactors, but with characteristic, internal structures in the range of micrometers. This difference gives rise to some promising options, such as increased mass and heat transfer rates, which allow short mixing times and an improved control about the experimental parameters.[25-26]

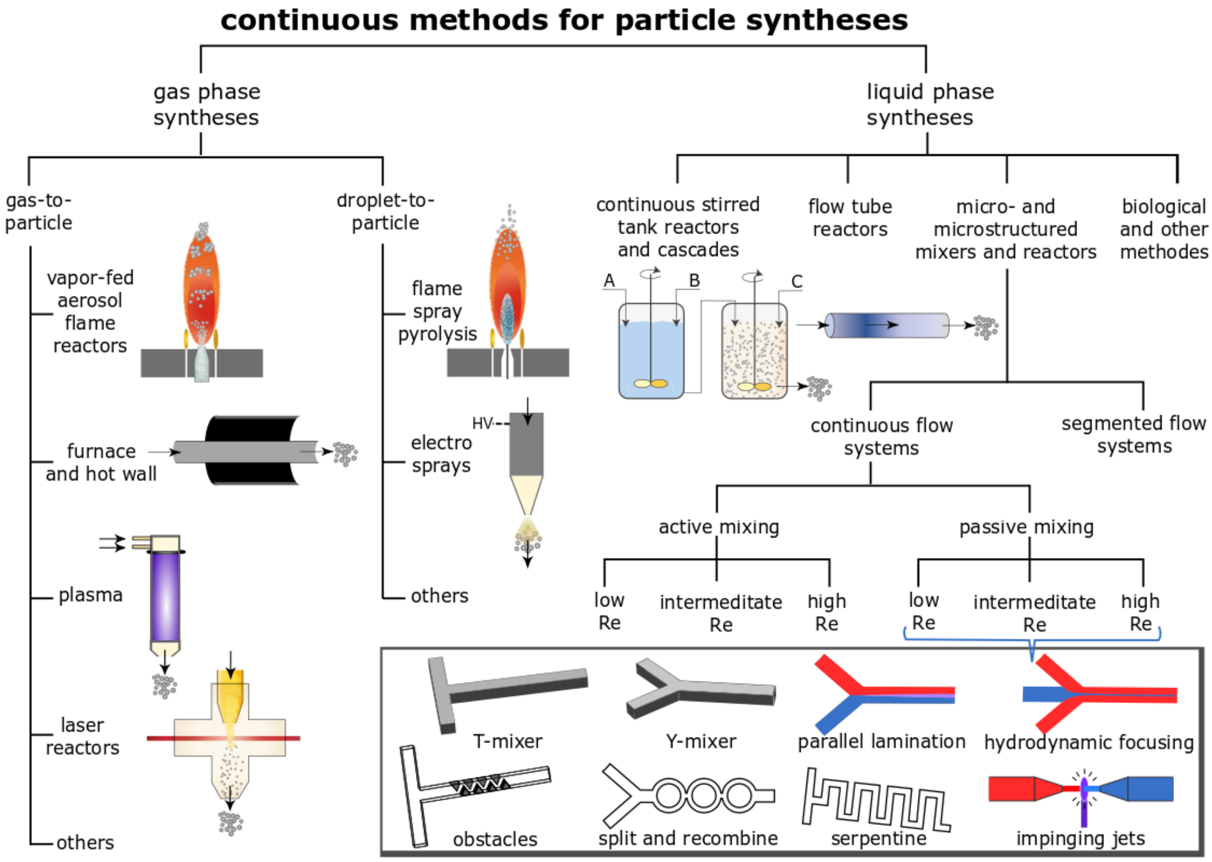

Figure 1: Overview of the two main strategies for the continuous synthesis of (nano-) particles and illustration of the most important reactor geometries.

The words *microreactor* and *micromixer* are often used synonymously whereby the word reactor is preferred if a chemical reaction takes place (in addition to a mixing process). However, through the similar setup and working principles of both devices, the transition is fluent and often not clear definable. In addition, it is more correct to call a device *microstructured* reactor or mixer if just some (characteristic) parts of the device are in the micrometer scale. However, for convenience, the entire working system is often called microreactor, including other components like heat exchangers or tubes.

The following text reviews microstructured reactors and mixers for the particle production in liquid phase (**Figure 1**, right-hand side). However, it is worth noting that these devices can also be applied for the synthesis of organic molecules[26], polymers[19] and for performing mixing processes such as dispersing and emulsifying[27].

Micromixers or reactors for liquid phase syntheses can be grouped into two categories depending on their flow operation mode: continuous flow and segmented flow systems. The latter one can be categorized again in liquid-liquid (droplet based) and gas-liquid (bubble based) segmented microfluidic reactors.[25] In both types, segments are generated, which act as small, confined reaction chambers. Controlling and manipulating the properties of the bubbles or droplets enables the adjustment of the product properties. This method is e.g. applied for the synthesis of colloidal dispersions of noble metal core/shell and multishell nanoparticles[28]. Continuous flow devices work with a single phase. Most of them operate at low (< 10) Reynolds numbers (see also section 1.1.4) with laminar flow and mixing is mainly achieved by molecular diffusion processes.[25-26] This principle usually requires long mixing channels, especially in the case of passive mixers. Passive means that the mixing is carried out without an external energy input. Some of the simplest designs for this type are T- or Y-geometries. The mixing occurs by parallel or serial lamination. The contact area between different fluids in passive mixers can be further increased by hydrodynamic focusing, injection of sub-streams or other split and recombining structures (box in **Figure 1**). Also some active mixers, in which the mixing efficiency is intensified through an external energy input, such as pressure, electrical, magnetic, acoustic or thermal fields, work at low Reynolds numbers.[29-32] These types of reactors and mixers are often arranged with other microfluidic units on a small platform as lab-on-a-chip[33]. A certain degree of chaotic advection can be introduced in passive mixers by the channel design and by adding obstacles into the channels. Popular examples are zigzag[34] and twisted channels or 3-D serpentine[35] structures with ribs or grooves[36].[31, 37] However, several studies show that a generation of eddies or recirculation at obstacles occurs mainly at higher Reynolds numbers.[30, 34, 38] For this reason, these reactor geometries are preferentially applied for operating systems working at intermediate (> 10) and high (> 100) Reynolds numbers.

Mixing at high Reynolds numbers usually relies on high pressure supplies and high streaming velocities. Impinging, high-velocity jets generate vigorous turbulences when they collide and thus the reactor systems can operate with short mixing lengths.[30] The resulting fast mixing times make them particularly suitable for the production of nanoparticles by precipitation: The mixing is in a similar time scale as the nucleation rate and thereby a uniform particle formation is supported.[39] Another example of a reactor geometry that works with turbulent flow conditions is the MicroJet reactor system, which can be considered as a modified impinging jets reactor. Both are described in detail in the following sections.

Besides the described techniques, other processes like biological methods can be applied for the continuous nanoparticles production[40], which will not be discussed in this work.

1.1.2 T-mixers and confined impinging jets reactors

T-mixers and confined impinging jets reactors (CIJRs) have similar geometries: Both consist of a mixing zone connected to two inlet and one outlet tubes. In T-mixers, however, the inlet and outlet tubes are directly connected with each other (**Figure 2 a**). In CIJRs, the pipes lead to a mixing chamber, which usually has a cylindrical geometry and a larger diameter than the inlet tubes (**Figure 2 b**).

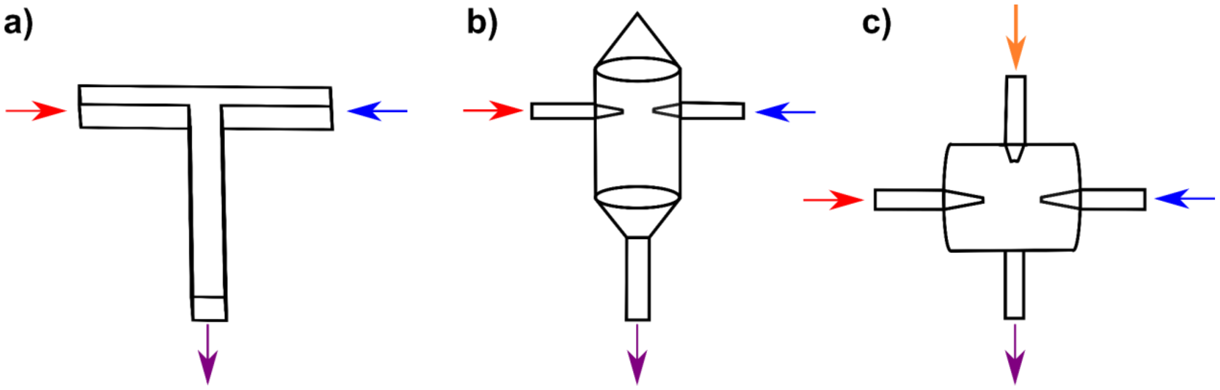

Figure 2: Reactor geometries of a) T-, b) confined impinging jets- and c) MicroJet reactors. In each reactor type, the educt streams (red and blue arrow) enter from opposing sides and collide inside the reactor. The product (purple arrow) leaves the reactors in vertical direction. The MicroJet reactor offers a further inlet (orange arrow) through which a support gas can be introduced.

Marchisio *et al.*[41] compared the efficiency of CIJRs and T-mixers under similar conditions for the production of polymer nanoparticles by solvent displacement. Further on, they developed a mathematical model for the devices under different operating conditions.

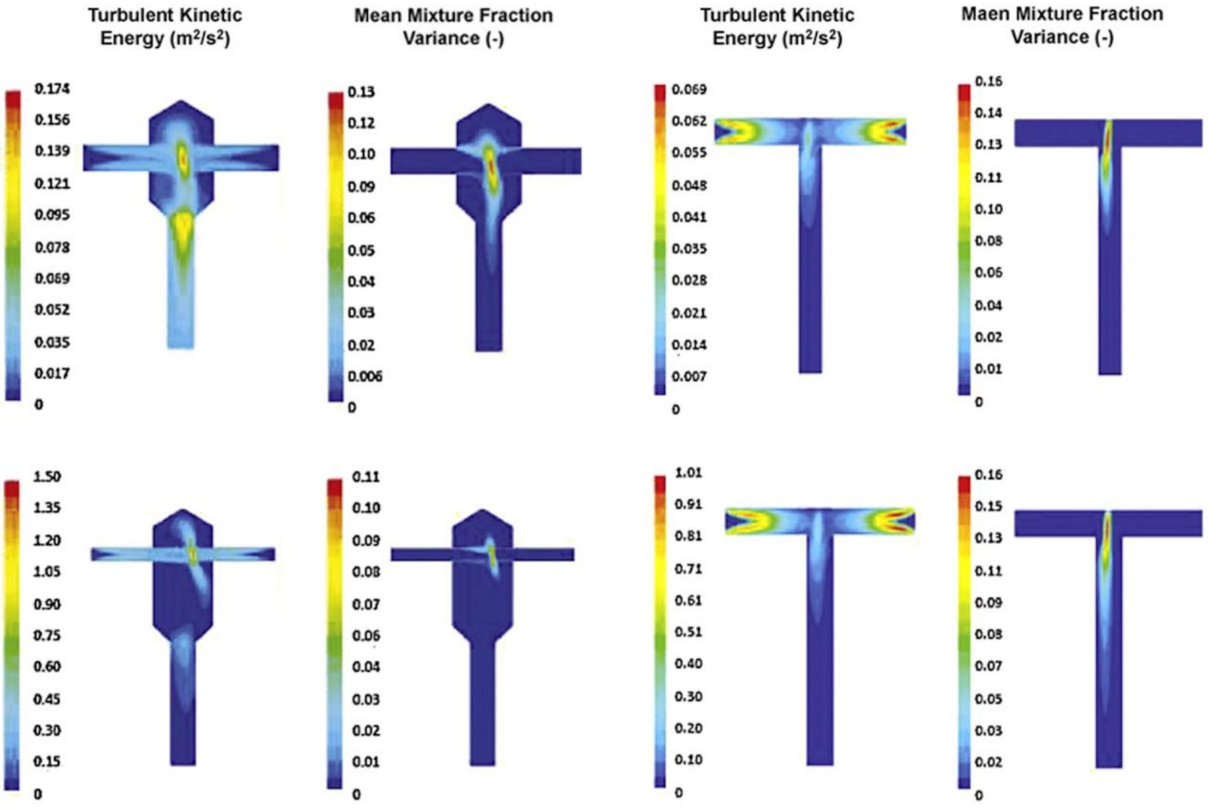

Figure 3: Contour plots of turbulent kinetic energy (m^2/s^2) and mixture fraction variance for CIJRs and T-mixers with inlet jet diameters of d = 2 mm (top) and d = 1 mm (bottom) predicted by computational fluid dynamics simulations. Reprinted from Ref.[41], Copyright 2011, with permission from Elsevier.

Their studies confirmed the importance of the mixing chamber of CIJRs in terms of the mixing performance. The CIJR seemed to be more efficient in converting pressure drops into turbulent kinetic energy and smaller particle sizes were obtained. They also observed that a reduction of the inlet jet diameter leads to an increase of the jet velocity and a faster and more efficient mixing (**Figure 3**).

1.1.3 MicroJet reactor

The MicroJet reactor is a further advancement of a CIJR and was invented and patented by Penth[42]. The improvement consists of a third inlet (vertical to the fluid inlets) through which a supporting gas is introduced into the reactor (**Figure 2 c**). This modification prevents clogging and qualifies the reactor particularly for the synthesis of solid particles. At the inlets, the fluid is forced through narrow nozzles (with diameters in the range of several hundred micrometers), which ensures high jet velocities and turbulent conditions. With this design, the product does not come into contact with the microstructured parts.

Through the varied reactor geometry and the additional gas stream new flow conditions and also new options for nanoparticle syntheses arise. During the last 15 years the MicroJet reactor was tested in academic research for different inorganic, pharmaceutical and hybrid particles (**Table 1**). Wille *et al.*[43] (Clariant GmbH) tested the MicroJet reactor 2004 as part of a screening study of several micro devices with numbering-up options for the production of model azo-pigments. While the process turned out as suitable in general for the pigment syntheses the authors criticized the restriction to only two reactant streams and the limitation concerning the maximum flow rate ratio: If the ratio of the flow rates exceeds a certain value, the collision point shifts in the close proximity of one of the nozzles and leads to clogging. This is why the reactor was impracticable for the desired, special azo-coupling reaction. Later on, Rüfer *et al.*[44] demonstrated the suitability of the MicroJet reactor for a solid forming process in general and studied the influence of different parameters (educt and stabilizer concentration, volume flow rates, support gas pressure) on the particle size. As a model reaction, they chose the precipitation of barium sulfate from barium chloride and potassium sulfate. It was possible to vary the particle size between 60 and 150 nm. Comparable batch experiments produced particles with a minimum size of 300 nm. The authors concluded that the fast and intense mixing in the MicroJet reactor have a positive effect on the nucleation and that clogging was reduced or fully prevented through the impinging jet principle. Dittert *et al.*[45] succeeded in the continuous synthesis of titania nanoparticles with different phase contents (anatase, brookite, rutile, amorphous). The strongest effect on the phase content was observed for changes in the temperature of the educts solutions. Kickelbick et al.[46] found suitable salt precursors for the wet chemical, continuous precipitation of zinc oxide, magnetite, and di-ammonium hydrogen phosphate (brushite) particles. They studied the influence of the flow rate and the process temperature on the particle size whereby it was possible to vary the size of zinc oxide (44–102 nm), magnetite (46–132 nm) and brushite (100–500 nm). The synthesis of the two, more complex ferric oxides ferrihydrite ($Fe_5O_7OH \cdot 4\,H_2O$) and schwertmannite ($Fe_8O_8(OH)_{4.5\text{-}6}(SO_4)_{1.75\text{-}4}$) was determined later from Bertau *et al.*[47]. They studied the influence of different parameters like the pH value, the educt concentrations and the ageing behavior on the chemical product properties. Further on, technical parameters such as the jet diameter and the application of a gas stream were investigated. A reduction of the nozzle and the jet diameter resulted in an increased jet velocity and an intensified mixing. However, reducing the jet diameter from 100 to 50 µm led to an only marginally decreased agglomerate diameter and no changes in the primary particle size. The authors concluded that the velocity with the larger nozzle diameter was already high enough to complete the mixing process before the nucleation start, and that a further increase in the jet velocity only reduces the Brownian agglomeration. The application of a gas stream also enabled a decrease in the agglomerate size and led to a better product homogeneity.

Table 1: Chronological overview of the studies on the MicroJet reactor published in academic literature.

Year	product	reference	year	product	reference
2004	azo-pigments	[43]	2017	ciprofloxacin complex loaded PLGA[c]	[48]
2009	barium sulfate	[44]	2017	carbide-derived carbon	[49]
2011	titania	[45]	2017	yttriumorthovanadate	[50]
2014	zinc oxide, magnetite, calcium hydrogen phosphate	[46]	2018	organically modified silica	[51]
2014	temoporfin loaded Eudragit® RS 100[a]	[52]	2018	cesium dihydrogen phosphate	[53]
2015	ferrihydrite, schwertmannite	[47]	2018	silicon oxycarbide	[54]
2015	danazol/ HPMCP[b], gliclazide/ Eudragit® S100[a], fenofibrate/ different matrices	[55]	2018	nitrogen doped carbide-derived carbon	[56]
2016	drug loaded PLGA[c] (improved by counter ion concept)	[57]	2019	tantalum-doped tin dioxide and cadmium sulfide	[58]
2016	ciprofloxacin complex loaded PLGA[c]	[59]			

[a] Eudragit® RS 100/ S 100 = copolymers of methyl methacrylate and ethyl acrylate/ methacrylic acid, [b] HPMCP = hydroxypropyl methyl cellulose phthalate, [c] PLGA = poly(lactic-co-glycolic) acid

In the period of 2015 to 2017, several articles have been published using the MicroJet reactor for the production of nanoparticles with pharmaceutical applications, e.g. for drug delivery. A. E. Türeli[55] (MJR PharmJet GmbH) proved the suitability of the MicroJet reactor technique for the continuous preparation of pharmaceutical nanoparticles based on solvent/non-solvent precipitation. Different drugs, matrix materials and the influence of several parameters (capillary and nozzle diameter, flow rate (ratio), solvent type, temperature, pressure) were tested, which lead to an efficient control over the particle properties (size, polydispersity index and drug loading). Hereby a novel oral drug delivery system was developed with better *in-vitro* characteristics compared to conventional nanoparticles. Schneider et al.[57] succeeded in the synthesis of nanocarriers with enhanced drug loading by the formation of counter-ion complexes. These reactions benefitted from MicroJet reactor technique by the improved control over the process parameters. In a further systematic design of experiment study[59] they determined the influence of the process parameters flow rate, temperature and gas pressure on the properties of ciprofloxacin loaded poly(lactic-co-glycolic) acid (PLGA) nanoparticles. Contrary to the usual behavior of low viscosity systems, a decrease in the particle size was recorded at lower flow rates. The authors cite the high viscosity of the solvent dimethyl sulfoxide (DMSO) and the high interfacial tension as the reason for this observation. A low flow rate reduces the volumes of solvent and non-solvent in the mixing chamber and a more efficient diffusion of DMSO into the water phase can occur. Other inorganic materials produced with the MicroJet reactor are yttrium orthovanadate particles[50] and metal chalcogenides[58]. Stöwe *et al.*[58] tested the synthesis of doped metal particles in a proof-of-principle study. They synthesized nanocrystalline Ta-doped tin dioxides and cadmium sulfide particles from salt precursor solutions.

This work and the corresponding published articles extend this list by the continuous production of cesium dihydrogen phosphate particles[53], functional organically modified silica (ORMOSIL)[49, 51, 54, 56] and tin(IV) oxide particles from sol-gel precursors.

1.1.4 Fluid conditions and mixing efficiency characterization in micromixers

1.1.4.1 Reynolds number

The flow conditions in microreactors/-mixers are characterized and compared with different dimensionless numbers and the mixing time. The most common value is the Reynolds number[30, 36], which is defined by the ratio between momentum and viscous friction (**eq. 1**)

$$\mathrm{Re} = \frac{u \cdot D_h}{\nu} = \frac{u \cdot D_h \cdot \rho}{\eta} \qquad \textbf{(eq. 1)}$$

With u = average flow velocity [m/s], D_h = hydraulic diameter [m], ν = kinematic viscosity [m^2/s], ρ = fluid density [kg/m^3] and η = dynamic viscosity [Pa·s].

Low Reynolds numbers represent laminar flows, while high Re numbers (above a critical value of approx. 2300 on the macroscale) stand for turbulent flow conditions. Most microreactors operate at Reynolds numbers < 100, whereas the MicroJet reactor technique supplies high pressures and generates turbulent conditions[39, 42, 44]. In **Table 2** the Reynolds numbers of the fluid jets in the reactor were estimated for different parameters (**eq. 1**). It was assumed that the dynamic diameter is equal to the nozzle diameter, that the pressure in the reactor chamber is about 1 bar and that the fluid is water or ethanol. For a flow velocity of ≈ 60 m/s, which is used in this thesis, Reynolds numbers between 1100 and 43000 at the reactor entrance were calculated. The Reynolds number at the mixing point or that of the mixed solutions could not be calculated. For this reason, the given values are not directly comparable with those from the literature. Due to the high Reynolds numbers calculated for the reactor inlet, it is assumed that the conditions present at the mixing point are also in the turbulent range and that the influences of the operating parameters (temperature, flow rate, solvents) on the flow conditions follow the same trend as shown in **Table 2**.

Higher volume flows lead to an increase in the Reynolds number and a reduction in the micromixing time. Various studies[60-63] have investigated the relationship between Reynolds number or micromixing time and particle size distribution.

Table 2: Reynolds numbers of the microjets at the reactor entrance calculated for different parameters with f = flow rate, u = flow velocity, D_h = hydraulic diameter, T = temperature, η = dynamic viscosity, ρ = fluid density and Re = Reynolds number

f [ml/min]	u [m/s]	D_h [m]	T [°C]	fluid	η (p = 1 bar)[64-65] [MPa·s]	ρ[64-65] [kg/m³]	Re
100	23.58	0.0003	20	**H_2O**	1.00	998.2	7061
250	58.95	0.0003	20	H_2O	1.00	998.2	17653
250	58.95	0.0003	**50**	H_2O	0.55	988.0	31769
250	58.95	0.0003	**70**	H_2O	0.40	977.8	43231
250	58.95	0.0003	20	**EtOH**	1.18	789	11825

The studies were carried out for the model system $BaSO_4$ using different reactor types (T-mixer, Y-mixer with connected tubular reactor, confined impinging jet reactor, conical ultrasound reactor). They showed that a faster mixing generates higher supersaturations and thus faster nucleation and growth rates. Consequently, with increasing Reynolds numbers, more and smaller particles are initially formed. However, if the reactant solutions are completely mixed before particle formation begins, a further increase in the Reynolds number has almost no influence on the (primary) particle size distribution (**Figure 4**).[63]

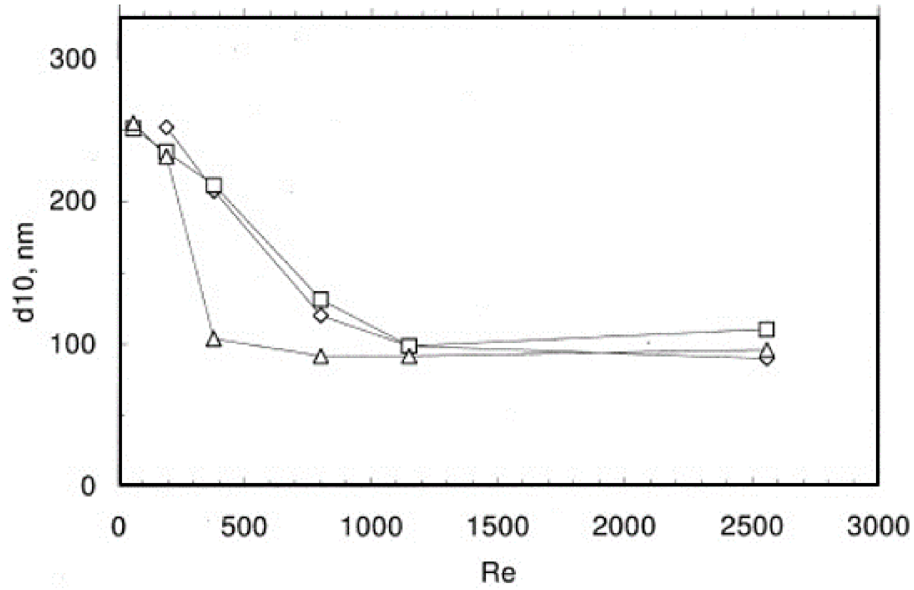

Figure 4: Effect of the jet Reynolds number Re on the number-averaged particle size of precipitated $BaSO_4$. Different concentrations of the aqueous educt solutions of barium chloride and sodium sulfate were tested. (Reprinted with permission from Ref.[61] Copyright 2006 American Institute of Chemical Engineers (AIChE).

1.1.4.2 Mixing time and mixing efficiency

The mixing times of micromixers are typically in the range of a second to a few milliseconds[26]. The simplest way to get information about the mixing time and the mixing efficiency is the flow visualization by adding a suitable dye to at least one of the liquid streams and follow the color change by photo, video or high-speed camera[66] (**Figure 5 a**). Also fluorescent species can be observed by the help of conventional fluorescent or confocal scanning microscopes[67]. The second category involves reaction-type experiments. Again colored species can be generated by simple reactions e.g. due to acid-base reactions with a pH-sensitive dye[68-69] (**Figure 5 b**). More complex experiments base on competitive reactions like it is described by Roessler *et al.*[70] or Fournier *et al.*[71-72] The product ratio of the two competitive reactions depends on the mixing parameters. After evaluating the obtained product ratio, conclusions about the mixing efficiency can be drawn[73] (**Figure 5 c**). A third possibility is to monitor the concentration of a certain species by fluorescent, UV/VIS, IR or Raman[74] spectrometer.[31, 75]

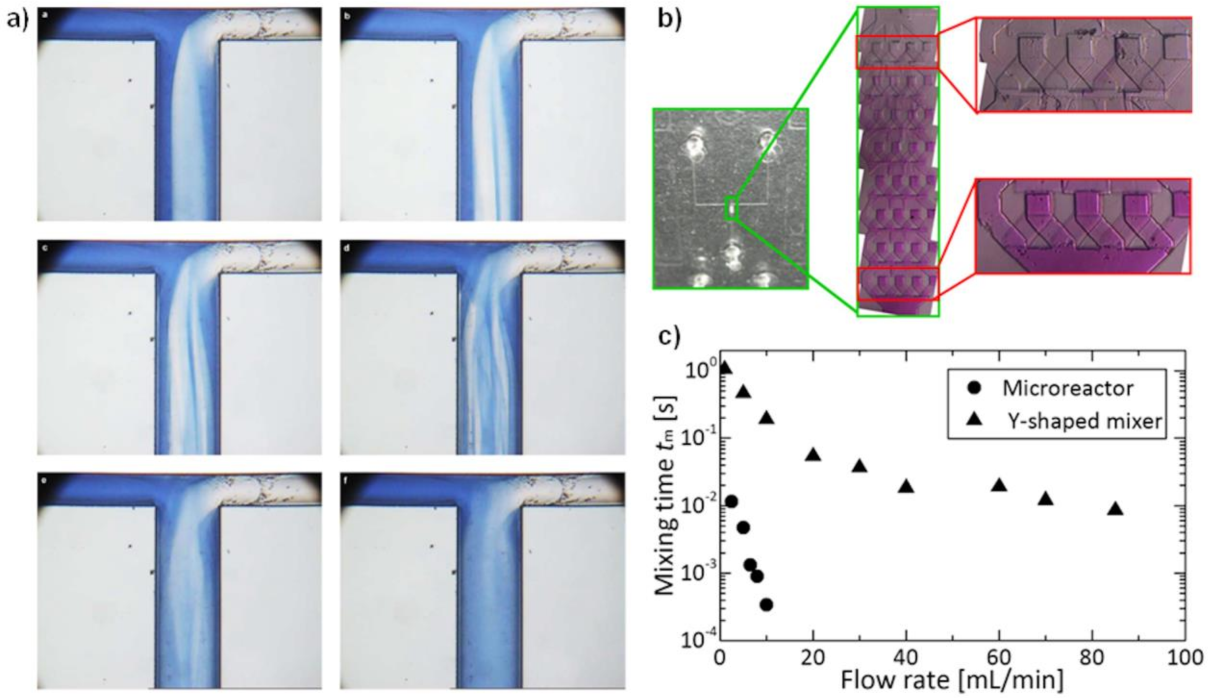

Figure 5: a) Observation of the mixing process between a commercial blue color dye solution and deionized water at applied pressures of (top to bottom) 1.12 bar, 1.88 bar, 2.11 bar; 2.48 bar 2.77 bar and 4.27 bar, reprinted from Ref.[66], Copyright 2004, with permission from Elsevier. b) Mixing experiment between a sodium hydroxide and a phenolphthalein solution in a passive, chessboard micromixer. Reproduced from Ref. [68], https://doi.org/10.1088/0960-1317/16/9/004, Copyright 2006, with permission from IOP Publishing Ltd. All rights reserved c) Dependence of the characteristic mixing time (t_m) on the flow rate. Reprinted from Ref[76], Copyright 2017, with permission from The Society of Powder Technology Japan. http://dx.doi.org/10.1016/j.apt.2017.09.005, https://creativecommons.org/licenses/by-nc-nd/4.0/. The mixing time was evaluated by employing the iodide/iodate test reaction also known as Villermaux-Dushman method[71-73].

1.2 Nanoparticle production by precipitation and sol-gel methods

1.2.1 Precipitation method

Precipitation is a widespread technique for the production of nanoparticles. The simplest version is to dissolve the desired substance in a suitable solvent and precipitate it again, in a controlled but fast manner by the removal of the solvent or by adding an anti-solvent[77]. This pathway is mainly applied for polymers and drug-containing particles[78-79]. For metal oxide particles, a reaction containing precipitation (or reactive precipitation) is preferred due to the low solubility of the oxides in most solvents: The precursors are separately dissolved in an aqueous or non-aqueous media, and by mixing the solutions, the insoluble product is formed by a chemical reaction. For metal oxides the metal species are usually applied as readily soluble salts (like chlorides, nitrates, acetates or oxychlorides etc.)[80] and are precipitated by the addition of a base or an acid. Other possibilities to induce the process are chemical or photo reduction, oxidation, temperature or concentration changes.[81]

Precipitation processes are usually divided into a nucleation and a growing step, which may overlap in their temporal progress. A new phase is formed by primary or secondary nucleation. Primary nucleation, in turn, distinguishes between homogenous and heterogeneous nucleation. During a homogenous nucleation the new phase is built in bulk without any influence of other crystals if the supersaturation is sufficiently high. In heterogeneous procedures, the nucleus forms at a solid surface (e.g. at a vessel wall or a solid impurity). A lower supersaturation is necessary. Secondary nucleation can occur if a population of previously formed particles or seeds of the same material already exist. After a nucleus is built it starts to grow. Ions diffuse to the surface of the precipitate and are incorporated into its structure by surface reaction. Depending on the degree of supersaturation, the growth rate is then determined by the diffusion rate (very high supersaturation) or the surface reactions (lower supersaturation). Furthermore, individual particles can form larger constructs by Ostwald ripening and aggregation. These secondary processes play a not negligible role for the product properties.[81-84]

The classical nucleation theory is the most common model to describe the kinetic of nucleation processes. The basic model[85-88] was developed in the 1930s and was initially applied for the formation of a condensed, liquid phase from a supersaturated vapor. Later it was also applied for liquid-solid transformations, such as crystallizations from melts and solutions[89-90]. During the homogeneous nucleation, a system that is in a stable thermal equilibrium state becomes metastable due to ordinary density or composition fluctuations[89, 91]. The formation of a spherical nucleus results in a changed free energy ΔG, which is composed of a bulk and a surface term (**eq. 2**):

$$\Delta G = \Delta G_b + \Delta G_s = -\frac{4}{3}\pi r^3 \Delta g_b + 4\pi r^2 \gamma \qquad \textbf{eq. 2}$$

$$\Delta g_b = \frac{-\,k_B T \ln(S)}{\nu} \qquad \textbf{eq. 3}$$

With ΔG_b = bulk free energy, ΔG_s = surface free energy, r = radius, Δg_b = difference in bulk free energy per unit volume, γ = surface energy, k_B = Boltzmann's constant, S = supersaturation of the solution, ν = molar volume

The first term describes the change of free energy per volume unit between the supersaturated phase and the phase of the nucleus (see also **eq. 3**). This term is proportional to the volume of the nucleus and negative (exergone). The second term describes the change in free energy, which is necessary to form the new interface between the original phase and the nucleus phases and is always positive (endergone).[89] The function of ΔG is therefore the sum of an r^2 and an r^3 term. While for small radii the surface term dominates and the value of ΔG(r) is > 0, for large radii the bulk term has a stronger impact and ΔG(r) is < 0. Because of this correlation the curve of ΔG versus r (**Figure 6**) passes through a maximum at r = r*, which is called the critical radius.[92]

Nuclei with r < r* are not able to overcome the nucleation barrier ΔG* and redissolve, whereas nuclei with r > r* are stable and can undergo growing processes in the following.[93]

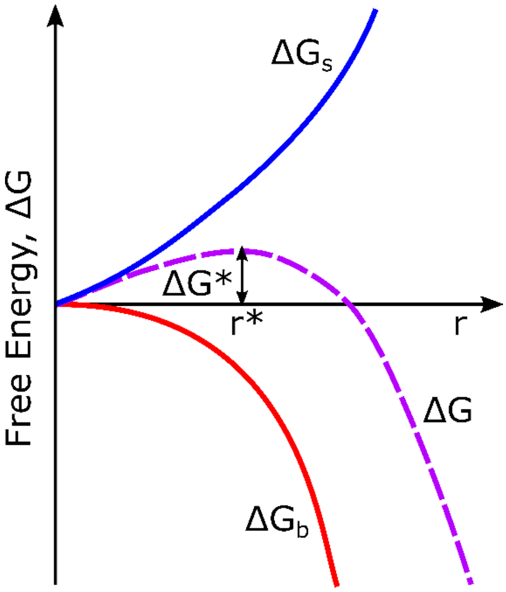

Figure 6: Schematic plot of free energy for nucleation of a sphere with radius r according to the classical nucleation theory.[86-88, 90]

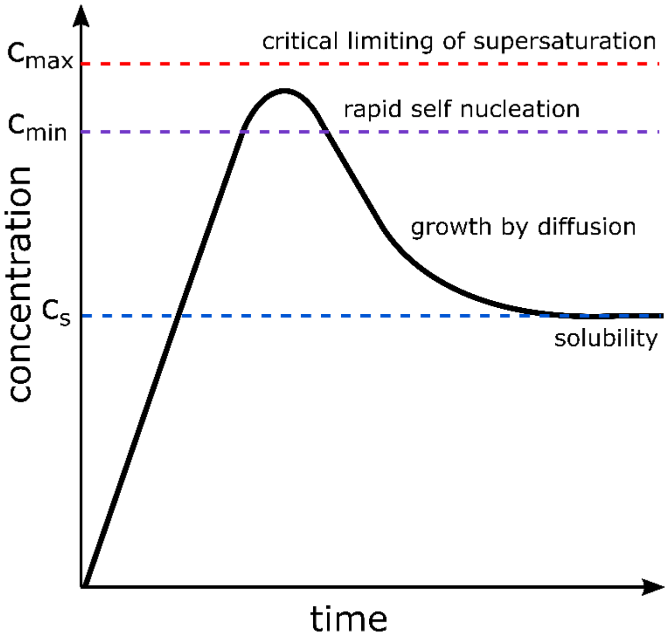

Figure 7: LaMer model of burst nucleation theory.[90, 94]

The nucleation rate can be expressed as Arrhenius based equation, demonstrating the strong influence of the supersaturation (**eq. 4 and eq. 5**)[93, 95]. Below a certain critical supersaturation S* the nucleation rate remains negligible[81].

$$J = A \exp\left[\frac{-B}{(lnS)^2}\right] \qquad \textbf{eq. 4}$$

$$S = \frac{C}{C_{eq.}} \qquad \textbf{eq. 5}$$

With J = nucleation rate, A and B = kinetic parameters, S = supersaturation ratio, C = solute concentration at saturation, $C_{eq.}$ = solute concentration at equilibrium

A further classical model that especially describes the precipitation of monodisperse particles was developed by LaMer and Dinnegar[94, 96]. The amount of a solved species is continuously increased until a minimal concentration for nucleation (c_{min}) is achieved (**Figure 7**). After exceeding this concentration limit, an abrupt, homogenous nucleation occurs, followed by nucleus growth. These processes decrease the supersaturation and if the concentration falls below the minimal value again, no further nucleus can be formed. During the last period of the precipitation process only diffusion controlled growth lead to a further reduction of monomers and the process comes to a standstill as soon as the concentration has fallen to equilibrium (c_s). Homogeneous particle sizes are the result.[92-93]

Based on these classical theories numerous extensions and new models were developed during the last 90 years[93]. They take into account that the nuclei are not always spherical[97-98], that the properties of the surface of the nuclei differ from bulk values[93], and that the surface tensions of the particles depend on their surface curvature[99]. Furthermore, it is doubted that – before particle formation starts – the system is homogenous (molecular disperse). Rather it is assumed that the reagents form long-lasting constructs with sizes smaller than the critical size[100]. Further extensions are developed in the field of multicomponent particles[101].[93]

If a precipitation reaction is applied in the MicroJet reactor the following parameters are deduced as preferential: The solid forming reaction has to be fast and the solubility product of the substance has to be very low to generate a high supersaturation during a short time interval. Thereby a high amount of nucleus is produced, which promote the building of small amorphous or nanocrystalline particles.[82] Also the application of high concentrations is helpful for this aim and a precise adjustment of the temperature. Narrow size distributions can be obtained by avoiding secondary nucleation. This can be realized by a fast reduction of supersaturation through fast surface reaction kinetics. Moreover, a uniform supersaturation without large local differences is beneficial for homogenous particles. Minimizing local concentration gradients requires an extremely fast mixing, ideally faster than the nucleation time.

1.2.2 Sol-gel method

The sol-gel process is a further low temperature synthesis method of which the most industrially relevant products are ceramics, glasses and metal oxides in form of powders, fibers or coatings.[102] Although sol-gel is also a wet-chemical pathway for the nanoparticle preparation, there are clear differences in the process mechanisms compared to traditional precipitations (see below). The reasons why sol-gel reactions are promising candidates to be applied in the MicroJet reactor are that they give access to further product groups, like inorganic-organic hybrids and that they avoid salt byproducts.

Broadly defined, precursors for sol-gel syntheses consist of a central atom that is surrounded by various ligands. For (transition) metal oxide nanoparticles most popular are alkoxides or hydrolysable metal salts, such as $Ti(O^iPr)_4$, $Sn(O^tBu)_4$, $Pb(OAc)_2 \cdot 3\ H_2O$ or $Bi(NO_3)_3 \cdot 5\ H_2O$**[103-104]**. The dissolved educts are transformed into a sol, a dispersion of colloidal particles, which are stabilized by repulsion of their charged double layers. Increasing the local concentration of the particles can lower the distance between them under a critical value and lead to particle attraction. Agglomeration and aggregation processes (normally undesired in nanoparticle synthesis) are the result. Another possibility is that the sol particles form a 3-D network with fluid filled pores, the so-called gel. Traditionally these proceedings are accompanied by hydrolysis and condensation reactions.**[102, 105-106]**

The most thoroughly described alkoxide is tetraethoxysilane (TEOS) and its sol-gel reaction with water to SiO_2 (**eq. 6**).

$$Si(OEt)_4 + 2\ H_2O \rightleftharpoons SiO_2 + 4\ EtOH \qquad (\textbf{eq. 6})$$

The alkoxy groups are first hydrolyzed to hydroxyl moieties (**eq. 7**), which can then undergo condensation reactions. Under the release of H_2O or EtOH molecules a Si-O-Si bonding formation takes place, which leads to a growing network structure ((**eq. 8**) and (**eq. 9**)).**[105]**

$$X_3Si\text{-}OEt + H\text{-}OH \rightleftharpoons X_3Si\text{-}OH + EtOH \qquad (\textbf{eq. 7})$$

$$X_3Si\text{-}OH + HO\text{-}SiX_3 \rightleftharpoons X_3Si\text{-}O\text{-}SiX_3 + H_2O \qquad (\textbf{eq. 8})$$

$$X_3Si\text{-}OEt + HO\text{-}Si\ X_3 \rightleftharpoons X_3Si\text{-}O\text{-}SiX_3 + EtOH \qquad (\textbf{eq. 9})$$

With X = –OEt, –OH or –OSi

For TEOS and other alkoxysilanes these reactions are traditionally catalyzed by an acid or a base. In general, the hydrolysis reactions for TEOS in both cases follow a bi-molecular nucleophilic substitution mechanism (S_N2) with a pentacoordinated transition state (**Figure 8**):

In an acid medium the alkoxy group is first protonated whereby a nucleophilic attack of water at the silicon atom is facilitated. The same mechanism is observed for the acid catalyzed condensation — The hydroxyl group is again protonated and a good leaving group is formed (H_2O). The second step is the release of HOR (hydrolysis) or H_2O (condensation). If the reactions are base catalyzed the nucleophilic attack occurs by a OH^- or a SiO^- molecule and the Si-OH (hydrolysis) or Si-O-Si (condensation) bonding formation is enabled by the elimination of OR^- or OH^-.**[105]**

The full range of sol-gel chemistry is consequently based on hydrolysis and condensation reactions. The tricky thing about controlling these reactions is that the kinetic depends on various parameters and that the hydrolysis and condensations are simultaneous and competing. First of all, the kind of precursor and its reactivity is an important factor, especially if several of them are applied in the same mixture. In this case, their reaction velocities have to be coordinated with each other. Other influencing parameters are the temperature, the kind of solvent, the concentration of the educts, possible additives or undesired contaminations, the mixing speed, the room moisture, the pH value and some more. As implied above, also the reactivity of each intermediate is different and changes constantly, depending on the actual electron donating or withdrawing substituents. The electron density at the silicon atom is lowered by the red marked substituents in the following order[105]:

X_3Si-R > X_3Si-OR > X_3Si-OH > X_3Si-O-SiX_3, with X = –OEt, -OH or –OSi

The morphologies of the products depend on the reaction conditions too: As described earlier, in the acid catalyzed case the protonation occurs at the silicon atom with the highest electronegativity (**Figure 8**). As a consequence, the hydrolysis velocity decreases with progressing network formation. Also, the protonation occurs preferentially at silicon atoms placed at the edge of an already formed larger structure, since these less condensed silicon atoms have a higher electron density. For this reason, the reaction in a weak acid medium (pH ca. 2–6) leads to chain-like, partially branched macromolecules.[81, 106] Under alkaline conditions, the nucleophiles (OH^- or SiO^-) preferentially attack the silicon atoms with high condensation degrees because of their lowered electron densities. As a consequence, the reaction kinetic increases with an increasing condensation degree. Furthermore, the attack of these high cross-linked atoms promotes particulate, spherical structures.[105] Under these basic conditions, the particles are negatively charged. The most popular synthesis method for SiO_2 particles under ammoniac conditions is the Stöber process[107].

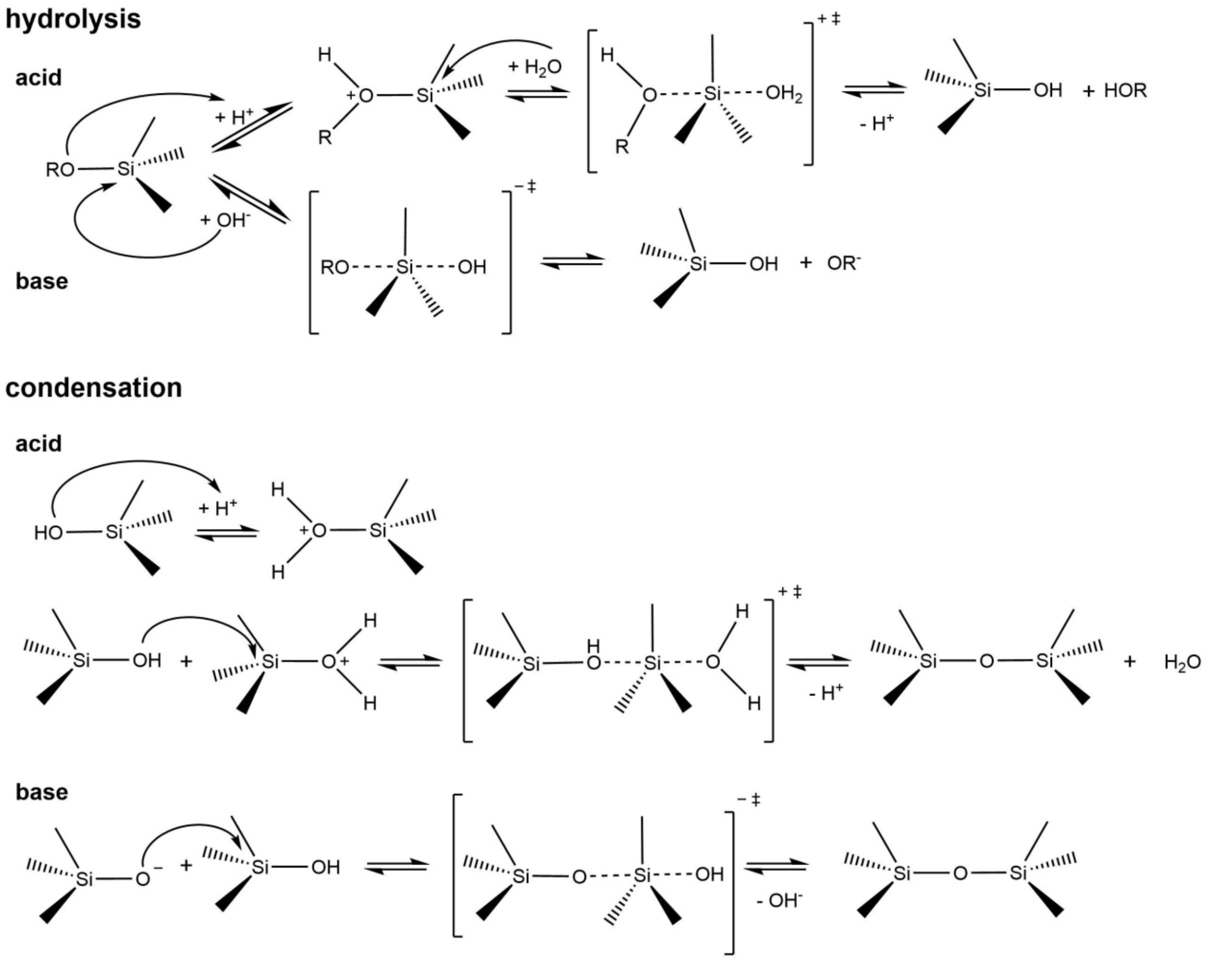

Figure 8: Acid and base catalyzed hydrolysis and condensation mechanisms for tetraethoxysilane.

]

By the application of organotrialkoxysilanes ($RSi(OR')_3$), organotriaminosilanes ($RSi(NR'_2)_3$) or organotrihalosilanes ($RSiX_3$) organically modified silica (ORMOSIL) particles can be produced (see section 1.5). In this case, further influencing parameters like the kind of the organic rest at the silicon atom and the hydrolysable group influence the rate constants. Furthermore, cyclization reactions can occur, which form soluble crystalline or amorphous oligomers or polymers[108].

The hydrolysis and condensation kinetic of trialkoxysilanes are strongly influenced by the organic substituent. The interaction of electronic and steric effects mainly determines the reactivity of the precursor and the reaction rates.

Echeverria et al.[109] compared the kinetic characteristics of hydrolysis and condensation processes for methyl-, ethyl-, propyl-, vinyl- and phenyltriethoxysilane in acidic media via ^{29}Si NMR spectroscopy. A high chemical shift (δ) corresponds to a low electron density on the silicon atom and from the NMR data, the following order was obtained (compare **Table 3** for substance abbreviations and exact chemical shift numbers):

δ (methyl) < δ (ethyl) < δ (propyl) < δ (vinyl) < δ (phenyl) < δ (ethoxy)

During the acidic hydrolysis (compare **Figure 8**) a positively charged transition state is formed, which can be stabilized by a high electron density at the silicon atom. High electron densities therefore lead to an accelerated first hydrolysis rate, which, as shown by Echeverria et al.[109], governs the total hydrolysis rate. The time dependent concentration decreases of the precursors were recorded and are given in **Figure 9**. The curves follow a second-order kinetic.

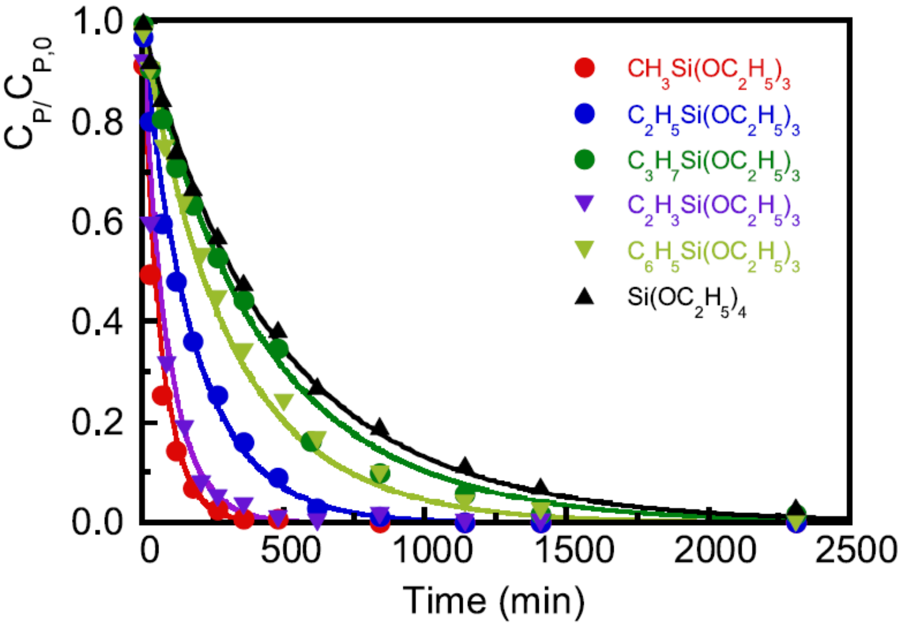

Figure 9: Relative concentration of alkoxysilane precursors as a function of time at 283 K. Reprinted with permission from Ref.[109] Copyright 2019, American Chemical Society.

The experiments reveal the following sequence of the kinetic constants for the first hydrolysis (k_{h1}), which apparently differs from the trend given by the electron densities[109]:

k_{h1} (methyl) > k_{h1} (vinyl) > k_{h1} (ethyl) > k_{h1} (phenyl) > k_{h1} (propyl) > k_{h1} (ethoxy)

Vinyl and phenyl precursors have higher kinetic constants (**Table 3**) than one might expect from their chemical shifts, which could be explained through a better stabilization of the pentacoordinated transition state by electrons from the π-bonds. Compared to all organically modified precursors, TEOS has the lowest hydrolysis constant due to the discussed electronic effects.[109]

For the acidic catalyzed condensation, there are further differences between TEOS and the organically modified precursors with regard to the starting point of the condensation reaction. For hybrid precursors, the condensation started at a precursor conversion of 0.95, while for TEOS the condensation began at a conversion of 0.60. In addition, lower activation energies for the hydrolysis and the condensation reaction were calculated for TEOS. The reasons for the lower condensation of organically modified precursors are the increased electron density at the silicon atom, which reduces the ability for a nucleophilic attack (see **Figure 8**), only three instead of four condensable groups, and the higher steric hindrance. For both kinds of precursors, the condensation rate turned out as the limiting step in terms of the overall reaction.[109]

Table 3: ^{29}Si NMR chemical shifts of different alkoxysilanes and kinetic constants for the first hydrolysis of the substances (data from Ref. [109])

$RSi(OC_2H_5)_3$	R	δ [ppm]	k_{h1} [1/M·min]
MTES	$-CH_3$	-42.7	1.85×10^{-3}
ETES	$-C_2H_5$	-44.4	6.79×10^{-4}
PTES	$-C_3H_7$	-45.3	2.90×10^{-4}
VTES	$-C_2H_3$	-58.0	1.41×10^{-4}
PhTES	$-C_6H_5$	-58.6	4.07×10^{-4}
TEOS	$-OC_2H_5$	-82.0	2.46×10^{-4}

For basic catalysis, few studies have been published that investigate the influence of alkyl, vinyl and phenyl substituents on the hydrolysis and condensation kinetics of organotrialkoxysilanes under comparable conditions. In general, electron-donating substituents in basic media slow down hydrolysis and accelerate condensation. Pohl et al.[110] analyzed the base catalyzed hydrolysis of alkyl tris-(2-methoxyethoxy)silanes. The rate constants for $R'Si(OCH_2CH_2OCH_3)_3$ with different substituents R had the following order:

k_h (R = vinyl) > k_h (R = methyl) > k_h (R = phenyl) > k_h (R = ethyl) > k_h (R = propyl)

These results also confirm that electronic and steric effects influence the reaction kinetics and that unsaturated substituents cause fast kinetics.

If other metal alkoxides are used instead of those of silicon the reaction mechanisms and relationships differ and are less precise investigated. The differences originate from the lower electronegativity and the resulting higher Lewis acidity of the metals compared to the semi-metal Si. A nucleophilic attack is easier and also the property that the metals can exist in several coordination states increases the reactivity. Tin, titanium or zirconium alkoxides are e.g. much more reactive than silicon alkoxides and the addition of a catalyst is often not necessary. The higher reactivity, however, complicates the handing of the precursors and the reaction control, which is why a decrease of the reaction kinetic is often induced by modification of the precursors, e.g. by the addition of protic compounds like carboxylic acids, β-diketone or amino alcohols, especially if gels are required.[105, 111] In contrast to silicon alkoxides, which exist only monomeric, other metal alkoxides can associate by the formation of alkoxy bridges. The driving force for this behavior is the preference of higher coordination numbers. If an association takes place depends on the bulkiness of the alkoxy groups, the size of the metal center and the solvent. The degree of oligomerization increases with an increasing metal size and a decrease in steric hindrance by the alkoxy groups. Another way to expand the coordination number is the addition of (polar) solvent molecules.[112] Tin(IV) *t*-butoxide is monomeric in solution, whereas tin(IV) *i*-propoxide or tin(IV) *i*-butoxide exist as dimeric complexes through the coordination of alcohol ligands ($[Sn(O^iPr)_4 \cdot HO^iPr]_2$ and $[Sn(O^iBu)_4 \cdot HO^iBu]_2$).[113-115] The degree of oligomerization and solvent addition affect the solubility and the reactivity of the alkoxide species.

The most important advantages of this sol-gel method are the variety of the molecular composition of the products, the great control over the size and morphology, the high purity and homogeneity as well as the low reaction temperatures and times.

1.3 Tin(IV) oxide nanoparticles

1.3.1 Properties and applications

Tin (IV) oxide in its cassiterite structure is a n-type, wide band gap (~ 3.6 eV) semiconductor. The combination of a high transparency and conductivity explains its application in many high-technology areas like solar cells[116], liquid crystal displays[117], or antistatic/ anticorrosive coatings[118-119]. Furthermore, SnO_2 is used as catalyst support[120], in membranes[121], transistors[122], lithium-ion batteries[123], or in (gas) sensors[124]. One reason for the outstanding qualities of SnO_2 lies in the dual valency of Sn. Depending on the oxygen partial pressure, tin can reversible change its valence from Sn^{4+} to Sn^{2+}. The conductivity of tin oxide also depends on this phenomenon. Stoichiometric SnO_2 without vacancies is an insulator. Only a certain amount of oxygen defects and the resulting Sn^{2+} ions in the material lead to the common conductivity. The electronic structure is content of many theoretical[125] and experimentally[126] studies. Doping of SnO_2 is a common procedure to influence the conductivity and it opens a further wide research field[127]. While the doping with group III elements generally decreases the conductivity, doping with group V elements lead to an increase. Frequently used doping elements are antimony, molybdenum and fluorine.[128]

1.3.2 Crystallography

Tin oxide reveals various polymorphic solid state structures showing different properties. Besides the most common rutile type (*P4₂/mnm*), SnO_2 can exist in the $CaCl_2$- (*Pnnm*), the α-PbO_2- (*Pbcn*), the pyrite- (*Pa-3*), the ZrO_2- (*Pbca*), the fluorite- (*Fm-3m*) and the cotunnite-type (*Pnam*) (**Figure 10**).[129]

At room temperature, the rutile-type is the thermodynamically most stable phase. It has a tetragonal symmetry with two tin and four oxygen atoms in each unit cell. The tin atoms are six coordinate and the oxygen atoms three coordinate whereby the octahedral share edges and form linear chains in the direction of the c-axis.[130]

During the last years nanostructured SnO_2 was more and more favored for many technologies due to its increased surface area. It was found out that the nanoparticles can also consist of high pressure phases, even if they do not originate from a high temperature and pressure synthesis. One explanation is that a stabilization of the phase is possible through the high surface tension.[131] The most important structures of SnO_2 nanoparticles produced under ambient conditions are the rutile-type, the $CaCl_2$-type and the PbO_2-type.

The cell parameters of this first high pressure phase ($CaCl_2$-structure) and those of rutile are very similar so that a differentiation is sparsely documented. Even from synchrotron measurements only a rough estimation is possible due to the large peak broadening through the nanoscale crystallites.[131] The XRD peaks from the rutile phase and the PbO_2 phase are better distinguishable. The orthorhombic PbO_2-type phase is metastable and forms in bulk under high temperature and pressure. Also a transition from the rutile structure at ca. 13 GPa is possible.[132-133]

Because the orthorhombic phase bears different physical and chemical properties compared to the tetragonal phase several methods were tested to increase the orthorhombic ratio in nanoparticles: The application of certain synthesis or post-treatment techniques (thermal evaporation of tin powder[134], heavy ion irradiation[135]), the use of special ligands or templates[136-137] and the doping of SnO_2 with suitable elements (with Zn[138], Cu[139], Ce[132] or Mg[140]) was studied. However, the building conditions and the possible synthesis strategies are still not fully understood.[132] Also mixed phase SnO_2 could be interesting for several technologies and is content of actual investigations.[141]

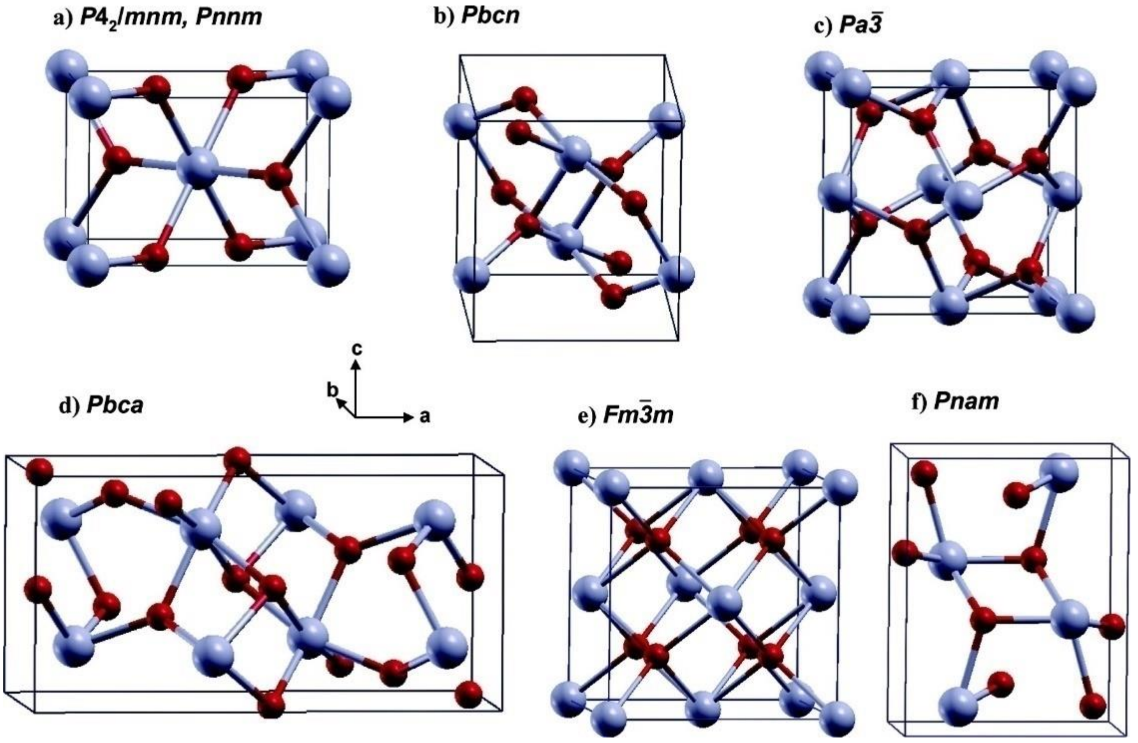

Figure 10: Crystal structures of the different SnO_2 phases: (a) rutile (*P4₂/mnm*) and $CaCl_2$ type (*Pnnm*), (b) a-PbO_2-type (*Pbcn*), (c) pyrite-type (*Pa-3*), (d) ZrO_2-type (*Pbca*), (e) fluorite-type (*Fm-3m*), and (f) cotunnite-type (*Pnam*). Reprinted with permission from Ref.[129] Copyright 2007, American Chemical Society.

1.3.3 Precursors and synthesis routes

The mentioned importance of SnO_2 in many application fields causes the numerous opportunities that were found for the batch nanoparticle preparation. Some examples are hydrothermal[142] or solvothermal[143] methods, microwave syntheses[144], sonochemical techniques[145], polyol syntheses[146], ball mill reactions[147], molten salt methods[148], sol-gel[149], precipitation,[150] and microemulsion[151] proceedings. As precursors, mainly tin (II) or tin (IV) chloride salts or elemental tin are preferred because they are easy to handle and inexpensive. If chloride contaminations should be prevented more sophisticated precursors like tin alkoxides are favored.[149] For many other metal alkoxides solely amorphous (precursor) particles can be produced by sol-gel reaction, which have to be calcined before a crystalline product is formed. In contrast, from tin alkoxides crystalline SnO_2 particles are obtained directly after the synthesis.[152]

Monomeric $Sn(O^tBu)_4$, dimeric $[(SnO^iPr)_4 \cdot HO^iPr]_2$ or polymeric $[Sn(OEt)_4]_n$ have been applied in the past for the production of SnO_2 nanoparticles with sizes between 70 and 250 nm. Because of the fact that the hydrolysis and condensation reactions of these compounds are often very fast and difficult to control, the incorporation of chelate ligands was tested (e.g. in $Sn(acac)_2(O^tAmyl)_2$[153]). A further kind of sol-gel precursors for SnO_2 syntheses are compounds that contain hydrolysable Sn-alkyne bonds like in $RSn(C{\equiv}CR')_3$[154] or $(RC{\equiv}C)_3Sn(spacer)Sn(C{\equiv}CR)_3$[155]. The latter ones are suitable to produce organic-inorganic hybrid materials $[O_{1.5}Sn(spacer)SnO_{1.5}]_n$, similar to ORMOSILS (section 1.5).[156]

Continuous preparation methods for tin(IV) oxide are sparsely described by now. Summarizing the literature about the continuous production of nanostructured SnO_2, SnO_2 composites and doped SnO_2 the applied techniques are hydrothermal[157-159] and solvothermal processes[160-161], flame/ spray pyrolysis[116, 162], or vapor phase deposition/ growth methods[163-164]. Less frequently used methods are electrochemical anodization[165] or microwave flow syntheses[166-167]. There is also one article[58] that applies the MicroJet reactor technique for Ta-doped SnO_2 nanoparticles, which primarily determines the changes in the lattice parameters for different doping levels.

1.4 Cesium dihydrogen phosphate particles

1.4.1 Structure and properties

Cesium dihydrogen phosphate is one of the best-known and well-studied representatives of solid acids, substances that possess properties of both, normal acids and salts[168]. The structure of solid acids correspond to the formula $M_aH_b(XO_4)_c$, whereby M is a monovalent or divalent (metal) cation, such as Li^+, Na^+, K^+, Rb^+, Cs^+, Tl^+ or NH_4^+, XO_4 is an oxyanion, such as SO_4^{2-}, PO_4^{3-}, SeO_4^{2-} or AsO_4^{3-} and a, b, c are integer values[169]. Solid acids are usually water soluble, brittle at room temperature and ductile at elevated temperatures[168]. The special feature of the substance CsH_2PO_4 and some other solid acids is that their proton conductivity, which is low at room temperature, increases abruptly by three to four orders of magnitude (to about $2.2 \cdot 10^{-2}$ S/cm at 240 °C) when a certain temperature (around 230 °C) is exceeded[168, 170]. So far, there are two different explanations for this increase[170]:

The first one assumes that the increase in conductivity is caused by a loss of water through thermal decomposition (**eq. 10**) and that the water enables the proton transfer in the material.[169, 171-172]

$$n\ MH_2XO_4 \rightarrow M_nH_2X_nO_{3n+1} + (n\text{-}1)\ H_2O,\ (n > 0) \qquad \textbf{(eq. 10)}$$

In the case of CsH_2PO_4, a two-stage decomposition, involving the release of water (**eq. 11**), is observed at elevated temperatures, which could explain the increased proton mobility.[169-170, 173] When protons are conducted via the vehicle mechanism, the protons are transported through the material as larger assemblies (e.g. as H_2O molecules)[174].

$$2\ CsH_2PO_4 \rightarrow Cs_2H_2P_2O_7 + H_2O \rightarrow 2\ CsPO_3 + 2\ H_2O \qquad \textbf{(eq. 11)}$$

The second explanation states a phase change of the solid as the reason for the conductivity increase[175-176]. Thereby the substance changes into a superprotonic phase, in which the oxyanions get more freedom of rotation. This creates more options for the formation of hydrogen bonds, allowing proton transfer via a Grotthus mechanism, in which the protons move along the proton defects by hopping [174, 177].[178]

At room temperature, CsH_2PO_4 has a monoclinic structure, in which all PO_4^{2-} tetrahedra are connected by hydrogen bonds and form two-dimensional corrugated layers[170]. As a result, all oxygen atoms participate in hydrogen bonds[178] and between the individual layers the cesium atoms are located[170]. At about 230 °C a phase transition to a cubic structure (CsCl-like) takes place, in which each PO_4^{2-} ion can occupy one of six possible positions in the center of the cube, while the cesium atoms are distributed on the corners.[170] Consequently, the oxyanions in this structure have several options to form hydrogen bonds.

Besides single-salt solid acids, mixed and multiple-salt solid acids or composites can be produced by combining several cations or oxyanions. Thereby certain properties of the material, such as the mechanical and thermal stability can be improved.[169]

1.4.2 Synthesis

Solid acids in general and cesium dihydrogen phosphate in particular are usually produced by wet chemical processes[169, 173, 178-180]. For CsH_2PO_4, an aqueous solution of cesium carbonate is mixed with an aqueous solution of phosphoric acid (**eq. 12**):

$$Cs_2CO_3 + 2\ H_3PO_4 \rightarrow 2\ CsH_2PO_4 + CO_2 + H_2O \qquad \textbf{(eq. 12)}$$

The dissolved product can be isolated by two methods, while the first one involves the addition of a solvent, such as methanol, ethanol or acetone, in which the solid acid is little or not soluble. The fast solvent induced precipitation of a polycrystalline powder opens the possibility of producing large quantities in a short time. As a variation Cs_2CO_3 and H_3PO_4 can be dissolved directly in methanol before joining them to precipitate the product directly during its formation[181].[169]

For the second method the solid is isolated by slowly evaporating the solvent at room temperature or slightly elevated temperatures whereby single crystals can be obtained.[169]

Instead of Cs_2CO_3, an aqueous solution of CsOH can be reacted with phosphoric acid (**eq. 13**):

$$CsOH + H_3PO_4 \longrightarrow CsH_2PO_4 + H_2O \quad \textbf{(eq. 13)}$$

This reaction produces only water as a by-product and the solid can be precipitated as described above. Since CsH_2PO_4 is hygroscopic, a subsequent rapid drying of the solid is essential[180].[169]

1.4.3 Applications

Since about the year 2000, solid acids have been considered as potential electrolytes and membranes for fuel cells[168]. The best known membranes for these applications to date are perfluorosulfonic acid polymers, such as Nafion®.[182] However, these polymers have the disadvantage that they only allow operating temperatures below 100 °C (50–80 °C), as they need liquid water for the proton transport[182]. The low temperatures, require high catalyst loads and pure gases.[169-170] In contrast, CsH_2PO_4 can conduct protons without liquid water, and its melting point is comparatively high (about 345 °C)[183], resulting in an optimal operating temperature of approx. 240 °C[170]. Solid acid fuel cells are therefore intermediate temperature fuel cells[173], offering accelerated electrode kinetics[184] and thus enable a reduced catalyst quantity[170]. Further advantages of SAFCs are their high fuel flexibility, their resistance against catalyst poisoning by CO[183, 185] and a less complicated water management compared to polymer electrolyte membrane fuel cells[186]. The solid state of the electrolyte avoids the risk of leakage, which is easier to handle[187]. Compared to phosphoric acid fuel cells, which operate at similar temperatures (160–220 °C) and contain a highly corrosive liquid electrolyte[182, 187], SAFCs require less complex and less expensive materials for cell design[173].

A current challenge in the development of SAFCs is the water solubility of the solid acids. For this reason, systems are required that prevent the accumulation of condensed water, especially during the fuel cell shut-down[170]. On the other hand, the substance decomposes continuously when operated under dry atmosphere[183], so that a specific humidification has to be performed[17, 188]. In addition, an improvement of the mechanical stability of the particles[189] and a reduction of the production costs[185] is targeted. The latter can be achieved by reducing the amount of platinum catalyst. Approaches based on a reduction of the particle size of catalyst and electrolyte particles have proven to be promising to fulfill this goal, as the electrocatalytically active surface is increased[53]. Furthermore, thinner membranes can be produced by using smaller particles.[53]

Besides the use of CsH_2PO_4 in fuel cells, the application in electrolyzers is tested in the literature[17].

1.5 Organically modified silica (ORMOSIL) particles

1.5.1 Definitions, synthesis methods and properties

Organically modified silica (ORMOSIL) and polysilsesquioxane (PSQ) particles are constituted of organic groups that are connected to an inorganic siloxane backbone. These hybrids combine the properties of an organic and an inorganic system at the molecular level and can serve as a basic unit to build up (nano)composite materials.[190-192]

The organic substituent can thereby act as a customized linker to a specific polymer matrix.[192-193] Furthermore, dyes or other functional molecules can be covalently connected to silica and act as sensors without leaching effects[194-196]. The introduced organic moieties may have the ability to change the original mechanical and chemical values of silica completely: for example, from polar to apolar, from non-adhesive to adhesive or from brittle to rubbery[197-200]. Even more interesting is the option to combine the unique functions of glasses and organic polymers in one material, which characteristics cannot be afforded by one of these classes alone. In this way, Bayindir *et al.*[201] synthesized flexible, transparent and thermally stable superhydrophobic ORMOSIL thin films with a good mechanical stability. Pagliaro *et al.*[202] adjusted the mechanical properties of their ORMOSIL thin films by varying the degree of alkylation. They demonstrated that the challenging aspect to achieve tailor-made properties is the fine tuning of the ORMOSIL constitution.

Commonly, ORMOSILs are synthesized applying the sol-gel process (see section 1.2.2). By mixing silicon alkoxides, amines or halides with various organic groups, several functionalities can be incorporated into the polymer network. Thus, amongst carbon, also other elements like nitrogen or sulfur can be introduced into the structure with this technique.[203-205]

In literature several systems are called ORMOSIL particles that differ in their structural constitution and their synthesis pathways (**Figure 11**):

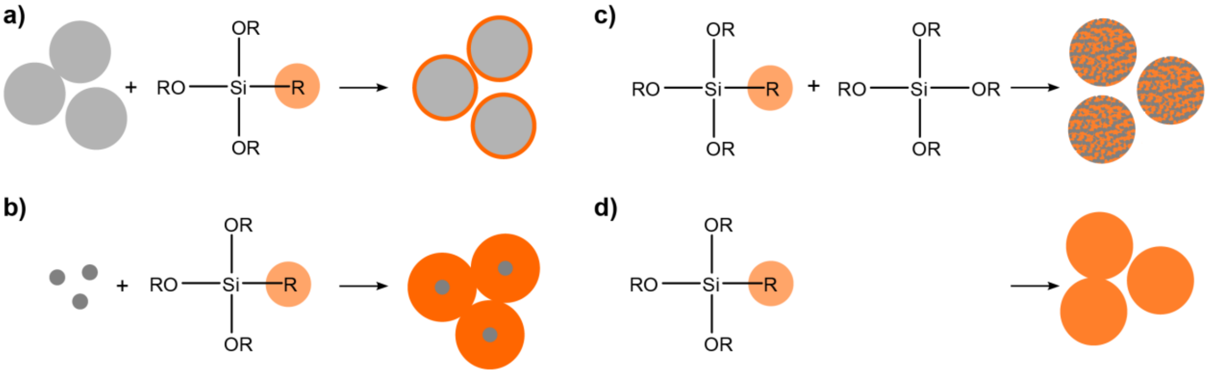

Figure 11: Different synthetic pathways for ORMOSIL particles: a) grafting of organic groups to presynthesized silica particles, b) application of small silica seeds, c) cocondensation of tri- and tetraalkoxysilanes, and d) synthesis solely from trialkoxysilanes.

One possibility is the grafting of organic groups to presynthesized silica particles[206], which are formed via the so-called Stöber route[107] (**Figure 11 a**). This method has the advantage that homogenous, monodisperse spheres with well adjustable sizes are obtained. However, the limited surface of the cores allows rather low organic contents and the particles do not have uniform properties in the profile.

A similar method, which significantly increases the organic content, is the use of a sodium silicate solution, which forms SiO_2 seeds[207] (**Figure 11 b**). Arkhireeva and Hay[207] synthesized ORMOSIL particles (60–180 nm in size) with various organic groups by this route and described it as particularly suitable for the preparation of particles in the intermediate size range. Due to the small size of the seeds, the product particles consist mainly of the trialkoxysilane units.

The third method, which enables a homogenous network structure, is the cocondensation of tetraalkoxides and organotrialkoxysilanes[206, 208] (**Figure 11 c**). This route is often favored because of its robustness.

However, the highest organic content and homogeneity can be achieved if solely the organotrialkoxysilanes are used for ORMOSIL/polysilsesquioxane[§] particle syntheses (**Figure 11 d**). This pathway has been successfully applied for particles based on one or more organoalkoxysilanes.[209-211] Since this method is often emulsion based, the help of surfactants is required, which can contaminate the final products.

Only a few examples have been published and just for a limited number of organic groups where ORMOSIL particles have been produced solely from organotrialkoxysilanes and with an additive-free route[20, 204, 212-213].

Besides the organic functionalities, also the degree of condensation has an effect on the chemical nature of the product, like the solubility or the thermal behavior. Silsesquioxanes can exist as cage or partial cage structured polyhedral oligomeric silsesquioxanes (POSS), ladder-like polysilsesquioxanes and random silsesquioxane networks (**Figure 12**)[193].

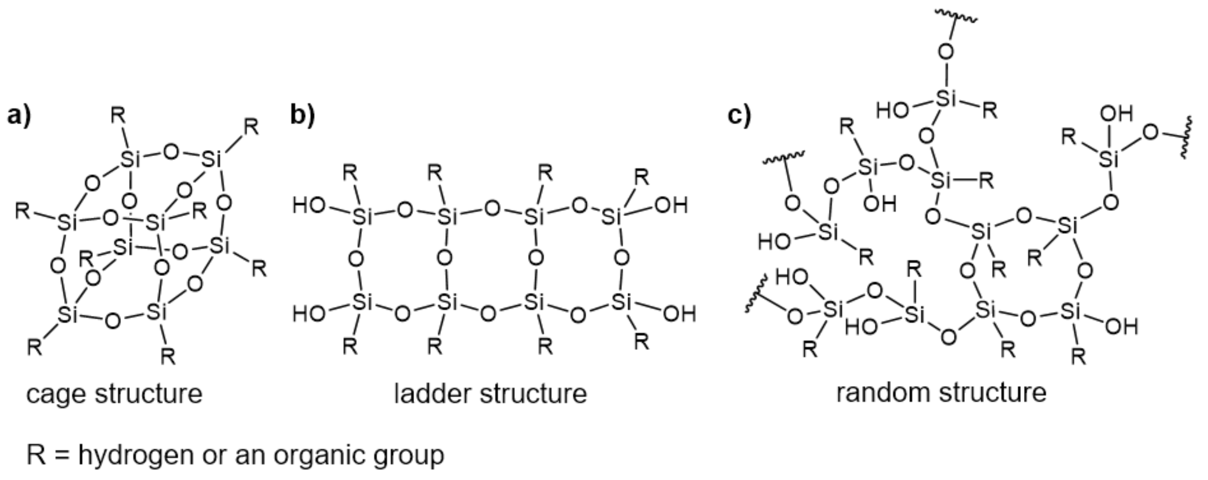

Figure 12: Different possible structures of (poly)silsesquioxanes.

[§] The differentiation between the words *ORMOSIL* and *polysilsesquioxane* is not consistent in literature. Most, polysilsesquioxane is used for oligomers and polymers that are solely build from trifunctional organo alkoxysilanes, whereas ORMOSILs cover a broader spectrum of modified silica (e.g. including surface functionalized SiO_2).

The particles from this work mainly correspond to the latter type. Furthermore, various mixtures of these species and different molar masses can appear. Each of these structures has different chemical properties and especially for phenyl polysilsesquioxane (PPSQ) the degree of crosslinking is an intensely discussed topic:

PPSQs are mostly produced from trifunctional monomers like phenyltrichlor-, phenyltrimethoxy- or phenyltriethoxysilane and exhibit the general repeat unit $PhSiO_{1.5}$. Minami[214], Tatsumisago[215] and Matsuda[216] *et al.* observed that phenylsilsesquioxane particles display a glass transition and a thermal softening at about 150 °C. Using this knowledge, they succeeded in preparing continuous layers from aggregates of spherical particles by thermal treatment (**Figure 13**). Later, they also determined the thermal behavior of copolymerized particles. The temperature and the extent of softening depend on the condensation level and the size and weight of the organic groups. The softening temperature as well as the thermal stability can be modified by adding other organic groups to the PPSQ particles[216-217]. Macan *et al.*[217] determined the influence of methyl, ethyl, pentyl and octyl groups on these material properties: Copolymerization with methyl groups can increase the softening temperature, while cocondensation with longer alkyl groups (e.g. pentyl or octyl) lead to a decrease. Tadanaga *et al.*[218] studied the structure of PPSQ particles and came to the conclusion that the materials, synthesized by a two-step acid–base catalyzed sol-gel reaction, consist of a 'core-shell structure'. The inner core comprised $PhSiO_{1.5}$ species with low molecular weights, which are soluble in ethanol, the outer shell consists of high molecular, insoluble species.

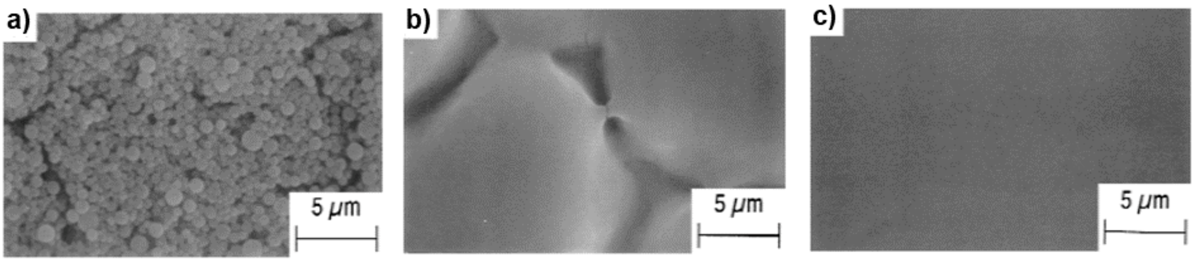

Figure 13: SEM images of $PhSiO_{1.5}$ thick films a) as prepared, b) heat-treated at 200 °C for 2 h and c) heat-treated at 400 °C for 2 h. Reprinted with permission from Ref.[214], Copyright 2005, The American Ceramic Society.

The data on the the thermal and the solubility behavior play a decisive role if the ORMOSIL particles should serve as a kind of a template. Removing the organic content – fully or partly – enables the production of hollow or porous ORMOSIL and SiO_2 particles:

Koo *et al.*[219] synthesized particles based on phenyltrimethoxysilane with a less condensed inner core and a well condensed outer shell. Through washing the particles with ethanol the core was dissolved and hollow spheres were obtained. Moreover, this concept can also be applied for the synthesis of mesoporous[220], raspberry and rattle type[221] particles: Thereby ORMOSIL spheres with different organic groups are formed, followed by a selective dissolution of certain network units.

Another possibility is the removal of all organic moieties by chemical etching (e.g. with oleum-sulfuric acid) or by a thermal treatment (above 650 °C). Thereby carbon free, mesoporous silica particles are prepared.[222-223]

Finally, the reverse procedure is also possible: By removing the silica network (e.g. by chlorine etching at 1200 °C), porous carbons can be synthesized under retaining the initial ORMOSIL morphology (see next section). For all these transformations the kind and amount of organic content, the degree of condensation and crosslinking of the network have a strong influence on the product structure.

1.5.2 ORMOSILs as precursors for silicon oxycarbides (SiOCs) and carbide-derived carbons (CDCs)

Silicon oxycarbides (SiOCs) and carbide-derived carbons (CDCs) are highly attractive as electrode materials for energy storage devices like Li-ion batteries[224] or supercapacitors[225]. The performance of these materials is decisively determined by their specific surface area, pore architecture and microstructure.[226-228] In order to optimize these parameters and recognize dependencies, it is essential to be able to control and adjust them.

One possible way to synthesize SiOCs is to use ORMOSIL particles as precursors and to expose them to a pyrolytic treatment (**Figure 14**, first step). During the heating process, further crosslinking and redistribution reactions take place under Si-O-Si and Si-C bond formation and the release of small molecules. A conversion to an amorphous, glasslike material proceeds (at temperatures < 1200 °C), which can be described as carbon containing silicate with the formula SiO_xC_{4-x}.[226, 229]

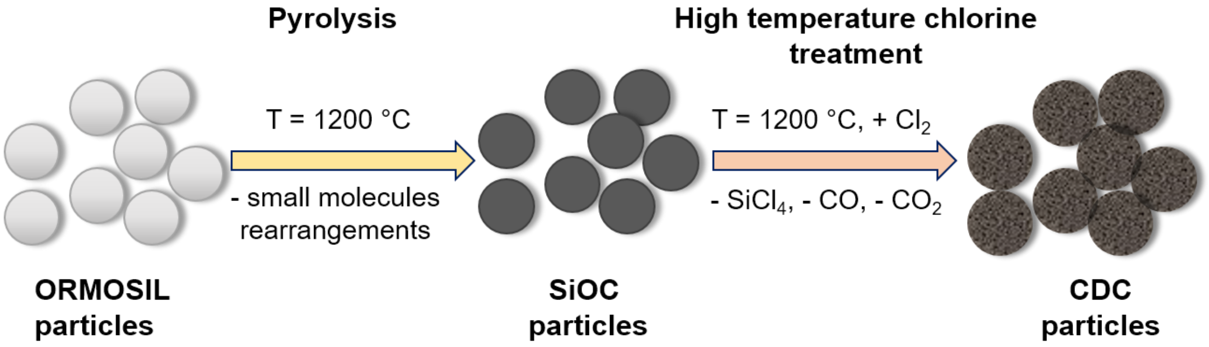

Figure 14: Synthesis strategy for silicon oxycarbides from ORMOSIL precursors by pyrolytic treatment and further processing to carbide-derived carbons by etching at high temperatures. The spherical morphology can be retained during the processes.

Through another network structure, the silicon oxycarbide glasses differ from normal silicate glass in some of their attributes, e.g. in their higher hardness and Young's modulus.[229] The phase composition and the appearance of the microstructure of SiOC have been the subject of several studies and are still not fully identified.[230-231] Silicon carbide and silicon oxide coexist as nanophases: these are built-up of corner-shared tetrahedrons with silicon in the center. The connection of the tetrahedral can occur via oxygen (can connect two tetrahedral) or via carbon atoms (can connect four tetrahedral), which consequently results in a higher crosslinking and the increased hardness. Besides the oxygen and carbon rich SiOC phase a segregated, disordered carbon phase exists. Pyrolysis treatments at higher temperatures result in polycrystalline SiOCs.[229, 232]

Carbide-derived carbons can be obtained from silicon oxycarbides by the removal of the silicon atoms, e.g. by subject them to a high temperature, gaseous chlorine treatment (**Figure 14**, second step). Under these conditions silicon is extracted by forming gaseous $SiCl_4$.[233] The resulting carbon structure, the porosity and the specific surface area depend on various parameters, such as the kind of the educt, the pyrolysis and the halogenation characteristics.[228]

Various precursor materials for the production of silicon oxycarbides and porous carbons have been studied in the literature, but many of them are not suitable for the large-scale production of highly tailor-made products. The application of ORMOSIL particles as precursors is attractive in many regards: the size of the ORMOSIL spheres is well tunable and the morphology can be conserved during the pyrolysis and halogenation process. The ORMOSIL composition can be controlled by the applied alkoxysilane educts. This is useful because the final porosity and specific surface area are highly influenced by the organic leaving groups. Furthermore, doping atoms like nitrogen can be introduced into the product in this way[56].

However not all ORMOSILs and polysilsesquioxanes are suitable for the described pathway. One important qualification is that the precursor polymer network is highly cross-linked so that the morphology can be retained during the pyrolysis step. Otherwise the aforementioned softening of the material can occur. Secondly, high molecular weights are favorable in order to avoid a complete evaporation and to minimize the yield loss during the conversion.

In this work, a spherical morphology of the SiOC and CDC materials was aimed for several reasons: The production of spheres instead of large bodies or thick films has the advantage of reducing or avoiding shrinkage cracks, which may occur during pyrolysis[234]. Furthermore, high packing densities can be achieved by mixing spheres of different sizes. Compared to bulk materials, small particles offer larger surface areas and, in combination with a distinct pore system, lead to electrode materials with high specific surface areas. In CDCs, a spherical morphology can help to ensure that all diffusion paths for the ions are of similar length. This could increase the performance of the supercapacitors at high rates. For SiOCs, the spherical morphology should lead to a homogeneous volume expansion during charge and discharge cycles, thus increasing the lifetime of the Li-ion battery.

2 AIMS AND SCOPE

The aim of this thesis is to extend the existing knowledge about the continuous, wet chemical production of nano- and microparticles.

The following work is submitted as a cumulative dissertation and comprises 5 articles, published in peer-reviewed journals. Additionally, it contains one chapter with unpublished results.

The work focuses on two main topics:

1. The investigation of the strengths and qualities of the continuous MicroJet reactor method with regard to:

    - its suitability for different reaction types, such as precipitation or sol-gel reactions
    - its suitability for particle syntheses compared to other wet chemical production methods

2. The continuous, wet-chemical production of ORMOSIL microspheres, which has been little or not investigated in the literature so far, and their application. This task includes:

    - the successful synthesis of the particles under control of their size and microstructure
    - the application of the particles in energy storage systems, such as Li-ion batteries and supercapacitors

Regarding the first research goal, continuous and batchwise wet chemical synthesis methods are compared for the production of tin(IV) oxide and cesium dihydrogen phosphate nanoparticles:

For SnO_2, a precipitation and a sol-gel pathway are accomplished in a MicroJet reactor, in a beaker, and in a beaker with ultrasonic assistance. The chemical composition, crystallography, morphology, and thermal behavior of the products are studied. Depending on the applied precursors, the resulting particles may be contaminated with chloride. In the literature, it is reported that these contaminations can lead to a changed agglomeration and stabilization behavior of the particles, higher sintering temperatures and a degradation of the electrical properties of SnO_2. Therefore, the influence of chloride on the particle properties and different purification methods are tested with respect to their efficiency and technical effort. The results of the investigations on SnO_2 have not yet been published and are presented in chapter 3.1.

The precipitation of CsH_2PO_4 is also performed as MicroJet reactor and as beaker reaction. For the synthesis, it is particularly important to avoid coalescence of the formed particles, as this leads to large particle sizes and wide distributions. Especially the influence of the fast mixing speed of the microreactor on these properties is investigated, as a more homogeneous reaction mixture could lead to uniform and small particles. These studies (chapter 3.2) were performed and published together with the group of Dr. Áron Varga from the Leibniz Institute of Surface Engineering (IOM) in Leipzig.

The second research goal is the production of ORMOSIL particles from sol-gel precursors. On this topic, four articles have been published (chapter 3.3).

The first article on this subject (chapter 3.3.1) focuses on the general feasibility of a continuous sol-gel synthesis of ORMOSIL particles. The knowledge gained from the sol-gel synthesis of SnO_2 in chapter 3.1 is transferred to the ORMOSIL system. An important initial difficulty is the low reaction velocity of the alkoxysilane precursors in the sol-gel reaction, which is caused by the lowered reactivity of the more stable Si-O bond. A two-step, acid-base catalyzed reaction pathway, which involves a pre-hydrolysis of the precursors, is the key to solve this limitation. Moreover, the mixing speed in the reactor for the given conditions is determined.

Based on these results, three cooperation projects are realized with the group of Prof. Volker Presser from Leibniz Institute for New Materials (INM) and Saarland University. Thereby, the ORMOSIL particles serve as a kind of a template for SiOC and CDC materials. By controlling the constitution and the morphology of the ORMOSILs it is possible to adjust the characteristic values of the SiOC and CDCs in respect to their application.

In the first cooperation project (chapter 3.3.2), phenyl-ORMOSIL particles should be applied as precursors for the synthesis of carbide-derived carbons. Thus, it turns out that the high temperature process, needed for the transformation of ORMOSIL to CDC beads, is only possible if the precursor particles offer a high degree of crosslinking. This condition is not fulfilled for pure phenyl silsesquioxane particles, which consequently lose their shape during the thermal process by undergoing further condensation reactions. The incorporation of vinyl groups into the ORMOSIL network ensures a higher condensation degree and the spherical shape can be conserved. ORMOSIL particles containing different ratios of vinyl and phenyl functionalities are prepared and tested. The studies reveal the correlation of the phenyl/vinyl ratio of the initial precursor particles with the pore structure and the total yield of the CDCs.

In the second study (chapter 3.3.3), the described ORMOSIL and CDC materials are further developed and the influence of a nitrogen doping on the supercapacitor performances is determined. Because of the influence of the pore size distribution on the capacitance, it is important that the particles with and without nitrogen doping have similar sizes and pore structures. Nitrogen is incorporated into the ORMOSIL network by a cocondensation reaction between vinyltrimethoxysilane and [3-(phenylamino)propyl]trimethoxysilane. The sizes and the pore architectures are adjusted by the educt concentrations and the reaction conditions.

The basis for carrying out the third study (chapter 3.3.4) is the ability to produce a broad variety of ORMOSIL particles in large scale. Methyl, vinyl, and phenyl/vinyl mixed precursor particles are synthesized. After pyrolysis the resulting SiOC beads distinguish in their amount of silicon-carbon bonds and the amount of free carbon. In further electrochemical experiments, the different materials are applied in anodes for lithium-ion batteries and the impact of the microstructure on the capacity and performance stability is determined.

3 RESULTS AND DISCUSSION

3.1 Tin(IV) oxide particles

3.1.1 Continuous and batch synthesis of nanocrystalline tin oxide by sol-gel method and precipitation

Tin(IV) oxide is a transparent semiconductor oxide, which is due to its excellent optical, electronic and chemical properties, used in many modern technologies, such as gas sensors[124], solar cells[116], catalysts[235] and it is increasingly debated as anode material for Li-ion batteries[236 237].[128] For the further optimization of these technologies and the development of new systems, two parameters are crucial: on the one hand, the availability of synthesis routes that provide a uniform, reproducible quality and variable scalability, and on the other hand, comprehensive knowledge of the material properties of tin oxide.

SnO_2 nanoparticles can be produced by various discontinuous and continuous synthesis routes:

Examples for batch syntheses are hydrothermal[238], solvothermal[143, 239], sol-gel[149, 240-241], microemulsion[148, 242], precipitation[243-244], microwave[144], ultrasound[245] and electrooxidation[246] methods. Especially the ultrasonic assisted precipitation led, as described by Majumdar and Devi[245], to interesting findings: They tested the influence of ultrasound on the precipitation of SnO_2 nanoparticles. During the process, a formation of gas bubbles takes place in the reaction medium. These bubbles grow in the further course of the process, implode and generate local hotspots (cavitation)[247]. Thereby the mixing conditions are enhanced and a faster and more uniform crystallization can occur, resulting in smaller and homogenous particle sizes[247]. Majumdar and Devi[245] found that extending the sonication time leads to a reduction in particle size and an increase in the particle surface area.

Continuous synthesis methods for nanostructured SnO_2, SnO_2 composites or doped SnO_2 are: hydrothermal[157-158, 160] and solvothermal processes[161], flame-[248-249] / spray-[162]/ and pyrolysis reactions or vapor growth methods[164]. Less commonly used methods are electrochemical anodization[165], microwave flow synthesis[166] and the MicroJet reactor synthesis[58].

Wet chemical synthesis methods have the advantage that less aggregated particles with active surface groups can be obtained[14]. The continuous MicroJet reactor method has already been used by Kickelbick et al.[46] for the synthesis of several other metal oxides, whereby large quantities of the materials could be produced in constant quality. The reactor is similar in design to a T-reactor, but with an additional, fourth inlet channel through which an auxiliary gas can be introduced. The two precursor solutions are forced into the reactor from opposite sides and collide there as fine, impinging jets. High shear forces occur in the collision area, which allow short mixing times and can influence the nucleation of the particles.[39]

In this thesis, both, the discontinuous ultrasonic assisted precipitation and the continuous MicroJet reactor method are applied to produce SnO_2 nanoparticles. It is investigated whether the energy input by ultrasound or by the impinging jets in the MicroJet reactor has an influence on the particle properties, especially the crystallite size and the phase composition. Furthermore, the samples are compared with particles produced by a standard beaker glass synthesis without ultrasound.

For the synthesis two different reactions, a precipitation and sol-gel reaction, with different precursors are used. Depending on the chemical precursors, different impurities are introduced into the products. Precipitation reactions usually involve chloride, which can have a negative effect on the surface and the electrical properties of SnO_2. In the literature, a changed agglomeration and stabilization behavior of the particles[250], a reduced performance of gas sensors[251], a negative impact of chloride on the sintering temperature[250] and an inhibition of catalytic processes[252] is described.

In order to remove chloride afterwards, the particles can be washed or subjected to a temperature treatment. The washing medium is usually water, alcohol or a mixture of both[157, 253-255]. Siciliano et al.[256] proved that a thermal treatment at 500 °C can successfully remove the chloride ions. Yeh et al.[257] describe that a chlorine elimination is also already possible at 350 °C if a H_2 (10 %)/ Ar atmosphere is applied.

In this thesis, the different methods for purification are evaluated under comparable conditions to answer the question which influence they have on the resulting particle surfaces and which is the most effective method in relation to its technical effort. IR, solid state NMR, TG-IR, CHN and EDX analyses are applied to get information about the resulting surface groups, the type of bonding and the temperature resistance.

The following results on tin oxide are therefore divided into two parts: The first part describes the comparison of the different synthesis methods and the material characterization, while the second part deals with the purification of the particles and their annealing behavior.

3.1.1.1 Experimental section

Materials

Tin(IV) chloride pentahydrate (98 %) and tin(IV) chloride, anhydrous (99 %) were purchased from ChemPur, aqueous ammonia (25 %) was obtained from VWR International GmbH. Diethylamine (> 99 %) and *t*-butanol (> 99 %) were purchased from Merck and Grüssing GmbH. All chemicals were used as received.

Precursor preparation: synthesis of $Sn(O^tBu)_4$

The precursor synthesis was carried out according to the methods described by Thomas[258] and Chandler *et al.*[259]. The synthesis was performed under argon atmosphere applying Schlenk techniques. In a three-necked, round bottom flask equipped with a reflux condenser, dropping funnel and magnetic stir bar, 9 ml (76.1 mmol, 1.0 eq.) anhydrous $SnCl_4$ were dissolved in 150 ml dry *n*-heptane and cooled to 15 °C. A solution of 34 ml (330 mmol, 4.3 eq.) diethylamine in 30 ml *n*-heptane were added dropwise and the mixture was stirred for 10 min at RT. After adding 26.56 g (358 mmol, 4.7 eq.) *t*-butanol, a white precipitate was formed. To retain an extensive mixing the solution was diluted by adding 60 ml of *n*-heptane and was stirred overnight (≈ 17 h) at RT. The precipitate was vacuum filtered and washed three times with 20 ml of cold *n*-heptane. The solvent of the filtrate was removed under reduced pressure and a pale yellow solid was obtained. The compound was purified by distillation/ sublimation at 41–43 °C (0.03 mbar) and 20.3 g (65 %) of a colorless, crystalline solid was obtained. ^1H NMR (400 MHz, C_6D_6): $\delta = 1.46$ (s, 12 x CH_3) ppm; ^{119}Sn NMR (149 MHz, C_6D_6): $\delta = -372.2$ ppm; $^{13}C[^1H]$ NMR (101 MHz, C_6D_6): $\delta = 75.0$ ($^2J_{Sn\text{-}C}$ = 23 Hz, 4 x $\mathbf{C}(CH_3)_3$), 34.1 ($^3J_{Sn\text{-}C}$ = 14 Hz, 12 x CH_3) ppm (**Figure S 1** – **Figure S 3**).

Apparatus

MicroJet reactor

The MicroJet reactor setup (**Figure 15 a**) consists of two HPLC pumps (LaPrep P110 preparative HPLC pumps, VWR), which transport the precursor solutions with high pressure (≈ 30–40 bar). The reagent solutions enter the mixing chamber (MicroJet reactor, Synthesechemie, Heusweiler, Germany) from opposing sides through micro nozzles (300 µm) and collide there as impinging jets. After mixing, the product suspension is directly removed from the reactor by a nitrogen gas stream (8 bar), which hits the colliding jets at an angle of 90°. The outlet tube (stainless steel) is 1.5 mm in diameter and had a length of circa 90 cm. The particle suspension was collected in a polyethylene or glass vessel. The desired reaction temperature was adjusted by placing the MicroJet reactor in a tempered water bath.

Beaker synthesis and ultrasonic assisted beaker synthesis

The ultrasonic syntheses are applied by using a Vibra Cell Processor (VCX 500) with a 139 mm probe and a replaceable tip (Sonics & Materials, Inc.). One of the precursor solutions was placed in a double walled beaker (250 ml) and stirred magnetically, the second solution was subsequently added by a dropping funnel (**Figure 15 b**). The temperature of the reacting solution can be adjusted and kept constant by a cryostat whereby a sensor in the solution constantly measured the actual values. The beaker synthesis was accomplished in a glass beaker (250 ml) placed on a hot plate stirrer with temperature sensor and dropping funnel (**Figure 15 c**).

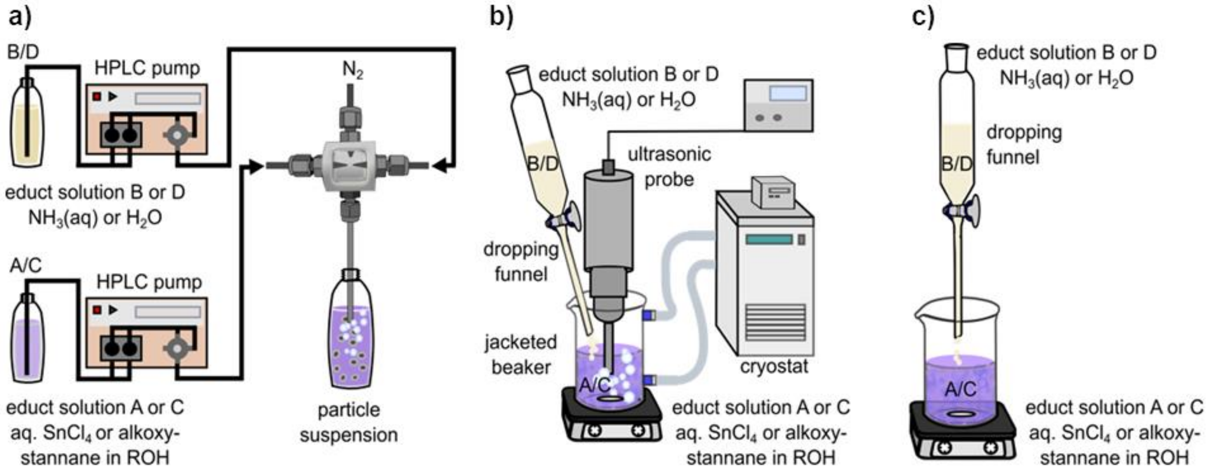

Figure 15: Set-up for SnO_2 nanoparticles preparation by a) MicroJet reactor technique, b) ultrasonic assisted- and c) beaker synthesis.

Preparation of nanoparticles

Synthesis

For the precipitation reactions an aqueous solution of tin(IV) chloride pentahydrate (0.1 M) (solution A) and an aqueous solution of ammonia (2 M) (solution B) were prepared. For the sol-gel reaction a solution of the tin(IV) *t*-butoxide (0.1 M) in *t*-butanol (solution C) and deionized water (solution D) were used. All experiments were carried out at 70 °C.

In the MicroJet reactor process the reagent solutions A and B (for samples from tin chloride) or C and D (for samples from tin alkoxide) were fed into the system with a flow rate of 250 ml/min. Precursor solutions with *t*-butanol ($T_m \approx 26$ °C) as solvent were warmed to 30 °C prior the reaction to liquefy the medium. The precursor solution C was stored under argon und was pumped in the system directly from the Schlenk flask. For the beaker syntheses 80 ml of solution B or D was added dropwise to 80 ml of solution A or C within a time interval of 15 min and stirred afterwards for another 5 minutes. For the ultrasonic assisted version, the ultrasonic treatment was applied during the whole time (20 min) with 150 W.

Post-treatment

The particles were isolated from suspension by centrifugation (8000 rpm, 7012 g, 10 min). A part of these particles were a) separated, b) washed with water (ca. 5 x 25 ml) and c) washed alternating with ethanol and water (ca. 5 x 25 ml). Separated from each other, all samples were dried at 100 °C. The particles were obtained as white or pale yellow powders.

Characterization methods

Solution NMR spectra were recorded with an Avance III HD 400 spectrometer (Bruker) at 25 °C in C_6D_6. The signals were referenced to solvent chemical shifts (for H and C) or to the device parameters (for Sn).

The binding of ethanol to the particle surface was determined by solid-state NMR spectroscopy in single pulse excitation or cross-polarization and magic-angle spinning mode (SPE-MAS- and CP-MAS-NMR) on an AV400WB spectrometer (Bruker). The samples were packed in zirconia rotors, which were spun at 13 kHz under nitrogen. The ^{13}C NMR spectra were recorded at a frequency of 100.7 MHz and a recycle delay of 10 s (SPE-MAS-NMR) and 3 s (CP-MAS-NMR). The contact time in the CP-MAS experiments was varied between 0.2 and 6 ms. Adamantane served as external standard.

Attenuated total reflectance Fourier transform infrared (ATR FT-IR) spectra were obtained by a Vertex 70 spectrometer (Bruker). Prior each sample measurement a reference spectrum was recorded. Then, the dried powders were scanned under ambient air. Each spectrum contains 64 scans with a resolution of 4 cm^{-1} in a wave number range of 500–4200 cm^{-1}. The spectra were normalized to provide a better comparability.

Thermogravimetric analyses (TGA) were performed on a TG 209 F1 Iris (Netzsch). The dried samples were filled in alumina crucibles and heated with 20 K/min from RT to 800 °C under synthetic air (10 ml/min O_2, 40 ml/min N_2).

For TG-FT-IR analyses the TG device was connected with the Vertex 70 IR spectrometer. The dried samples (≈ 50 mg) were filled in alumina crucibles and heated with 20 K/min from RT to 800 °C under synthetic air (10 ml/min O_2, 40 ml/min N_2). The evolving gases were transferred through a heated line (200 °C) to the IR spectrometer. The FT-IR spectra were recorded with 32 scans, a resolution of 4 cm^{-1} and in a range of 4500 to 600 cm^{-1}.

Powder X-ray diffraction was carried out with a Bruker D8 Advance A25 diffractometer in Bragg-Brentano θ-θ-geometry (goniometer radius 280 mm) with Cu-K_α-radiation (λ_1 = 154.0596 pm) and a 192-channel LYNXEYE detector. XRD patterns were recorded in a 2θ range of 7 up to 130° with a step size of 0.013° and a total scan time of one or two hours. The program TOPAS V5 (Bruker) was applied for the Rietveld refinements. For *in-situ* measurements at elevated temperatures the heating chamber XRK 900 from Anton Paar was used. The sample was heated with 20 K/min and kept at constant temperatures during the measurements. Prior each measurement the temperature was equilibrated for at least 10 min. The background was fitted by a Chebychev polynomial function of 15th degree (standard measurements) or 4th degree (measurements at elevated temperatures), the fluorescence induced background was reduced by discriminating the detector. The structure and microstructure refinements were accomplished by the help of crystal structure data from the inorganic crystal structure database (ICSD)[260]. Instrumental line broadening was empirically determined by LaB_6 as a reference material and taken into account for evaluation of the other scans using the fundamental parameters approach[261].

Transmission electron microscopy (TEM) was carried out using a JEM-2010 microscope (JEOL). The samples were suspended in ethanol or water, supported by an ultrasound treatment (10 min). The suspension (30 µL) was applied dropwise on Plano S160-3 copper grids. Unless otherwise stated, the size distributions of the particles were determined by measure the diameter of at least 50 individual particles with the image analysis software ImageJ[262].

The chemical composition and the content of chlorine of the particles was quantified with energy-dispersive X-ray spectroscopy (EDX). Therefore, a Genesis 2000 spectrometer (EDAX) was attached to the chamber of a SEM-7000 microscope. A voltage of 20 kV was applied.

Elemental analyses were performed with a 900 CHN analyzer (Leco).

3.1.1.2 Results and discussion

Comparison of different synthesis methods

Synthesis

Tin oxide nanoparticles were synthesized 1) by precipitation reaction from $SnCl_4 \cdot 5\ H_2O$ and NH_3 and 2) by sol-gel reaction starting from $Sn(O^tBu)_4$ and H_2O. The reactions were performed a) in a beaker b) in a beaker with ultrasound assistance and c) in the MicroJet reactor. The particles were isolated by centrifugation, dried at 100 °C and characterized without further treatments. The samples from precipitation reaction are labeled as: Prec:B_{ap}, Prec:U_{ap} and PrecM_{ap}, according to the applied synthesis method (beaker, ultrasound, or microreactor). For sol-gel samples analogous abbreviations (Sol:B_{ap}, Sol:U_{ap} and Sol:M_{ap}) were chosen. The subscript indicates the post-treatment, whereby ap stands for “as prepared”.

Material characterization

All FT-IR spectra (**Figure 16A**) show a characteristic, broad vibration band at 500 cm^{-1} from bulk metal-oxygen vibration with a shoulder at 655 cm^{-1}. Absorption bands in the range of 830–1350 cm^{-1} can be attributed to the bending modes of different types of surface OH-groups.[263-265] The vibration band at 1042 cm^{-1} from sol-gel samples might also originate from *t*-butoxy groups[266]. The absorption peak at ca. 1635 cm^{-1} is related to the deformation mode of water[263, 265], whereas the peak at 1450 cm^{-1} seems to originate from a derivate of ammonia because it is only present for precipitation samples. In literature this peak is also assigned to N-H stretching vibration and disappears between 200 and 300 °C[250]. The broad vibration band at 2560 to 3660 cm^{-1} can be related to stretching vibration of O-H bonds due to hydroxide groups and adsorbed water.[263, 267]

The XRD scans of the powders (**Figure 16 B**) were analyzed by Rietveld refinement to determine the phase composition, as well as the crystallite size and lattice parameters. The main phase could be identified as tetragonal SnO_2 (rutile type, $P4_2/mnm$, ICSD collection code 647465[268]), whereas a refinement with solely this phase resulted in an inadequate fit in some regions (e.g. at 2θ = 29–31°). In this area the fit is underrepresented. From literature also two orthorhombic high pressure phases HT1 and HT2 ($CaCl_2$-type, *Pnnm* and α-PbO_2, *Pbcn*) are known for SnO_2. The *Pnnm* structure is closely related to the tetragonal phase and cannot be clearly distinguished in powder XRD[131]. The ratio of this phase is therefore attributed to the tetragonal phase and is not separately documented. Implementing the phase *Pbcn* (structure data adapted from Jensen *et al.*[131]) into the Rietveld refinement improves the overall fit. E.g. for the sample Prec:M_{ap} the goodness of fit (GOF) value decreases from 1.48 to 1.10 if a *Pbcn* phase is added and especially the area of 2θ = 29–31° is better described (**Figure S 4**). It is also likely that an amorphous phase is present, which cannot be fully isolated from the *Pbcn* phase due to the large peak broadening, even if an internal standard (α-Al_2O_3) is used.

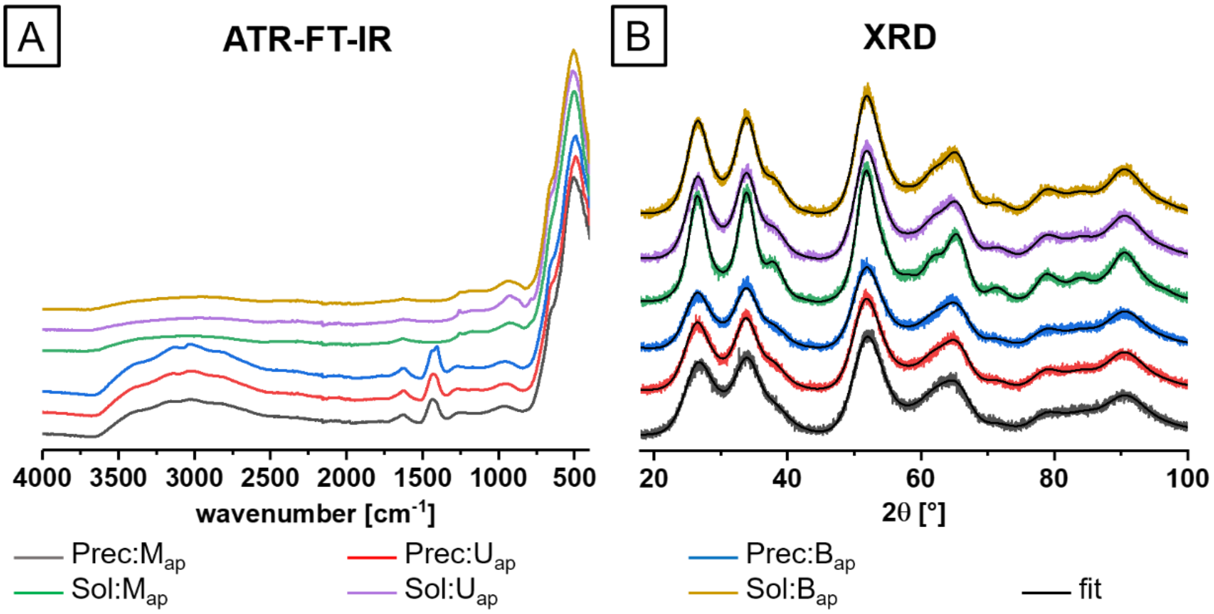

Figure 16: (A) ATR-FT-IR spectra and (B) XRD patterns of the samples prepared by different precursors and synthesis methods arranged in a staggered manner.

For the rutile-type phase, cell parameters of a = 4.742 (1) Å, b = 3.178 (1) Å and for the $CaCl_2$-type phase cell parameters of a = 4.632 (6) Å, b = 5.973 (10) Å and c = 5.330 (6) Å were obtained at room temperature. The portions of the different phases for all samples were refined by keeping these cell parameters constant. By doing so, crystallite sizes (main phase) between 1.7 and 2.3 nm were calculated, whereby the crystallites from sol-gel samples are slightly larger than those from precipitation (**Table 4**).

Table 4: Crystallite, particle sizes and ratios of the rutile ($P4_2/mnm$) and orthorhombic (*Pbcn*) phases obtained by XRD and TEM measurements.

	XRD			TEM
	crystallite size ($P4_2/mnm$) [nm]	ratio $P4_2/mnm$ [%]	ratio *Pbcn* [%]	particle size [nm]
Prec:B_{ap}	1.82 (03)	83	17	2.7 (4)
Prec:U_{ap}	1.86 (03)	78	22	2.3 (4)
Prec:M_{ap}	1.67 (03)	72	28	≈ 1.7[a]
Sol:B_{ap}	2.09 (03)	80	20	3.0 (8)
Sol:U_{ap}	2.05 (03)	80	20	2.7 (4)
Sol:M_{ap}	2.25 (03)	86	14	2.9 (6)

[a] The average size was determined by measuring only 40 individual particle diameters because the particles were very small and therefore highly agglomerated.

Comparing the crystallite sizes from different preparation methods, almost no differences could be observed and also no clear trends appear. The initial assumptions that the high energy input from ultrasound or impinging jets would change the crystallite size could not be confirmed for SnO_2. For precipitation samples the highest orthorhombic fraction is observed for the particles from the microreactor (28 %), the lowest from the beaker synthesis (17 %). For sol-gel samples, in contrast, the values are the same for the beaker and the ultrasonic syntheses (20 %) and the lowest value was calculated for the microreactor pathway (14 %). In addition to the signals of SnO_2 an extra peak at $2\theta = 32.7°$ is visible in some samples, which could be assigned to NH_4Cl[269], the byproduct of the precipitation reaction.

The values of the XRD analyses are comparable with those of similar experiments: Toledo-Antonio et al.[244] precipitated SnO_2 nanoparticles by mixing an aqueous tin(IV) chloride solution and an ammonia solution. The diffraction peaks of the dried (110 °C) sample were indexed to the tetragonal rutile structure ($P4_2/mnm$) with lattice parameters of a = 4.726 (1) Å and c = 3.180 (1) Å and an average crystallite size of 2.6 nm was measured. They also found that the particles from the aqueous precursors contain a large amount of hydroxyl groups in their lattice. This leads to a distortion of the tin-oxygen octahedron symmetry. Sedghi et al.[270] performed an ultrasonic assisted precipitation. For this purpose, ammonia was added to an aqueous tin(IV) chloride solution and treated with ultrasound at 70–80 °C for 2 hours. XRD measurements of the dried (70 °C) powder confirmed that the tetragonal cassiterite structure was obtained with a crystallite size of 2.2 nm. SnO_2 powders produced from Majumdar et al.[245] by a sol-gel reaction had the same crystal structure with crystallite sizes between 2–3 nm.

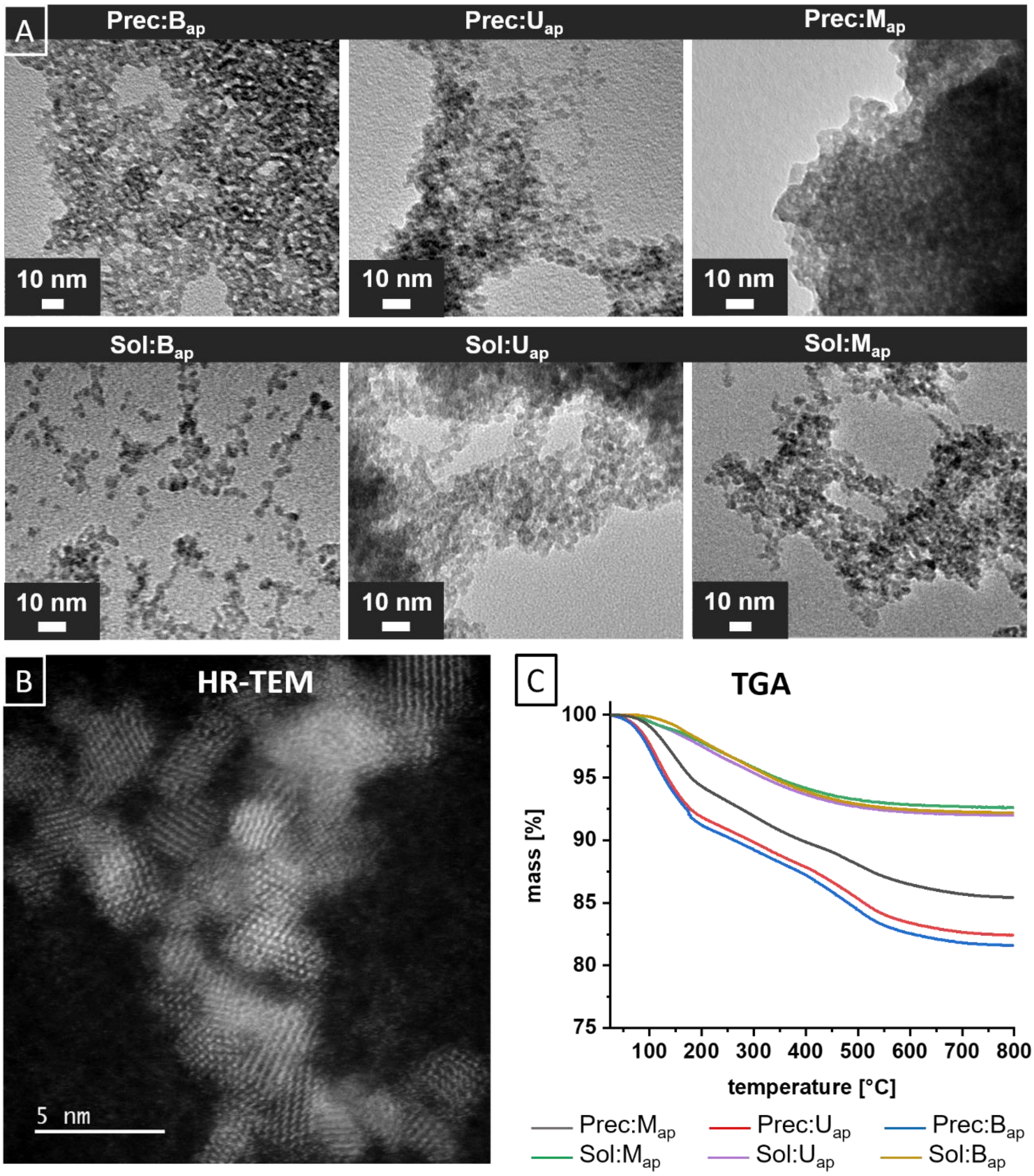

Figure 17: (A) TEM images and (C) TG curves of the SnO_2 samples prepared by different methods and precursors. (B) HR-TEM image of the sample Prec:U$_{ap}$.
Pre:M$_{ap}$, Prec:U$_{ap}$ and Prec:B$_{ap}$ are the samples obtained by precipitation reaction in the microreactor, in a beaker with ultrasonic treatment and in a beaker without additional external energy input. The samples Sol:M$_{ap}$, Sol:U$_{ap}$ and Sol:B$_{ap}$ were obtained with the same technical methods but from sol-gel precursors. All samples were used "as prepared", which means without any further purification.

TEM images (**Figure 17 A**) confirm the formation of ultrafine particles with sizes of 2–3 nm for all samples, independent of their preparation route (**Table 4**). The particle sizes are close to the measured crystallite sizes and are also comparable with the particle sizes obtained from other groups under similar conditions[243, 271].

The presence of an orthorhombic phase was additionally determined by HR-TEM (**Figure 17 B and Figure S 5**). The images showed clearly the atomic planes of the nanocrystallites from the sample prepared by the ultrasonic assisted precipitation. Most measured interplanar distances could be assigned to the tetragonal rutile phase (d ≈ 3.4 Å and d ≈ 2.7 Å). However, no hints for the existence of an orthorhombic phase (d ≈ 2.9 Å) could be detected. Due to the little amount and the small size of the crystallites the Fourier transformed signals were not sharp enough to decide if there is a signal for the orthorhombic (111) crystal plane between the signals from the (110) and (101) crystal plane from the tetragonal phase (**Figure S 5**). Consequently, an existence of an orthorhombic phase in addition to the rutile phase could not be confirmed or excluded by TEM analysis.

Thermal properties

TGA curves (**Figure 17 C**) display significant mass differences between precipitation and sol-gel samples. The mass loss of precipitation samples is between 15 % (Prec:M_{ap}) and 18 % (Prec:B_{ap}), for sol-gel samples the values lie between 7 % (Sol:M_{ap}) and 8 % (Sol:U_{ap}). The type of leaving groups causing the different losses are determined in the second part of the article. Comparing the samples produced by different methods (beaker, ultrasound, microreactor), no strong influences on the mass losses are observed, leading to the conclusion that the particles have similar surface areas and groups.

Table 5: Chemical composition of the as prepared SnO_2 particles obtained from elemental analysis and EDX. n. d.: not detectable

	elemental analysis			EDX			atomic ratio	
	C [wt.%]	H [wt.%]	N [wt.%]	Sn [wt.%]	O [wt.%]	Cl [wt.%]	O:Sn	Cl:Sn
Prec:B_{ap}	n. d.	2.0	2.7	74.3	17.6	6.2	1.8	0.3
Prec:U_{ap}	n. d.	2.0	2.3	75.6	16.2	5.7	1.6	0.3
Prec:M_{ap}	0.2	1.8	2.0	74.7	19.4	4.6	1.9	0.2
Sol:B_{ap}	0.4	1.3	n. d.	78.7	18.7	0.5	1.8	0.02
Sol:U_{ap}	0.5	1.3	n. d.	78.6	18.6	0.4	1.8	0.02
Sol:M_{ap}	0.4	1.5	n. d.	79.6	17.6	0.6	1.6	0.02

The chemical composition of the particles was studied with elemental analysis and EDX (**Table 5**). The particles from precipitation involve 2.0–2.7 wt.% nitrogen and 4.6–6.2 wt.% chlorine, introduced by the educts. In the sol-gel samples the nitrogen content was below the detection limit, and a slightly increased amount of carbon was recorded. Surprisingly the sol-gel samples also contain a small amount of chlorine (≈ 0.5 wt.%), which must be derived from the tin(IV) chloride used for the synthesis of the sol-gel precursor tin(IV) *t*-butoxide. All samples display similar oxygen to tin ratios (1.6–1.9).

According to the presented results, small SnO_2 nanoparticles (2–3 nm in size) could be produced by different methods. It turned out that the type of the synthesis method has only a slight influence on the resulting particle properties. However, important differences between precipitation and sol-gel particles could be detected, especially with respect to their mass loss in TGA and the type and quantity of contaminations.

Purification methods

Since these aspects could be relevant for certain applications, different purification methods were studied regarding to their efficiency and technical effort to free the particles from chlorides and carbon hydrogen species. Therefore the microreactor samples from the precipitation reaction were a) washed with water (Prec:M_{H2O}) b) washed alternately with water and ethanol (Prec:M_{EtOH}), and c) tempered at 550 °C (Prec:M_{temp}).

Material characterization

ATR-FT-IR spectra (**Figure 18 A**) show a slight decreased N-H absorption band for samples washed with H_2O or EtOH. After tempering the particles, all vibration bands in the range of 4000–900 cm^{-1} disappeared and new bands at 600 and 465 cm^{-1} for the antisymmetric and symmetric stretching vibrations of Sn-O-Sn groups became visible.[145]

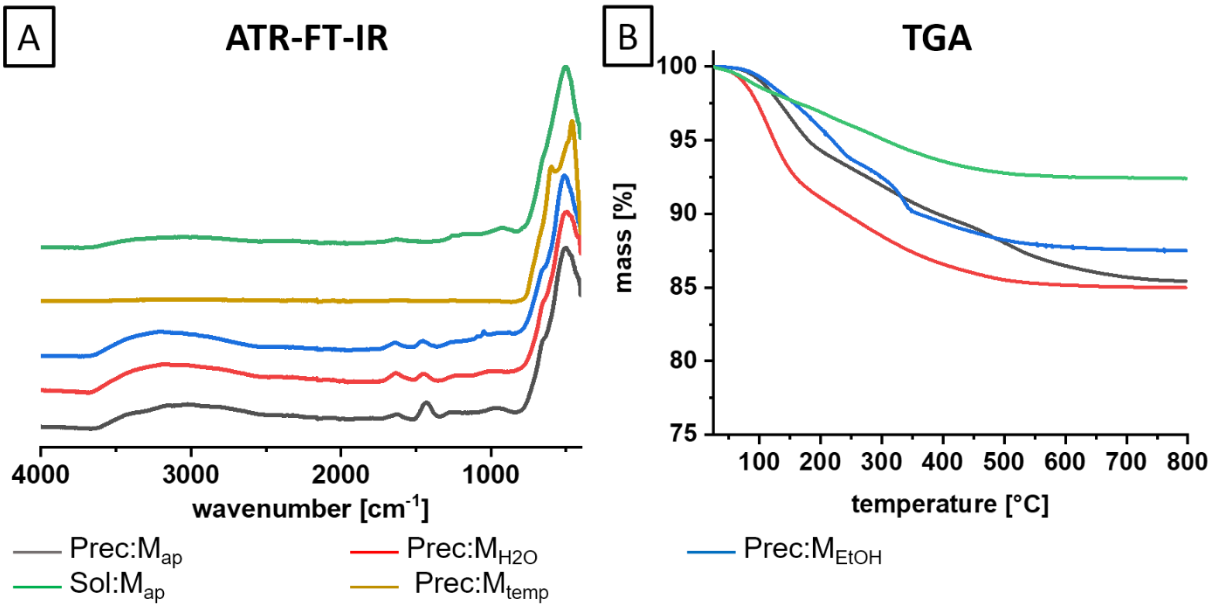

Figure 18: (A) ATR-FT-IR spectra and (B) TGA curves of the SnO_2 powders with different post-treatments.

The crystallite sizes obtained from XRD of the washed particles correspond with those of untreated samples. The signal of NH_4Cl at $2\theta = 32.7°$ is no longer observed, implying that the amount of the chloride byproduct after washing is at least below the XRD detection limit (**Figure S 6**).

The purification of the particles with water had the problem of high yield losses. It is known that in water, especially in ammoniac containing medium, soluble tin hydroxide and oxide hydrate complexes are formed[272]. The extent depends on numerous parameters, such as the washing volume, the amount of washing medium, the washing duration, the dispersion and segregation method, the pH, the temperature etc. These disadvantages can be avoided by using ethanol as washing solvent.

Thermal properties

The thermal behavior of the samples was investigated with TGA under synthetic air (10 ml/min O_2, 40 ml/min N_2) (**Figure 18 B**). The mass losses (Δm) of all samples are listed in **Table 6** and vary between 8 and 15 %, whereas it is noticeable that Δm of the as prepared sample and the sample that was washed with H_2O are almost identical and higher than the mass loss of the sample that was washed with EtOH. For a better insight into the decomposition processes the emerging gases were identified by FT-IR spectroscopy. Using a TG-IR coupling measuring system, temperature-dependent 3D-IR spectra were recorded (**Figure 19**) and give an overview which gases come up, reach maximums and disappear during the temperature program (see also **Table 6**).

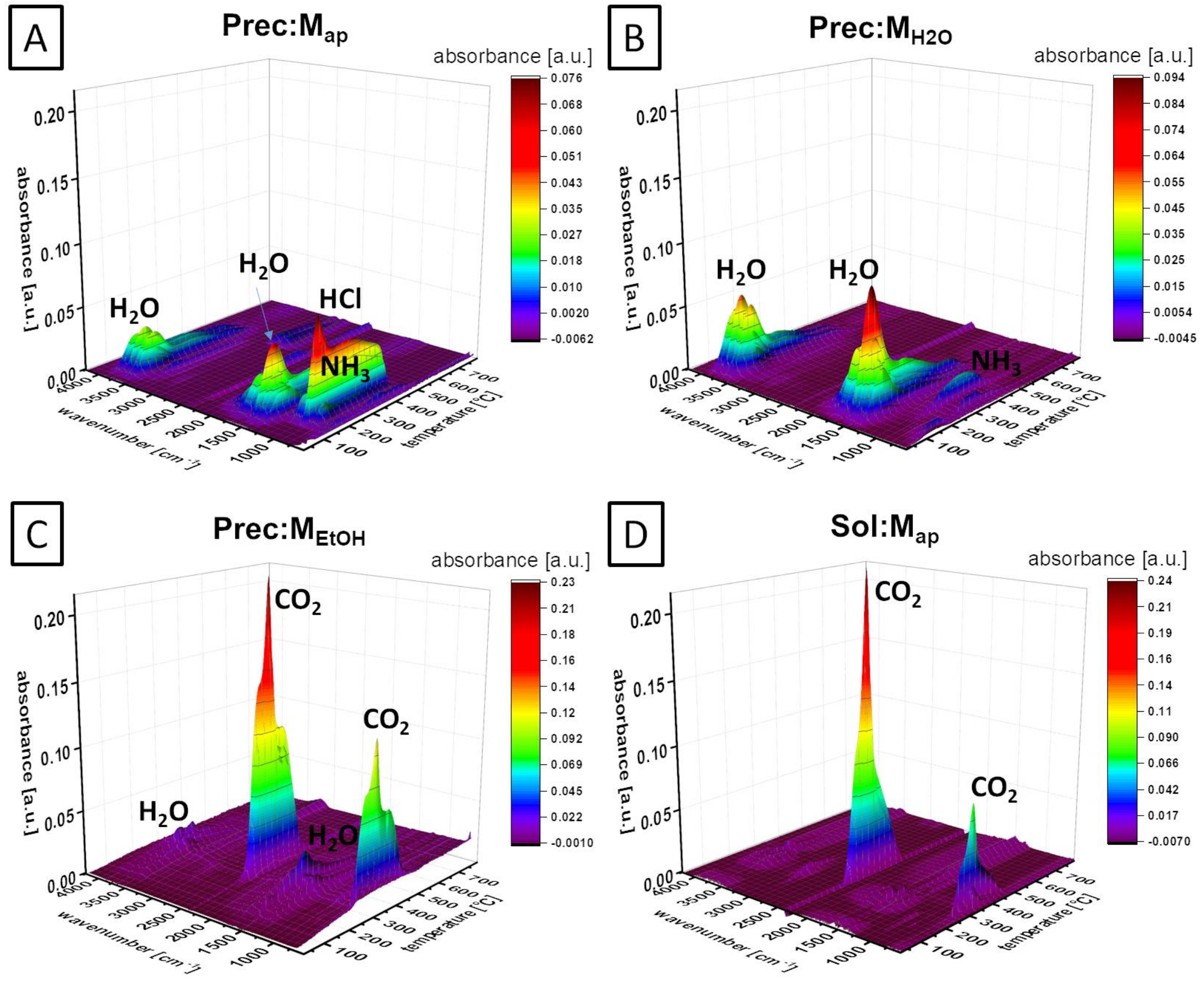

Figure 19: 3D-FT-IR spectra of the SnO_2 samples with different post-treatments. The spectra show the gas emission of the samples during the TG measurements. The different microreactor samples from the precipitation (Prec:M) and sol-gel reaction (Sol:M) were analyzed. In addition to the samples without post-treatment (Prec:M_{ap} and Sol:M_{ap}), the precipitation samples were tested that were purified with water (Prec:M_{H2O}) or with water and ethanol (Prec:M_{EtOH}).

Up to high temperatures, gas evolutions were detected and it is obvious that the sample Prec:M_{EtOH} and the Sol:M_{ap} show high CO_2 signals, contrary to Prec:M_{ap} and Prec:M_{H2O}.

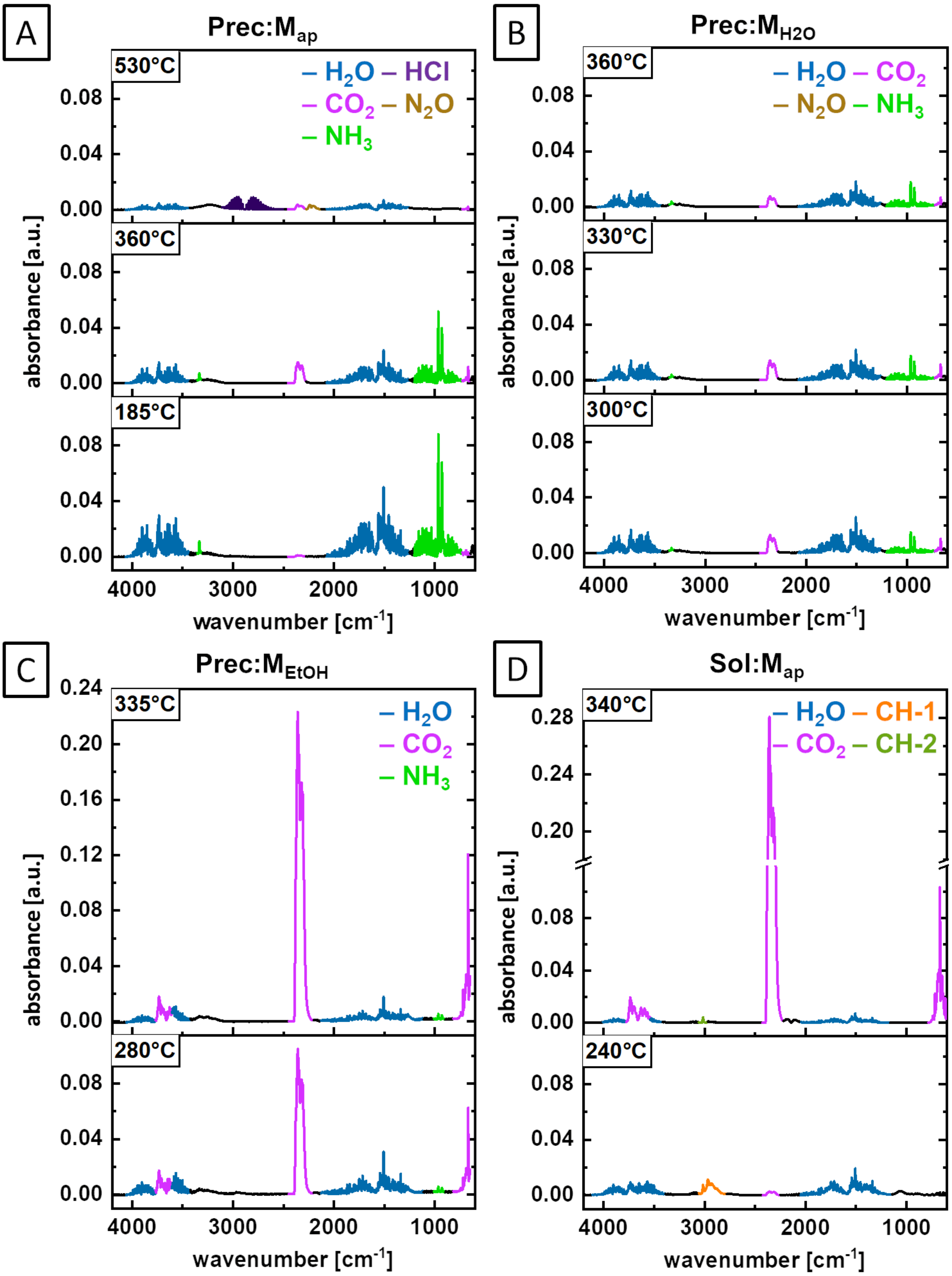

Figure 20: Selected 2D-spectra extracted from 3D-FT-IR plot of the SnO_2 samples with different post-treatment.

In **Figure 20** isolated spectra for each sample are displayed in which several detected gas species exhibit a maximum in absorption and the single vibration bands are clearly recognizable. The related temperatures are also given. H_2O, CO_2, NH_3, HCl and N_2O gases were identified for the sample Prec:M_{ap} (**Figure 20 A**). It is important to mention that the amount of different gas species cannot be compared using their absolute absorption intensity due to the different binding energies.

Figure 21 shows their temperature dependent absorption profiles. Initially the evolution of H_2O is observed which reaches its maximum at 140 °C and is present up to 600 °C. The release of ammonia starts at 110 °C and finds a maximum at 180 °C. The signal is present up to 500 °C. At 275 °C a slight CO_2 evolution starts and from 490 °C characteristic vibration bands for HCl at 2570–3090 cm^{-1} are visible (**Figure 20 A**, 530 °C). This observation agrees with the findings of Siciliano *et al.*[256] and confirms that chlorides can be (partly) removed from the sample by heating it above 500 °C.

Table 6: Temperature ranges of TGA mass losses, released gases and total mass loss of the samples obtained by TGA (25–800 °C, synthetic air)

	Δm_{total} [%]	ΔT1 and gases	ΔT2 and gases	ΔT2b and gases	ΔT3 and gases
Prec:M_{ap}	15	25–190 °C H_2O, NH_3	190–450 °C H_2O, NH_3 CO_2		450–800 °C H_2O, NH_3, CO_2, HCl, N_2O
Prec:M_{H2O}	15	25–185 °C H_2O	185–370 °C H_2O, NH_3, CO_2		370–800 °C H_2O,NH_3, CO_2
Prec:M_{EtOH}	11	25–165 °C H_2O, NH_3	165–350 °C H_2O, NH_3, CO_2		350–800 °C H_2O, NH_3, CO_2
Sol:M_{ap}	8	25–130 °C H_2O, CO_2, CH-2	130–240 °C H_2O, CO_2, CH-1, CH-2	240–360 °C H_2O, CO_2, CH-1, CH-2	360–800 °C CO_2, CH-1

The four mass loss steps of the TGA curve (**Figure 18 B**) can therefore be classified as follows: The first steep mass loss between 25–190 °C is mainly attended by an evolution of NH_3 and H_2O gas. The second step from 190–450 °C is generated by the release of H_2O, NH_3 as well as CO_2. In a third step (450–800 °C) H_2O, CO_2, HCl and N_2O were detected. Probably N_2O is formed due to the decomposition of an ammonia derivate. The results for the other samples are listed in detail in **Table 6 and Table 7**.

The sample Prec:M_{H2O} shows a similar thermal behavior as the sample Pre:M_{ap}, but the amount of water released in the first TG step is higher and the amount of NH_3 decreased. The temperature for the NH_3 release is also higher, which can be explained by the assumption that Pre:M_{ap} contains a high amount of unbound or weakly bound NH_3 aq. (because it has been added in excess), so that it vaporizes at lower temperatures. Further on, no signals from HCl or N_2O were recorded, which leads to the assumption that the washing was successful and most of the chloride was removed. The same behavior is valid for the sample Prec:M_{EtOH}.

These results were verified by EDX measurements (**Table 8**): after washing the samples, the values for chlorine are much lower than in the as prepared sample. The TG curve of the sample Prec:M_{EtOH} differs from the other described samples by a low mass loss in the temperature range 25–200 °C and a strong CO_2 release in the temperature range 230–470 °C. The CO_2-evolution up to these high temperatures indicates chemisorbed EtOH. During the washing steps with EtOH, hydroxy groups undergo an etherfication and form Sn-OEt groups. The exchange of the surface groups and the fact that high temperatures are necessary to remove these groups might change the surface reactivity and could play a role for further surface modifications, catalyst activities or low temperature sensor measurements.

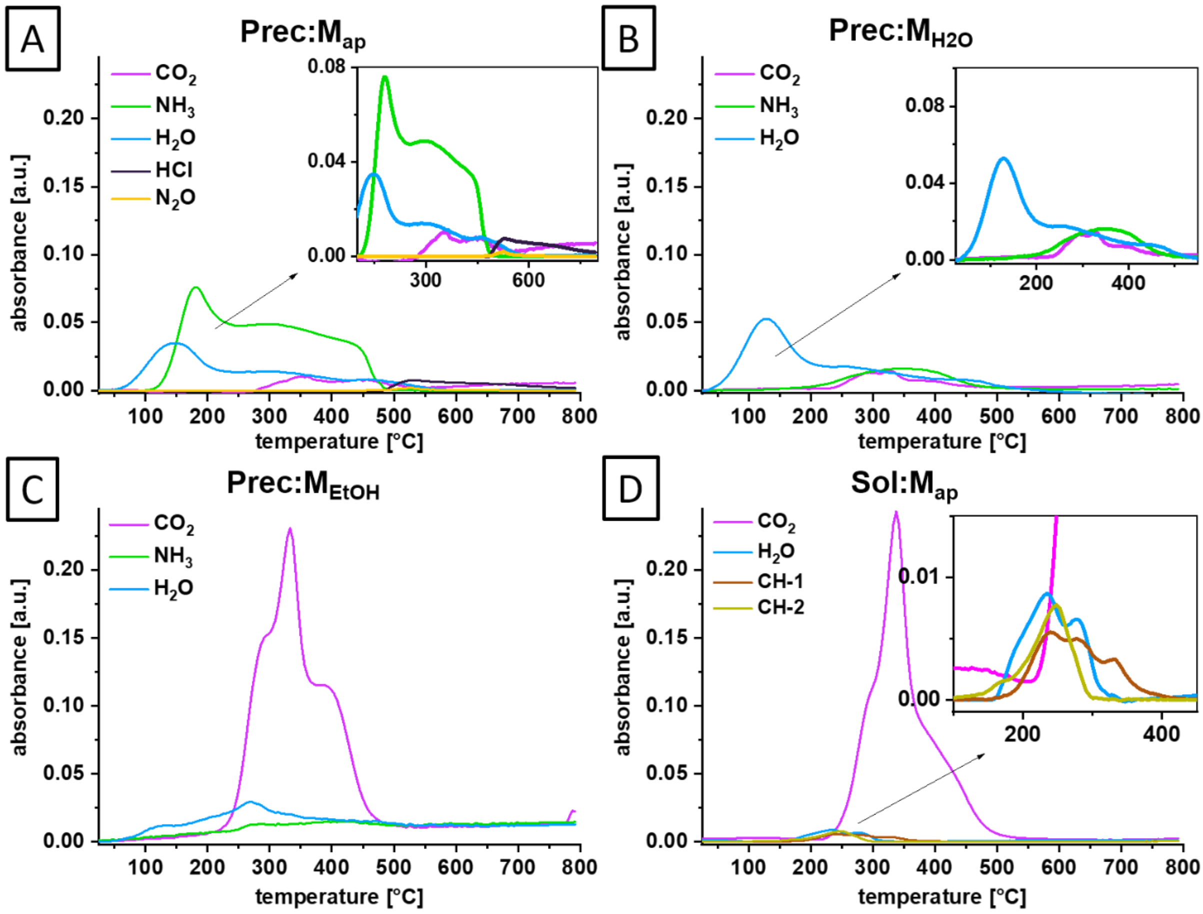

Figure 21: Temperature depending absorption profiles of the detected gases during TG-IR measurement and magnifications. The different microreactor samples from the precipitation (Prec:M) and sol-gel reaction (Sol:M) were analyzed. In addition to the samples without post-treatment (Prec:M$_{ap}$ and Sol:M$_{ap}$), the precipitation samples were tested that were purified with water (Prec:M$_{H2O}$) or with water and ethanol (Prec:M$_{EtOH}$).

The sol-gel sample displays a similar CO_2-evolution as the sample Prec:M$_{EtOH}$, also in the same temperature range and with a comparable mass loss. Between 200 and 300 °C two additional gases were detected at 2790–3000 cm^{-1} and 3016 cm^{-1}, which could not be clearly identified. The corresponding wavenumber range is characteristic for C-H stretching vibrations of alkyl and alkenyl groups, so that it is likely that the signals originate from decomposition products of *t*-butoxy groups of the educt and the solvent. As expected, no chloride or ammonia signals were detected in this sample.

Elemental analyses (**Table 8**) confirm the results from TG-IR. For the washed samples a lower nitrogen content was measured than for the as prepared sample. The carbon content of the sample Prec:M$_{EtOH}$ and the sample Sol:M$_{ap}$ are significantly increased.

Table 7: List of detected gases (temperature range for their appearance and temperature for their maximal intensity) measured by TGA-IR.

sample	T(H_2O)	T(CO_2)	T(NH_3)	T(others)
Prec:M_{ap}	60–360 °C max.: 140 °C	285–490 °C max.: 355 °C	130–480 °C max.: 180 °C	HCl: 500–550 °C max.: 530 °C
Prec:M_{H2O}	50–450 °C max.: 330 °C	245–425 °C max.: 330 °C	165–485 max.: 340 °C	-
Prec:M_{EtOH}	95–470 °C max.: 280 °C	230–470 °C max.:335 °C	250–470 °C max.: 290 °C	-
Sol:M_{ap}	150–390 °C max.: 290 °C	240–490 °C max.: 335 °C	-	CH-1: 195–360 °C, max.: 240 °C CH-2: 155–290 °C, max.: 230 °C

Ethanol binding

If EtOH is chemisorbed on the particles, like the TG-IR studies indicate, can be proofed by solid-state NMR measurements. As it was demonstrated by Raftery *et al.*[273] a distinction between chemisorbed and physisorbed molecules is possible by contact time variation in CP-MAS-NMR studies due to the different mobility of the determined species. In **Figure 22 A** the spectra of the sample Prec:M_{EtOH} measured in SPE-MAS mode and CP-MAS mode with different contact times are presented. In the SPE-MAS spectrum, where the signal intensity is not enhanced by abundant hydrogen atoms, two distinct peaks are visible at 15.6 ppm (methyl C) and at 56.6 ppm (methylene C). At a contact time of 6 ms and CP-MAS mode a broad, small signal appears beside each of the original peaks at 17.0 and 59.2 ppm. By further deceasing the contact time the broad signals get more and more dominant and the sharp signals disappear. The mobility of chemisorbed, covalently bound ethanol is more limited than the mobility of physisorbed ethanol, which is just attached by hydrogen bond. Depending on the mobility, different contact times are necessary to detect certain species. With long contact times (e.g. 6 ms) it is possible to observe mainly signals from hydrogen bonded ethanol, which has a more flexible conformation. The spectra confirm that both, physisorbed and chemisorbed ethanol are present in the ethanol washed sample.

Table 8: Chemical composition from elemental analysis and EDX. n. d.: not detectable.

	elemental analysis			EDX			atomic ratio	
	C [wt.%]	H [wt.%]	N [wt.%]	Sn [wt.%]	O [wt.%]	Cl [wt.%]	O:Sn	Cl:Sn
Prec:M_{ap}	0.2	1.8	2.0	74.7	19.4	4.6	1.9	0.2
Prec:M_{H2O}	0.1	1.9	0.6	78.4	19.7	0.2	1.9	0.01
Prec:M_{EtOH}	1.4	1.9	0.6	78.1	19.7	0.1	1.9	0.003
Prec:M_{temp}	n. d.	0.2	n. d.	83.3	15.1	0.4	1.4	0.003
Sol:M_{ap}	0.4	1.5	n. d.	79.6	17.6	0.6	1.6	0.02

High temperature behavior

A comparison of the crystallite size growth and the phase composition at elevated temperatures for SnO_2 samples with and without chloride contaminations (samples Pre:M$_{ap}$ and Pre:M$_{H2O}$) were performed by *in-situ* XRD measurements. The sample Pre:M$_{H2O}$ was measured with an internal standard (30 wt.% α-Al_2O_3) in order to improve the height adjustment of the sample during the measurement and to ensure an accurate determination of the SnO_2 reflection position.

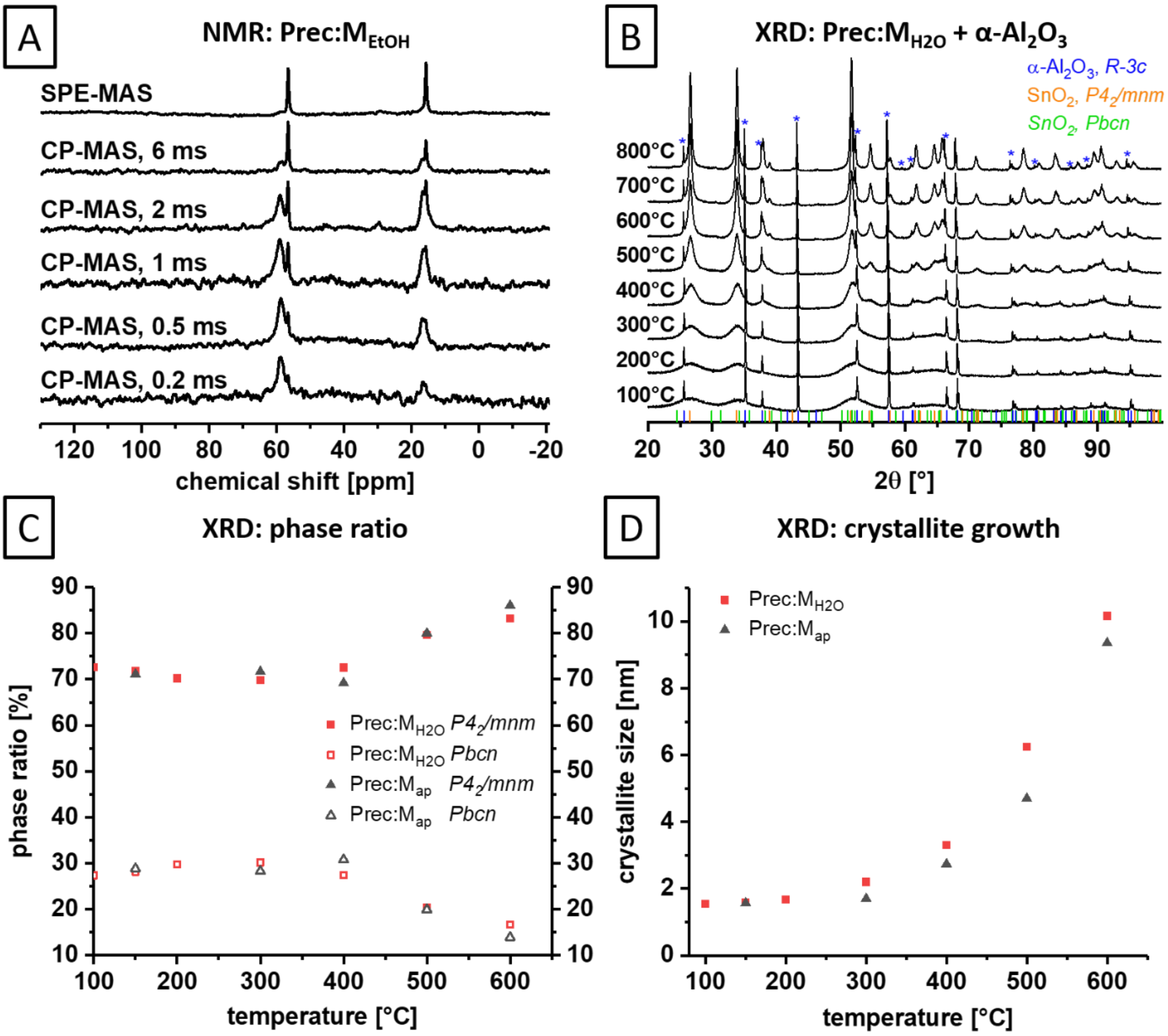

Figure 22: (A) SPE- and CP-MAS-NMR spectra of the sample Prec:M$_{EtOH}$ with different contact times (0.2–6.0 ms) and (B) *in-situ* XRD measurements of the water washed sample (Prec:M$_{H2O}$) containing an internal standard (Al_2O_3) and assignment of the reflections. (C) Phase portions and (D) crystallite sizes of the as prepared (Prec:M$_{ap}$) and water washed (Prec:M$_{H2O}$) samples at different sintering temperatures obtained from *in-situ* XRD.

The scans display broad reflection bands for SnO_2 at low temperatures, which are characteristic for nanocrystalline materials, and with increasing temperatures the peaks get sharper and more defined, caused by the crystallite growing **(Figure 22 B)**. The reflection at $2\vartheta = 43.4°$ is generated by the steel sample holder and is not specific for the samples. A possible amorphous content is low or stays constant during the heat treatment because the refined α-Al_2O_3 content keeps also unchanged. To be sure that a varying amorphous phase is not described by the background function it was only refined by a 4th order polynomial, so that an amorphous part should be mainly covered by the less defined, orthorhombic phase. However, an exact quantification of the amorphous phase was not possible.

The analysis of the XRD-data revealed that the crystallite size for the rutile phase increases, while the size for the orthorhombic crystallites remains constant or even decreases slightly (**Figure 22**). During the heat treatment, a reduction of defects takes place, which produces a crystallite growth for the particles in the tetragonal phase. Furthermore, it can be assumed that for the orthorhombic crystallites the reduction of defects and growth also occurs, but is accompanied by a transformation into the tetragonal structure.

In order to achieve a reliable and consistent monitoring of the changes in lattice parameters and phase ratios, a reduction of the amount of variable parameters was necessary: The crystallite size of the orthorhombic phase was set to a constant value of 1.6 nm and its lattice parameters were set to literature values[131]. With these simplifications the behavior of the phase composition was determined exemplary for the sample Pre:M_{H2O}. The initial orthorhombic phase portion of the sample, which was dried at 100 °C, was ca. 27 %. When the sample was heated, the content of the PbO_2-type structure slightly increased up to 30 % at 300 °C. After exceeding this temperature, a proceeding decrease of this phase was observed (**Figure 22 C**). Brito *et al.*[274] described a similar trend. They determined the phase processes of a monolithic SnO_2 xerogel during a thermal sintering by extended X-ray absorption fine structure (EXAFS) experiments and XRD and found that due to dehydration and oxolation reactions between 110 and 250 °C, an amorphization of the cassiterite structure takes place. Above 250 °C, the condensation reactions of surface OH-groups of adjacent crystallites re-enforce the long-range crystalline order and a progressive crystal growth is observed in the temperature range between 300 and 700 °C. In this study, no indications for amorphization processes could be found. Instead it is proposed that an initial increase of the *Pbcn* phase in the tested material is the cause for the decrease of the tetragonal structure in the relevant temperature range.

After the intense study of the changes in crystal structure for the sample Pre:M_{H2O}, the gained knowledge was used for the data analysis of the sample Pre:M_{ap}. **Figure 22 D** describes the crystal growing during heat treatment for the precipitation samples with and without water washing. At temperatures below 200 °C only a slow crystallite growth occurs, whereas in the temperature range from 200–600 °C the rate is increased. Both samples start from almost the same initial crystallite size (1.6 nm). During the thermal treatment, a slightly increased growth is observed for the sample Pre:M_{H2O}, resulting in a crystallite size of 10.2 nm, while the crystallites of sample Pre:M_{ap} end up with an average size of 9.4 nm at 600 °C. Consequently, this study could not confirm a strong influence of chloride contamination on the crystallite growth in terms of the crystallite size or the growth process.

3.1.1.3 Conclusions

This study gave a detailed overview on how the chemical and crystallographic properties of SnO_2 nanoparticles are influenced by their synthesis and purification pathways. It has been demonstrated that SnO_2 nanoparticles can be successfully produced by precipitation as well as by sol-gel reaction in batch operation (beaker and ultrasonic assisted beaker reaction) and continuously. While the kind of the processing method under the tested synthesis conditions did not seem to have a significant influence on the particle properties (e.g. on the crystallite size), the kind of precursor had: Particles from sol-gel precursors were slightly larger than particles from precipitation precursors, showed less chloride contamination and contained residual organic groups. The XRD results indicated that the small particles consist of a mixture of the rutile phase and an orthorhombic high-pressure phase. Different methods were tested to free the precipitated SnO_2 particles from chloride contaminations. Purification with water achieved the lowest chloride quantities, but also resulted in high yield losses due to dissolution processes. Ethanol as a washing medium resulted in low residual chloride contents with only low yield losses. However, etherification was observed during washing with ethanol, which led to an occupation of the particle surfaces with alkoxy groups. These groups are stable up to approx. 470 °C and could have negative effects in certain applications, such as gas sensors or catalysis. The thermal removal of the chloride showed the advantage of a low technical effort, but crystallite growth from 1.6 to 9.4 nm (from 100−600 °C) took place and the phase composition changed to pure tetragonal SnO_2. The study clearly showed that all tested methods are capable of reducing the chloride content. However, each of the methods is associated with certain side effects, which should be considered depending on the application project. The overview given in this work can therefore help to find the perfect synthesis and purification method for SnO_2 particles for a given application. The MicroJet reactor technique turned out as well suitable method for the continuous production of SnO_2 nanoparticles and ensured a constant product quality. Further studies could aim on the production and characterization of more complex systems like Zn-doped SnO_2 particles or the application of the particles as sensitive coating on gas sensors.

3.1.1.4 Supporting Information

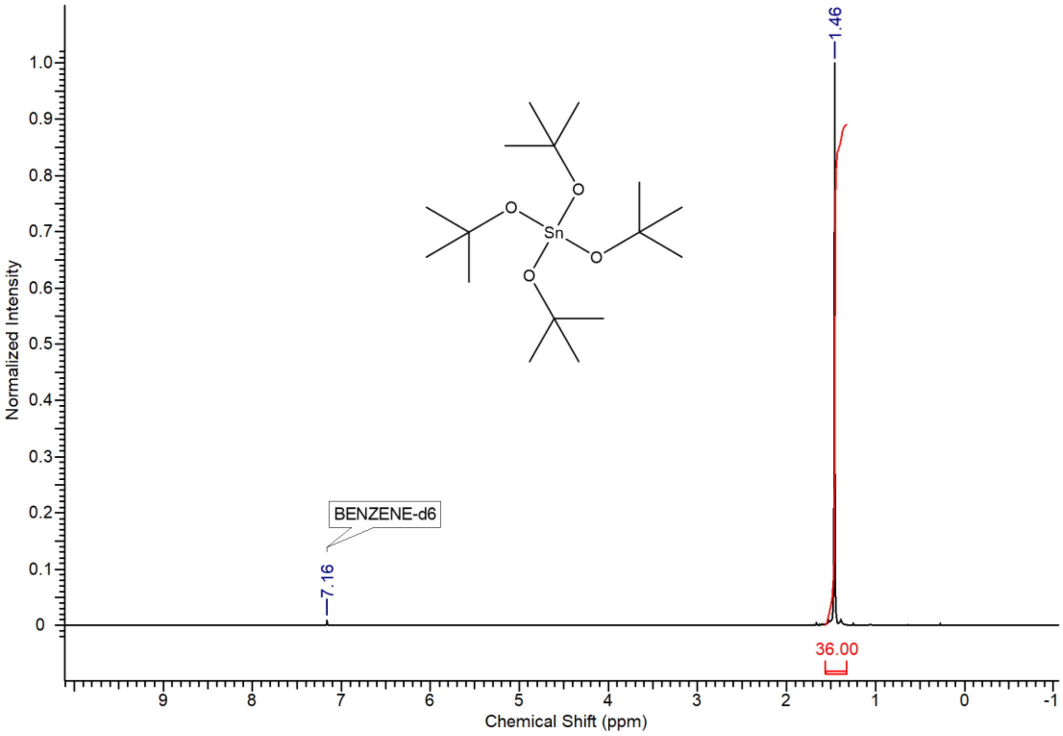

Figure S 1: ^{1}H NMR spectrum of Sn(O^{t}Bu)$_4$.

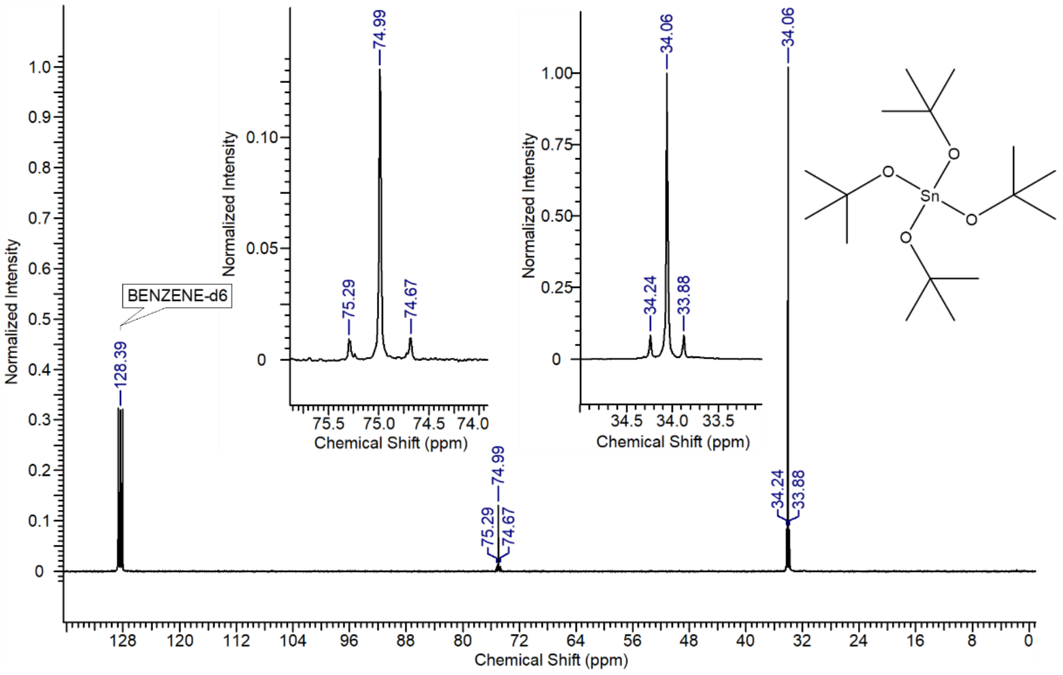

Figure S 2: ^{13}C NMR spectrum of Sn(O^{t}Bu)$_4$.

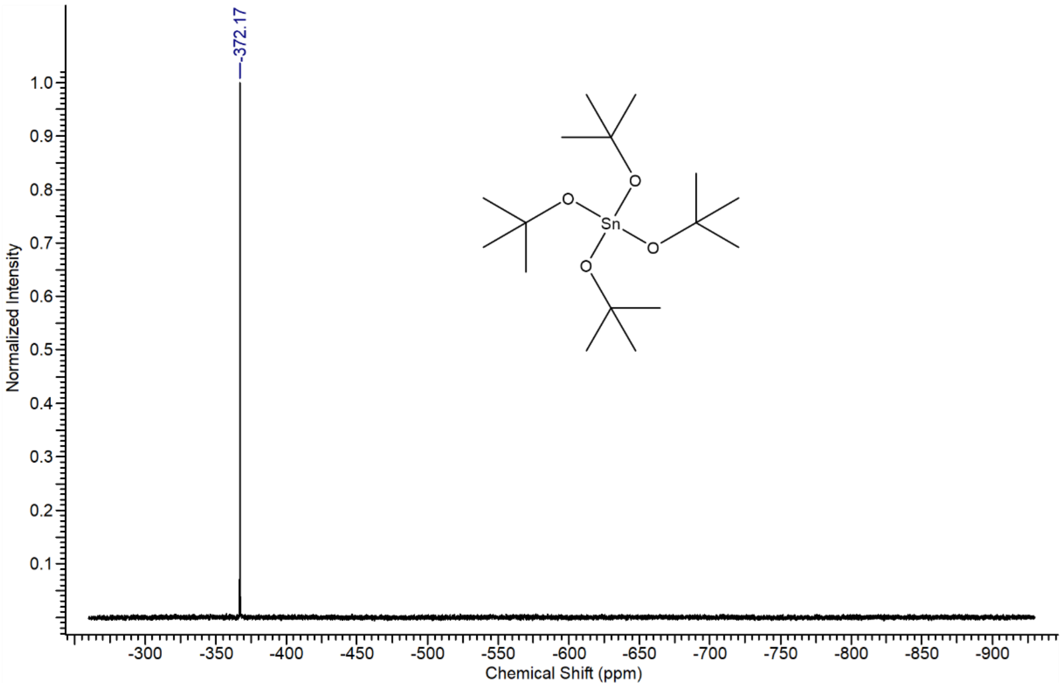

Figure S 3: ^{119}Sn NMR spectrum of $Sn(O^tBu)_4$.

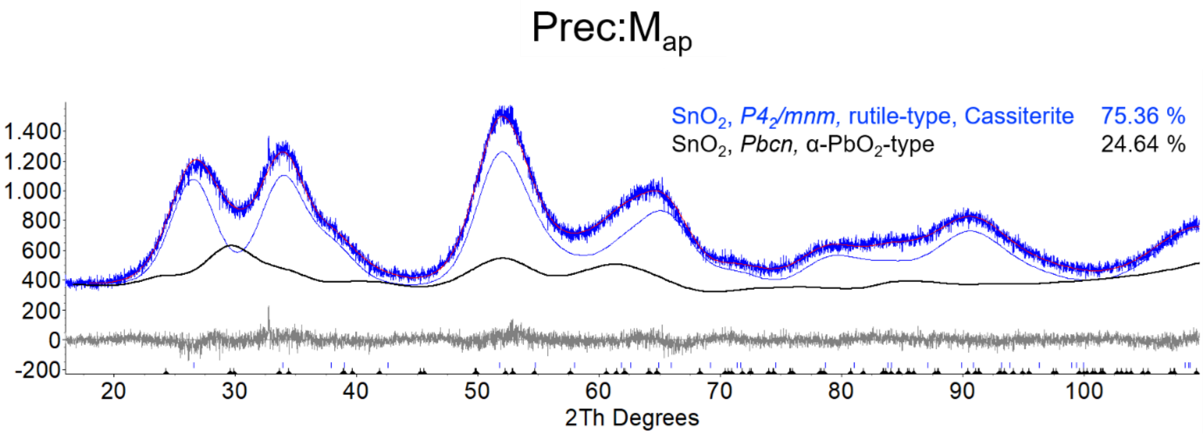

Figure S 4: Rietveld refinement of Prec:M_{ap} with the tetragonal (*$P4_2/mnm$*) and orthorhombic (*Pbcn*) structure of SnO_2.

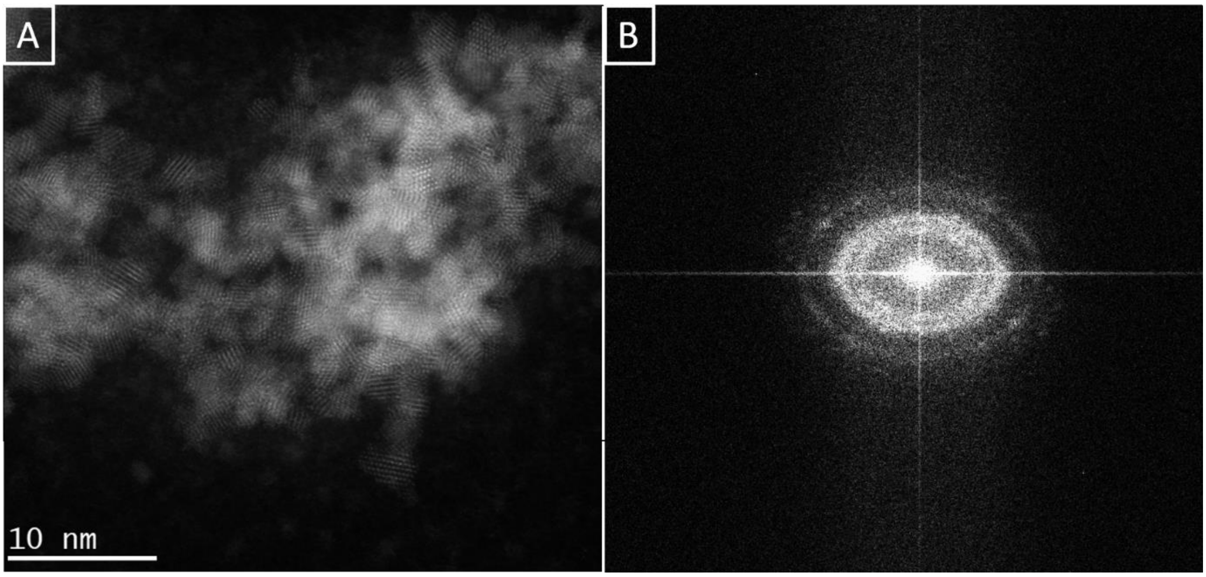

Figure S 5: (A) HRTEM image of the sample Prec:U_{ap} and (B) fast Fourier transform.

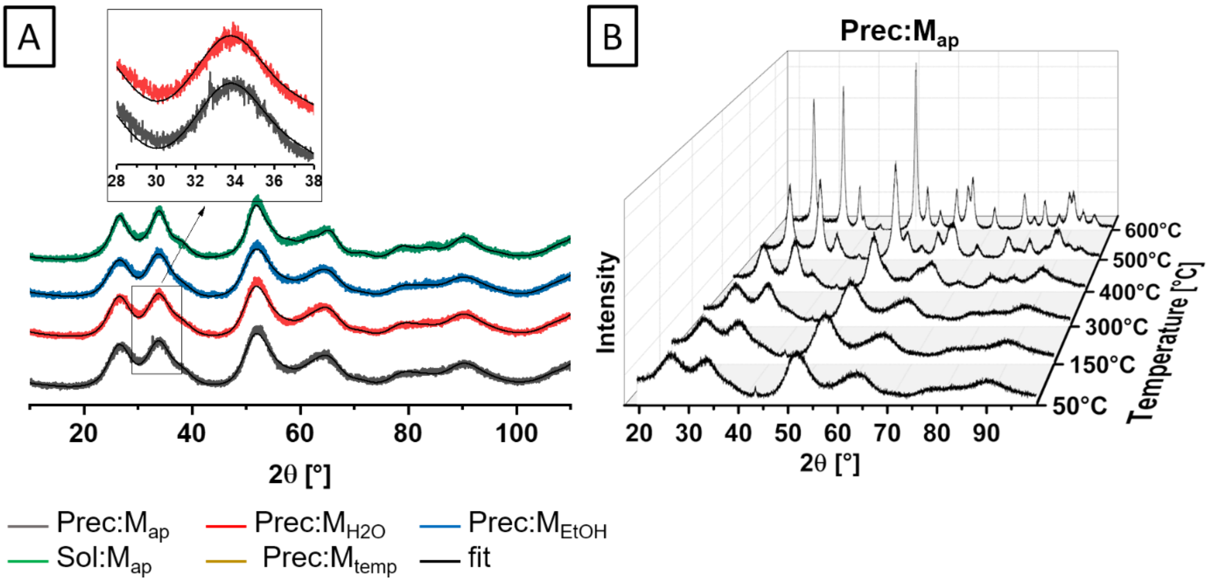

Figure S 6: (A) XRD scans of SnO_2 samples with different post-treatment and (B) *in-situ* XRD measurements of sample Prec:M_{ap} at different temperatures.

Based on these results, the produced particles can now be tested in various applications. First studies have already been carried out that test the performance of the SnO_2 particles as a sensitive layer on gas sensors under different conditions. These results will be published soon, in a separate article and are not part of this thesis.

The data presented above confirmed the general suitability of the MicroJet reactor for carrying out sol-gel reactions, exemplified by the alkoxystannane precursors. In chapter 3.3 this reaction is extended to the less reactive alkoxysilanes.

3.2 Cesium dihydrogen phosphate particles

3.2.1 Facile and scalable synthesis of sub-micrometer electrolyte particles for solid acid fuel cells

In this chapter the MicroJet reactor process is transferred to the precipitation reaction of cesium dihydrogen phosphate. The solid acid has a good thermal stability and forms a superprotonic phase at elevated temperatures. Therefore, it is applied in electrodes and electrolyte membranes of fuel cells operating at medium temperatures.

Small particles are of particular interest for solid acid fuel cells, as several studies have measured significant performance improvements when the particle diameter is reduced to the submicron range. However, the production of these small particle sizes is hindered by their tendency to coalesce and sinter if they are not sufficiently stabilized. Various low throughput processes, such as spray drying or electrospray deposition have been used to produce small particle sizes, but until now, there has been a lack of a simple, robust process that allow high throughput rates. In the following article a new synthesis protocol for the production of CsH_2PO_4 submicroparticles is developed.

In the standard synthesis procedure for CsH_2PO_4, alcohol is added to an aqueous precursor solution of Cs_2CO_3 and H_3PO_4 until the product precipitates. In the synthesis protocol presented here, alcoholic precursor solutions of CsOH and H_3PO_4 are mixed, resulting in a low water content and reduced agglomeration. Furthermore, a commercial dispersion additive (MelPers 0045) is supplied to one of the precursors and its quantity is optimized. The additive leads to a significant improvement in the stability of the suspensions and effects the particle sizes. The influence of the precursor concentration, the batch size and the type of solvent is investigated for the precipitation. In order to determine the influence of the mixing efficiency on the particle size, the optimized batch synthesis is subsequently transferred to the continuous MicroJet reactor process and the properties of the products are compared. The fast mixing times of the reactor produce homogeneous synthesis conditions leading to uniform particle formation.

Contributions:

Christina Odenwald: Planning and conducting of continuous syntheses of CsH_2PO_4 particles, SEM images of continuously produced particles, discussion and revision of the manuscript. **Felix P. Lohmann-Richters:** Design, planning, CsH_2PO_4 beaker synthesis, particle analysis, writing the manuscript. **Guido Kickelbick:** Discussion and revision of the manuscript. **Bernd Abel:** Discussion and revision of the manuscript. **Áron Varga:** Supervision, discussion, and revision of the manuscript.

Reprinted from: Lohmann-Richters, F. P.; Odenwald, C.; Kickelbick, G.; Abel, B.; Varga, Á., *Facile and scalable synthesis of sub-micrometer electrolyte particles for solid acid fuel cells. RSC Adv.* **2018,** *8* (39), 21806-21815. http://dx.doi.org/10.1039/c8ra03293a — Published by The Royal Society of Chemistry.

RSC Advances

PAPER

Cite this: RSC Adv., 2018, 8, 21806

Facile and scalable synthesis of sub-micrometer electrolyte particles for solid acid fuel cells†

F. P. Lohmann-Richters,[a] C. Odenwald,[b] G. Kickelbick,[b] B. Abel[a] and Á. Varga*[a]

Received 17th April 2018
Accepted 29th May 2018

DOI: 10.1039/c8ra03293a

rsc.li/rsc-advances

Nanostructuring fuel cell electrodes is a viable pathway to reach high performance with low catalyst loadings. Thus, in solid acid fuel cells, small CsH_2PO_4 electrolyte particles are needed for the composite powder electrodes as well as for thin electrolyte membranes. Previous efforts have resulted in significant improvements in performance when using sub-micrometer CsH_2PO_4 particles, but laborious methods with low throughput were employed for their synthesis. In this work, we present a simple, robust, and scalable method to synthesize CsH_2PO_4 particles with diameters down to below 200 nm. The method involves precipitating CsH_2PO_4 by mixing precursor solutions in alcohol in the presence of a dispersing additive. The influence of the concentrations, the batch size, the solvent, and the mixing process is investigated. The particle size decreases down to 119 nm with increasing amount of dispersing additive. Mixing in a microreactor leads to a narrower particle size distribution. The particle shape can be tuned by varying the solvent. The ionic conductivity under solid acid fuel cell conditions is 2.0×10^{-2} S cm^{-1} and thus close to that of CsH_2PO_4 without dispersing additive.

1 Introduction

The design of electrodes with a large electrocatalytically active surface area is crucial for most fuel cells. This is particularly challenging for fuel cells with solid electrolytes. Here, not only the electrocatalyst with its conductive support has to be optimized, but also the mixing with the electrolyte particles.

Solid acid fuel cells (SAFC) are usually based on CsH_2PO_4 as electrolyte. At the operating temperature of *ca.* 240 °C the electrolyte is in the superprotonic phase with high proton conductivity.[1,2] The solid-state electrolyte and the intermediate operating temperature lead to a number of advantages, such as resistance to catalyst poisoning, cost-effective engineering materials, ease of handling, and simple water management.[3] Nevertheless, the loading of platinum as electrocatalyst in SAFCs still has to be reduced to allow broad application. Small electrolyte particles can improve the performance of both the membrane and the electrodes in SAFCs.

SAFCs with electrolyte membranes as thin as 25 μm and a power density of 415 mW cm^{-2} have been reported in literature. However, the membranes were mechanically unstable and the cells showed a rapid decrease of power output.[4] Composites of CsH_2PO_4 and inorganic oxides[3,5,6] or polymers[7–9] revealed improved mechanical stability and are promising for creating stable, thin electrolyte membranes. In any case, the membrane thickness is limited by the size of the electrolyte particles. To form a dense, non gas-permeable layer, a thickness of at least several particle diameters is necessary.

The electrode of state-of-the-art SAFCs consists of a mixture of electrolyte particles and platinum as electrocatalyst. The platinum utilization was significantly improved by using carbon nanotubes (CNT) as catalyst support.[10–12] For electrodes in which the catalyst is deposited directly on the electrolyte particles, the power output was significantly increased by reducing the size of the electrolyte particles in the range of 100 to 200 nm.[3] Here, the surface increase directly translates to an increase of the electrocatalytically active surface area (ECSA). Small electrolyte particles are therefore advantageous for high-performance electrodes and electrolyte membranes in SAFCs. The particle size is probably limited by the particle stability toward sintering or coalescence.[17] It appears that an optimal size has not yet been determined. Only recently, a method to measure the ECSA in SAFCs *in situ* has been put forward.[13]

The conventional method to prepare CsH_2PO_4 is by precipitation from an aqueous solution through the addition of methanol,[2] yielding particles in the range of several micrometers. The particle size can be reduced to about 1 μm using ball milling.[14] Particles down to 0.5 μm were obtained by injecting an aqueous solution of CsH_2PO_4 through a fine needle into methanol under ultrasonication. Larger particles had to be removed by centrifugation, resulting in low yields.[15]

---

[a] *Leibniz Institute of Surface Engineering (IOM), Permoserstr. 15, D-04318 Leipzig, Germany. E-mail: aron.varga@iom-leipzig.de; Tel: +49 341 2353364*

[b] *Saarland University, Inorganic Solid State Chemistry, Campus, Building C4 1, 66123 Saarbrücken, Germany*

† Electronic supplementary information (ESI) available. See DOI: 10.1039/c8ra03293a

Even smaller particle diameters of 0.4 μm and 0.1 μm were achieved by spray drying[16] and electrospray deposition,[17] respectively. Both techniques resulted in improved platinum utilization (the inverse of the electrode impedance, divided by the platinum loading) when the particles were stabilized by the addition of polyvinylpyrrolidone (PVP) of high molecular weight. Unfortunately, the throughput of these techniques is insufficient for production-scale synthesis at this time.

The use of surfactants to synthesize nanoparticles of controlled size is well known and established for a large variety of materials. Hosseini *et al.* applied this approach for the precipitation of CsH_2PO_4.[18] The authors reported particle sizes of approximately 10 nm in diameter. The amount of surfactant necessary to achieve such a small size was very high, 62 wt% in relation to CsH_2PO_4. Unfortunately, the stability and agglomeration of the particles under SAFC operating conditions was not investigated. Even significantly larger particles from electrospray deposition needed to be stabilized by the addition of PVP, and the melting point of the surfactant employed here is near the operating temperature of SAFCs. It is therefore unlikely that a stable electrode performance can be obtained.

For SAFC electrodes, it can be beneficial to employ electrolyte particles which are not only small, but also have a high aspect ratio, such as rods or platelets. These shapes facilitate the percolation of the electrolyte in a porous powder electrode. Ahn *et al.* have shown that the shape and size of CsH_2PO_4 particles can be influenced by the addition of ethylene glycoles and acetonitrile in the precipitation.[19]

The supersaturation of the solution is one of the most important factors determining the size of precipitated particles.[20] Apart from the concentration of the involved solutions, it depends heavily on the mixing process. An extremely fast and very well controlled way to mix two liquids is the use of micromixers or -reactors. Microreactors are generally three-dimensional devices with inner dimensions in the range of 1–1000 μm.[21] Above all, microreactors offer rapid mixing times, typically in the order of milliseconds. This improves the mass transport and leads to homogeneous conditions that are ideal for the particle formation in fast precipitation reactions. The constant operating conditions lead to better process control, higher reproducibility, and improved yield, compared to batch methods.[22,23] The suitability of the microjet reactor method[24] for different precipitation reactions was already demonstrated, *e.g.* for barium sulfate,[25] titanium dioxide,[26] zinc oxide, brushite and magnetite particles,[27] and for the sol–gel synthesis of ORMOSIL microspheres.[28,29]

The precipitation of $BaSO_4$ is a common model reaction for studying the formation and agglomeration of nanoparticles.[20,25,30,31] Often, dispersing additives are employed in order to stabilize the nanoparticle suspensions. To our knowledge, for the precipitation of CsH_2PO_4 neither the use of microreactors or other continuous mixing devices, nor the addition of dispersing additives have been reported in literature.

In this work, we present the simple and scalable precipitation process yielding sub-micrometer CsH_2PO_4 particles for the application in SAFCs. This is achieved by the addition of a commercially available dispersing additive. The influence of the concentrations, the solvent, and the mixing procedure is investigated.

2 Materials and methods

MelPers 0045, identified as a promising dispersing additive in preliminary tests, was kindly provided by BASF Construction Solutions. It is a *ca.* 45 wt% aqueous solution of polycarboxylate ether comb copolymer with a charged backbone, providing electrostatic as well as steric stabilization. MelPers 0045 is usually employed to disperse inorganic pigments.[32] CsOH hydrate (99.9% metal basis, abcr; est. water content 12.5%) was used as Cs^+-source instead of the widely used Cs_2CO_3 to avoid carbonate residues and gas formation, especially in the microreactor.

2.1 Batch precipitation

The synthesis of CsH_2PO_4 particles *via* batch precipitation was typically performed as follows: H_3PO_4 (0.13 g, 1.09 mmol; 85%, Carl Roth) was mixed with EtOH (technical grade, Carl Roth) and MelPers 0045 (0.05 g, 20 wt% of the expected dry product) was added. The solution was diluted to 25 mL and a solution of CsOH (0.17 g, 1.09 mmol) in EtOH (25 mL) was added under intense stirring with a magnetic stir bar. The solution immediately turned white, indicating the formation of the product. This protocol with 20 wt% MelPers 0045, nominally 0.25 g of CsH_2PO_4 with a nominal concentration of 5 g L^{-1} served as reference point for varying the parameters.

Different amounts of the dispersing additive, relative to the expected product, were used (0, 2, 5, 20, 40 wt%). Note, that the dispersing additive has a solid content of 45 wt%. The expected fractions of polymer in the dried products are therefore 0, 0.9, 2.3, 9.0 and 18.0 wt%. For comparison, CsH_2PO_4 was also prepared by the conventional precipitation method[1,2] by adding EtOH to an aqueous solution, but with the addition of 20 wt% dispersing additive.

The batch size was scaled from 0.25 g over 1 g to 4 g, with all concentrations kept constant. From the latter, a part of the product was collected for further analysis by centrifugation (Sigma 3-18K) with a relative centrifugal force of 4248 for 30 min and dried at 120 °C under reduced pressure.

The nominal product concentration was varied from 1 g L^{-1} over 5, 10 and 40 g L^{-1} to 50 g L^{-1}. For the latter, 35 mL of EtOH had to be employed to dissolve the CsOH, due to its limited solubility.

To investigate the influence of the solvent, the precipitation was also performed using MeOH (99%, Carl Roth), isopropanol (iPrOH, technical grade, Carl Roth), a 1 : 1 (vol) mixture of EtOH and acetonitrile (Uvasol quality, Merck) (denoted EtOH–ACN), and a 1 : 1 (vol) mixture of EtOH and ethylene glycol (99.8%, Sigma-Aldrich) (denoted EtOH–EtGly).

2.2 Microreactor precipitation

The influence of the mixing process was investigated by comparing the batch experiments with the precipitation in a microreactor.

A 125 mL solution of CsOH (1.02 g, 5.45 mmol; 99.9% metal basis, 15–20% H_2O, alfa aesar) in EtOH (99%) was prepared. H_3PO_4 (0.55 g, 5.45 mmol; 98% p.a., Merck) with 5 and 20 wt% (0.06 g and 0.25 g) MelPers 0045 was diluted with 125 mL EtOH. The nominal resulting CsH_2PO_4 concentration was 5 g L^{-1}.

The microreactor setup has been described in detail in a previous publication.[29] In short, two HPLC pumps were used to press the precursor solutions through opposing horizontal nozzles of 300 μm diameter. The solutions collide as fine impinging jets in the middle of the chamber where a fast mixing in the order of 10 ms takes place. A nitrogen gas flow (8 bar) orthogonal to the feeding streams supports the transfer of the mixture to the collecting vessel. The reaction was performed at 20 °C with a flow rate of 250 mL min^{-1} for each precursor solution.

2.3 Characterization

The particle size distributions were measured with dynamic light scattering (DLS) using a Zetasizer Nano ZS (ZEN3600, Malvern Instruments, 173° scattering angle) using the as-precipitated suspensions. The measurements were performed at 20 °C with an equilibration time of 2 min. No significant particle concentration in EtOH or the solution of the dispersing additive in EtOH was observed. The viscosity and the refractive index of the pure solvents was employed for the data analysis. The data is reported as intensity distributions as this is the quantity directly obtained from DLS. A conversion to the distribution by number or volume would be possible, but involves additional assumptions and requires detailed data on the particles' complex refractive index.

To confirm the particle size from DLS and to observe the morphology, scanning electron microscopy (SEM) images were recorded in a Carl Zeiss Ultra 55. For the microreactor samples, SEM images were recorded with a JEOL JSM-7000F after deposition of a gold layer to avoid charging effects.

The samples for SEM were prepared by drying a drop of the product suspension on a Si-wafer at 80 °C, or on a glass slide with subsequent transfer to a SEM sample holder. In order to evaluate the particles' agglomeration behavior, one SEM sample was exposed to SAFC operating conditions (240 °C, H_2, *ca.* 0.4 atm H_2O) for 13 h.

Using the product from the 4 g batch, X-ray diffraction (XRD) patterns were recorded on a Rigaku Ultima VI with Cu Kα1 radiation to confirm the phase. The crystallite size was calculated according to Scherrer from the full width at half maximum of the reflex at 29° assuming a shape factor of $K = 1$. Thermogravimetric analysis (TGA) (STA 449 C Jupiter, Netzsch) was performed with a heating rate of 10 °C min^{-1} under air to detect the additive's decomposition and the dehydration of CsH_2PO_4. Differential scanning calorimetry (DSC) (DSC 8500, PerkinElmer) was recorded with a heating rate of 10 °C min^{-1} to observe the dispersing additive's glass transition and the superprotonic phase transition of CsH_2PO_4.

For conductivity measurements under SAFC operating conditions, a 0.5 mm thick dense pellet with a radius of 1 cm was prepared by uniaxial pressing with 4 t for 1 min followed by 8 t for 5 min (Atlas Auto 15T, Specac Ltd.). The pellet was sandwiched between discs of carbon paper (TP-060, Toray) followed by stainless steel gas diffusion layers (PACOPOR ST 60 AL3, Paul GmbH und Co. KG) and heated to 240 °C under argon with 0.4 atm H_2O. Impedance spectra (10 mV amplitude, 1 MHz to 200 mHz) were recorded with a VSP-300 potentiostat (Bio-Logic Science Instruments).

3 Results and discussion

3.1 Batch precipitation

The conventional synthesis of CsH_2PO_4 for SAFCs is based on the precipitation from an aqueous solution of the precursors by the addition of a non-solvent, usually methanol.[1,2] The addition of the methanol gradually decreases the solubility of CsH_2PO_4, leading to precipitation. While the precursors are soluble in alcohols, the product is not. Thus, the precipitation can also be induced by mixing separate solutions of the precursors in alcohol, as in the new synthetic procedure presented in this work. The lower water content can be expected to reduce the agglomeration of the CsH_2PO_4 particles. A dispersing additive can be added to reduce the agglomeration further.

3.1.1 Dispersing additive quantity. The precipitation of CsH_2PO_4 was performed with different amounts of the dispersing additive MelPers 0045. The obtained suspensions varied in their stability. In the sample without dispersing additive, complete sedimentation occurred within *ca.* 10 min. The suspensions with 2 wt% to 20 wt% of dispersing additive exhibited first indications of sedimentation between 10 min and several hours, increasing with the amount of MelPers. However, the sedimentation was not complete: even after several days the supernatant remained turbid. With 40 wt% of MelPers 0045, slight sedimentation was only observed after one week. After the partial sedimentation, the particles in all samples could be easily redispersed by vigorous shaking. This was even the case several months after the synthesis.

The sedimentation behavior of the sample conventionally precipitated from aqueous solution was similar to the above-mentioned suspension with 2 wt% dispersing additive, although it contained 20 wt% MelPers. However, the particles could not be redispersed after sedimentation, even with prolonged ultrasonication. Most probably, the much higher water content leads to coalescence of the sedimented particles. For stable CsH_2PO_4 nanoparticles it might thus be beneficial to have a low water content in the suspension. The amount of water in the samples precipitated from ethanol could be further reduced by employing reactants and solvents with low water content.

From the scattering intensity distribution in DLS (Fig. 1), it can be seen, that the particle sizes decrease with increasing content of MelPers 0045. As the scattering intensity depends on the sixth power of the particle diameter, larger particles are over-represented in these intensity distributions. However, this distribution is the one directly obtained from the measurement, and any conversion involves additional assumptions. From 0 to 2 wt% dispersing additive, the maximum of the scattering intensity shifts from 998 nm to 278 nm. Between 2 wt% and

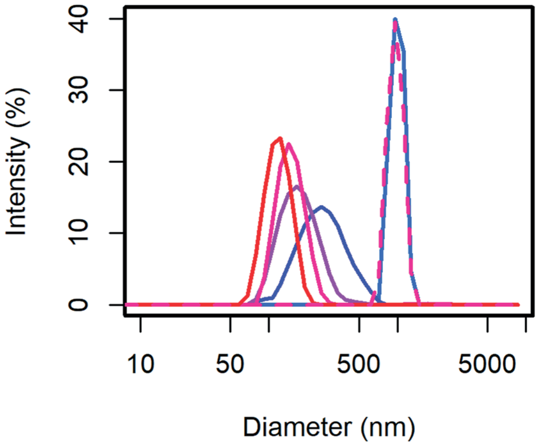

Fig. 1 The CsH_2PO_4 particle size as measured with DLS decreases with the dispersing additive content of 0 (blue) to 40 wt% (red). Even with 20 wt%, the conventional precipitation from aqueous solution yields large particles (dashed).

40 wt% the particle size decreases further and the distribution gets narrower (Table 1). With 40 wt% the distribution extends clearly to below 100 nm. The sample precipitated from aqueous solution with 20 wt% yields a particle size distribution similar to the 0 wt% sample, illustrating the benefit of the precipitation protocol presented in this work.

The particle size distribution of the samples with 20 and 40 wt% MelPers 0045 was measured again after 1, 3, and 7 days (Fig. 2). With 20 wt%, the size distribution stabilized at slightly increased diameters. With 40 wt%, the size distribution developed a shoulder in the same diameter range in which the 20 wt% sample stabilized. The higher water content in the sample with higher additive concentration can be expected to play a role in the aging of the particles. However, both particle size distributions are remarkably stable, leaving more than enough time for further processing and analysis.

To validate the particle size measured by DLS, SEM images of selected samples were recorded (Fig. 3). Due to severe drying artifacts that can occur during the preparation of the SEM samples, the images can only serve for qualitative analysis. In accordance with DLS, many particles in the range of *ca.* 200 nm are observed with 20 wt% dispersing additive. In addition to small spherical particles, also rod-like particles and larger particles in the micrometer range are present. Such particles and large rods are also observed in the samples with lower content of dispersing additive. The larger particles might not be accounted for in the DLS measurements, as they sediment too fast. With 40 wt% of MelPers 0045, SEM reveals particles below 100 nm. This is in good agreement with the DLS data. Note, that neither large nor rod-shaped particles are observed. We presume that at this concentration the dispersing additive covers the particles' surface fast and completely, suppressing the growth of particles with increased size or aspect ratio. It is not yet clear, whether the rod-shape of some particles observed at lower additive concentrations is induced by the solvent, by the dispersing additive, by impurities in either, or a combination of these factors.

Table 1 Intensity maxima and standard deviations (SD) from DLS depending on the amount of dispersing additive (DA)

DA (wt%)	Intensity maximum (nm)	SD (nm)
0	998	121
2	278	117
5	178	64
20	150	37
40	119	27

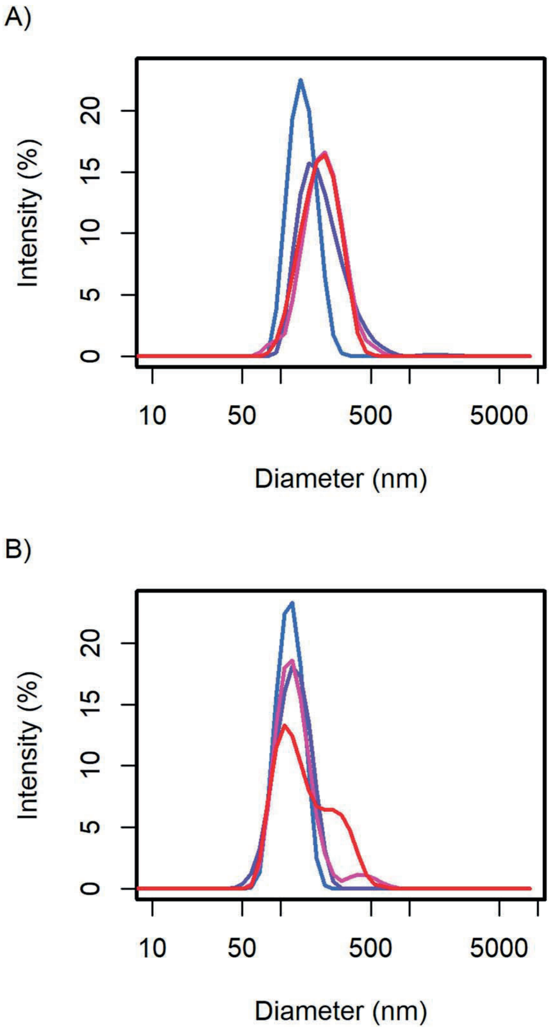

Fig. 2 The CsH_2PO_4 particle size distributions of (A) the 20 wt% and (B) 40 wt% additive samples show minor changes over time from the first measurement (blue), after 1, 3, and 7 days (red).

Despite the different measurement principles and different sources of error, the particle sizes observed in DLS and in SEM show good agreement. The determined particle sizes are therefore reliable. We note, that a dispersing additive content of 20 wt% is sufficient to yield particles of *ca.* 200 nm in diameter. The particle size shows no drastic changes between 5 and 40 wt%. The precipitation with 20 wt% MelPers 0045 is therefore employed in all following experiments.

3.1.2 Batch size. The change of the CsH_2PO_4 particle size with the batch size of the experiment with constant

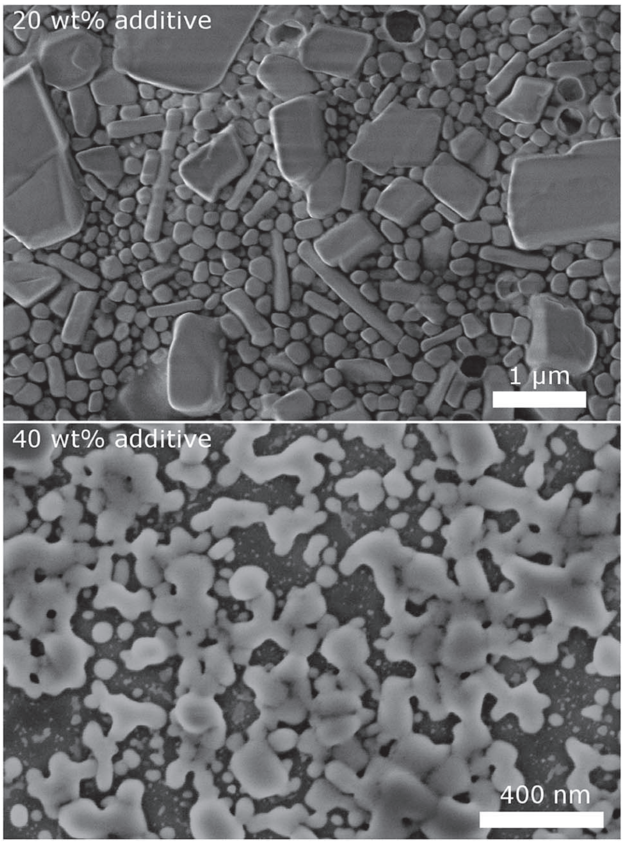

Fig. 3 SEM images of CsH_2PO_4 particles show a decrease of particles size and changes in the shape with increasing amount of dispersing additive.

concentrations is presented in Fig. 4A. A slight variation of the particle size can be observed, but no trend is evident. Small differences in the mixing process in the beaker when pouring the precursor solutions together might be the origin of this variation.

From the 4 g batch size, the product was separated by centrifugation. Even after prolonged centrifugation not all particles had sedimented. A DLS measurement of the supernatant resulted in practically the same particle size distribution as the sample with 40 wt%. The smallest particles formed in the precipitation in the presence of the dispersing additive in a beaker are thus of a similar size, independent of its concentration. The reason might be that the microscopic mixing in the precipitation in a beaker is not well controlled. However, due to the strong size-dependence of the scattering intensity the smaller particles are not always evident in DLS.

3.1.3 Nominal product concentration. The concentration of the solutions in the precipitation reaction influences the supersaturation and thus the particle size. Additionally, high concentrations are desired for large-scale synthesis. Thus the concentration dependence of the particle size was investigated.

We observe, that the samples with very low and very high concentration show faster sedimentation. This correlates very well with the particle size distribution observed in DLS (Fig. 4B). The suspensions with 1, 40, and 50 g L^{-1} show bimodal distributions: one part of the particles is in the range of 200 nm and thus similar to the particle size with 5 and 10 g L^{-1}. A second part of the particles has significantly larger diameters.

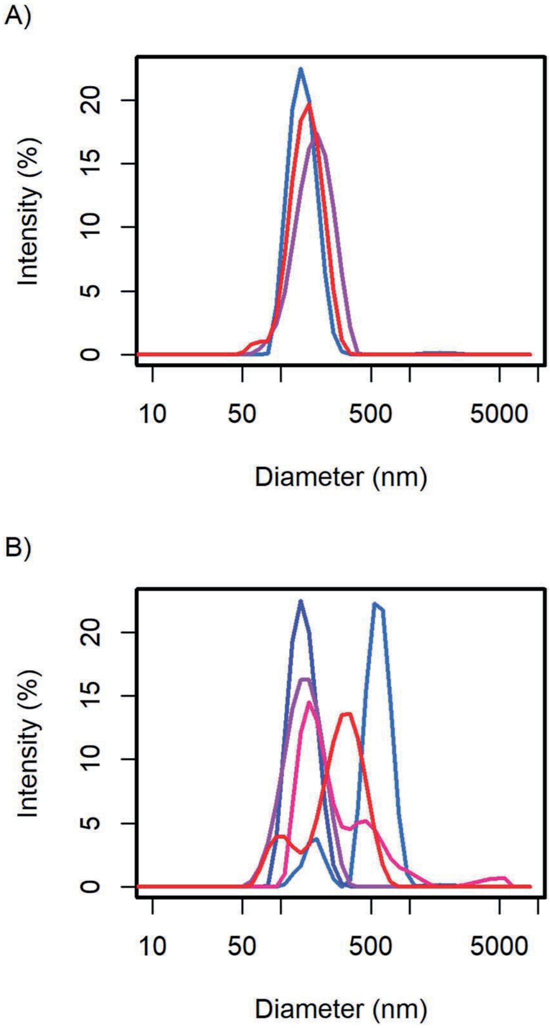

Fig. 4 The CsH_2PO_4 particle size as measured with DLS shows (A) no clear trend when scaling the synthesis (0.25 (blue), 1, and 4 g (red)) but (B) changes with the nominal product concentration: 1 (blue), 5, 10, 40, and 50 g L^{-1} (red).

At 1 g L^{-1} the larger particles might form because the lower concentration leads to a lower supersaturation and thus less nucleation. The lower concentration of the dispersing additive in the solvent could also lead to a less adsorption of the additive onto the surface, reducing its stabilizing effect. At elevated concentrations, the viscosity of the solutions probably increases, leading to slower mixing and thus again less supersaturation and fewer crystal nuclei. In addition, agglomeration should be more severe at higher concentration as more particle collisions occur. In the range of 5–10 g L^{-1} the size distribution shows only one peak around 200 nm. Here, the above-mentioned effects are not inhibiting the formation of stabilized small particles.

3.1.4 Shape control. It has been reported, that the solvent can influence the shape of the precipitated CsH_2PO_4 particles.[19] In Fig. 5 SEM images of particles precipitated from various solvents are presented, with all concentrations as in the

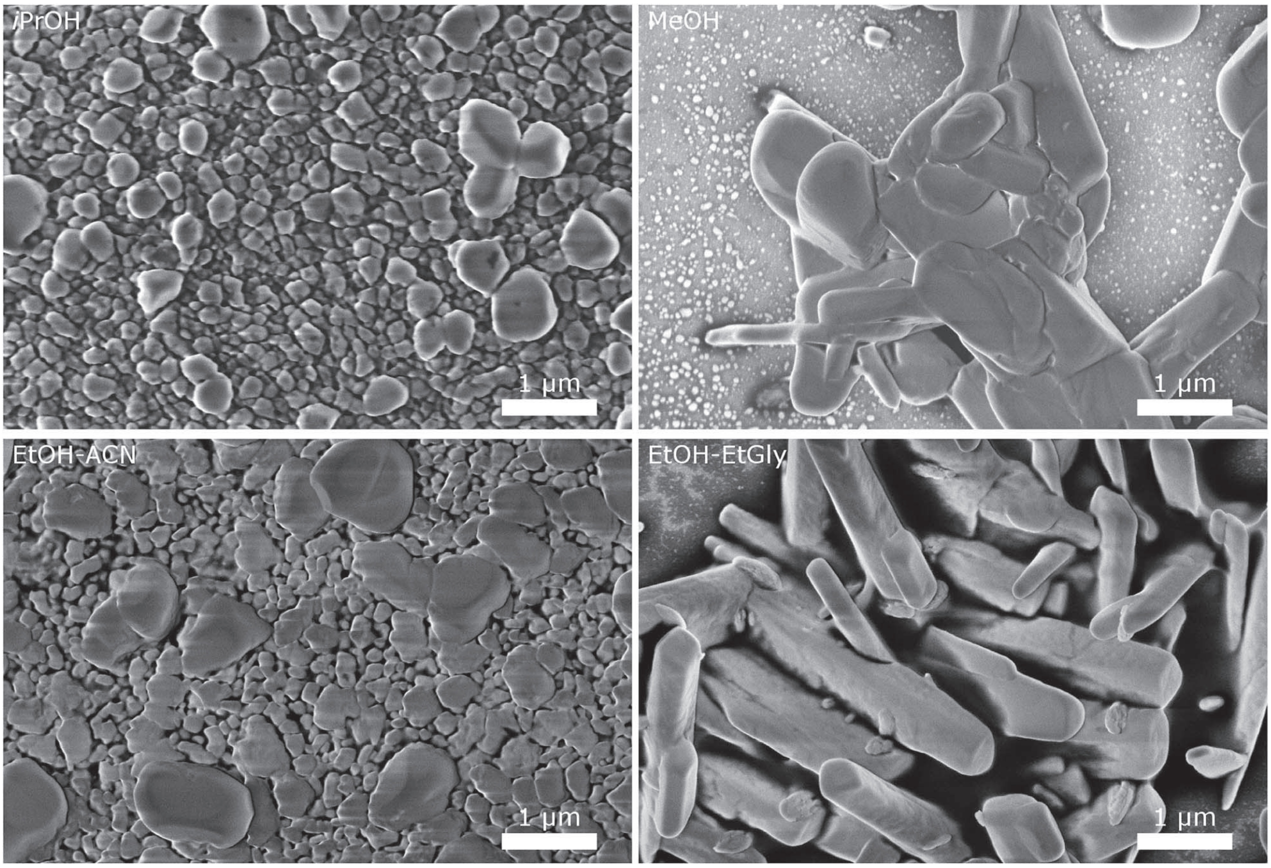

Fig. 5 SEM images of CsH_2PO_4 particles precipitated in different solvents illustrate the influence of the solvent on the particle size and morphology.

reference experiment with 5 g L^{-1} and 20 wt% MelPers 0045. The DLS particle size distributions of sufficiently stable suspensions are given in the ESI (Fig. S1†).

The particles from EtOH are mostly spherical, but with a significant number of rod-shaped particles and some larger ones, as observed in the experiments described above. Isopropanol yields spherical particles with a broader size distribution and no rods are observed. In MeOH, we observe a tendency for larger particles, although a significant number of small particles below 200 nm is also present. The mixture of EtOH with acetonitrile (EtOH–ACN) yielded mostly spherical particles, as in EtOH. While acetonitrile has been reported to lead to rod-shaped particles,[19] we do not observe this effect with our precipitation protocol.

With a mixture of EtOH and ethylene glycol (EtOH–EtGly), no precipitation was observed when mixing the precursor solutions. Only on the next day, fine needles could be recognized. SEM revealed the presence of rod-shaped particles of slightly larger dimensions than in the precipitation with pure EtOH. This agrees with the finding of Ahn *et al.*, who observed the formation of rods in a mixture of MeOH and ethylene glycol.[19] In addition, more than 3 µm long needles were observed. However, these probably formed while drying the SEM sample.

These results show, that the particle morphology and size can be influenced by the choice of the solvent, also in presence of the dispersing additive. While small spherical particles are good for producing thin layers as electrolyte membranes for SAFCs, particles with a large aspect ratio are beneficial for producing porous electrodes. Further investigations with different solvents and solvent mixtures, should allow the precipitation of such particles. Our results with ethanol and ethylene glycol are already very promising. Good control of the mixing process should be essential for homogeneous particle shapes.

3.2 Microreactor precipitation

To determine, how the mixing process and its time scale influence the particle size, we conducted the precipitation in a microreactor with an extremely short mixing time (*ca.* 10 ms (ref. 29)), compared to the conventional experiments in simple glass beakers. In Fig. 6 SEM images of the particles obtained with the same concentrations as the standard 5 g L^{-1} precipitation with 5 and 20 wt% of dispersing additive are given. Although the particles partly agglomerated during the drying process, a decrease in size can be observed with increasing concentration of dispersing additive. For both samples the particles have similar sizes, below 200 nm, as those precipitated by mixing in a beaker. However, in contrast to these, no significantly larger particles are observed. This indicates that as expected, the continuous, thorough mixing in the microreactor yields a narrower particle size distribution than the rather uncontrolled mixing in a beaker.

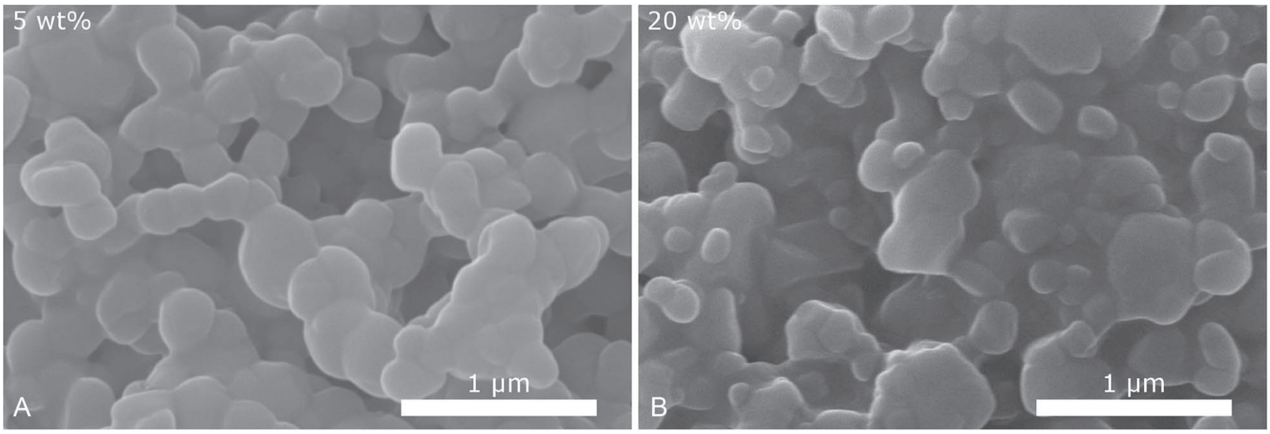

Fig. 6 SEM images of CsH_2PO_4 particles produced with the microjet mixer with (A) 5 wt% and (B) 20 wt% of dispersing additive show similar sizes but narrower size distribution than precipitation in a beaker.

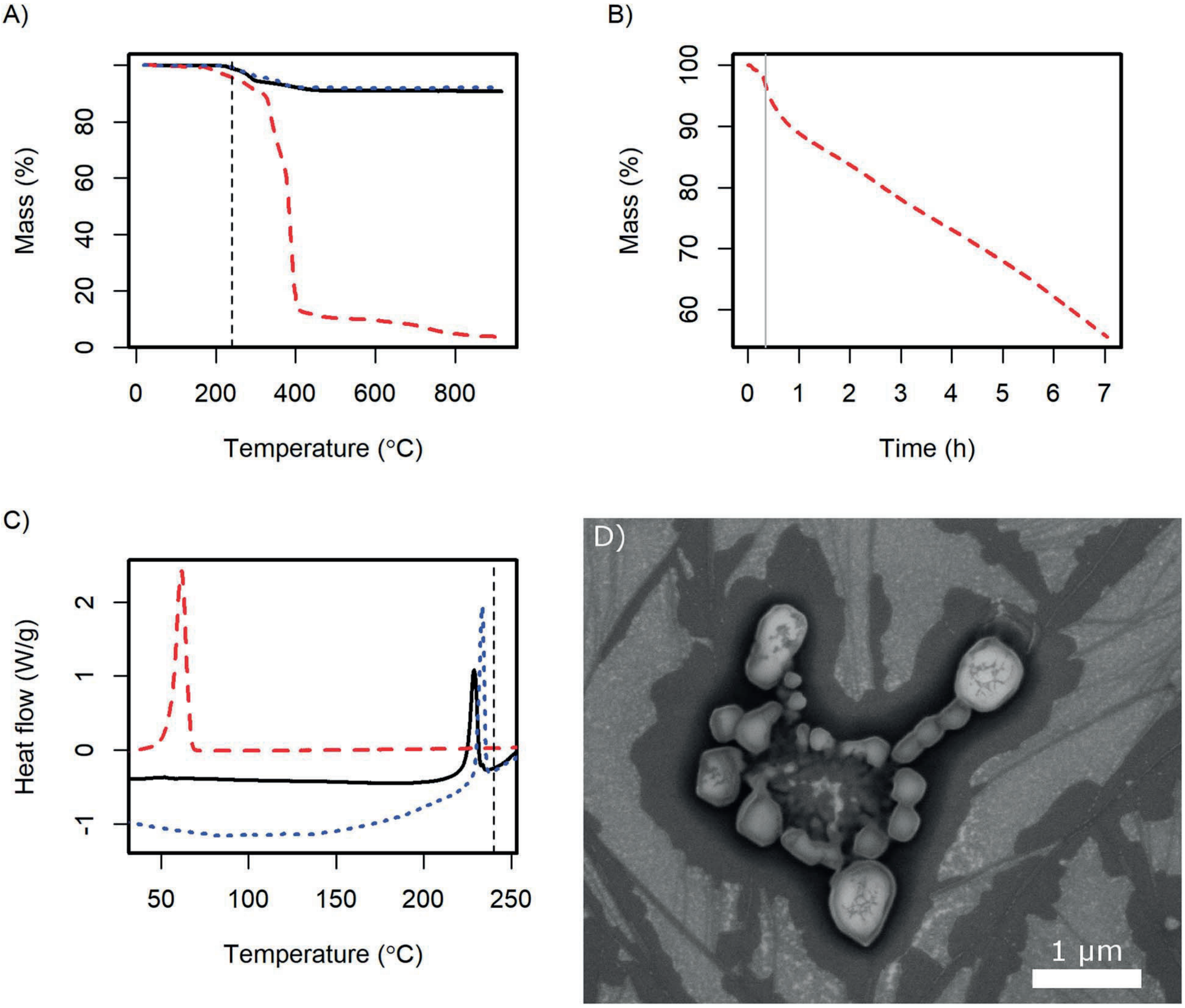

Fig. 7 TGA (A) shows the thermal stability of the CsH_2PO_4 particles (black line) and its constituents, CsH_2PO_4 (dotted blue line) and MelPers 0045 (dashed red line) under air, and (B) the weight change of MelPers 0045 at 240 °C after a short ramp to this temperature (grey line). In DSC (C), the glass transition of MelPers 0045 as well as the superprotonic transition of CsH_2PO_4 is observed for the CsH_2PO_4 particles. The SAFC operating temperature of *ca.* 240 °C is indicated by a vertical dashed line. (D) SEM image of CsH_2PO_4 particles after exposure to SAFC operating conditions (240 °C, H_2, 0.4 atm H_2O) for 13 h.

For an otimized precipitation of $BaSO_4$ in a microreactor particles down to 60 nm have been reported.[25] The authors mentioned that although the primary particles and the crystallite size from XRD were in the order of 25 nm, increasing the amount of dispersing additive did not yield smaller particles. The particle size was mainly controlled by agglomeration and not by crystal growth.

We analyzed the crystallite size of selected samples from the batch precipitation by XRD: the crystallite size of the 4 g batch product was 42 nm. XRD of the sample without dispersing additive yielded 44 nm, the conventional precipitation from aqueous solution without dispersing additive 41 nm. Keeping in mind the limitations of the Scherrer equation, the differences are not significant. The particle size is thus not determined by the crystallite size but by the degree of agglomeration, as in the precipitation of $BaSO_4$. It can therefore be expected, that the particle size can still be slightly reduced employing the microreactor with a high concentration of dispersing additive. However, the study on $BaSO_4$ indicates that the diameter will probably remain above two times the crystallite size.

3.3 Application in SAFCs

For the application of the CsH_2PO_4 particles in SAFCs, their conductivity and stability under the operating conditions are important. Therefore, further analysis was performed with the product of the 4 g batch. The X-ray diffractogram (ESI Fig. S2†) shows the same pattern as pure CsH_2PO_4. Slight variations in the intensity of the reflexes probably arise from different preferred orientations of the crystallites.

In DSC the glass transition of the polymer as well as the superprotonic transition of CsH_2PO_4 are observed as in the pure compounds (Fig. 7C). The content of the dispersing additive in the dry product is nominally 9 wt% and the glass transition probably changes due to the interaction with the CsH_2PO_4. Therefore the glass transition peak in the product is very small. The observed enthalpy of the superprotonic transition of the particles is 10 kJ mol^{-1}. Given, that the nominal content of CsH_2PO_4 is 91%, this is in good agreement with the literature value of 11.7 ± 1.1 kJ mol^{-1}.[33]

TGA reveals, that the dispersing additive exhibits minor weight loss starting at 170 °C and a very rapid decrease above 320 °C (Fig. 7A). Held at the SAFC operating temperature at 240 °C, a continuous weight loss is observed (Fig. 7B). The additive can therefore be removed by thermal decomposition, which should allow the use of high quantities of the dispersing additive in the precipitation without diminishing the proton conductivity under SAFC conditions.

The weight loss of CsH_2PO_4 precipitated with MelPers 0045 is essentially a superposition of the degradation of the dispersing additive and the well-known dehydration of the salt.[1] Unfortunately, these two processes overlap and might slightly differ from the pure compounds. As the dispersing additive is decomposed to a large extent at high temperatures, calculating its mass fraction in the product is prone to error. Nevertheless, with the weight loss at the plateau at 550 °C we calculate a fraction of 9.5 wt%. This is in good agreement with the amount of employed dispersing additive, which was 20 wt% of the 45 wt% solution of the dispersing additive.

As the crystal structure of the CsH_2PO_4 particles corresponds to bulk CsH_2PO_4 and the superprotonic transition is observed in DSC, proton conduction can be expected. The conductivity of a 0.5 mm thick pellet under SAFC operating conditions increased to 2.0 10^{-2} S cm^{-1} within 4 h. The impedance spectrum is given in Fig. S3.† The observed conductivity is slightly lower than the value of 2.2×10^{-2} S cm^{-1} reported for pure CsH_2PO_4.[1] This difference can be assigned to the dispersing additive or its decomposition products at the particle interfaces. However, the conductivity kept increasing toward the literature value with the slope depending on the gas flow at the electrodes. The dependence on time and gas flow probably reflects the continuous decomposition of the additive, which can be expected to proceed more slowly in the dense pellet than in the loose powder in TGA under air.

The stability of the particles with respect to sintering was evaluated by exposing SEM samples to SAFC operating conditions, Fig. 7D. It can be seen that the particles sinter but do not coalesce completely. So although the additive is not stable at 240 °C, the electrolyte particles are surprisingly stable. The long-term stability of a porous electrode fabricated from these particles needs further investigation. It might be necessary to add a temperature-resistant polymer like PVP to stabilize the

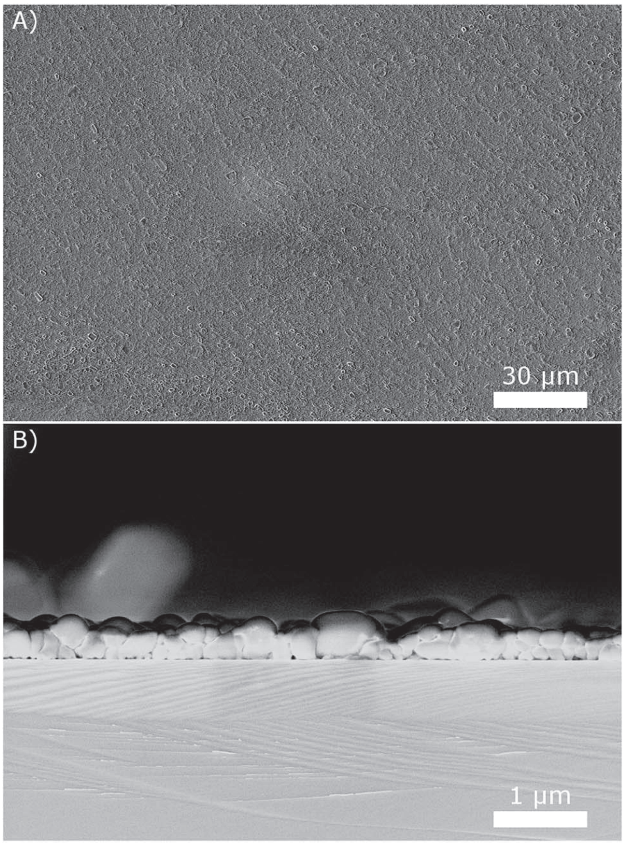

Fig. 8 (A) SEM images of CsH_2PO_4 particles precipitated with 10 g L^{-1} and drop coated on a wafer show good coverage of the surface. (B) The side view of the sample broken in half reveals the thickness of the layer.

structure, see ref. 16 and 17. However, such polymers also have a negative effect on the ion conductivity in the electrodes, which will be discussed in a different publication. For preparing thin electrolyte membranes, sintering is not an issue as a dense layer is desired.

The next step is the development of fabrication processes for SAFC electrolyte membranes and electrodes from the obtained suspensions. As for thin electrolyte membranes, we observed that drop coating the suspensions on silicon wafers at 80 °C results in quite uniform thin layers with good surface coverage. An example is given in Fig. 8, using the 10 g L^{-1} suspension. The side view of the layer reveals that it is only a few particles thick, resulting in a total thickness below 1 μm. Repeating the coating several times resulted in correspondingly thicker layers.

4 Outlook and conclusion

In this work, we presented a simple, robust, and scalable method to prepare CsH_2PO_4 particles down to below 200 nm in diameter for application in solid acid fuel cell electrodes and electrolyte membranes. Stable suspensions of CsH_2PO_4 particles were obtained by mixing solutions of CsOH and H_3PO_4 in alcohols in the presence of the commercially available dispersing additive MelPers 0045. We investigated the influence of the concentrations, the batch size, the solvents, and the mixing process and found that the particle size and shape can be tuned. Compared to electrospray deposition and spray drying, which are the state-of-the art methods for synthesizing sub-micrometer CsH_2PO_4 particles, the presented precipitation is much simpler and at the same time yields similar particle sizes. The new method should be suitable for continuous production of small electrolyte particles for the application in SAFCs on a commercial scale.

The next step is to establish protocols for fabricating thin electrolyte membranes and porous electrodes from the suspensions. Our preliminary drop-coating results point out the potential for obtaining dense CsH_2PO_4 layers of only few micrometers in thickness. For application to larger areas, the stable suspensions could be applied with a spray gun as commonly used in painting. Independent of the mode of application, polymeric binders like PVDF or epoxi resin can be added to improve the mechanical properties of the layer.[7–9] Another promising candidate would be polyamide-imides as these are thermally and mechanically stable, available in soluble form, and can be cured at temperatures around the operating temperature of SAFCs.

For the preparation of porous composite electrodes for SAFCs, the particles could for example be transferred to toluene and mixed with the supported electrocatalyst to form a slurry or suspension, which can be applied by spraying or screen printing. Here, the new sub-micrometer particles could be combined with recently reported platinum nanoparticles on CNTs to yield high-power SAFCs.[10,11] First experiments adding CNTs before and after the precipitation as described in this work, indicate, that very intimate mixtures can be obtained, potentially maximizing the amount of active sites.

Conflicts of interest

There are no conflicts of interest to declare

Acknowledgements

The authors would like to thank Ingrid Reinhard for DSC and TGA measurements, Andrea Prager for several SEM sessions, and Jan Griebel for XRD measurements. We would like to thank Tovhowani I. Kwinda, Jan Henke, and Maria Krause, for lab assistance and to the latter two and Nadja Schönherr for recording DLS data. Furthermore, we thank Torben Gaedt, BASF Construction Solutions, for fruitful discussion on dispersing additives, and Maximilian Wagner for advise on conductivity measurements. F. L.-R. is grateful for a scholarship from the 'German Federal Environmental Foundation' DBU. The authors acknowledge funding through the ESF-Forschergruppe 'Applied and theoretical molecular electrochemistry as a key for new technologies in the area of energy conversion and storage' and the 'Volkswagen Foundation'.

Notes and references

1 S. M. Haile, C. R. I. Chisholm, K. Sasaki, D. A. Boysen and T. Uda, *Faraday Discuss.*, 2007, **134**, 17–39.
2 N. Mohammad, A. B. Mohamad, A. A. H. Kadhum and K. S. Loh, *J. Power Sources*, 2016, **322**, 77–92.
3 C. R. Chisholm, D. A. Boysen, A. B. Papandrew, S. Zecevic, S. Cha, K. A. Sasaki, Á. Varga, K. P. Giapis and S. M. Haile, *Electrochem. Soc. Interface*, 2009, **18**, 53.
4 T. Uda and S. M. Haile, *Electrochem. Solid-State Lett.*, 2005, **8**, A245–A246.
5 A. I. Baranov, V. V. Grebenev, A. N. Khodan, V. V. Dolbinina and E. P. Efremova, *Solid State Ionics*, 2005, **176**, 2871–2874.
6 P. Bocchetta, G. Chiavarotti, R. Masi, C. Sunseri and F. Diquarto, *Electrochem. Commun.*, 2004, **6**, 923–928.
7 D. A. Boysen, C. R. I. Chisholm, S. M. Haile and S. R. Narayanan, *J. Electrochem. Soc.*, 2000, **147**, 3610.
8 G. Qing, R. Kikuchi, A. Takagaki, T. Sugawara and S. T. Oyama, *J. Electrochem. Soc.*, 2014, **161**, F451–F457.
9 G. Qing, R. Kikuchi, A. Takagaki, T. Sugawara and S. T. Oyama, *Electrochim. Acta*, 2015, **169**, 219–226.
10 F. P. Lohmann, P. S. C. Schulze, M. Wagner, O. Naumov, A. Lotnyk, B. Abel and A. Varga, *J. Mater. Chem. A*, 2017, **5**, 15021–15025.
11 A. B. Papandrew, R. A. Elgammal, M. Tian, W. D. Tennyson, C. M. Rouleau, A. A. Puretzky, G. M. Veith, D. B. Geohegan and T. A. Zawodzinski, *J. Power Sources*, 2017, **337**, 145–151.
12 V. S. Thoi, R. E. Usiskin and S. M. Haile, *Chem. Sci.*, 2015, **6**, 1570–1577.
13 F. P. Lohmann-Richters, B. Abel and Á. Varga, *J. Mater. Chem. A*, 2018, **6**, 2700–2707.
14 A. B. Papandrew, C. R. I. Chisholm, R. A. Elgammal, M. M. Özer and S. K. Zecevic, *Chem. Mater.*, 2011, **23**, 1659–1667.

15 K. A. Sasaki, Electrochemical Characterization of Solid Acid Fuel Cell Electrodes, PhD thesis, California Institute of Technology, Pasadena, California, 2010.

16 R. C. Suryaprakash, F. P. Lohmann, M. Wagner, B. Abel and A. Varga, *RSC Adv.*, 2014, **4**, 60429–60436.

17 A. Varga, N. A. Brunelli, M. W. Louie, K. P. Giapis and S. M. Haile, *J. Mater. Chem.*, 2010, **20**, 6309–6315.

18 S. Hosseini, W. R. W. Daud, M. Badiei, A. A. H. Kadhum and A. B. Mohammad, *Bull. Mater. Sci.*, 2011, **34**, 759–765.

19 Y. S. Ahn, I. R. Mangani, C. W. Park and J. Kim, *J. Power Sources*, 2006, **163**, 107–112.

20 H. C. Schwarzer and W. Peukert, *Chem. Eng. Technol.*, 2002, **25**, 657.

21 K. Jahnisch, V. Hessel, H. Lowe and M. Baerns, *Angew. Chem., Int. Ed. Engl.*, 2004, **43**, 406–446.

22 C. Tonhauser, A. Natalello, H. Löwe and H. Frey, *Macromolecules*, 2012, **45**, 9551–9570.

23 S. A. Khan, A. Gunther, M. A. Schmidt and K. F. Jensen, *Langmuir*, 2004, **20**, 8604–8611.

24 B. Penth, *Kontinuierliche Produktion in Mikroreaktoren*, 2007, German Patent DE 102006004350 A1, August.

25 A. Rüfer, K. Räuchle, F. Krahl and W. Reschetilowski, *Chem. Ing. Tech.*, 2009, **81**, 1949–1954.

26 B. Dittert, A. Gavrilović, S. Schwarz, P. Angerer, H. Steiner and R. Schöftner, *J. Eur. Ceram. Soc.*, 2011, **31**, 2475–2480.

27 A. Betke and G. Kickelbick, *Inorganics*, 2014, **2**, 1–15.

28 B. Kruner, C. Odenwald, A. Tolosa, A. Schreiber, M. Aslan, G. Kickelbick and V. Presser, *Sustainable Energy Fuels*, 2017, **1**, 1588–1600.

29 C. Odenwald and G. Kickelbick, *J. Sol-Gel Sci. Technol.*, 2018, DOI: 10.1007/s10971-018-4626-x.

30 R. T. Kügler, S. Doyle and M. Kind, *Chem. Eng. Sci.*, 2015, **133**, 140–147.

31 M. Pieper, S. Aman, W. Hintz and J. Tomas, *Chem. Eng. Technol.*, 2011, **34**, 1567–1574.

32 BASF Construction Solutions, Technical Data Sheet: MelPers 0045, 2017.

33 A. Ikeda and S. M. Haile, *Solid State Ionics*, 2012, **213**, 63–71.

Supporting information

Facile and scalable synthesis of sub-micrometer electrolyte particles for solid acid fuel cells

F. P. Lohmann-Richters,[a] C. Odenwald,[b] G. Kickelbick,[b] B. Abel,[a] and Á. Varga*[a]

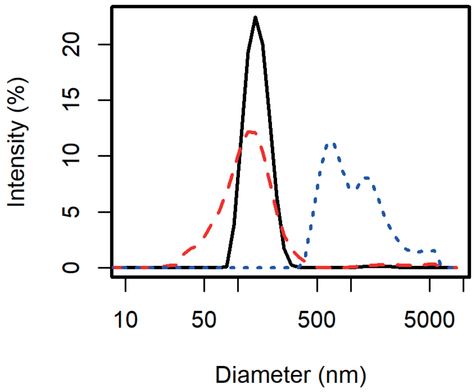

Figure S1: The CsH_2PO_4 particle size as measured with DLS depends on the choice of the solvent; EtOH (black), *i*PrOH (dashed, red), MeOH (dotted, blue).

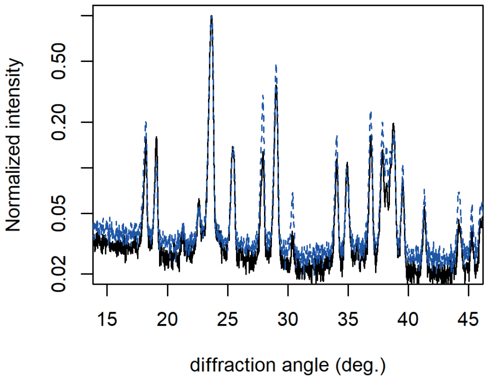

Figure S2: The X-ray diffractogram of CsH_2PO_4 prepared with 20 wt% dispersing additive (black) shows good agreement with that of pure CsH_2PO_4 (blue, dashed).

---

[a] *Leibniz Institute of Surface Engineering (IOM), Permoserstr. 15, D-04318 Leipzig, Germany. Tel: +49 341 2353364; E-mail: aron.varga@iom-leipzig.de*
[b] *Saarland University, Inorganic Solid State Chemistry, Campus Building C4 1, 66123 Saarbrücken, Germany.*

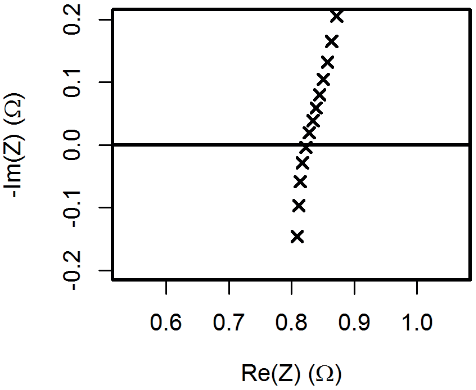

Figure S3: The electrochemical impedance spectrum of a 1 cm radius and 0.5 mm thick pellet of the material from the 4 g batch.

The last two studies investigated how the operating parameters of the MicroJet reactor process affect the properties of the products from precipitation reactions. In the following articles, the performance of sol-gel reactions in the reactor is tested and mainly chemical parameters are varied.

3.3 ORMOSIL particles

3.3.1 Additive-free continuous synthesis of silica and ORMOSIL micro- and nanoparticles applying a MicroJet reactor

This chapter describes the development of a procedure to transform trialkoxysilanes continuously into ORMOSIL particles in the MicroJet reactor. The mixing rate of the reactor is investigated by a suitable test reaction and, compared to other methods, a relatively short mixing time (of about 10 ms) is determined, which is the basis for producing particles with narrow size distributions. However, since the residence time in the reactor is also short, the alkoxysilane reagents have to be pre-treated in such a way that they can react with each other within this short time interval. Small amounts of acid are therefore added to the alkoxysilanes and the solutions are stirred for a certain time. In this way, the alkoxysilanes are partially hydrolyzed, so that the condensation of these species in the reactor can proceed more quickly afterwards. Additionally, a basic catalyst is added to the MicroJet reactor to further accelerate the reaction.

In order to find a general synthesis method for a wide range of different ORMOSIL materials, the describe procedure is tested for many different precursors. In this way, it is also possible to identify superordinate relationships.

Besides the synthesis, the following article focuses on the detailed characterization of the products. The results give an overview of how the different organic groups influence the structure and properties of the ORMOSILs. This is particularly important for the further processing of the particles and the selection of certain organic groups for specific applications.

Contributions:

Christina Odenwald: Design, planning, writing, synthesis of ORMOSIL particles, SEM, particle size analysis, FT-IR, TGA, analysis of NMR spectra. **Guido Kickelbick:** Supervision, discussion and revision of the manuscript.

The following paper is reprinted by permission from Springer Nature: Springer Nature, Journal of Sol-Gel Science and Technology, Additive-free continuous synthesis of silica and ORMOSIL micro- and nanoparticles applying a MicroJet reactor, Christina Odenwald, Guido Kickelbick, Copyright © Springer Science Business Media, LLC, part of Springer Nature, 2018, https://doi.org/10.1007/s10971-018-4626-x

Journal of Sol-Gel Science and Technology (2019) 89:343–353
https://doi.org/10.1007/s10971-018-4626-x

ORIGINAL PAPER: SOL-GEL, HYBRIDS AND SOLUTION CHEMISTRIES

Additive-free continuous synthesis of silica and ORMOSIL micro- and nanoparticles applying a microjet reactor

Christina Odenwald[1] · Guido Kickelbick[1]

Received: 14 December 2017 / Accepted: 3 March 2018 / Published online: 13 March 2018

Abstract

The continuous wet chemical preparation of micro- and nanoparticles is a major challenge for the large-scale production of functional colloids. Here we present a general synthetic strategy for sol–gel-based materials via an additive free homogenous approach avoiding emulsion-based systems. A variety of different silica and organically-modified silica (ORMOSIL) spherical particles were prepared applying a condensation of prehydrolyzed alcoholic solution of organotrialkoxysilanes in a microjet reactor. This method presents a unique wet chemical production method for nano- and microscale materials. Methyl-, ethyl-, propyl-, vinyl-, phenyl-, and mixed ORMOSIL particles in the range of 75 nm–2 µm were successfully synthesized without the addition of stabilizing surfactants. The method was also investigated for the continuous preparation of pure silica particles, and we succeeded to produce continuously up to 23 g particles per minute. The influence of different organic groups on the crosslinking of the siloxane network was systematically studied applying various spectroscopic and thermoanalytical methods. The degree of condensation of the obtained particles depends on the organic rests of the trialkoxysilanes, which was studied with ^{29}Si CP-MAS NMR. We were able to show that phenyl silsesquioxanes show less condensation in the particles than smaller alkyl or vinyl groups. In addition, the silane concentration has a significant influence on the particle size. Generally, smaller particle diameters are obtained after decreasing the silane concentration. The described process delivers a fast and large scale wet chemical production of various silsesquioxane and silica particles without the use of additives and is therefore suited for a variety of potential applications where high purity of the particles is necessary.

Graphical Abstract

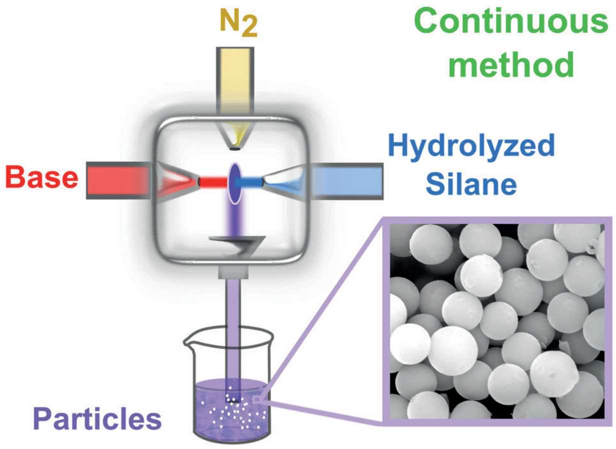

Electronic supplementary material The online version of this article (https://doi.org/10.1007/s10971-018-4626-x) contains supplementary material, which is available to authorized users.

✉ Guido Kickelbick
guido.kickelbick@uni-saarland.de

[1] Saarland University, Inorganic Solid State Chemistry, Campus, Building C4 1, 66123 Saarbrücken, Germany

Keywords Continuous synthesis · microreactor · ORMOSIL · polysilsesquioxanes · silica nanoparticles · additive-free

Highlights

- The paper shows for the first time the continuous, wet chemical preparation of ORMOSIL micro-and nanoparticles applying a microjet reactor.
- No additives for the stabilization of the particles are required.
- The particles can be prepared with yields up to 23 g min^{-1}.
- Well-defined particle morphologies were obtained of methyl-, ethyl-, propyl-, vinyl-, and phenyl-ORMOSILs as well as pure silica particles.
- The condensation degrees of the particles vary depending on the organic substitution pattern at the silicon atom.

1 Introduction

Various applications of micro- and nanoparticles were investigated extensively during the last two decades in areas such as catalysis [1], sensing [2], photovoltaic devices [3], medicine [4], food industry [5], and textiles [6]. In literature typical reaction conditions in the synthesis of these particles vary depending on the composition and the size of the targeted particles. However, most of the methods have in common that they are based on batch processes, which reveal disadvantages such as long mixing times and therefore heterogeneous distributions of reactant concentrations, temperatures, and pH values. Uncontrolled particle growth, broad size distributions, and a batch-to-batch reproducibility are thus reported consequences depending on the used precursors and the targeted particles [7].

Compared to batch processes, continuous preparation methods offer in general a better controllability, reproducibility, and higher yields [8]. For the continuous nanoparticle production only a few methods can be used, but many of them are based on precursor treatment under high temperatures, such as the pyrogenic particle synthesis [9]. Continuous wet chemical methods for the synthesis of micro- and nanoparticles are very rarely employed. Only microfluidic methods especially microchannel devices were studied in a broader range [10, 11].

Microreactors offer the advantage of short mixing times that lead to a homogenous environment during the particle formation process and narrow size distributions [12]. Upscaling is possible by a parallel reactor design. In a previous work [13] we demonstrated the continuous synthesis of various metal oxide as well as apatite particles in a so called microjet reactor [14]. We showed that the properties of these particles could be controlled by regulating process parameters such as the temperature or the flow rate and thus the velocity in which the two precursor streams collide in the focal point of the reactor. We proved this mainly on the precipitation of metal oxide particles under basic conditions, which is—due to the low solubility—a quite fast process. Generally, other reactions such as typical sol–gel reactions based on alkoxysilane precursors are relatively slow and are usually not ideally suited for micromixers. Only a few previous studies showed the suitability of related methods for the synthesis of pure silica particles [15, 16], or for the preparation of soluble polysilsesquioxanes under acid conditions [17]. While the production of silica particles under basic conditions applying the so-called Stöber process [18] is a well-established robust method, the production of organically-modified silicas (ORMOSILs) is still a challenge. One reason for that is the influence of the organic substituents at the silicon atom, which change the hydrolysis and condensation rates dramatically in the sol–gel process. In addition, the reduced surface-charge compared to Stöber conditions leads to particle agglomeration and non-stable suspensions. In literature several alternative routes to such types of particles are described, which are: (i) the grafting of organic groups to presynthesized Stöber silica particles [19], (ii) the cocondensation of a mixture of tetraalkoxides and organotrialkoxysilanes [19, 20], (iii) the usage of small SiO_2 nanoparticles as a seed [21], or (iv) emulsion methods that use solely the organotrialkoxysilane [22]. The latter represent often reactions in biphasic systems that require stabilizing additives [23], i.e., surfactants, which contaminate the final particles.

In our investigation, we show the preparation of ORMOSIL micro- and nanoparticles without the addition of stabilizing agents in a continuous sol–gel synthesis based on a microjet reactor. Different reaction parameters such as precursor composition and reaction temperature were systematically varied. The resulting ORMOSIL particles provide a high organic group density and an enhanced porosity compared to silica particles. Their organic–inorganic nature enables access to various other applications, e.g., as catalyst supports, as fillers in composites, as additives in polymers to improve their mechanical properties or antireflective coatings [24]. In a recently published paper we demonstrated that such ORMOSIL particles can be used as precursors of highly porous carbon materials which can be used as electrode materials for supercapacitors [25]. The ORMOSIL approach offers here the advantage that the porosity can be tailored by the precursor composition.

2 Experimental

2.1 Materials

Tetraethyl orthosilicate was provided by the Wacker Silicones (Burghausen, Germany), methyltriethoxysilane (MTES) (98%), n-propyltriethoxysilane (PTES) (97%), phenyltriethoxysilane (PhTES) (97%), ethyltrimethoxysilane (ETMS) (97%), phenyltrimethoxysilane (PTMS) (97%), and vinyltrimethoxysilane (VTMS) (99%) were obtained from ABCR (Karlsruhe, Germany). Ammonia (25%, techn.) was purchased from the VWR International GmbH. All chemicals were used as received.

2.2 Apparatus

Two HPLC pumps (LaPrep P110 preparative HPLC pumps (VWR)) were used to transport the solutions A (containing the hydrolyzed silane(s) in water (pH ≈ 6) and alcohol) and B (containing the aqueous solution of ammonia) through the system. The reagent solutions were forced with high pressure through narrow nozzles (with a nozzle diameter of 300 micrometers) in a reaction chamber (microjet reactor, Synthesechemie, Heusweiler, Germany). The growing particles were directly removed from the reactor by the use of a nitrogen gas flow (8 bar). The diameter of the outlet tube was 1.5 mm and the length was 85 cm. The particle solution was collected in a polyethylene or glass vessel. The product suspension collected during the first 10–15 s was discarded to avoid impurities from previous runs.

2.3 Synthesis of nano- and microparticles

For each sample, two precursor solutions were prepared (Table 1). The polarity and the reactivity of the alkoxysilane and its condensation products have a strong influence on the solubility and the reaction kinetics. The silane concentration affects the particle size whereas the acid concentration has

Table 1 Compositions of the precursor solutions A and B that were used for the syntheses of the ORMOSIL and silica particles and hydrolysis times t_H in hours

Sample	System Solution A[a], solution B	n(R'Si(OR)$_3$) mmol	n(ROH) mol	n(H_2O) mol	n(HCl) mmol	t_H h	c(NH_3) mol/l
SiO_2	TEOS/EtOH/HCl, NH_3/H_2O	138.8	2.8	2.8	0.028	27.2	2.2
Methyl-$SiO_{1.5}$	MTES/EtOH/HCl, NH_3/H_2O	138.8	2.8	2.8	0.028	26.4	2.2
Methyl-$SiO_{1.5}$-conc.2	MTES/EtOH/HCl, NH_3/H_2O	69.0	2.8	4.2	0.014	26.4	2.2
Methyl-$SiO_{1.5}$-conc.3	MTES/EtOH/HCl, NH_3/H_2O	35.0	2.8	4.9	0.007	26.4	2.2
Methyl-$SiO_{1.5}$-5 min	MTES/EtOH/HCl, NH_3/H_2O	138.8	2.8	2.8	0.028	0.08	2.2
Methyl-$SiO_{1.5}$-without HCl	MTES/EtOH/HCl, NH_3/H_2O	138.8	2.8	2.8	–	26.4	2.2
Ethyl-$SiO_{1.5}$	ETMS/MeOH/HCl, NH_3/H_2O	138.8	1.2	5.6	0.056	18.0	2.2
Ethyl-$SiO_{1.5}$-5 min	ETMS/MeOH/HCl, NH_3/H_2O	138.8	1.2	5.6	0.056	0.08	2.2
Ethyl-$SiO_{1.5}$-without HCl	ETMS/MeOH/HCl, NH_3/H_2O	138.8	1.2	5.6	–	18.0	2.2
n-Propyl-$SiO_{1.5}$	PTES/EtOH/HCl, NH_3/H_2O	138.8	2.8	2.8	0.056	29.3	2.2
n-Propyl-$SiO_{1.5}$-5 min	PTES/EtOH/HCl, NH_3/H_2O	138.8	2.8	2.8	0.056	0.08	2.2
n-Propyl-$SiO_{1.5}$-without HCl	PTES/EtOH/HCl, NH_3/H_2O	138.8	2.8	2.8	–	29.3	2.2
Vinyl-$SiO_{1.5}$	VTMS/MeOH/HCl, NH_3/H_2O	138.8	3.2	2.8	0.028	25.5	2.2
Vinyl-$SiO_{1.5}$ -5 min	VTMS/MeOH/HCl, NH_3/H_2O	138.8	3.2	2.8	0.028	0.08	2.2
Vinyl-$SiO_{1.5}$-without HCl	VTMS/MeOH/HCl, NH_3/H_2O	138.8	3.2	2.8	–	25.5	2.2
Phenyl-$SiO_{1.5}$	PhTES/EtOH/HCl, NH_3/H_2O	138.8	2.8	2.8	0.278	23.2	2.2
Phenyl-$SiO_{1.5}$-conc.2	PhTES/EtOH/HCl, NH_3/H_2O	69.0	2.8	4.2	0.139	23.2	2.2
Phenyl-$SiO_{1.5}$-conc.3	PhTES/EtOH/HCl, NH_3/H_2O	35.0	2.8	4.9	0.069	23.2	2.2
Phenyl-$SiO_{1.5}$-5 min	PhTES/EtOH/HCl, NH_3/H_2O	138.8	2.8	2.8	0.278	0.08	2.2
Phenyl-$SiO_{1.5}$-without HCl	PhTES/EtOH/HCl, NH_3/H_2O	138.8	2.8	2.8	–	23.2	2.2
$Me_{0.4}Ph_{0.6}$-$SiO_{1.5}$	PhTMS(60%)/MTMS (40%)/MeOH/HCl, NH_3/H_2O	138.8	3.2	2.8	0.028	25.7	2.2
$Me_{0.4}Ph_{0.6}$-$SiO_{1.5}$-conc.2	PhTMS(60%)/MTMS (40%)/MeOH/HCl, NH_3/H_2O	69.0	3.2	4.2	0.014	25.7	2.2
$Me_{0.4}Ph_{0.6}$-$SiO_{1.5}$-conc.3	PhTMS(60%)/MTMS (40%)/MeOH/HCl, NH_3/H_2O	35.0	3.2	4.9	0.007	25.7	2.2
$Me_{0.25}Ph_{0.75}$-$SiO_{1.5}$	PhTMS(75%)/MTMS (25%)/MeOH/HCl, NH_3/H_2O	138.8	2.8	2.8	0.028	20.1	2.2
$Vi_{0\cdot25}Ph_{0.75}$-$SiO_{1.5}$	PhTMS(75%)/VTMS (25%)/MeOH/HCl, NH_3/H_2O	138.8	3.2	2.8	0.028	17.8	2.2

[a] Percentage given in mol%

an important impact on the particle size distribution and the hydrolysis conditions that differs for each precursor. The alcohol is necessary to adjust the solvent polarity and ensure that the alkoxysilanes and the condensation products are both soluble and that homogenous particles are formed. The ratio of the mentioned substances was optimized experimentally to obtain well-defined particles. For solution A the respective silanes were dissolved in alcohol. In some cases an aqueous solution of HCl was added. The solution was stirred for 5 min or overnight (hydrolysis time (t_H), Table 1). For solution B, ammonia (25 wt% in water) was diluted with deionized water. During the microjet reactor process (Scheme 1) each reagent solution was fed into the system by using a flow rate of 250 ml min^{-1} and a temperature of 20 °C. The suspension was collected for 15–50 s (depending on the needed amounts) and the formed solids were isolated by centrifugation (8000 rpm, 7012 × G, 10 min) and dried in vacuum at 30 °C. The compounds were characterized applying Fourier transform infrared (FTIR)- and NMR-spectroscopy, TG- and elemental analysis, as well as scanning electron microscopy (SEM).

For studying the influence of the alkoxysilane concentration on the Me-, Ph-, and $Me_{0.4}Ph_{0.6}SiO_{1.5}$ particle size 138.8, 69.4, and 34.7 mmol of alkoxysilane were used (Table 1, samples with suffix conc.2/3). The amount of HCl added was adapted to the silane concentration. That means if the silane concentration was halve the HCl concentration was halve as well. The total volume was kept constant. The particles were produced in the way that is described above (with the addition of HCl and stirring the alkoxysilane solution overnight). The batch synthesis of ORMOSIL microparticles is presented in the supplementary material (Instruments and characterization section).

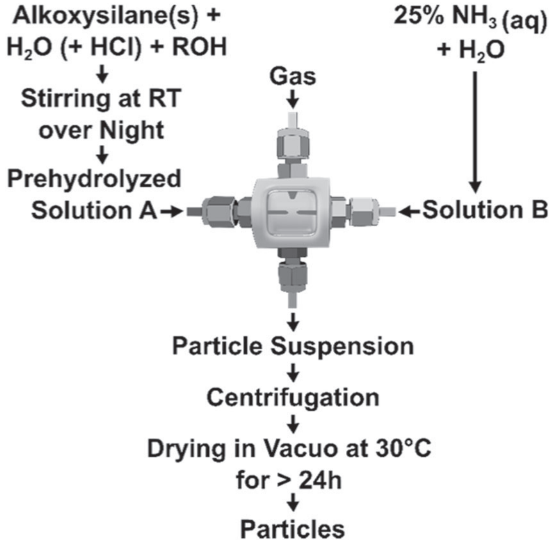

Scheme 1 Schematic preparation procedure for the synthesis of ORMOSIL and silica particles using a microjet reactor

2.4 Instruments and characterization

FTIR measurements of the dried powder samples were performed under ambient air in attenuated total reflectance (ATR) mode on a Bruker Vertex 70 spectrometer (Bruker Optics, Germany). The spectra were recorded by averaging 32 scans at a spectral resolution of 4 cm^{-1} in the wave number range of 500–4200 cm^{-1}. The intensities of the spectra were normalized. Thermogravimetric analyses (TGA) of the samples were carried out on a Netzsch Iris TG 209 C (Netzsch Group, Germany). The samples (≈15 mg) were placed in an alumina crucible and were heated with a rate of 10 K min^{-1}, from room temperature to 1010 °C in a mixture of 5 ml min^{-1} O_2 and 95 ml min^{-1} N_2. The extrapolated degradation onset temperatures were determined by using the tangents method. Elemental analyses were performed with a Leco 900 CHN analyzer. SEM images were obtained using a JEOL JSM-7000 F microscope operating at 20 kV with a working distance of 10 mm. The SEM samples were prepared by placing a small amount of the dry powder on a specimen stub covered with a carbon adhesive foil followed by deposition of a gold layer (JEOL JFC-1300 auto fine coater, 30 mA, 40 s) in order to avoid charging effects. The size distributions of the particles were determined by measure the diameter of 200 individual spheres with the image analysis software ImageJ [26]. Solid state CP-MAS NMR spectra were measured with a Bruker AV400WB spectrometer (^{13}C 100.6 MHz, ^{29}Si 79.5 MHz) at 25 °C. The samples were measured with a spin rate of 13 kHz and a delay time of 3–6 s. As external standard adamantane was used for ^{13}C NMR and octakis(trimethylsiloxy)silsesquioxane for ^{29}Si NMR. All spectra were normalized in the range of 0–1 except the ^{13}C spectrum of the sample of pure SiO_2. This spectrum was normalized by the factor 10 because otherwise the baseline was not comparable with the other samples due to its low signal to noise ratio. Schematic diagrams (graphical abstract and Scheme 1) were drawn with inkscape 0.92 [27].

3 Results and Discussion

3.1 Preparation of ORMOSIL microspheres with different organic groups

The microjet reactor is a unique tool for mixing two different precursor solutions through nozzles of low diameters (in our case 300 µm) in a focal point and directly removing the formed mixture from that location by an inert gas stream, which is the difference to typical T-mixing microreactors. Due to the special design of this tool, high collision energies are produced in the focal point. We currently investigate in further studies how this energy influences the final material. In this current study the continuous synthesis of methyl-, ethyl-, propyl-, vinyl-, and phenyl-modified silsesquioxane particles as well as spheres with more than one functional group and unmodified silica particles was performed by using the microjet reactor. As precursors ethoxy as well as methoxy silanes were used. The mixing efficiency of the reactor was investigated by the Villermaux–Dushman test reaction [28–30]. For our setup (300 µm nozzles and a flow rate of 250 ml min^{-1}) a mixing time of 10 ms was detected (Tables S1 and S2 and Figs. S1 and S2). Our first approach was to induce the sol–gel reaction directly in the reactor by mixing the alcoholic trialkoxysilane solution with the second solution under basic conditions applying ammonia (Table 1 "samplename-without HCl"). These conditions replicate those of a typical Stöber [18] synthesis. But the conditions resulted in inhomogeneous particles with broad size distributions or no solids at all (Fig. S3). We assume that the reaction kinetics was too slow for the fast microjet reactor process and that the particle formation started only after the reaction mixture left the reactor. As a consequence we have chosen a two-step acid-base-catalyzed reaction [31] instead of Stöber conditions. Under basic conditions it is well-known that the alkyl substituted trialkoxylsilanes show slower hydrolysis reactions than pure tetraalkoxysilanes due to inductive effects that lower the stability of the transition state [32]. Hence prehydrolysis is a good tool to form a precursor solution for the particle producing basic conditions in the sol–gel process. Such reaction conditions are regularly used for the preparation of sol–gel processes containing a high amount of organic groups located at the silicon atom [33]. The prehydrolysis time was approximately 24 h per sample in an alcohol-water mixture under addition of diluted HCl at pH 6 in a stirred vessel. According to the literature [34, 35] we used liquid state ^{29}Si NMR to follow the kinetics of this process and to prove if there are already highly condensed species. The spectra showed that after the prehydrolysis mainly T^0 and T^1 signals are present and also no solid phase was visually observed. As an example the spectra of ethyltrimethoxysilane during hydrolysis is shown in Figure S4. At shorter prehydrolysis times the resulting products after applying the microjet reactor either contained no solid products or inhomogeneous particles with a broad size distribution (Fig. S5). The prehydrolysis times were optimized with regard to the homogeneity of the resulting particles and vary between ~18 and 29 h depending on the trialkoxysilane precursor (Table 1). Depending on the type and concentration of the applied precursor solutions and the molecular mass of the alkoxysilane, 9–23 g particles per minute were obtained. The particles were collected in a 0.5 l polyethylene flask. For reasons of comparison we also prepared methyl-, ethyl-, propyl, vinyl-, and phenyl-$SiO_{1.5}$ in batch reactions under the same conditions as applied in the microjet approach (same precursor ratios, hydrolysis times, and similar basic solution) (Table S3). Contrary to the microjet reactions the particles produced under the batch conditions were partially nonspherical (ethyl-$SiO_{1.5}$-batch) and irregular with broad size distributions (methyl-, phenyl-$SiO_{1.5}$) (Fig. S6). For propyl-$SiO_{1.5}$-batch almost no separated particles could be observed. Solely the sample vinyl-$SiO_{1.5}$-batch formed particles that were comparable with the samples from the continuous preparation.

3.2 Particle size and morphology

SEM images of the samples (Fig. 1) prove that the used synthesis conditions led to spherical ORMOSIL microparticles with sizes in the range of 0.7–2.0 µm. Pure SiO_2 particles prepared under similar conditions exhibit sizes one order of magnitude less than these values. Particle size distributions (averaged over 200 or more particles), average particle diameters ($d_{avg.}$), standard deviations (σ), and polydispersities ($100*\sigma/d_{avg.}$) of the samples were determined analyzing the SEM pictures. The narrowest size distributions were obtained for methyl-$SiO_{1.5}$, ethyl-$SiO_{1.5}$, and SiO_2 particles whereas samples with large or mixed organic groups tend to have broader distributions. The small size of the silica particles (Fig. 1 (i) and magnified version Fig. S7) is effected by a denser network structure. Unlike trialkoxysilanes TEOS can connect to the network with four bonds instead of three and no organic group is present that takes space in the structure. As mentioned above a prehydrolysis step under acid conditions is necessary to obtain optimized particle morphologies and size distributions. To investigate the influence of this step an experiment without hydrolyzing the precursor solution overnight was carried out in which the same precursor concentrations as in the other experiments were used (Table 1, "samplename-5 min"). The silane solution was just stirred for 5 min before the reaction mixture was injected in the microjet reactor. SEM images of the samples (Fig. S5) showed that only for methyl-, ethyl-, and vinyl-$SiO_{1.5}$ solids were formed but most of the thus formed particles have a broad size distribution and also non-spherical structures were obtained. The vinyl-$SiO_{1.5}$-5 min particles are slightly bigger ($d_{avg.} = 0.9$ µm) than those that were hydrolyzed for >12 h. Propyl- and phenylalkoxysilanes showed no reaction and a phase separation after centrifugation from the water/alcohol phase was observed. This shows that prehydrolysis times of more than 12 h are necessary for homogeneous particle formation. The second experiment was performed without the addition of HCl but stirring the alkoxysilane with water and alcohol overnight. The results were similar to the just mentioned study (Fig. S3). Only samples with ethyl- and vinyl groups (ethyl-$SiO_{1.5}$-without HCl and vinyl-$SiO_{1.5}$-without HCl) formed solids and only the sample with vinyl groups

Fig. 1 SEM images of **a** Methyl-, **b** Ethyl-, **c** Propyl-, **d** Vinyl-, **e** Phenyl-, **f** $Me_{0.4}Ph_{0.6}$-, **g** $Me_{0.25}Ph_{0.75}$-, **h** $Vi_{0.25}Ph_{0.75}$-$SiO_{1.5}$, and **i** SiO_2 with size distribution curves, average particle diameters ($d_{avg.}$), standard deviations (σ), and polydispersities (100*σ/$d_{avg.}$) of the prepared particles (250 ml min^{-1}, 20 °C)

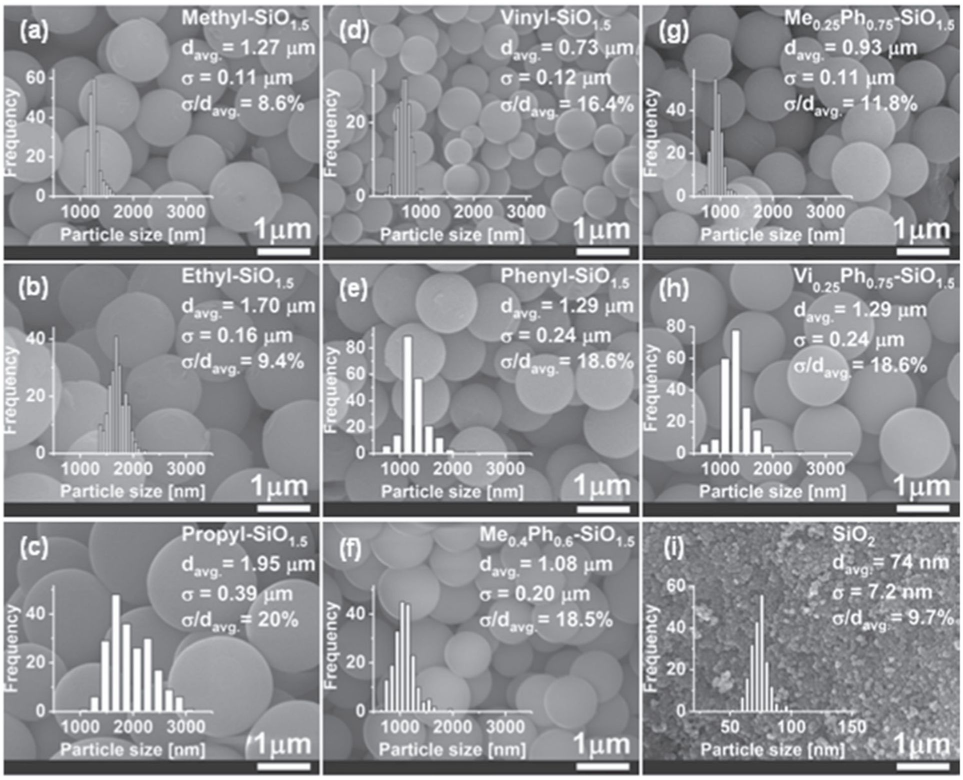

resulted in spherical particles with a broad size distribution. A phase separation was observed for methyl-, propyl- and phenyl-$SiO_{1.5}$-without HCl. The observed behavior can be explained by the fact that methyl-, propyl-, and phenyl-modified samples are based on an ethoxysilane precursors and need more time for hydrolysis reactions than those from methoxysilanes. The studies also reveal that both methoxy- and ethoxysilanes can be applied in the continuous synthesis of ORMOSIL particles if a prehydrolysis step is used. Without the addition of acid or limiting the hydrolysis time to less than 12 h no solids are formed or an inhomogeneous particle growing occurs. Only vinyl-modified samples led to acceptable particles also for smaller prehydrolysis times.

3.3 FTIR-spectroscopy

The presence of functional groups in the prepared samples was analyzed applying ATR FTIR-spectroscopy. All samples show the expected signals based on the presence of their organic moieties (Fig. 2, Table 2).

Pure silica particles without organic groups exhibit a characteristic peak at 795 cm^{-1}, which is related to –Si–O–Si– symmetric stretching vibration and at 950 cm^{-1} resulting from Si–O–Si–OH vibration. The peak at 1050 cm^{-1} can be assigned to –Si–O–Si– stretching vibration and the broad weak peak between 3100 and 3600 cm^{-1} is related to vibrations from surface OH-groups [15]. ORMOSIL particles show in addition characteristic vibration bands for the organosilane functionalities. All organo-modified samples exhibit C–H stretching vibrations between 2800 and 3095 cm^{-1}. The samples modified with alkyl chains show well-defined absorption peaks at ca. 1200–1280 cm^{-1} related to Si–R deformations and C–H

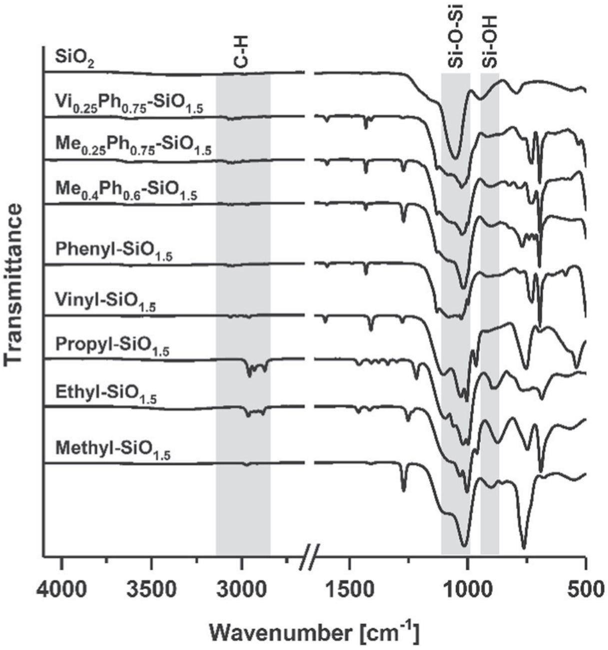

Fig. 2 FTIR spectra of the prepared ORMOSIL and silica particles

Table 2 FTIR data of the particles and references that were used for the assignments

Sample	R group	R (C–H, C–C) [cm^{-1}]	Si–R [cm^{-1}]	Si–O–Si [cm^{-1}]	References
SiO_2	–	–	–	795, 990–1260	[15]
Methyl-$SiO_{1.5}$	Methyl	1410, 2910, 2970	1270	960–1180	[21, 36]
Ethyl-$SiO_{1.5}$	Ethyl	1415, 1460, 2860–3000	1250	940–1170	[28, 29]
Propyl-$SiO_{1.5}$	n-propyl	1300–1460, 2855–2980	1220	950–1170	[21, 29]
Vinyl-$SiO_{1.5}$	Vinyl	1410, 1600, 2925–3100	1275	980–1190	[37]
Phenyl-$SiO_{1.5}$	Phenyl	690, 1590, 2990–3090	1130, 1430	955–1200	[21, 31]
$Me_{0.4}Ph_{0.6}$-$SiO_{1.5}$	Phenyl, methyl	690, 1410, 1595, 2900–3100	1130, 1270, 1430	950–1200	[21, 27, 31]
$Me_{0.25}Ph_{0.75}$-$SiO_{1.5}$	Phenyl, methyl	695, 1410, 1594, 2825–3095	1130, 1270, 1430	950–1200	[21, 27, 31]
$Vi_{0.25}Ph_{0.75}$-$SiO_{1.5}$	Phenyl, vinyl	690, 1408, 1594, 2820–3130	1130, 1275, 1430	950–1220	[31, 37]

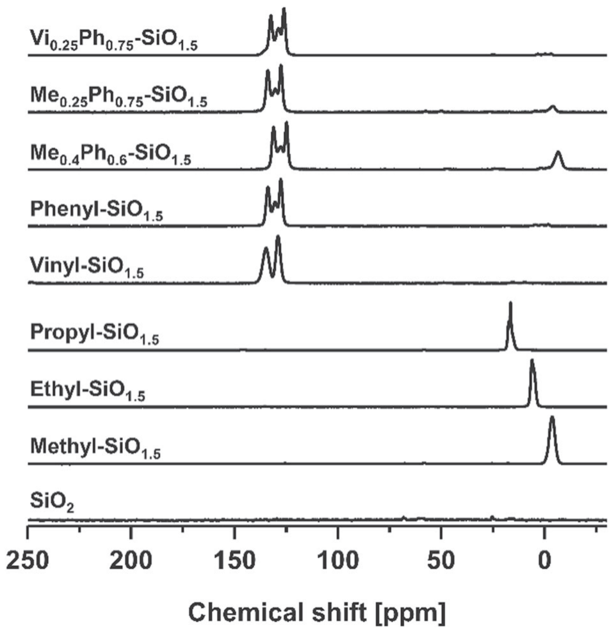

Fig. 3 ^{13}C CP-MAS NMR spectra of the prepared particles

deformation vibrations at 1300–1480 cm^{-1}. Samples with phenyl groups show characteristic C=C vibration bands at 1590 cm^{-1} and Si–C vibrations at 1430 and 1130 cm^{-1}. The peaks at 690 and 735 cm^{-1} are assigned to C–H out of plane vibrations of the aromatic groups. Samples with vinyl groups also show well-defined absorptions at 1600 and 1275 cm^{-1} from C=C and Si–C vibrations. Signals at 1410 cm^{-1} are assigned to =CH_2 bending vibrations. In the spectra of the samples MePh-$SiO_{1.5}$ and ViPh-$SiO_{1.5}$ the above mentioned characteristic absorptions of both functional groups are visible. Comparing the spectra of $Me_{0.4}Ph_{0.6}$-$SiO_{1.5}$ and $Me_{0.25}Ph_{0.75}$-$SiO_{1.5}$ shows that the difference in their composition is also reflected in the ratio of the intensities of the Si–Me and Si–Ph absorptions. The ratio decreases with decreasing MTMS content in the precursor solution [15, 21, 36–40].

3.4 CP-MAS-NMR spectroscopy

Solid-state ^{13}C NMR spectroscopy was used to investigate the chemical structure of the prepared powders and to confirm the results obtained from FT-IR-spectroscopy. Solid state ^{29}Si NMR spectroscopy was used to gain quantitative information about the condensation degree of the samples to enable a better understanding of the results obtained from other methods (e.g., thermogravimetric analysis) and the chemical behavior of the products (e.g., solubility behavior).

^{13}C NMR spectra (Fig. 3) show intensive peaks that are characteristic for the corresponding organic groups. Only very weak signals from residual alkoxy groups (at ca. 60 ppm) are visible in the spectra, meaning that almost all alkoxy groups were hydrolyzed during the reaction and that OH-groups are the additional functional groups among the alkyl, alkenyl, and aryl groups in the T^2 species.

^{29}Si NMR spectra (Fig. 4) of the ORMOSIL particles that were prepared from trialkoxysilanes show peaks in the range of −48 to −90 ppm that can be assigned to T^2 and T^3 species. The lack of T^0 and T^1 species suggest that no unreacted precursor is present. Signals of fully condensed T^3 species were found at –64.8, −65.7, −67.3, −82.7, and −77.2 ppm for methyl-, ethyl-, propyl-, vinyl-, and phenyl-$SiO_{1.5}$. The peaks at –55.6, −55.9, −57.3, −73.9, and −68.8 ppm can be assigned to T^2 species of the abovementioned samples.

The spectrum of the unmodified SiO_2 particles shows the expected peaks at −109 ppm (Q^4), −101 ppm (Q^3), and −92 ppm (Q^2).

To get further information about the networks of the ORMOSIL particles the peak areas of the T^2 and T^3 signals were fitted by a Gaussian function, integrated and an approximation of the degree of condensation (DC) was received according to the following equation [41–43]:

$$\mathrm{DC}[\%] = \frac{T^3[\%] \times 3 + T^2[\%] \times 2}{3} \qquad (1)$$

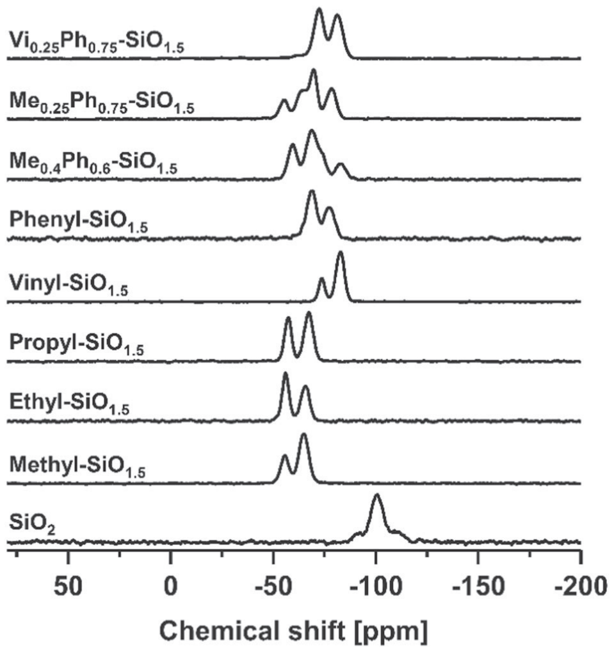

Fig. 4 ^{29}Si CP-MAS NMR spectra of the prepared particles

Table 3 Ratio of condensation products T^2 and T^3 and degree of condensation (DC)

	T^2 [%]	T^3 [%]	DC [%]
Methyl-$SiO_{1.5}$	32	68	89
Ethyl-$SiO_{1.5}$	51	49	83
Propyl-$SiO_{1.5}$	42	58	86
Vinyl-$SiO_{1.5}$	27	73	91
Phenyl-$SiO_{1.5}$	60	40	80
$Me_{0.25}Ph_{0.75}$-$SiO_{1.5}$	44	56	85
$Me_{0.4}Ph_{0.6}$-$SiO_{1.5}$	40	60	87
$Vi_{0.25}Ph_{0.75}$-$SiO_{1.5}$	52	48	83

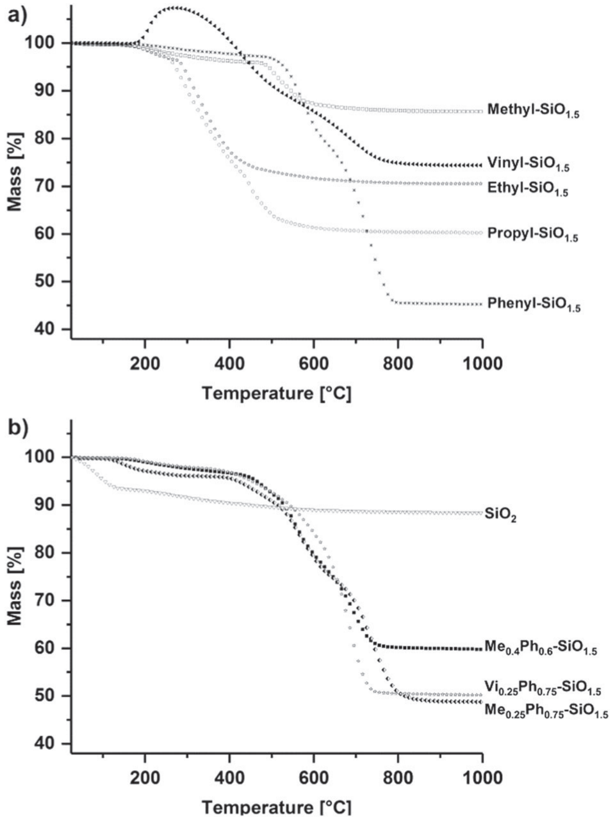

Fig. 5 Thermogravimetric analysis of the prepared ORMOSIL particles with a (**a**) homogenous substitution pattern and (**b**) mixtures of different organic rests and silica particles

Table 3 shows that generally high condensation degrees (>80%) were obtained. Methyl-$SiO_{1.5}$ and vinyl-$SiO_{1.5}$ particles reveal the highest degrees of condensation. Particles with only phenyl groups (phenyl-$SiO_{1.5}$) exhibit mainly T^2 species and the resulting condensation degree is the lowest of the observed particles. This low degree of condensation leads to a more polymer-like behavior. As a consequence the obtained particles dissolve in various organic solvents, e.g., toluene, tetrahydrofuran, and dichloromethane. In addition the particles typically melt, to form a dense film during a thermal treatment. This is a literature known phenomenon already described for phenyl-based silsesquioxanes [38, 44]. The results (Table 3) indicate that small substituents promote the building of dense networks with high DCs (e.g., methyl-$SiO_{1.5}$) whereas bulky groups lead to particles with lower DCs (ethyl-, propyl-, and phenyl-$SiO_{1.5}$).

The combination of phenyl and methyl or vinyl groups ($Me_{0.25}Ph_{0.75}$-$SiO_{1.5}$, $Me_{0.4}Ph_{0.6}$-$SiO_{1.5}$, $Vi_{0.25}Ph_{0.75}$-$SiO_{1.5}$) led to an increased condensation. However, using a ^{29}Si CP MAS NMR experiment, the condensation degrees in the mixed samples might not be reliable, because of the different proton concentrations in the proximity of the silicon atoms and can only serve as indication.

3.5 Thermogravimetric and elemental analysis

Thermogavimetric analysis was applied to investigate the thermal stability and the composition of the prepared particles (Fig. 5). TGA under inert gas atmosphere leads to an incomplete degradation of the sample causing a residual mass, which still contains graphitic carbon from the organic groups. Application of pure oxygen or air leads to strong exothermic reactions and irreproducible TG curves. Therefore, a gas flow of 5 ml min^{-1} for O_2 and 95 ml min^{-1} for N_2 was used in the measurements. Most samples show a slight mass loss in the temperature range of 100–300 °C from desorbing solvent molecules and water that is built by the condensation of hydroxyl groups. This first mass loss can also overlap the following steps in the TGA curve from the decomposition of the organic group that is bound to Si

Table 4 Calculated and measured amounts of C and H in weight% obtained from elemental analysis and weight loss from thermogravimetric analysis

	Calculated		Elemental analysis		Thermogravimetric
	wt.% C calcd.	wt.% H calcd.	wt.% C exp.	wt.% H exp.	Δm (organic groups)
SiO_2	0	0	1.2	1.6	–
Methyl-$SiO_{1.5}$	17.9	4.5	15.5	4.8	15.2
Ethyl-$SiO_{1.5}$	29.6	6.2	29.0	6.4	32.6
Propyl-$SiO_{1.5}$	37.9	7.4	36.2	7.4	43.6
Vinyl-$SiO_{1.5}$	30.4	3.8	30.0	4.0	–
Phenyl-$SiO_{1.5}$	55.8	3.9	53.6	4.2	55.2
$Ph_{0.6}Me_{0.4}$-$SiO_{1.5}$	41.8	4.1	40.0	4.6	41.2
$Ph_{0.75}Me_{0.25}$-$SiO_{1.5}$	50.2	4.5	49.7	4.5	52.7
$Ph_{0.75}Vi_{0.25}$-$SiO_{1.5}$	51.5	3.9	50.0	4.1	50.6

atoms. ORMOSIL particles with alkyl chains as organic substituents reveal that the decomposition temperature of the organic group decreases with increasing chain length (methyl 481 °C, ethyl 283 °C, and propyl 257 °C). The vinyl-$SiO_{1.5}$ sample shows a temperature behavior that differs from the other samples. In the temperature range of 180–275 °C the mass increases is caused by the partial oxidation of the vinyl groups. The increase is followed by a mass loss that can be assigned to the degradation of organic groups. This is a well-known behavior of vinyl silsesquioxanes which was already described in literature [45]. If the vinyl samples are measured under nitrogen atmosphere the increase is not observed (Fig. S8). ORMOSIL particles with aromatic groups show generally higher degradation temperatures than those with alkyl chains (Phenyl-$SiO_{1.5}$ 527 °C).

The samples with mixed phenyl and methyl groups show onset degradation temperatures that are lower than the values for the samples with only one of these groups.

The mass loss caused by the thermal degradation of the organic groups ($\Delta m_{(\mathrm{org.groups})}$) was determined by calculating the mass difference at the onset temperature and the residual mass at 1000 °C. Then the mass increase through the oxygen absorption was subtracted (Eq. 2).

This procedure allows comparing the obtained data with the results from the elemental analysis (Table 4).

$$\Delta m_{(\mathrm{org.groups})} = \Delta m\left(1 + \frac{M\left(\frac{1}{2}\,O\right)}{M(\mathrm{org.group})}\right) \quad (2)$$

The results obtained by elemental analysis correlate well with the calculated values. Generally, mass losses obtained from TGA are slightly lower than the calculated values and those from elemental analysis. A reason for this deviation might be that for the elemental analysis also the mass loss caused by the evaporation of residual solvent is registered.

Table 5 Particle sizes and standard deviations of Me-, Ph- and $Me_{0.4}Ph_{0.6}$-$SiO_{1.5}$/-conc.2/3 (identified from REM images by measuring the size of 200 particles per sample) that were produced with different silane concentrations

Sample name	Particle size [µm]
Methyl-$SiO_{1.5}$	1.27 ± 0.11
Methyl-$SiO_{1.5}$-conc.2	0.84 ± 0.38
Methyl-$SiO_{1.5}$-conc.3	0.69 ± 0.09
Phenyl-$SiO_{1.5}$	1.29 ± 0.24
Phenyl-$SiO_{1.5}$-conc.2	0.70 ± 0.05
Phenyl-$SiO_{1.5}$-conc.3	0.64 ± 0.07
$Me_{0.4}Ph_{0.6}$-$SiO_{1.5}$	1.10 ± 0.20
$Me_{0.4}Ph_{0.6}$-$SiO_{1.5}$-conc.2	0.72 ± 0.06
$Me_{0.4}Ph_{0.6}$-$SiO_{1.5}$-conc.3	0.50 ± 0.13

3.6 Influence of the alkoxysilane concentration on the particle size

The effect of the alkoxysilane concentration on the particle size was determined for methyl-, phenyl- and $Me_{0.4}Ph_{0.6}$-$SiO_{1.5}$ under equal terms. The particle sizes and standard deviations were identified from REM images by measuring the size of 200 particles per sample (Table 5 and Fig. S9). A decrease in the silane concentration results in a reduction of the particle size (however not in a linear manner). The value of the particle size distribution does not follow this trend and shows no obvious dependency from the silane concentration. The experiment demonstrates that varying the silane concentration is a possibility to adjust the particle size.

4 Conclusion

Micro- and nanoparticles, in detail ORMOSIL spheres, were synthesized in a continuous process without applying additives to stabilize the spherical growth. Realizing the sol–gel reaction in the reactor and use its advantages optimally requires the tailoring of the reaction kinetics of the sol–gel process. This was managed by the prehydrolysis of the trialkoxysilane solutions. In order to synthesize a wide range of ORMOSIL particles (with different organic groups) the ratio of silane, alcohol and acid had to be optimized for each precursor composition. After doing so spherical ORMOSIL particles in a scale of 9–23 g min^{-1} were prepared. The detailed characterization of these substances gives an overview of the chemical and thermal properties to estimate the suitability of the materials for further applications. A dependency of the nature of the organic group of the alkoxysilane precursor on the DC was detected. Samples with less bulky groups (e.g., methyl) and spheres with vinyl groups showed the highest condensation degrees (89% and 91%). By incorporate these groups to Phenyl-$SiO_{1.5}$ particles the condensation degree was increased (to 83%–87%) compared to pure phenyl particles (80%). Particle size distributions were the smallest for methyl-, ethyl-$SiO_{1.5}$, and pure SiO_2. TGA of the samples demonstrated that the thermal degradation temperature for alkyl-$SiO_{1.5}$ decreases with increasing chain length. Phenyl-$SiO_{1.5}$ particles had the highest values (527 °C). Mixing different groups led to a decreased thermal stability. Varying the alkoxysilane concentration allowed the formation of smaller particles. The study shows the advantages of a continuous synthesis method for the preparation of ORMOSIL particles that can be used in various applications. Further on, we plan to expand the application of the microjet approach to the sol–gel synthesis of metal oxide particles from metal alkoxide precursors, which are definitely more suited for the fast mixing times in the reactor, due to faster hydrolysis and condensation rates.

Acknowledgements We thank Dr. Michael Zimmer for the CP-MAS-NMR measurements and Susanne Harling for elemental analyses.

Compliance with ethical standards

Conflict of interest The authors declare that they have no conflict of interest.

References

1. Pachón LD, Rothenberg G (2008) Transition-metal nanoparticles: synthesis, stability and the leaching issue. Appl Organomet Chem 22(6):288–299. https://doi.org/10.1002/aoc.1382
2. Wang L, Wang L, Xia T, Dong L, Bian G, Chen H (2004) Direct fluorescence quantification of chromium(VI) in wastewater with organic nanoparticles sensor. Anal Sci 20(7):1013–1017
3. Barbé CJ, Arendse F, Comte P, Jirousek M, Lenzmann F, Shklover V, Grätzel M (1997) Nanocrystalline titanium oxide electrodes for photovoltaic applications. J Am Ceram Soc 80 (12):3157–3171
4. Ito A, Shinkai M, Honda H, Kobayashi T (2005) Medical application of functionalized magnetic nanoparticles. J Biosci Bioeng 100(1):1–11. https://doi.org/10.1263/jbb.100.1
5. Mihindukulasuriya SDF, Lim L-T (2014) Nanotechnology development in food packaging: a review. Trends Food Sci Tech 40(2):149–167. https://doi.org/10.1016/j.tifs.2014.09.009
6. Becheri A, Dürr M, Lo Nostro P, Baglioni P (2008) Synthesis and characterization of zinc oxide nanoparticles: application to textiles as UV-absorbers. J Nanopart Res 10(4):679–689. https://doi.org/10.1007/s11051-007-9318-3
7. Rahman MT, Rebrov EV (2014) Microreactors for gold nanoparticles synthesis: from Faraday to flow. Processes 2(2):466–493. https://doi.org/10.3390/pr2020466
8. Khan SA, Günther A, Schmidt MA, Jensen KF (2004) Microfluidic synthesis of colloidal silica. Langmuir 20(20):8604–8611. https://doi.org/10.1021/la0499012
9. Gutsch A, Krämer M, Michael G, Mühlenweg H, Pridöhl M, Zimmermann G (2002) Gas-phase production of nanoparticles. KONA 20:24–37
10. Suh YK, Kang S (2010) A review on mixing in microfluidics. Micromachines 1(3):82–111. https://doi.org/10.3390/mi1030082
11. Marre S, Jensen KF (2010) Synthesis of micro and nanostructures in microfluidic systems. Chem Soc Rev 39(3):1183–1202. https://doi.org/10.1039/b821324k
12. Zhao C-X, He L, Qiao SZ, Middelberg APJ (2011) Nanoparticle synthesis in microreactors. Chem Eng Sci 66(7):1463–1479. https://doi.org/10.1016/j.ces.2010.08.039
13. Betke A, Kickelbick G (2014) Bottom-up, wet chemical technique for the continuous synthesis of inorganic nanoparticles. Inorganics 2(1):1–15. https://doi.org/10.3390/inorganics2010001
14. Penth B (2007) Kontinuierliche Produktion in Mikroreaktoren. German Patent DE102006004350 A1.
15. Gutierrez L, Gomez L, Irusta S, Arruebo M, Santamaria J (2011) Comparative study of the synthesis of silica nanoparticles in micromixer–microreactor and batch reactor systems. Chem Eng J 171(2):674–683. https://doi.org/10.1016/j.cej.2011.05.019
16. Su M, Su H, Du B, Li X, Ren G, Wang S (2014) The properties of silica nanoparticles with high monodispersity synthesized in the microreactor system. J Sol-Gel Sci Technol 72(2):375–384. https://doi.org/10.1007/s10971-014-3445-y
17. Kessler D, Löwe H, Theato P (2009) Synthesis of defined poly (silsesquioxane)s: fast polycondensation of trialkoxysilanes in a continuous-flow microreactor. Macromol Chem Phys 210 (10):807–813. https://doi.org/10.1002/macp.200800611
18. Stöber W, Fink A, Bohn E (1968) Controlled growth of monodisperse silica spheres in the micron size range. J Colloid Interface Sci 26:62–69
19. Van Blaaderen A, Vrij A (1993) Synthesis and characterization of monodisperse colloidal organo-silica spheres. J Colloid Interface Sci 156:1–18
20. Etienne M, Lebeau B, Walcarius A (2002) Organically-modified mesoporous silica spheres with MCM-41 architecture. New J Chem 26(4):384–386. https://doi.org/10.1039/b110741k
21. Arkhireeva A, Hay JN (2003) Synthesis of sub-200 nm silsesquioxane particles using a modified Stöber sol–gel route. J Mater Chem 13(12):3122–3127. https://doi.org/10.1039/b306994j
22. Choi JY, Kim CH, Kim DK (1998) Formation and characterization of monodisperse, spherical organo-silica powders from organo-alkoxysilane-water system. J Am Ceram Soc 81 (5):1184–1188
23. Ottenbrite RM, Wall JS (2000) Self-catalyzed synthesis of organo-silica nanoparticles. J Am Ceram Soc 83(12):3214–3215
24. Boday DJ, Tolbert S, Keller MW, Li Z, Wertz JT, Muriithi B, Loy DA (2014) Non-hydrolytic formation of silica and polysilsesquioxane particles from alkoxysilane monomers with formic

acid in toluene/tetrahydrofuran solutions. J Nanopart Res 16 (3):1–13. https://doi.org/10.1007/s11051-014-2313-6

25. Krüner B, Odenwald C, Tolosa A, Schreiber A, Aslan M, Kickelbick G, Presser V (2017) Carbide-derived carbon beads with tunable nanopores from continuously produced polysilsesquioxanes for supercapacitor electrodes. Sustain Energy Fuels 1:1588–1600. https://doi.org/10.1039/C7SE00265C10.1039/c7se00265c
26. Schneider CA, Rasband WS, Eliceiri KW (2012) NIH Image to ImageJ: 25 years of image analysis. Nat Methods 9(7):671–675. https://doi.org/10.1038/nmeth.2089
27. Bah T (2011) Inkscape: guide to a vector drawing program, 4th edn.
28. Fournier M-C, Falk L, Villermaux J (1996) A new parallel competing reaction system for assessing micromixing efficiency - experimental approach. Chem Eng Sci 51(22):5053–5064
29. Dushman S (1904) The rate of the reaction between iodic and hydriodic acids. J Phys Chem 8(7):453–482. https://doi.org/10.1021/j150061a001
30. Commenge J-M, Falk L (2011) Villermaux–Dushman protocol for experimental characterization of micromixers. Chem Eng Process 50(10):979–990. https://doi.org/10.1016/j.cep.2011.06.006
31. Brinker CJ, Tallant DR, Roth EP, Ashley CS (1986) Sol-gel transition in simple silicates III. Structural studies during densification. J Non-Cryst Solids 82:117–126
32. Brinker CJ (1988) Hydrolysis and condensation of silicates: effects on structure. J Non-Cryst Solids 100:31–50
33. Klein LC, Jitianu A (2010) Organic–inorganic hybrid melting gels. J Sol-Gel Sci Technol 55(1):86–93. https://doi.org/10.1007/s10971-010-2219-4
34. Brochier Salon M-C, Bayle P-A, Abdelmouleh M, Boufi S, Belgacem MN (2008) Kinetics of hydrolysis and self condensation reactions of silanes by NMR spectroscopy. Colloids Surf A: Physicochem Eng Asp 312(2-3):83–91. https://doi.org/10.1016/j.colsurfa.2007.06.028
35. Brochier Salon M-C, Belgacem MN (2010) Competition between hydrolysis and condensation reactions of trialkoxysilanes, as a function of the amount of water and the nature of the organic group. Colloids Surf A: Physicochem Eng Asp 366 (1–3):147–154. https://doi.org/10.1016/j.colsurfa.2010.06.002
36. Rao AV, Kulkarni MM, Amalnerkar DP, Seth T (2003) Superhydrophobic silica aerogels based on methyltrimethoxysilane precursor. J Non-Cryst Solids 330:187–195. https://doi.org/10.1016/j.jnoncrysol.2003.08.048
37. Sharma RK, Das S, Maitra A (2004) Surface modified ormosil nanoparticles. J Colloid Interface Sci 277(2):342–346. https://doi.org/10.1016/j.jcis.2004.04.019
38. Macan J, Tadanaga K, Tatsumisago M (2010) Influence of copolymerization with alkyltrialkoxysilanes on condensation and thermal behaviour of poly(phenylsilsesquioxane) particles. J Sol-Gel Sci Technol 53(1):31–37. https://doi.org/10.1007/s10971-009-2051-x
39. Jesson DA, Abel M-L, Hay JN, Smith PA, Watts JF (2006) Organic-inorganic hybrid nanoparticles: Surface characteristics and interactions with a polyester resin. Langmuir 22 (11):5144–5151
40. Launer PJ (1987) Infrared analysis of organosilicon compounds: Spectra-structure correlations. In Anderson R, Arkles B, Larson GL (eds) Silicone Compounds Register and Review, 4th edn, pp 100–103
41. Nam K-H, Lee T-H, Bae B-S, Popall M (2006) Condensation reaction of 3-(methacryloxypropyl)-trimethoxysilane and diisobutylsilanediol in non-hydrolytic sol-gel process. J Sol-Gel Sci Technol 39(3):255–260. https://doi.org/10.1007/s10971-006-7884-y
42. Komori Y, Nakashima H, Hayashi S, Sugahara Y (2005) Silicon-29 cross-polarization/magic-angle-spinning NMR study of inorganic–organic hybrids: homogeneity of sol–gel derived hybrid gels. J Non-Cryst Solids 351(2):97–103. https://doi.org/10.1016/j.jnoncrysol.2004.10.005
43. Loy DA, Jamison GM, Baugher BM, Russick EM, Assink RA, Prabakar S, Shea KJ (1995) Alkylene-bridged polysilsesquioxane aerogels: highly porous hybrid organic-inorganic materials. J Non-Cryst Solids 186:44–53
44. Li Z, Tolbert S, Loy DA (2013) Hybrid organic-inorganic membranes on porous supports by size exclusion and thermal sintering of fluorescent polyphenylsilsesquioxane nanoparticles. Macromol Mater Eng 298(7):715–721. https://doi.org/10.1002/mame.201200091
45. Deng T-S, Marlow F (2012) Synthesis of monodisperse polystyrene@vinyl-SiO_2 core–shell particles and hollow SiO2 spheres. Chem Mater 24(3):536–542. https://doi.org/10.1021/cm203099m

Supporting Information for Journal of Sol-Gel Science and Technology

Additive free Continuous Synthesis of Silica and ORMOSIL Micro- and Nanoparticles applying a Microjet Reactor

Christina Odenwald[1] *and Guido Kickelbick*[*, 1]

[1] Saarland University, Inorganic Solid State Chemistry, Campus Building C4 $_1$, 66123
Saarbrücken, Germany

1. Characterization of the mixing efficiency in the microjet reactor

The mixing efficiency of the used micro reactor was determined by applying the Villermaux-Dushman method[1,2] (also known as iodide/iodate reaction). Therefore, the protocol from Commenge and Falk[3] that describes the characterization procedure step-by step was followed. The procedure is based on a parallel/competing reaction (Eq. S1 and S2)

$$H_2BO_3^- + H^+ \leftrightarrow H_3BO_3 \qquad (S1)$$

$$IO_3^- + 5\ I^- + 6\ H^+ \leftrightarrow 3\ I_2 + 3\ H_2O \qquad (S2)$$

The neutralization reaction is quasi-instantaneous whereas the time for the second reaction is in the range of micromixing what means: still fast but slower than the first reaction. The time for the redox reaction can be adjusted by the used concentrations. In the reactor an iodide/iodate solution that is buffered with $H_2BO_3^-/H_3BO_3$ collides with a sulfuric acid solution. In the case of perfect mixing, all protons are consumed by the faster neutralization reaction and a transparent product solution is obtained. In real mixing situations local over-concentrations of acid occur and protons can react with surrounding iodide and iodate ions. The resulting iodine ions form a quasi-stationary equilibrium with iodide and triiodide ions (Eq. S3) and the solution is colored yellow.

$$I_2 + I^- \leftrightarrow I_3^- \qquad (S3)$$

The concentration of I_3^- can be determined by UV-VIS spectroscopy by measuring the absorption at 353 nm.

The mixing time t_m can be estimated with the measured optical density (OD) by using a diagram given from Falk and Commenge (if one of the suggested concentration sets is used).

1.1 Experimental

Two aqueous stock solutions were prepared with deionized water that was previously stripped with nitrogen to eliminate dissolved oxygen. Solution 1 was prepared by solving the amounts that were recommend for concentration set 1c (Table S1) of boric acid (99.8%., Merck, Germany), sodium hydroxide (99%, Grüssing, Germany), potassium iodide (99.5%, Grüssing, Germany) and potassium iodate (> 98%, Riedel de Haen AG, Germany) in water. Therefore, the amount of each substance that is recommend for concentrations set 1c was first dissolved individual in ca. 100 ml water. Then the solutions were united in a volumetric flask (1000 ml) in the mentioned order whereas each beaker was rinsed two times with ca. 50 ml water before the flask was brought to volume. The second solution was prepared by diluting a 0.5 M sulfuric acid stock solution (1.09981 Titrisol, Merck, Germany). The solutions were prepared fresh for each day.

Table S1 Composition of the solutions for determining the mixing efficiency for concentration set 1c adapted from Falk et al.[3]

	substance	mass [g]	c [mol/l]
solution 1	H^+	-	0.040
solution 2	H_3BO_3	5.565	0.090
	NaOH	3.600	0.090
	KI	5.312	0.032
	KIO_3	1.284	0.006

The microjet reactor system was flushed with deionized water for each run. The solutions (1 and 2) were put in dry polyethylene flasks and were fed into the reactor with the HPLC pumps. The product solution was first collected in vessel A to ensure constant conditions. After a consumption of approximately 50 ml of each educt solution, a three-way cock was used to reroute the product solution in vessel B for ca. 10 seconds. The three-way cock was activated again before the system was stopped. The absorption of the solution from vessel B was measured prompt after each experiment. UV-VIS transmission measurements were performed on a Lambda 25 instrument (Perkin Elmer Inc., USA) equipped with a 2 nm increment and 0.2 s integration times.

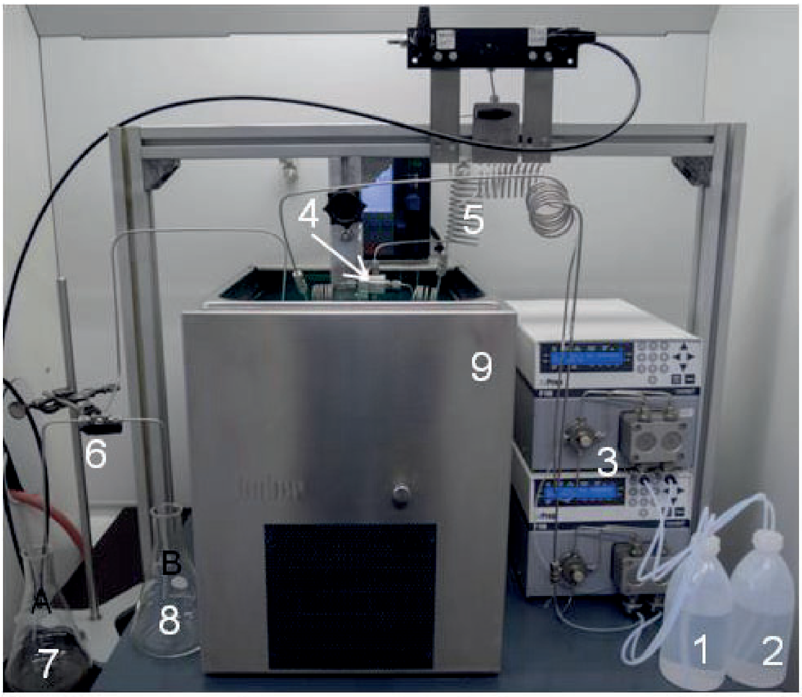

Fig. S1 Microjet reactor set-up in the laboratory and assignment of the most important components. 1), 2) educt solutions, 3) HPLC-pumps, 4) microjet reactor, 5) gas (N_2) inlet pipe 6) three-way cock, 7) collecting vessel A, 8) collecting vessel B for product solution, water bath.

1.2 Results and discussion

The test was performed on three different days at 20°C. The absorptions of the product solutions were directly measured off-line by UV-VIS spectroscopy in a 10 mm cell after the preparation (Figure S2).

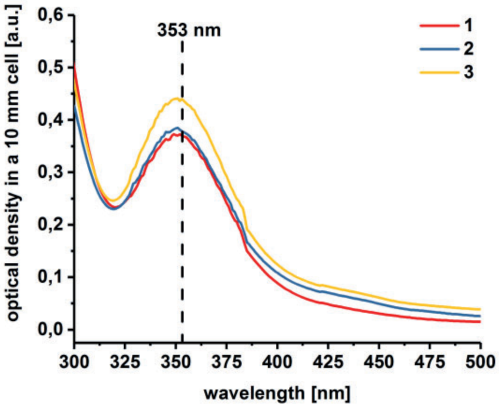

Fig. S2 UV-VIS spectra of the solutions after performing the Villermaux-Dushman reaction.

The optical densities (OD) measured at 353 nm in the 10 mm cell were converted into values for a 5 mm cell to enable a better comparability with the data provided by Commenge and Falk[3]. The mixing times were identified by the help of the authors' diagram[3].

Table S2 Optical densities at 353 nm of the solutions after the Villermaux-Dushman experiment in a 10 and a 5 mm cell and resulting mixing times

experiment No.	OD at 353 nm in a 10 mm cell [a.u.]	OD at 353 nm in a 5 mm cell [a.u.]	mixing time (t_m) [s]
1	0.37	0.18	0.009
2	0.38	0.20	0.010
3	0.44	0.22	0.012

An average mixing time of 10 ms was found for the microjet reactor at 20°C and a flow rate of 250 ml/min. It is also noteworthy that the obtained values only express an estimation of the mixing time and that the authors (Commenge and Falk) point out that they only give an order of magnitude.

2 Preparation of ORMOSIL and silica particles

2.1 Syntheses without the addition of HCl

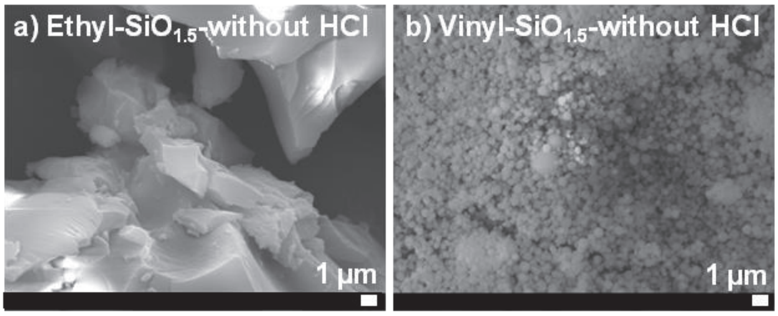

Fig. S3 SEM images of samples Methyl-$SiO_{1.5}$-without HCl and Vinyl-$SiO_{1.5}$-without HCl.

2.2 ^{29}Si liquid state NMR study for the prehydrolysis of ethyltrimethoxysilane

The hydrolysis and condensation behavior of ethyltimethoxysilane was followed by NMR. 55.5 µl ethyltrimethoxysilane, 123.3 µl methanol and 251.1 µl of acidified D_2O (containing $1.38*10^{-4}$ mmol HCl) were directly filled in a NMR tube. After shaking, the solution was measured several times with a Bruker Avance 300 spectrometer at 25°C at 60 MHz.

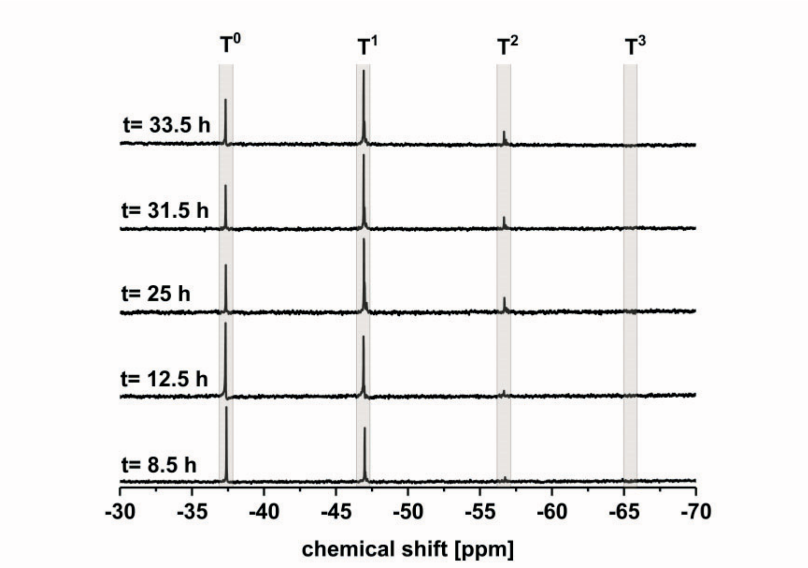

Fig. S4 ^{29}Si NMR of a mixture of ethyltrimethoxysilane, methanol, D_2O and HCl after different hydrolysis times and assignments of the formed silicon species.

2.3 Syntheses with a hydrolysis time of 5 minutes

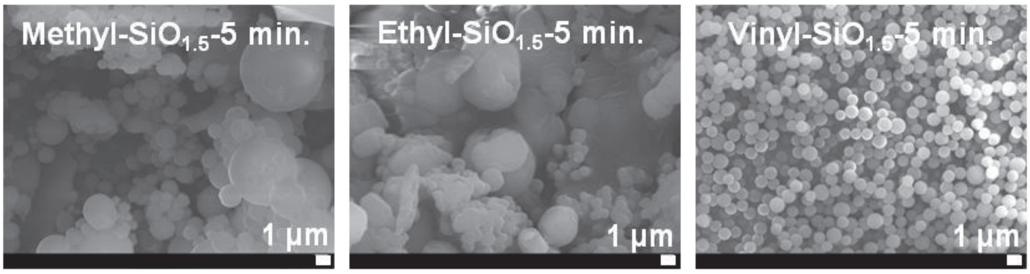

Fig. S5 SEM images of samples Methyl-, Ethyl- and Vinyl-$SiO_{1.5}$-5 min. The hydrolysis time was 5 minutes.

2.4 Batch synthesis of ORMOSIL microparticles

2.4.1 Experimental

The two precursor solutions (alkoxysilane- and NH_3 solution) were prepared for every sample like it was described for the continuous syntheses (2.3.). E.g. for Methyl-$SiO_{1.5}$-batch 6.187 g (34.7 mmol) methyltriethoxysilane (MTES) were dissolved in 31.97 g (0.69 mol) ethanol. Then 12.50 g of an aqueous HCl-stock solution were added and the solution was stirred at RT for 26.4 h. The ammonia solution (2.2 M) was prepared by diluting a 25% NH_3 solution. 10 ml of each solution were poured together simultaneously in a 100 ml beaker in which a magnetic stir bar was already stirring. After a reaction time of 10 minutes the suspension was centrifuged (10 min, 8000 rpm, 7012 x G) and the solid was dried in vacuum.

Table S3 Compositions of the precursor solutions A and B that were used for the batch experiments for the syntheses of ORMOSIL particles.

sample	system solution 1a), solution 2	$n(R'Si(OR)_3)$ mmol	n(ROH) mol	$n(H_2O)$ mol	n(HCl) µmol	$c(NH_3)$ mol/l
Methyl-$SiO_{1.5}$-batch	MTES/EtOH/HCl, NH_3/H_2O	34.7	0.69	0.69	7.5	2.2
Ethyl-$SiO_{1.5}$-batch	ETMS/MeOH/HCl, NH_3/H_2O	34.7	0.30	1.39	15	2.2
n-Propyl-$SiO_{1.5}$-batch	PTES/EtOH/HCl, NH_3/H_2O	34.7	0.69	0.69	15	2.2
Vinyl-$SiO_{1.5}$-batch	VTMS/MeOH/HCl, NH_3/H_2O	34.7	0.80	0.69	7.5	2.2
Phenyl-$SiO_{1.5}$-batch	PhTES/EtOH/HCl, NH_3/H_2O	34.7	0.69	0.69	75	2.2

a) percentage given in mol%

2.4.2 Results

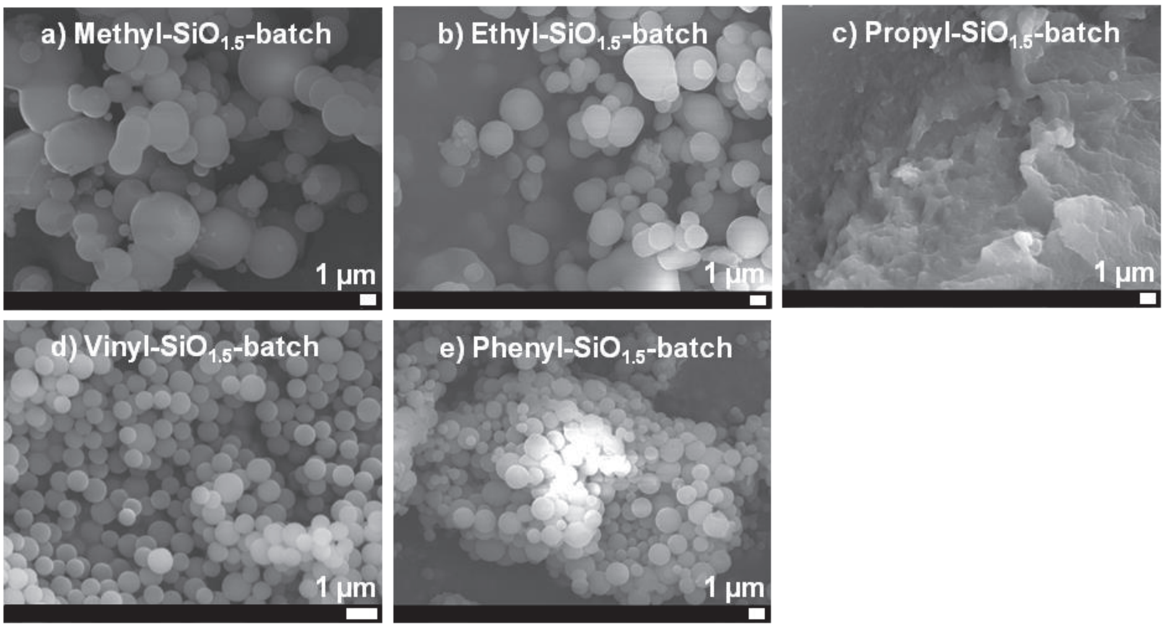

Figure S6 Compositions of the precursor solutions A and B that were used for the batch syntheses of the ORMOSIL particles.

2.5 Silica particles

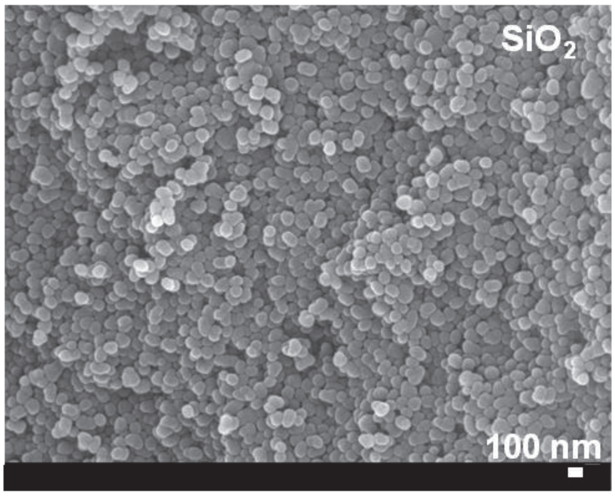

Fig. S7 SEM image of the sample SiO_2 with higher magnification (30.000).

2.6 Thermogravimetric analysis

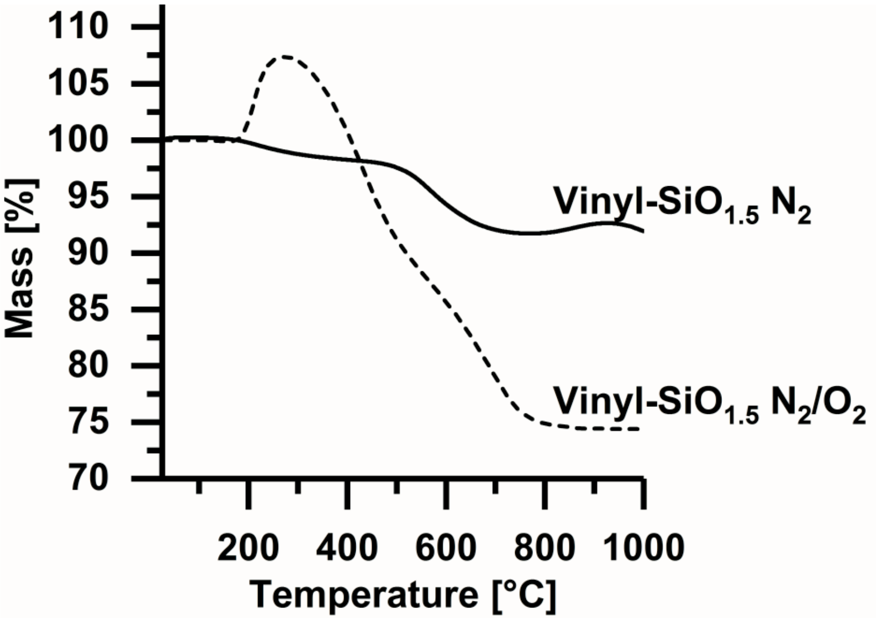

Fig. S8 Thermogravimetric analysis of Vinyl-$SiO_{1.5}$ particles measured under a) 100% N_2 and b) with 5% O_2 and 95% N_2.

2.7 Syntheses with different alkoxysilanes concentrations

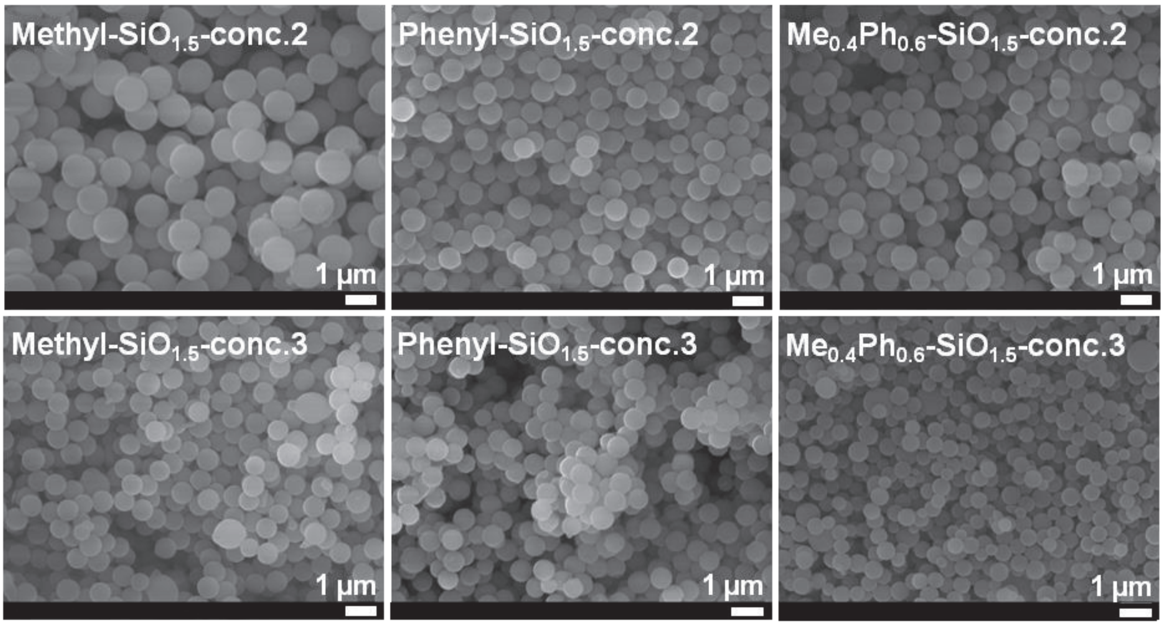

Figure S9 SEM images of ORMOSIL particles synthesized with 0.069 mmol (conc.2) and 0.035 mmol (conc.3) alkoxysilane.

3 References

1 Fournier M-C, Falk L, Villermaux J (1996) A new parallel competing reaction system for assessing micromixing efficiency - experimental approach Chem Eng Sci 51 (22):5053-5064

2 Dushman S (1904) The rate of the reaction between iodic and hydriodic acids. J Phys Chem 8 (7):453-482. doi:10.1021/j150061a001

3 Commenge J-M, Falk L (2011) Villermaux–Dushman protocol for experimental characterization of micromixers. Chem Eng Process 50 (10):979-990. doi:10.1016/j.cep.2011.06.006

3.3.2 Carbide-derived carbon beads with tunable nanopores from continuously produced polysilsesquioxanes for supercapacitor electrodes

The experience gained in continuous ORMOSIL synthesis is used in the following three articles to develop tailor-made materials for energy storage.

The following article describes how ORMOSILs are transformed into carbide-derived carbons, which serve as electrode material in supercapacitors. A special challenge is to preserve the spherical morphology of the particles during the high-temperature process of CDC conversion. Purely phenyl-modified systems show a thermal softening due to their low cross-linking degree and lose their shape. However, the solid state NMR investigations from the previous article already revealed that vinyl groups lead to a significantly higher degree of crosslinking compared to phenyl groups. By incorporating both rests (phenyl and vinyl), a stable material is obtained that allows the successful conversion to spherical CDCs.

Based on this result, a study is conducted that varies the proportion of vinyl and phenyl groups and investigates the effects on the (morphological) properties of the CDCs. It is shown that especially the porosity of the materials is influenced by the choice of organic substituents. As a consequence, the correlation between the porosity and the electrochemical parameters of the supercapacitor can be examined.

Contributions:

Christina Odenwald; Design, planning, writing, synthesis of the polymer particles, NMR analysis, discussion, and revision of the manuscript. **Benjamin Krüner:** Design, planning, writing, pyrolysis, chlorine gas treatment, SEM, particle size analysis, EDX analysis, TGA coupled with MS analysis, CO_2 and N_2 sorption analysis, Raman analysis, XRD, and electrochemical analysis for double-layer capacitors. **Aura Tolosa:** TEM, FTIR analysis, discussion, and revision of the manuscript. **Anna Schreiber:** Electrochemical measurements, discussion, and revision of the manuscript. **Mesut Aslan:** Chlorine gas treatment, discussion, and revision of the manuscript. **Guido Kickelbick:** Discussion and revision of the manuscript. **Volker Presser:** Supervision, discussion, and revision of the manuscript.

The following paper is reproduced by permission of The Royal Society of Chemistry. Krüner, B.; Odenwald, C.; Tolosa, A.; Schreiber, A.; Aslan, M.; Kickelbick, G.; Presser, V. Carbide-derived carbon beads with tunable nanopores from continuously produced polysilsesquioxanes for supercapacitor electrodes, *Sustain. Energ. Fuels* **2017**, 1 (7), 1588–1600, https://doi.org/10.1039/C7SE00265C

Sustainable Energy & Fuels

PAPER

View Article Online
View Journal

Cite this: DOI: 10.1039/c7se00265c

Carbide-derived carbon beads with tunable nanopores from continuously produced polysilsesquioxanes for supercapacitor electrodes†

Benjamin Krüner,‡[ab] Christina Odenwald,‡[c] Aura Tolosa,[ab] Anna Schreiber,[a] Mesut Aslan,[a] Guido Kickelbick*[c] and Volker Presser*[ab]

The MicroJet reactor technique is an excellent continuous method to produce spherical and homogeneous organically modified silica (ORMOSIL) particles in a large scale (10–15 g min^{-1}). We applied this method to manufacture polyorganosilsesquioxanes with different ratios of phenyl and vinyl functional groups, which were later pyrolyzed to obtain silicon oxycarbides. Such polymer-derived ceramic (PDC) materials are highly suited as precursor for carbide-derived carbon (CDC) synthesis. Chlorine etching of PDC at high temperatures removed silicon and oxygen, yielding the formation of nanoporous carbon. Pure poly(phenyl-silsesquioxane) spheres lost their shape during the thermal process by undergoing further condensation reactions. Yet, the spherical shape was conserved during thermal processing after adding vinyl functionalities. The ratio of vinyl and phenyl functionalities controlled the pore structure and the total CDC yield, enabling an increase from 2 mass% to 22 mass%. The total pore volume varied between 1.3-2.1 $cm^3\ g^{-1}$ and the specific surface area between 2014–2114 $m^2\ g^{-1}$. The high surface area and large pore volume makes these materials attractive for high power supercapacitor electrodes. The specific capacitance of the best sample at low rates in 1 M tetraethylammonium tetrafluoroborate in acetonitrile was 116 F g^{-1} (at 5 mA g^{-1}) and still 80 F g^{-1} at very high rates (at 100 A g^{-1}).

Received 23rd May 2017
Accepted 15th July 2017

DOI: 10.1039/c7se00265c

rsc.li/sustainable-energy

1. Introduction

Highly porous carbon materials are attractive for many applications such as gas storage,[1,2] catalysis,[3] or electrochemical energy storage.[4] Electrical double-layer capacitors, also known as supercapacitors, are particularly efficient energy storage devices, capitalizing on rapid and reversible ion electrosorption.[5] Due to fast polarization, it is possible to achieve a high specific power, but only a moderate specific energy.[4] Beside high power ratings, supercapacitors exhibit a very long lifetime and high Coulombic efficiency.[6]

Carbide-derived carbons (CDCs) are a broad family of carbon materials,[7] which can be obtained from metal carbides,[8] carbonitrides,[9] or oxycarbides.[10,11] Depending on the precursor and the synthesis temperatures it is possible to produce CDC materials with different pore architectures[11] and carbon structures.[12] Oxycarbides, like SiOC, are promising precursors to synthesize highly porous CDCs with a high BET specific surface area (SSA) of 3089 $m^2\ g^{-1}$ and a large pore volume of 1.8 $cm^3\ g^{-1}$.[13] SiOC-CDC micrometer-sized particles have been obtained from commercial polymethyl- and polymethylphenylsilsesquioxanes by pyrolysis of monoliths, followed by chlorine etching at 1200 °C of the grinded monoliths.[10] Thereby, it was possible to obtain BET SSA up to 2600 $m^2\ g^{-1}$ and a total pore volume up to 1.7 $cm^3\ g^{-1}$. Polymethylsilsesquioxane can also be used in an emulsion process to obtain spherical particles with a diameter of 50–600 nm, 1–10 μm, and 10–100 μm, which were successfully converted to polymer-derived ceramics (PDCs).[14] Sub-micrometer CDCs with a diameter of 20–200 nm and a SSA of ~2300 $m^3\ g^{-1}$ were successfully obtained by emulsion soft templating using a commercial allylhydriopolycarbosilane precursor.[15] The specific capacitance of this material in 1 M tetraethylammonium tetrafluoroborate (TEA-BF_4) in acetonitrile (ACN) was 130 F g^{-1} and 110 F g^{-1} in aqueous 1 M Na_2SO_4.[15] The small size of the individual particles is beneficial to achieve a high power within supercapacitor applications. Yet, a disadvantage of the mentioned methods to produce PDC precursors for CDC synthesis is the need to add a hazardous metal crosslinking agent like hydrogen hexachloroplatinate(IV),[15] zirconium acteylacetonate,[16] or zinc acetylacetonate.[13] The crosslinking agent is necessary because the oligomers can melt before converted to PDCs.[13]

---

[a] INM – Leibniz Institute for New Materials, 66123 Saarbrücken, Germany. E-mail: volker.presser@leibniz-inm.de

[b] Department of Materials Science and Engineering, Saarland University, 66123 Saarbrücken, Germany

[c] Inorganic Solid State Chemistry, Saarland University, 66123 Saarbrücken, Germany. E-mail: guido.kickelbick@uni-saarland.de

† Electronic supplementary information (ESI) available. See DOI: 10.1039/c7se00265c

‡ These authors contributed equally

Wet chemical preparation methods for the synthesis of defined nano- and microparticles are commonly used as batch processes which exhibit several disadvantages like a variation in the product quality from batch-to-batch and a limited and complex scale-up. Continuous preparation methods offer in general a better controllability and reproducibility and are attractive for industrial scale production.[17,18] There are few continuous pathways to obtain spherical particles from oxycarbides. For example, electrospraying yields spherical particles and can be carried out with a commercial polymethylphenylsilsesquioxane.[13] The diameter of these particles was 1–6 μm, which is significant larger than soft-templated emulsion beads. The BET SSA of these micrometer spheres was up to ~2230 $m^2 g^{-1}$ and the specific capacitance was 112 F g^{-1} for 1 M TEA-BF_4 in ACN.

An advanced continuous method is the MicroJet reactor technique.[19] Thereby, two reagent solutions are forced with high pressure through micro-nozzles into the reactor which is exposed to a constant gas flow. A fast and homogenous mixing is obtained due to the high shear forces that are generated by the impinging jets. The gas flow pushes the products out of the reactor into a reservoir, which also effectively avoids clogging. The MicroJet reactor technique was already used to synthesize inorganic nanoparticles, such as TiO_2,[20] $BaSO_4$,[21] ZnO, Fe_3O_4, or $CaHPO_4$.[22]

In this work, we synthesized for the first time polyorganosilsesquioxane spheres with different ratios of phenyl and vinyl groups from organotrialkoxysilanes by using a MicroJet reactor. Poly(benzyl)silsesquioxane or poly(phenyl)silsesquioxane beads obtained by a sol–gel process have a softening point at ~50 °C and ~140 °C.[23,24] This property makes them unsuitable to produce PDCs that conserve the initial shape during pyrolysis. By adding vinyl groups to the system, it was possible to obtain a higher condensation degree and to conserve the spherical shape of the particles after the pyrolysis to obtain SiOC-PDCs. Afterwards the samples were treated in chlorine gas to obtain highly porous SiOC-CDCs. The variation of the organic groups of the silanes has a strong influence for the yield and porosity of the CDCs, which relates directly to the rate performance in the supercapacitor.

2. Experimental description

2.1. Materials

Phenyltrimethoxysilane (PTMS; 97%) and vinyltrimethoxysilane (VTMS; 99%) were obtained from ABCR GmbH. Ammonia (25%) was purchased from VWR International GmbH. All chemicals were used as received.

2.1.1. Synthesis of siloxane beads. For the synthesis of the polymer microparticles, two precursor solutions (A and B) were used as schematically shown in Fig. 1. Solution A was prepared by dissolving the respective amount of trialkoxysilane(s) in methanol (MeOH) followed by the addition of an aqueous solution of HCl (Table 1). A prehydrolization of the silane(s) was performed by stirring the solution overnight at room temperature. For solution B, we used an aqueous solution of ammonia (2.2 mol L^{-1}).

The particles were synthesized at room temperature in a MicroJet reactor of stainless steel (Synthesechemie Dr. Penth GmbH). The precursor solutions A and B were transported through the system with two HPLC-pumps (LaPrep P110 preparative HPLC pumps, VWR International GmbH) with a flow rate of 250 mL min^{-1}. The solutions were forced through opposing nozzles (nozzle diameter 300 μm) into a reaction chamber where they collide as impinging jets and a fast mixing occurs effected by the high jet velocities. A nitrogen gas flow helped to transport the product out of the reactor and avoided clogging. The outlet tube was 1.5 mm in diameter and *ca.* 85 cm in length. The product suspension was collected in a polyethylene flask. The particles were isolated by centrifugation (8000 rpm, 7012 G, 10 min) and dried in vacuum at 30 °C.

2.1.2. Pyrolysis and chlorine treatment. The polymer beads were pyrolyzed in a graphite heated furnace (Thermal Technology) in an argon atmosphere (flow rate: 50 $cm^3 min^{-1}$) at 1200 °C for 2 h with a heating rate of 2 °C min^{-1}. The resulting polymer-derived ceramic samples were labelled with the ending SiOC in the following. The materials were then transferred to a quartz tube furnace (Carbolite Gero) and heated to 1200 °C with a rate of 15 °C min^{-1}. An argon flow (50 $cm^3 min^{-1}$) was constantly supplied and the chlorine flow (10 $cm^3 min^{-1}$) was added when the target temperature (1200 °C) was reached

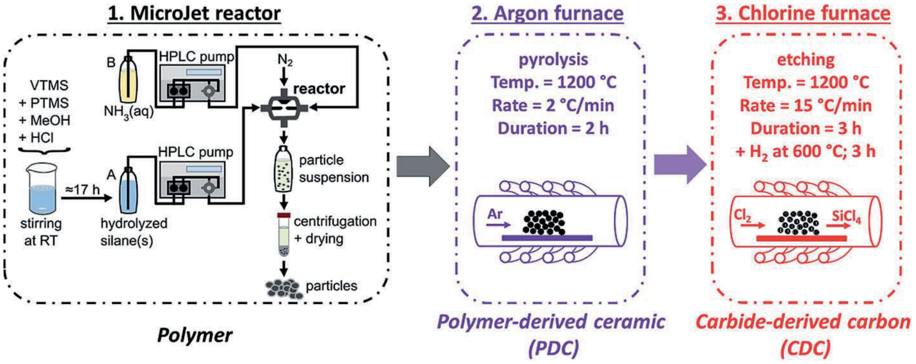

Fig. 1 Schematic overview of the synthesis method: (1) the production of the polymer beads with the MicroJet reactor, (2) the pyrolysis, and (3) the chlorine treatment. VTMS: vinyltrimethoxysilane; PTMS: phenyltrimethoxysilane; MeOH: methyl alcohol; RT: room temperature; (A and B): solution A or solution B; HPLC: high performance liquid chromatography.

Table 1 Compositions of precursor solutions A and B that were used for the synthesis of polysilsesquioxane microparticles. VTMS: vinyltrimethoxysilane; PTMS: phenyltrimethoxysilane; MeOH: methyl alcohol

	Solution A					Solution B
	$n_{(\mathrm{VTMS})}$ (mmol)	$n_{(\mathrm{PTMS})}$ (mmol)	$n_{(\mathrm{MeOH})}$ (mol)	$n_{(\mathrm{H_2O})}$ (mol)	$n_{(\mathrm{HCl})}$ (mmol)	$C_{(\mathrm{NH_3})}$ (mol L^{-1})
Vi-SiO$_{1.5}$	138.8	—	3.2	2.8	0.03	2.2
Ph$_{0.25}$Vi$_{0.75}$-SiO$_{1.5}$	104.1	34.7	2.8	2.8	0.03	2.2
Ph$_{0.5}$Vi$_{0.5}$-SiO$_{1.5}$	69.4	69.4	3.0	2.8	0.03	2.2
Ph$_{0.75}$Vi$_{0.25}$-SiO$_{1.5}$	34.7	104.1	3.2	2.8	0.03	2.2

(holding time: 3 h). Afterwards chlorine gas was switched off and the furnace was cooled to 600 °C under argon flow and hold at that temperature for 3 h under inlet of additional hydrogen (10 cm^3 min^{-1}) to remove residual chlorine from the sample. The cooling from 600 °C to room temperature was carried out in argon atmosphere. The carbide-derived carbon materials are referred to as CDC.

2.2. Material characterization

Solid-state CP-MAS NMR spectra were recorded at 25 °C using a Bruker AV400WB spectrometer (^{13}C 100.62 MHz, ^{29}Si 79.50 MHz). A contact time of 2.0 ms and a variable power contact time (ramp 10050) were used. The spin rate was 13 kHz and the delay time 3–6 s. For ^{13}C NMR, adamantane, and for ^{29}Si NMR, octakis(trimethylsiloxy)silsesquioxane was used as external standards. The intensity of all NMR spectra was normalized.

Fourier transform infrared (FT-IR) spectroscopy was applied on the dried polysilsesquioxane samples in attenuated total reflectance (ATR) mode on a Vertex 70 spectrometer (Bruker Optics). The measurements were accomplished in the wave number range of 500–4500 cm^{-1} and under ambient air. For each spectrum, 32 scans were averaged with a spectral resolution of 4 cm^{-1}.

The XRD patterns were measured with a D8 Advance diffractometer (Bruker AXS) using Cu-K$_\alpha$ radiation (40 kV and 40 mA) and a Goebel mirror with point focus and a two-dimensional X-ray detector (Vantec-500). The sample holder was a sapphire single crystal.

Raman spectroscopy was carried out with a Renishaw inVia Raman microscope with a wavelength of 532 nm and a grating of 2400 lines mm^{-1}. The spectral resolution was 1.2 cm^{-1}, the numeric aperture 0.9, and the incident power on the sample ~0.02 mW. A spectrum was recorded for 30 s and averaged over 10 accumulations. The D- and G-mode with the amorphous contribution of carbon in the Raman spectra were fitted using five Voigt functions for the SiOCs and four Voigt functions for the CDCs.

The thermogravimetric measurements combined with a mass spectrometer (TGA-MS) were carried out with a STA449F3 Jupiter and QMS 403C Aëolos from Netzsch. The heating rate for the measurement was 10 °C min^{-1} to 1200 °C in Argon (purity: 5.0).

Scanning electron microscopy (SEM) was performed in a field emission scanning electron microscope JSM-7500F from JEOL. The samples were sputtered with gold to increase the surface conductivity. The size of 150 individual spheres was measured to obtain an average diameter with the image analysis software ImageJ.[25] A X-MAX silicon detector from Oxford Instruments was used to perform the energy dispersive X-ray spectroscopy (EDX) attached to the SEM chamber. The operating voltage for the SEM and EDX was 5 kV.

High-resolution transmission electron microscopy (TEM) was executed with a JEM-2100F from JEOL at 200 kV. The polymer samples were dispersed and sonicated in water to deposit them on a lacey carbon film on a copper grid (Gatan). Ethanol was used instead of water to perform this step for the CDCs.

Nitrogen gas sorption analysis (N$_2$ GSA) was performed with an Autosorb iQ system from Quantachrome. The samples were degassed at 100 mbar at 200 °C for 1 h and at 300 °C for 20 h. The temperature during the measurement was −196 °C and the relative pressure was varied between 5×10^{-7} to 1.0 in 76 steps. A quenched-solid density functional theory (QSDFT) kernel assuming slit-like pores (QSDFT) was applied to obtain the pore size distribution from the adsorption isotherms.[26] The Brunauer–Emmett–Teller (BET) surface area was calculated with the BET equation in the linear region of the isotherm between 0.02 and 0.3 partial pressure.[27] The value of the total pore volume was obtained by the adsorbed volume at a relative pressure of 0.95 and the average pore size (d_{50}) represents the pore size with a half of the total pore volume.[11] The data analysis of the nitrogen sorption isotherms was performed with ASiQwin 3.0 from Quantachrome.

Contact angle measurements of the CDC electrodes were carried out with an OC 25 system from Data Physics with demineralized water (volume per drop: 3 μL) in air.

2.3. Electrochemical measurements

Free-standing carbon electrodes were prepared by dispersing the CDC powder in ethanol and adding 5 mass% of polytetrafluoroethylene binder (PTFE, 60 mass% in water, Sigma-Aldrich). The slurry was crushed in a mortar until a doughy carbon paste was formed, which was rolled with a rolling machine from MTI Corporation to a thickness of ~110 μm. The electrodes were dried for 48 h at 120 °C in a vacuum oven at 2×10^3 Pa. For electrochemical measurements, electrode discs with a diameter of 8 mm were punched out (geometrical information about the electrodes is given in ESI, Table S1†). Custom-built symmetrical two-electrode cells were assembled with carbon-coated aluminum current collectors (type Zflo 2653, Coveris

Advanced Coatings) for the organic electrolyte (1 M TEA-BF$_4$ in ACN; BASF, battery grade).[28] Graphite foil current collectors were used for the aqueous electrolyte (1 M Na$_2$SO$_4$ prepared with Milli-Q water; pH 5.2). A glass fiber separator (GF/A from Whatman) with a diameter of 13 mm was used between the electrodes. The cell for the organic electrolyte was placed in a vacuum oven (2×10^3 Pa) at 120 °C for 16 h.

All electrochemical measurements were carried out in a climate chamber (Binder) at 25 ± 1 °C with a VMP300 potentiostat/galvanostat from BioLogic. Electrochemical impedance spectra were recorded in a symmetrical full cell for 100 kHz to 100 mHz at 0 V with ten points per decade and averaged over five measurements. The electrical serial resistance (ESR) and the electrical distribution resistance (EDR) were normalized to the geometrical area of the electrode. The capacitance from cyclic voltammograms (CV) was calculated with eqn (1) and from galvanostatic cycling with potential limitation (GCPL) with eqn (2). The specific capacitance was normalized to the active mass (95%) of one electrode. The IR-drop of the GCPL measurements was obtained after a resting time of 10 s. The electrochemical performance is benchmarked against PTFE bonded film electrodes from YP-80F (Kuraray Co.), which is referred to as AC (activated carbon).

$$C_\mathrm{S} = \frac{4I(t)}{\mathrm{d}U(t)/\mathrm{d}t \times m} \tag{1}$$

C_S: specific capacitance per electrode, $I(t)$: current, $\mathrm{d}U(t)/\mathrm{d}t$: scan rate, and m: mass of carbon in the electrode.

$$C_\mathrm{S} = \frac{4Q_\mathrm{dis}}{Um} \tag{2}$$

C_S: specific capacitance per electrode, Q_dis: charge of the discharging cycle, U: IR-drop corrected cell voltage, and m: mass of carbon in the electrode.

Stability testing *via* voltage floating for 100 h was also conducted in the climate chamber at 25 °C at 1.4 V for the aqueous and 2.7 V for the organic electrolyte. Every 10 h, galvanostatic cycling was performed at a cell voltage of 1.2 V (aqueous) or 2.5 V (organic). After voltage floating, the electrodes with the aqueous electrolyte were washed with Milli-Q water for further post mortem analysis.

3. Results and discussion

3.1. Particle characterization

FT-IR measurements of the polymer particles confirm the presence of the desired organic groups (Fig. S1†). All samples exhibit peaks from the inorganic backbone in the range of 935–1230 cm^{-1} from –Si–O–Si– vibrations. In addition, the samples show vibration bands from the organic groups. At 2800–3095 cm^{-1}, in each spectrum C–H stretching vibrations are present and at 1600 cm^{-1} peaks from C═C vibrations. Samples with phenyl groups show characteristic signals from Si–C-vibrations at 1430 cm^{-1} and 1130 cm^{-1}. Samples that contain vinyl groups also show well-defined modes at 1275 cm^{-1} from Si–C vibrations and peaks at 1410 cm^{-1} that can be assigned to ═CH$_2$ bending vibrations.[29–31] The increasing vinyl content of the samples Ph$_{0.75}$Vi$_{0.25}$-SiO$_{1.5}$, Ph$_{0.5}$Vi$_{0.5}$-SiO$_{1.5}$, Ph$_{0.25}$Vi$_{0.75}$-SiO$_{1.50}$, and Vinyl-SiO$_{1.5}$ is reflected by the increasing intensity of the Si-vinyl vibration (1275 cm^{-1}) compared to the Si-phenyl vibration (1430 cm^{-1}).

^{13}C NMR spectra (Fig. 2A) of the prepared polysilsesquioxane particles show characteristic signals for the vinyl and phenyl groups. For the samples with both organic groups overlapping peaks were obtained. Samples exhibit no or only weak signals from residual alkoxy groups (at *ca.* 60 ppm), which suggests that almost all alkoxy groups were hydrolyzed during polymerization and that in T^2 units OH-groups are present in addition to the vinyl and phenyl groups. ^{29}Si NMR spectra (Fig. 2B) give important information about the network structure. The peaks at ≈−73 ppm and ≈−82 ppm of the organically modified silica (ORMOSIL) particles can be assigned to T^2 and T^3 species, meaning silicon atoms that are connected to the network with two or three bonds. The spectra also show that the T^2 to T^3 ratio decrease with an increasing vinyl content. This behavior confirms the incorporation of vinyl groups into the network, which leads to an enhanced cross-linking that is desired to obtain a better thermal stability.

The XRD pattern of the mixed polymers in Fig. 2C show a shift of very broad peaks to higher 2θ values with an increasing amount of vinyl groups. Polyphenylsiloxanes can have a ladder like structure and two peaks in the XRD pattern can be identified with the plane-to-plane peak at ~7.3° 2θ and the chain-to-chain peak of the Si–O–Si frame at ~18.8° 2θ.[32] Polyvinylsiloxanes with a ladder structure exhibit a plain-to-plain peak at ~10° 2θ.[33] The corresponding chain-to-chain peak is at around 23° 2θ due to the lower required space of the vinyl group compared to the phenyl group.[33] The measured peak positions of the Vi-SiO$_{1.5}$ is similar to the reported values in the literature.[33] The three samples with mixtures synthesized with different ratios of phenyl- and vinyltrimethoxysilane show peaks in between the pure polyphenyl- and polyvinylsiloxanes, which indicates a homogeneous mixture. From the peak width, it is possible to estimate domain sizes by use of the Scherer equation which were below 5 nm.[34] These small domain sizes point out the mainly amorphous character of the synthesized polymers. The absence of long-range order can also be seen in the transmission electron micrographs in the ESI, Fig. S2.†

The pyrolysis of the polysiloxanes was monitored with TGA-MS (Fig. 2D and E, ESI Fig. S1C and D†). All four polymers show a degradation of the ladder structure around 560 °C (Fig 2D), which would be an untypical degradation behavior for a cage structure.[35] The mass loss of the vinyl-polymer is the lowest and the mass loss increases constantly with the amount of added phenyl-groups. The mass spectra of the most important evolving groups are plotted in Fig. 2E, while all relevant leaving groups of Ph$_{0.5}$Vi$_{0.5}$-SiO$_{1.5}$ are displayed in the ESI (Fig. S1C and D†). The mass spectra in Fig. 2E identify evolving groups during heating. Water (*m*/*z*: 18) is removed from the samples in two main temperature regimes: first, between 135 °C and 430 °C, and second, at temperatures from 450 °C to 800 °C, where also the other organic groups are being removed. Samples with more phenyl groups (*m*/*z*: 78 at ~570 °C) or vinyl groups (*m*/*z*: 28 at ~550 °C) show a larger loss of these functional groups. The

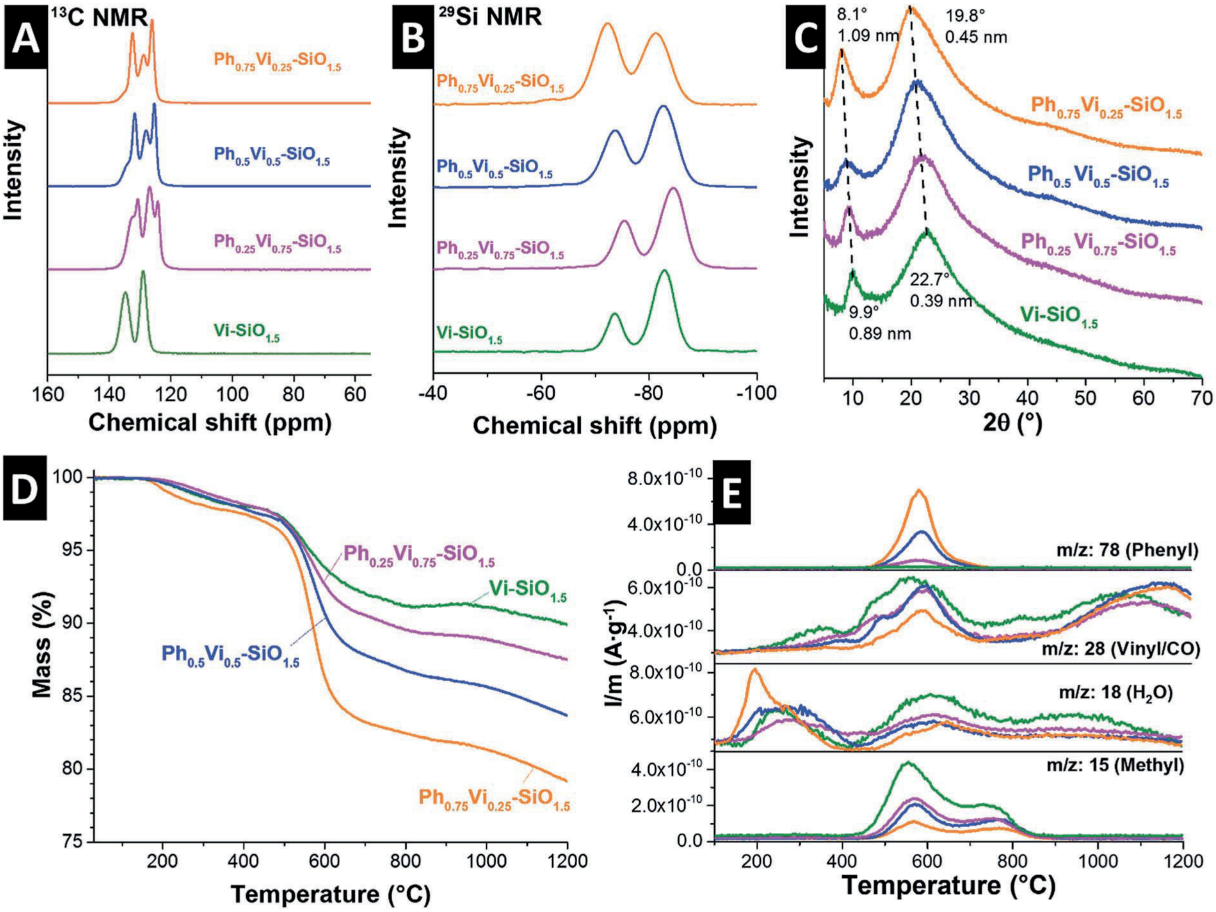

Fig. 2 Solid-state ^{13}C NMR (A), ^{29}Si NMR (B), and XRD pattern (C) of the four polymer beads. TGA curve of the pyrolysis process (D) and the corresponding mass spectra of selected leaving groups (E).

atomic mass of 28 can also be related to carbon monoxide, which is formed at higher temperatures (>900 °C) with residual oxygen. Another major leaving group is the methyl group formed by the decomposition of organic chains from the vinyl groups, which shows two peaks at 550 °C and 750 °C.

3.2. Properties of the polymer-derived ceramics and carbide-derived carbons

The chemical composition of the SiOCs is denoted in Table 2. Of our samples, the carbon content of the Vi-SiOC is the lowest with 32.2 ± 4.8 mass% and increases with an increasing amount of phenyl groups to 50.8 ± 1.8 mass% for $Ph_{0.5}Vi_{0.5}$-SiOC. Yet, the carbon content is not increasing when the amount of phenyl groups is increased from 50% to 75%, which can be explained with the higher mass loss of $Ph_{75}Vi_{25}$-SiOC.

As can be seen from our EDX results (Table 2), the removal of silicon and oxygen by chlorine treatment at high temperatures was successful and we only found a low amount of residual silicon and oxygen. The mass losses after pyrolysis and chlorine treatment of samples with different ratios of phenyl and vinyl functional groups are quite different (Table 3). The sample Vi-SiOC had the lowest mass loss after pyrolysis of only 11 mass% and shows the highest mass loss after the etching of 97.6 mass%. The total yield of Vi-SiOC-CDCs synthesis amounts to only 2.2 mass%. The addition of phenyl groups increases the total yield to 21.9 mass%, which can be explained by the higher carbon and aromatic content introduced by the phenyl groups.

The Raman spectra and XRD pattern of the SiOCs and CDCs with different ratios of vinyl- and phenyltrimethoxysilanes are very similar; therefore, Fig. 3 only depicts data for the $Ph_{0.5}Vi_{0.5}$-SiOC samples (and the remaining Raman spectra and XRD patterns are found in ESI, Fig. S3†). The SiOC Raman spectra (Fig. 3A) show the presence of incompletely graphitic carbon,

Table 2 Chemical composition of all SiOCs and CDCs measured with EDX

	C (mass%)	O (mass%)	Si (mass%)
Vi-SiOC	32.2 ± 4.8	31.5 ± 4.0	36.3 ± 8.2
$Ph_{0.25}Vi_{0.75}$-SiOC	41.9 ± 2.4	26.2 ± 1.6	31.9 ± 4.0
$Ph_{0.5}Vi_{0.5}$-SiOC	50.8 ± 1.8	25.2 ± 0.8	24.0 ± 2.5
$Ph_{0.75}Vi_{0.25}$-SiOC	50.2 ± 1.5	25.9 ± 1.0	23.9 ± 2.4
Vi-SiOC-CDC	97.9 ± 0.3	1.9 ± 0.3	0.3 ± 0.1
$Ph_{0.25}Vi_{0.75}$-SiOC-CDC	98.4 ± 0.7	1.3 ± 0.4	0.4 ± 0.3
$Ph_{0.5}Vi_{0.5}$-SiOC-CDC	98.4 ± 0.2	1.4 ± 0.1	0.2 ± 0.1
$Ph_{0.75}Vi_{0.25}$-SiOC-CDC	97.1 ± 0.4	2.9 ± 0.4	n.d.

Table 3 Mass loss by pyrolysis and chlorine treatment

	Mass loss after pyrolysis (mass%)	Mass loss after chlorine gas treatment (mass%)	Total mass loss (mass%)
Vi-SiOC-CDC	11.0	97.6	97.8
$Ph_{0.25}Vi_{0.75}$-SiOC-CDC	13.0	85.1	87.1
$Ph_{0.5}Vi_{0.5}$-SiOC-CDC	15.0	76.1	79.6
$Ph_{0.75}Vi_{0.25}$-SiOC-CDC	20.7	72.4	78.1

Table 4 Fitted values of the D- and G-mode from the Raman spectroscopy of all SiOCs and CDCs

	Mode	Position (cm^{-1})	FWHM (cm^{-1})	I_D/I_G
Vi-SiOC	D	1334	181	4.27
	G	1587	111	
$Ph_{0.25}Vi_{0.75}$-SiOC	D	1331	162	4.67
	G	1601	67	
$Ph_{0.5}Vi_{0.5}$-SiOC	D	1333	159	4.58
	G	1603	62	
$Ph_{0.75}Vi_{0.25}$-SiOC	D	1324	167	4.40
	G	1599	66	
Vi-SiOC-CDC	D	1333	85	2.80
	G	1593	65	
$Ph_{0.25}Vi_{0.75}$-SiOC-CDC	D	1337	89	2.40
	G	1597	66	
$Ph_{0.5}Vi_{0.5}$-SiOC-CDC	D	1337	84	2.55
	G	1596	68	
$Ph_{0.75}Vi_{0.25}$-SiOC-CDC	D	1339	76	2.56
	G	1601	67	

due to the position of the D- and G-mode at 1331 cm^{-1} and 1603 cm^{-1}. The Vi-SiOC shows a higher amount of amorphous carbon than the other SiOC samples, which can be recognized by having a look to the broader full-width at half-maximum (FWHM) of 181 cm^{-1} and 111 cm^{-1}, compared to 159 cm^{-1} and 62 cm^{-1} of $Ph_{0.5}Vi_{0.5}$-SiOC (Table 4). The I_D/I_G ratios of the SiOCs ranged between 4.27 and 4.67.

The Raman spectra of the CDCs (Fig. 3A) show nanocrystalline graphitic carbon nature. This can also be recognized by the position of the D- and G-mode at 1337 cm^{-1} and 1596 cm^{-1}.[36] The FWHM decreased significantly to 84 cm^{-1} for the D-mode and 68 cm^{-1} for the G-mode. The I_D/I_G ratios of the CDCs are lower (2.40–2.80) compared to the SiOCs. It appears that the amount of amorphous carbon is reduced by comparing the SiOC with the CDC. Yet, it is reasonable to assume that amorphous carbon formed by the pyrolysis did not entirely disappear after the chlorine gas treatment. Instead, additional nanocrystalline carbon is formed by the chlorine treatment at 1200 °C by converting the SiOC to CDC; this leads to a relative lower amount of the amorphous phase compared to the carbon with more structural ordering.[37,38] Due to the high temperature during the CDC formation, the carbon of all CDCs has a similar (narrow) FWHM and positions of the D- and G-mode (Table 4).

The XRD pattern of the SiOC in Fig. 3B show mainly two broad signals at 22° 2θ and 44° 2θ. The broad peak at 22° 2θ is related to the short-range order of SiO_4 tetrahedra and the 44° 2θ is related to (101)-graphite. The results from EDX, Raman spectroscopy, and XRD show that all PDCs contain amorphous silicon oxide and carbon, which is consistent with the literature.[39,40] The XRD pattern of the CDCs in Fig. 3B show no signal related to amorphous silicon oxide; only the peak at 44° 2θ from (101)-graphite is visible. The results of Raman spectroscopy and the X-ray diffraction indicate only carbons are present in the CDC.

Fig. 4 illustrates the morphology of the CDCs by SEM and TEM images. The average diameters of the particles obtained by the SEM images are given in Table 5. The Vi-SiOC-CDCs are the smallest with the narrowest distribution wide (0.68 ± 0.09 μm). Particles with vinyl and phenyl groups are larger and have a broader size distribution of 2.20 ± 0.48 μm ($Ph_{0.25}Vi_{0.75}$-SiOC-CDC), 2.54 ± 0.58 μm ($Ph_{0.5}Vi_{0.5}$-SiOC-CDC), and 1.81 ± 0.28 μm ($Ph_{0.75}Vi_{0.25}$-SiOC-CDC). The broad size distribution of the particles favors effective packing in the electrode, which may benefit the electrical conductivity. On the surface of the particles, small fractures are noticeable where the particles were agglomerated. The TEM images of all CDC samples show disordered carbon, which is consistent with the XRD pattern (Fig. 3B).

$Ph_{0.75}Vi_{0.25}$-SiOC-CDC, $Ph_{0.5}Vi_{0.5}$-SiOC-CDC, and $Ph_{0.25}Vi_{0.75}$-SiOC-CDC have a type I isotherm resulting from a high amount

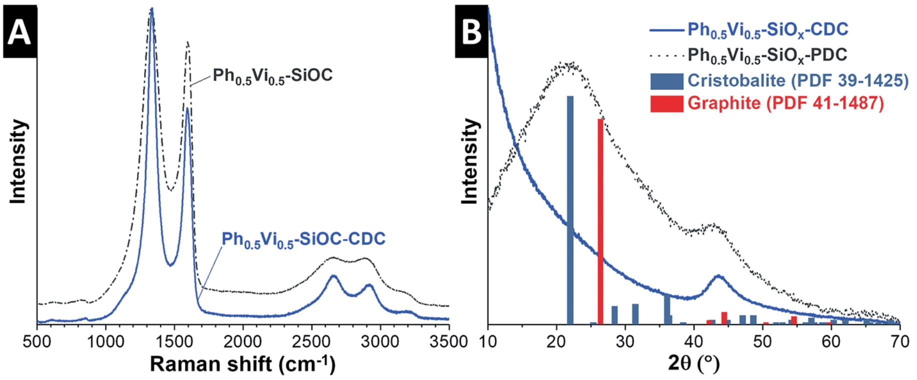

Fig. 3 Raman spectra (A) and XRD pattern (B) of the SiOC and CDC from $Ph_{0.5}Vi_{0.5}$-SiOC.

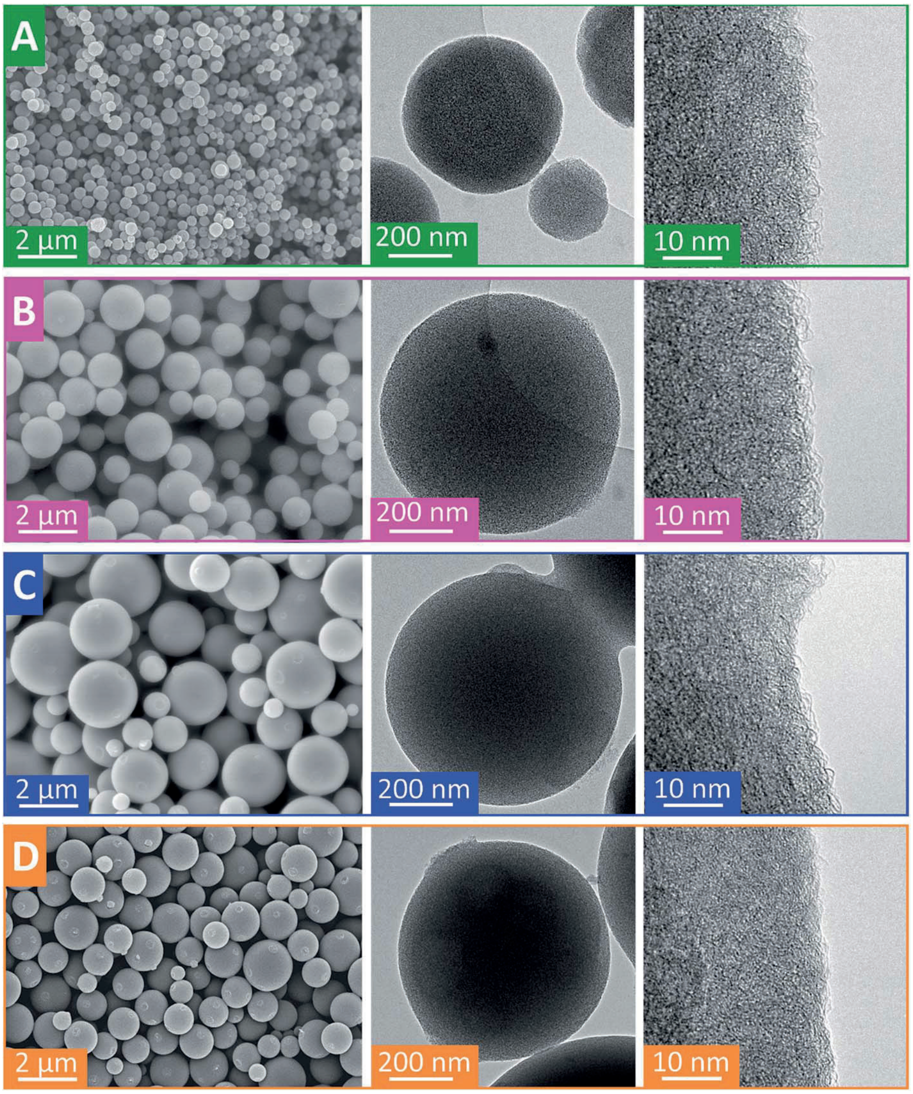

Fig. 4 Scanning and transmission electron micrographs of Vi-SiOC-CDC (A), $Ph_{0.25}Vi_{0.75}$-SiOC-CDC (B), $Ph_{0.5}Vi_{0.5}$-SiOC-CDC (C), and $Ph_{0.75}Vi_{0.25}$-SiOC-CDC (D).

of micropores measured with N_2 GSA in Fig. 5A. Only Vi-SiOC-CDC has a type IV isotherm because it has also a high amount of mesopores, which increase the pore volume. Therefore, Vi-SiOC-CDC shows the highest total pore volume with 2.06 $cm^3\ g^{-1}$. The total pore volume is steadily reduced by adding a higher amount of phenyl groups to the siloxane to 1.67 $cm^3\ g^{-1}$ for $Ph_{0.25}Vi_{0.75}$-SiOC-CDC, 1.40 $cm^3\ g^{-1}$ for $Ph_{0.5}Vi_{0.5}$-SiOC-CDC, and 1.27 $cm^3\ g^{-1}$ for $Ph_{0.75}Vi_{0.25}$-SiOC-CDC. Also, the average pore size was reduced from 2.9 nm to 1.4 nm. Yet, the DFT SSA remains rather constant with values between 2014 $m^2\ g^{-1}$ and 2198 $m^2\ g^{-1}$. In Table 5, we provide values obtained from the N_2 GSA. We clearly see that the CDC porosity can be modified in a controllable way by adjusting the functional groups of the silanes which were used as precursor.

Table 5 Volume depended average particle size obtained by SEM images and porosity of the carbide-derived carbons measured with nitrogen gas sorption

	Average particle size (µm)	SSA_{DFT} ($m^2\ g^{-1}$)	SSA_{BET} ($m^2\ g^{-1}$)	Total pore volume ($cm^3\ g^{-1}$)	Average pore size (nm)
Vi-SiOC-CDC	0.68 ± 0.09	2044	2473	2.06	2.9
$Ph_{0.25}Vi_{0.75}$-SiOC-CDC	2.20 ± 0.48	2198	2905	1.67	1.7
$Ph_{0.5}Vi_{0.5}$-SiOC-CDC	2.54 ± 0.58	2114	2729	1.40	1.5
$Ph_{0.75}Vi_{0.25}$-SiOC-CDC	1.81 ± 0.28	2014	2554	1.27	1.4

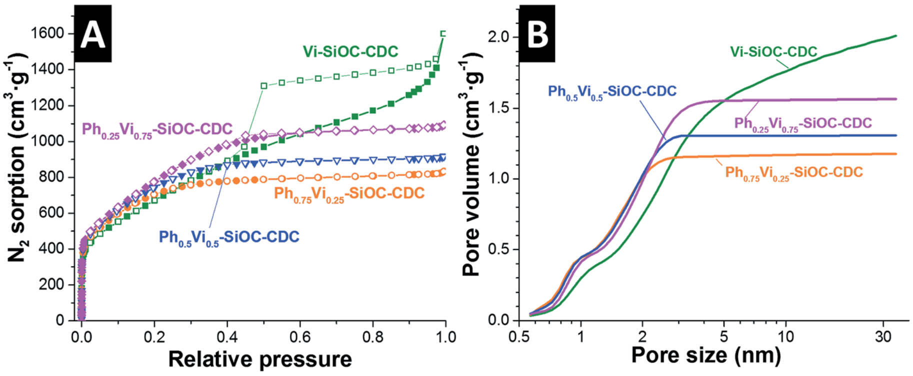

Fig. 5 Nitrogen gas sorption isotherms recorded at −196 °C of the CDC samples (A) and the corresponding pore size distributions applying a QSDFT model assuming slit-like pores (B).

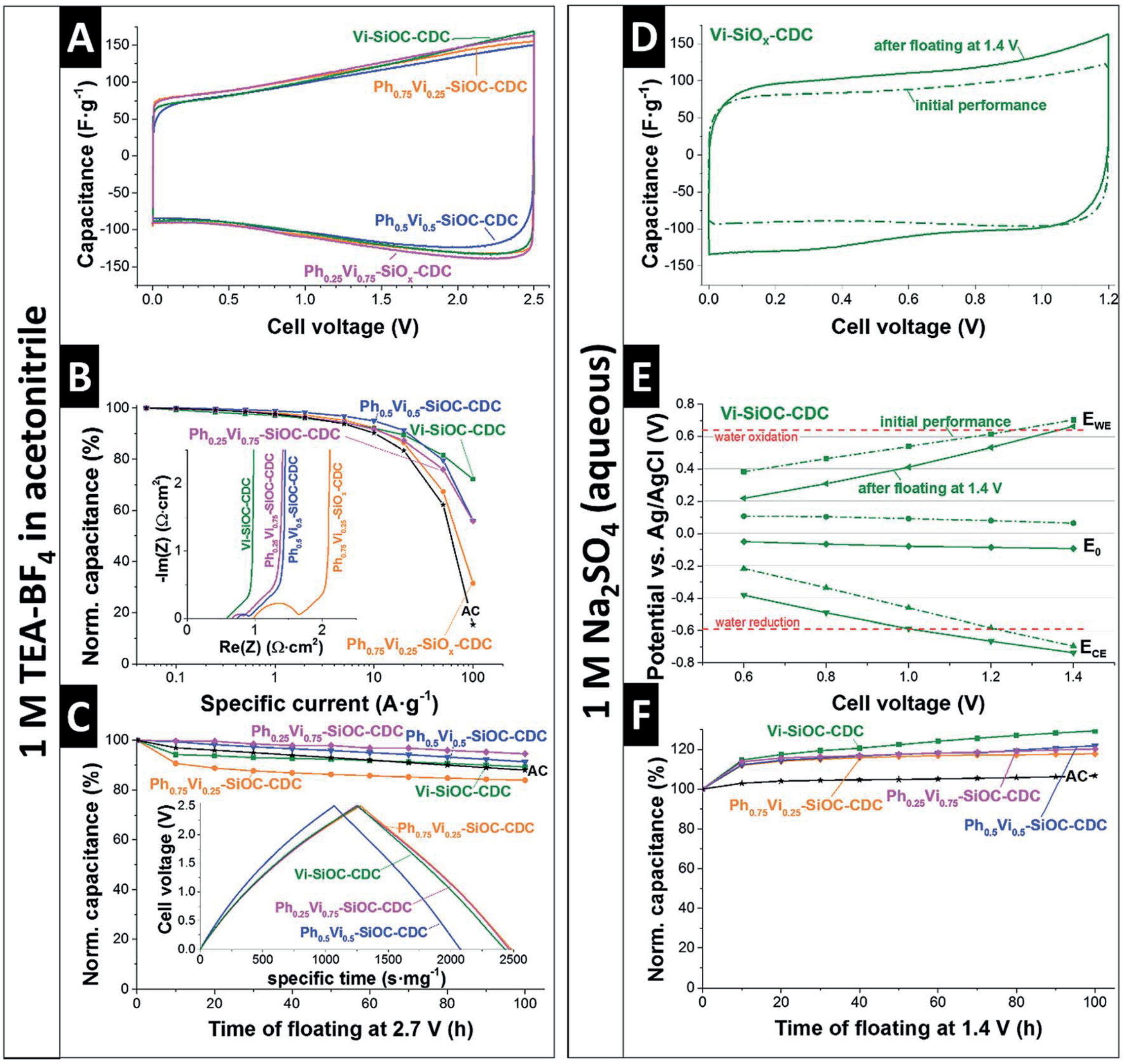

Fig. 6 Cyclic voltammograms (A), rate handling behavior with Nyquist plot as inset (B), and the stability test operating with voltage floating at 2.7 V including the GCPL curve to 2.5 V at 0.05 A g^{-1} as inset (C) of the CDCs in TEA-BF$_4$ in ACN. Cyclic voltammograms (D) of Vi-SiOC-CDC before and after the voltage floating test at 1.4 V (F), and monitored potentials of the positive and negative electrode including the zero-charge potential (E) in aqueous Na$_2$SO$_4$.

3.3. Supercapacitor performance

The electrochemical performance of the SiOC-CDC electrodes was tested in a symmetrical supercapacitor cell using the most commonly used organic electrolyte (1 M in TEA-BF_4 in ACN). The CVs with the organic electrolyte in Fig. 6A shows a typical rectangular shape, typical for nanoporous carbon.[28] A significant difference of the mass-normalized CVs of the different samples is not distinguishable. The specific capacitances measured in GCPL mode are denoted in Table 6. $Ph_{0.25}Vi_{0.75}$-SiOC-CDC has a slightly higher specific capacitance in TEA-BF_4 in ACN with 116 F g^{-1} than the other materials (Vi-SiOC-CDC: 111 F g^{-1}; $Ph_{0.5}Vi_{0.5}$-SiOC-CDC: 106 F g^{-1}; $Ph_{0.75}Vi_{0.25}$-SiOC-CDC: 112 F g^{-1}). Commercial microporous activated carbon (AC; see ref. 41 for AC properties) has a similar specific capacitance of 110 F g^{-1} under the same measurement conditions. The variable porosity of the SiOC-CDCs influences the rate handling behavior much stronger than the total capacitance plotted in Fig. 6B. While the AC has only a residual capacitance of 15% at an ultrahigh specific current of 100 A g^{-1}, the sample $Ph_{0.75}Vi_{0.25}$-SiOC-CDC retains twice as much capacitance under the same conditions (31%). With an increasing mesoporous fraction and an increasing pore volume, the capacitance retention at 100 A g^{-1} increases to 56% for $Ph_{0.5}Vi_{0.5}$-SiOC-CDC and $Ph_{0.25}Vi_{0.75}$-SiOC-CDC and to up to 72% for Vi-SiOC-CDC. We can explain the superior power handling ability of Vi-SiOC-CDC also by the smaller particle size.[42] In Table 6, we see a comparison of the performance of the MicroJet SiOC-CDCs with literature values. There is a clear advantage of the MicroJet SiOC-CDCs of retaining a high specific capacitance at high specific currents (10 A g^{-1} or 100 A g^{-1}). Even materials optimized for high power handling, such as electrospun CDC fiber mats,[13] show a higher capacitance loss at 10 A g^{-1} or 100 A g^{-1} than electrodes made from Vi-SiOC-CDC when using a similar thickness and measurement conditions. The Coulombic efficiencies are plotted in the ESI (Fig. S4A†) and we see all values approaching 99% at around 1 A g^{-1}.

Table 7 ESR and EDR obtained from EIS in 1 M TEA-BF_4 in ACN

	ESR (Ω cm^2)	EDR (Ω cm^2)
Vi-SiOC-CDC	0.59	0.35
$Ph_{0.25}Vi_{0.75}$-SiOC-CDC	0.66	0.51
$Ph_{0.5}Vi_{0.5}$-SiOC-CDC	0.74	0.49
$Ph_{0.75}Vi_{0.25}$-SiOC-CDC	0.98	0.44

The rate handling ability is influenced by the resistance of the electrodes. Using electrochemical impedance spectroscopy (EIS), we quantified the electrical serial resistance (ESR) and electrical distribution resistance (EDR), as seen in Table 7. Vi-SiOC-CDC, which shows the best rate behavior, has the lowest ESR with 0.59 Ω cm^2. $Ph_{0.25}Vi_{0.75}$-SiOC-CDC and $Ph_{0.5}Vi_{0.5}$-SiOC-CDC have a slightly higher ESR of 0.66 Ω cm^2 and 0.74 Ω cm^2, respectively. $Ph_{0.75}Vi_{0.25}$-SiOC-CDC, which was also the CDC with the lowest performance at high rates has the highest ESR of 0.98 Ω cm^2. An increasing ESR value correlates with a reduced performance at high specific currents. The EDR value of Vi-SiOC-CDC is also the lowest with 0.35 Ω cm^2. The other EDR values are very close and vary in the range of 0.44–0.51 Ω cm^2 without a systematic trend.

Also, the performance stability of the system is very high, as can be seen in Fig. 6C. After voltage floating at 2.7 V for 100 h in 1 M TEA-BF_4 in ACN, all materials show a residual specific capacitance between 84% and 95%. The commercial AC has a similar residual capacitance of 89%.[41] Yet, a comparison with literature values is difficult because the electrochemical stability is influenced by the carbon structure,[41] presence and type of functional groups,[41] the electrochemical operation window,[43] measurement conditions,[44] and other cell components like the current collector.[45]

In addition to a common organic electrolyte, we also benchmarked the supercapacitor performance in an aqueous medium. We see important differences of the supercapacitor performance by using an aqueous electrolyte as compared to

Table 6 Overview of the supercapacitor performance of the SiOC-CDCs in 1 M TEA-BF_4 in ACN and aqueous 1 M Na_2SO_4 and the comparison with other carbon-based electrode materials for supercapacitors (n.r.: not reported)

	1 M TEA-BF_4 in ACN			Aqueous 1 M Na_2SO_4			
	Low-rate capacitance (F g^{-1})	Capacitance loss at 10 A g^{-1} (%)	Capacitance loss at 100 A g^{-1} (%)	Initial specific capacitance (F g^{-1})	After floating, specific capacitance (F g^{-1})	SSA_{DFT} (m^2 g^{-1})	Ref.
Vi-SiOC-CDC	111 (at 0.05 A g^{-1})	8	28	98	126	2044	This work
$Ph_{0.25}Vi_{0.75}$-SiOC-CDC	116 (at 0.05 A g^{-1})	8	44	113	135	2198	This work
$Ph_{0.5}Vi_{0.5}$-SiOC-CDC	106 (at 0.05 A g^{-1})	5	44	116	135	2114	This work
$Ph_{0.75}Vi_{0.25}$-SiOC-CDC	112 (at 0.05 A g^{-1})	8	69	104	123	2014	This work
AC	110 (at 0.05 A g^{-1})	10	85	143	152	1756	This work
Emulsion CDC-NS-70-30	130 (at 0.05 A g^{-1})	8	n.r.	103	n.r.	2298	Ref. 15
Electro-sprayed SiOC-CDC beads	117 (at 0.1 A g^{-1})	20	95	n.r.	n.r.	2227	Ref. 13
Electrospun SiOC-CDC fiber mat	130 (at 0.1 A g^{-1})	14	37	n.r.	n.r.	2394	Ref. 13
Activated carbon black (BP2000)	86 (at 0.1 A g^{-1})	9	n.r.	n.r.	n.r.	1389	Ref. 55
Carbon onions	24 (at 0.1 A g^{-1})	10	n.r.	n.r.	n.r.	404	Ref. 59
N-doped activated Lignin-derived carbon	147 (at 0.1 A g^{-1})	19	n.r.	n.r.	n.r.	2353	Ref. 60

the organic electrolyte. The initial CV of Vi-SiOC-CDC in Fig. 6D shows a typical rectangular shape of a supercapacitor with a relatively low specific capacitance of only 98 F g^{-1}. All other CVs are very similar (ESI, Fig. S4†). The capacitance was not reduced after voltage floating at 1.4 V for 100 h; yet, the specific capacitance of Vi-SiOC-CDC increased to 126 F g^{-1} instead of an assumed loss of capacitance (Fig. 6F). It was already shown that aqueous supercapacitors with Na_2SO_4 can have a very high stability at high potentials which exceed the thermodynamic stability window of water of 1.2 V.[46] The improved performance after floating can be related to (i) progressing wetting,[47–50] and (ii) reversible faradaic redox-reactions of oxygen functional groups,[51] and reversible hydrogen reaction.[52–54]

A three-electrode cell with an Ag/AgCl reference electrode provides information about the potential development in the symmetrical setup (Fig. 6E). The initial electrodes have a zero-charge potential of +64 mV *versus* Ag/AgCl at a cell voltage of 1.4 V. The potential at the positive electrode is 0.70 V *versus* Ag/AgCl, exceeding the thermodynamic water oxidation of 0.64 V *versus* Ag/AgCl.[46] Also, the potential at the negative electrode is at −0.70 V *versus* Ag/AgCl below the limit of water reduction at −0.59 V *versus* Ag/AgCl.[46] The high potential at the positive electrode leads to the assumption that an irreversible oxidation of the carbon took place during the voltage holding at 1.4 V. The zero-charge potential was reduced from +64 mV to −93 mV *versus* Ag/AgCl after the longtime test which can be explained with an increase of oxygen containing functional groups on the carbon surface introduced by the oxidation at high cell voltages.

The aqueous Vi-SiOC-CDC cell was disassembled after the stability test to perform a post mortem analysis *via* gas sorption analysis, EDX, and contact angle measurements. By comparing the nitrogen sorption isotherms of the powder (Fig. 5A) with the isotherms of the electrodes (Fig. 7A) it is striking that the porosity is reduced. The addition of PTFE-binder leads to a smaller porosity due to an additional mass and pore blocking.[55] By comparing the isotherms of the initial electrode with the electrodes after the voltage floating in Fig. 7A, a significant pore volume loss is evident. Table S2† (ESI) supplies the detailed values obtained from the isotherms. The DFT surface area was reduced from 1756 m^2 g^{-1} to 980 m^2 g^{-1} at the negative and 897 m^2 g^{-1} at the positive electrode. The total pore volume also decreased from 1.83 m^2 g^{-1} to 1.23 m^2 g^{-1} at the negative, and 1.19 m^2 g^{-1} at the positive side, which might also be influenced by residual salt from the electrolyte. We see from the normalized pore size distribution in Fig. 7B (*i.e.*, normalized to 100%) that the pore volume is reduced mainly in the micropore range. The reduction of the micropores explains the loss of surface area of 49% compared to a relative low reduction of the total pore volume of 35% of the positive electrode. This is an indication for surface functionalities which block small micropores for N_2 during the GSA measurement. The increase of oxygen content further supports this assumption (Fig. 7D).

Post mortem EDX analysis was conducted, showing an increase in the oxygen-to-carbon ratio from 0.055 of the initial electrode to 0.075 on the negative, and 0.115 on the positive electrode after the voltage floating (ESI, Table S3†). The increase

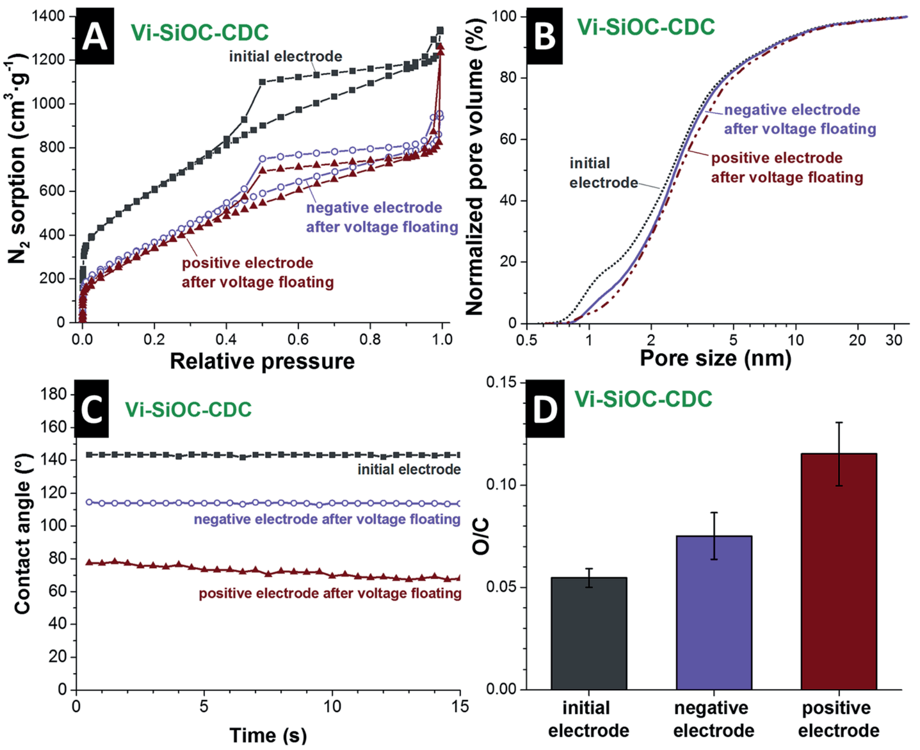

Fig. 7 Post mortem analysis of the Vi-SiOC-CDC electrodes after the voltage floating in aqueous 1 M Na_2SO_4 at 1.4 V cell voltage compared to the initial electrodes. N_2 gas sorption isotherms (A), normalized pore size distribution (B), contact angle (C), and the oxygen/carbon ratio measured *via* EDX (D).

of oxygen-containing functional groups also influences the wetting behavior of the electrodes (Fig. 7C). Initially, the Vi-SiOC-CDC electrode exhibits a contact angle with water of 143° after 1 s. This is relatively high compared to other highly porous carbon materials, like the AC with an initial contact angle of 63° (ref. 56) or CO_2-activated novolac-derived carbons with 121° (ref. 57). The contact angle of the negative electrode after the voltage floating is reduced to 114°. At the positive electrode, oxidation mainly takes place during electrochemical operation, leading to an even lower contact angle of 77° after 1 s and faster water absorption. Besides functional surface groups of the carbon, the contact angle is also influenced by the hydrophobic character of the PTFE-binder,[58] which allows only a relative comparison of the samples. The oxidation of the carbon surface and the permanent operation during the testing led to an increase of the wettability of the carbon. Thereby, we enabled enhanced access for the aqueous electrolyte to the surface of the CDCs, which led to an increase of the capacitance after the voltage floating of 16–29%.

4. Conclusions

In this study, phenyl- and vinyltrimethoxysilane mixtures with four different ratios were used to synthesize polysiloxane polymer beads. The MicroJet reactor technique allows continuous manufacturing of polysiloxanes beads with a constant quality at rates of 10–15 g min^{-1}. These beads were found as highly suited for pyrolysis, to obtain SiOC, and chlorine gas treatment, to obtain CDC by removal of non-carbon elements and still conserving the spherical morphology. An increase of phenyl groups increased the total yield after pyrolysis and etching from 2.2 mass% to 21.9 mass%, which is relevant for the economic efficiency to produce highly porous carbon materials. A possible way to increase the yield might be the use of organic functional groups with a higher amount of carbon, like naphthyl or anthracenyl groups. Also, the combination of the pyrolysis and chlorine treatment should be considered to improve the process.

By varying the ratio of phenyl and vinyl groups it was possible to produce highly porous CDCs with DFT SSA ranging between 2014-2198 $m^2 g^{-1}$ with a total pore volume in the range of 1.27–2.06 $cm^3 g^{-1}$ without any additional activation step. A higher amount of vinyl groups leads to a higher total pore volume. The increased mesoporosity influences mainly the rate handling behavior of the supercapacitor, while the specific capacitance at low ranges (5 mA g^{-1}) is in 1 M TEA-BF_4 in ACN very similar for all synthesized CDCs (106–116 F g^{-1}). The highest residual capacitance of 72% at high current rates (100 A g^{-1}) was also obtained from the sample with the highest amount of mesopores.

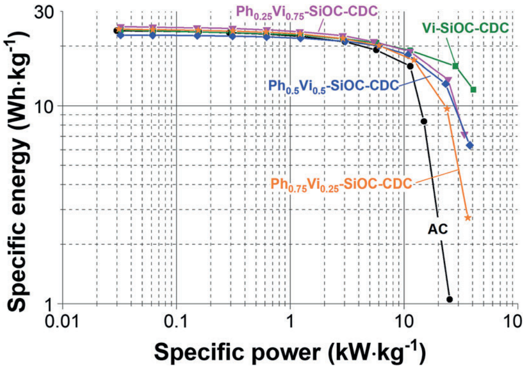

Fig. 8 Ragone chart of the four spherical CDC materials and the AC as comparison, measured in 1 M TEA-BF_4 in ACN (electrode thickness: 110–130 μm).

The Ragone chart (Fig. 8) illustrates the specific energy of the CDC materials of 25 W h kg^{-1} at low specific powers and the excellent performance at high specific power. In the best case (Vi-SiOC-CDC), the specific energy only decreases slightly to 12 W h kg^{-1} at high specific powers of 41 kW kg^{-1}. For comparison: AC shows a very low rate handling ability with only 1 W h kg^{-1} at 25 kW kg^{-1} (which is lower than any of the samples studied in this work). The low wettability of the relatively graphitic carbons is unfavorable for aqueous electrolytes, but a long-time testing shows an increase of the specific capacitance of almost 30% when floated at 1.4 V for 100 h. Functional groups are formed by the operation, which improves the wettability as well as the specific capacitance.

In conclusion, the high porosity of the SiOC-CDCs is attractive for electrochemical energy storage with supercapacitors. The excellent rate handling behavior and the high stability in organic electrolyte documents suitability for common supercapacitors.

Acknowledgements

The INM authors kindly acknowledge the continuing support of Prof. Eduard Arzt (INM). We also thank Robert Drumm (INM) for the TGA-MS, Dr Ingrid Grobelsek (INM) for the help with the SEM, Dr Michael Zimmer (UdS) for CP-MAS NMR, and Juhan Lee, Simon Fleischmann, and Nicolas Jäckel (all INM) for fruitful discussions and their support. The INM acknowledges funding from the German Federal Ministry for Research and Education (BMBF) in support of the nanoEES^{3D} project (award number 03EK3013) as part of the strategic funding initiative energy storage framework.

References

1 L. Schlapbach and A. Züttel, Hydrogen-Storage Materials for Mobile Applications, *Nature*, 2001, **414**(6861), 353–358.

2 R. E. Morris and P. S. Wheatley, Gasspeicherung in Nanoporösen Materialien, *Angew. Chem.*, 2008, **120**(27), 5044–5059.

3 A. Taguchi and F. Schüth, Ordered Mesoporous Materials in Catalysis, *Microporous Mesoporous Mater.*, 2005, **77**(1), 1–45.

4 P. Simon and Y. Gogotsi, Materials for Electrochemical Capacitors, *Nat. Mater.*, 2008, **7**(11), 845–854.

5 M. Lu, F. Beguin, E. Frackowiak, *Supercapacitors: Materials, Systems and Applications*, John Wiley & Sons, 2013.

6 M. Salanne, B. Rotenberg, K. Naoi, K. Kaneko, P.-L. Taberna, C. P. Grey, B. Dunn and P. Simon, Efficient Storage

Mechanisms for Building Better Supercapacitors, *Nat. Energy*, 2016, **1**, 16070.

7 V. Presser, M. Heon and Y. Gogotsi, Carbide-Derived Carbons–From Porous Networks to Nanotubes and Graphene, *Adv. Funct. Mater.*, 2011, **21**(5), 810–833.

8 R. Dash, G. Yushin and Y. Gogotsi, Synthesis, Structure and Porosity Analysis of Microporous and Mesoporous Carbon Derived from Zirconium Carbide, *Microporous Mesoporous Mater.*, 2005, **86**(1), 50–57.

9 S.-H. Yeon, P. Reddington, Y. Gogotsi, J. E. Fischer, C. Vakifahmetoglu and P. Colombo, Carbide-Derived-Carbons with Hierarchical Porosity from a Preceramic Polymer, *Carbon*, 2010, **48**(1), 201–210.

10 C. Vakifahmetoglu, V. Presser, S.-H. Yeon, P. Colombo and Y. Gogotsi, Enhanced Hydrogen and Methane Gas Storage of Silicon Oxycarbide Derived Carbon, *Microporous Mesoporous Mater.*, 2011, **144**(1), 105–112.

11 V. Presser, J. McDonough, S.-H. Yeon and Y. Gogotsi, Effect of Pore Size on Carbon Dioxide Sorption by Carbide Derived Carbon, *Energy Environ. Sci.*, 2011, **4**(8), 3059–3066.

12 S. Welz, M. J. McNallan and Y. Gogotsi, Carbon Structures in Silicon Carbide Derived Carbon, *J. Mater. Process. Technol.*, 2006, **179**(1), 11–22.

13 A. Tolosa, B. Krüner, N. Jäckel, M. Aslan, C. Vakifahmetoglu and V. Presser, Electrospinning and Electrospraying of Silicon Oxycarbide-Derived Nanoporous Carbon for Supercapacitor Electrodes, *J. Power Sources*, 2016, **313**, 178–188.

14 V. Bakumov, M. Schwarz and E. Kroke, Emulsion Processing and Size Control of Polymer-Derived Spherical Si/C/O Ceramic Particles, *Soft Mater.*, 2007, **4**(2–4), 287–299.

15 M. Oschatz, M. Zeiger, N. Jäckel, P. Strubel, L. Borchardt, R. Reinhold, W. Nickel, J. Eckert, V. Presser and S. Kaskel, Emulsion Soft Templating of Carbide-Derived Carbon Nanospheres with Controllable Porosity for Capacitive Electrochemical Energy Storage, *J. Mater. Chem. A*, 2015, **3**(35), 17983–17990.

16 A. Guo, M. Roso, M. Modesti, J. Liu and P. Colombo, Preceramic Polymer-Derived SiOC Fibers by Electrospinning, *J. Appl. Polym. Sci.*, 2014, **131**(3), 39836.

17 S. A. Khan, A. Günther, M. A. Schmidt and K. F. Jensen, Microfluidic Synthesis of Colloidal Silica, *Langmuir*, 2004, **20**(20), 8604–8611.

18 N. Jongen, M. Donnet, P. Bowen, J. Lemaître, H. Hofmann, R. Schenk, C. Hofmann, M. Aoun-Habbache, S. Guillemet-Fritsch and J. Sarrias, Development of a Continuous Segmented Flow Tubular Reactor and the "Scale-out" Concept–In Search of Perfect Powders, *Chem. Eng. Technol.*, 2003, **26**(3), 303–305.

19 B. Penth, Kontinuierliche Fällung von Nanoskaligen Produkten in Mikroreaktoren, German Patent DE102006004350 A1, 2007.

20 B. Dittert, A. Gavrilović, S. Schwarz, P. Angerer, H. Steiner and R. Schöftner, Phase Content Controlled TiO_2 Nanoparticles using the MicroJetReactor Technology, *J. Eur. Ceram. Soc.*, 2011, **31**(14), 2475–2480.

21 A. Rüfer, K. Räuchle, F. Krahl and W. Reschetilowski, Kontinuierliche Darstellung von Bariumsulfat-Nanopartikeln im MicroJet-Reaktor, *Chem. Ing. Tech.*, 2009, **81**(12), 1949–1954.

22 A. Betke and G. Kickelbick, Bottom-Up, Wet Chemical Technique for the Continuous Synthesis of Inorganic Nanoparticles, *Inorganics*, 2014, **2**(1), 1–15.

23 A. Matsuda, T. Sasaki, K. Hasegawa, M. Tatsumisago and T. Minami, Thermal Softening Behavior of Poly (Phenylsilsesquioxane) and Poly (Benzylsilsesquioxane) Particles, *J. Ceram. Soc. Jpn.*, 2000, **108**(1261), 830–835.

24 K. Katagiri, K. Hasegawa, A. Matsuda, M. Tatsumisago and T. Minami, Preparation of Transparent Thick Films by Electrophoretic Sol-Gel Deposition Using Phenyltriethoxysilane-Derived Particles, *J. Am. Ceram. Soc.*, 1998, **81**(9), 2501–2503.

25 C. A. Schneider, W. S. Rasband and K. W. Eliceiri, NIH Image to ImageJ: 25 Years of Image Analysis, *Nat. Methods*, 2012, **9**(7), 671.

26 G. Y. Gor, M. Thommes, K. A. Cychosz and A. V. Neimark, Quenched Solid Density Functional Theory Method for Characterization of Mesoporous Carbons by Nitrogen Adsorption, *Carbon*, 2012, **50**(4), 1583–1590.

27 S. Brunauer, P. H. Emmett and E. Teller, Adsorption of Gases in Multimolecular Layers, *J. Am. Chem. Soc.*, 1938, **60**(2), 309–319.

28 D. Weingarth, M. Zeiger, N. Jäckel, M. Aslan, G. Feng and V. Presser, Graphitization as a Universal Tool to Tailor the Potential-Dependent Capacitance of Carbon Supercapacitors, *Adv. Energy Mater.*, 2014, **4**(13), 1400316.

29 R. K. Sharma, S. Das and A. Maitra, Surface Modified Ormosil Nanoparticles, *J. Colloid Interface Sci.*, 2004, **277**(2), 342–346.

30 A. Arkhireeva and J. N. Hay, Synthesis of Sub-200 nm Silsesquioxane Particles using a Modified Stöber Sol–Gel Route, *J. Mater. Chem.*, 2003, **13**(12), 3122–3127.

31 J. Macan, K. Tadanaga and M. Tatsumisago, Influence of Copolymerization with Alkyltrialkoxysilanes on Condensation and Thermal Behaviour of Poly (Phenylsilsesquioxane) Particles, *J. Sol-Gel Sci. Technol.*, 2010, **53**(1), 31–37.

32 J. F. Brown Jr, L. H. Vogt Jr, A. Katchman, J. W. Eustance, K. M. Kiser and K. W. Krantz, Double Chain Polymers of Phenylsilsesquioxane, *J. Am. Chem. Soc.*, 1960, **82**(23), 6194–6195.

33 Z. Li, X. Cao, H. Xu, P. Xie, M. Cao and R. Zhang, Synthesis and Characterization of Reactive Ladderlike Polyallylsilsesquioxane and Polyvinylsilsesquioxane, *React. Funct. Polym.*, 1999, **39**(1), 1–7.

34 P. Scherrer, Bestimmung der Größe und der inneren Struktur von Kolloidteilchen mittels Röntgenstrahlen, *Nachrichten von der Gesellschaft der Wissenschaften zu Göttingen*, 1918, **2**, 3.

35 S.-S. Choi, A. S. Lee, S. S. Hwang and K.-Y. Baek, Structural Control of Fully Condensed Polysilsesquioxanes: Ladderlike vs Cage Structured Polyphenylsilsesquioxanes, *Macromolecules*, 2015, **48**(17), 6063–6070.

36 A. C. Ferrari and J. Robertson, Interpretation of Raman Spectra of Disordered and Amorphous Carbon, *Phys. Rev. B: Condens. Matter Mater. Phys.*, 2000, **61**(20), 14095.

37 V. Presser, L. Zhang, J. J. Niu, J. McDonough, C. Perez, H. Fong and Y. Gogotsi, Flexible Nano-felts of Carbide-Derived Carbon with Ultra-high Power Handling Capability, *Adv. Energy Mater.*, 2011, **1**(3), 423–430.

38 Y. Gao, V. Presser, L. Zhang, J. J. Niu, J. K. McDonough, C. R. Pérez, H. Lin, H. Fong and Y. Gogotsi, High Power Supercapacitor Electrodes Based on Flexible TiC-CDC Nano-felts, *J. Power Sources*, 2012, **201**, 368–375.

39 A. Scarmi, G. D. Sorarù and R. Raj, The Role of Carbon in Unexpected Visco (an) Elastic Behavior of Amorphous Silicon Oxycarbide Above 1273K, *J. Non-Cryst. Solids*, 2005, **351**(27), 2238–2243.

40 H.-J. Kleebe and Y. D. Blum, SiOC Ceramic with High Excess Free Carbon, *J. Eur. Ceram. Soc.*, 2008, **28**(5), 1037–1042.

41 N. Jäckel, D. Weingarth, A. Schreiber, B. Krüner, M. Zeiger, A. Tolosa, M. Aslan and V. Presser, Performance Evaluation of Conductive Additives for Activated Carbon Supercapacitors in Organic Electrolyte, *Electrochim. Acta*, 2016, **191**, 284–298.

42 C. R. Pérez, S. H. Yeon, J. Ségalini, V. Presser, P. L. Taberna, P. Simon and Y. Gogotsi, Structure and Electrochemical Performance of Carbide-Derived Carbon Nanopowders, *Adv. Funct. Mater.*, 2013, **23**(8), 1081–1089.

43 D. Weingarth, H. Noh, A. Foelske-Schmitz, A. Wokaun and R. Kötz, A Reliable Determination Method of Stability Limits for Electrochemical Double Layer Capacitors, *Electrochim. Acta*, 2013, **103**, 119–124.

44 D. Weingarth, A. Foelske-Schmitz and R. Kötz, Cycle versus Voltage Hold–Which is the better Stability Test for Electrochemical Double Layer Capacitors?, *J. Power Sources*, 2013, **225**, 84–88.

45 J. Busom, A. Schreiber, A. Tolosa, N. Jäckel, I. Grobelsek, N. J. Peter and V. Presser, Sputtering of Sub-Micrometer Aluminum Layers as Compact, High-Performance, Light-Weight Current Collector for Supercapacitors, *J. Power Sources*, 2016, **329**, 432–440.

46 M. Bichat, E. Raymundo-Piñero and F. Béguin, High Voltage Supercapacitor Built with Seaweed Carbons in Neutral Aqueous Electrolyte, *Carbon*, 2010, **48**(15), 4351–4361.

47 J. Lee, D. Weingarth, I. Grobelsek and V. Presser, Use of Surfactants for Continuous Operation of Aqueous Electrochemical Flow Capacitors, *Energy Technol.*, 2016, **4**(1), 75–84.

48 K. Fic, G. Lota and E. Frackowiak, Effect of Surfactants on Capacitance Properties of Carbon Electrodes, *Electrochim. Acta*, 2012, **60**, 206–212.

49 M. Aslan, D. Weingarth, P. Herbeck-Engel, I. Grobelsek and V. Presser, Polyvinylpyrrolidone/Polyvinyl Butyral Composite as a Stable Binder for Castable Supercapacitor Electrodes in Aqueous Electrolytes, *J. Power Sources*, 2015, **279**, 323–333.

50 J. Lee, S. Kim and J. Yoon, Rocking Chair Desalination Battery Based on Prussian Blue Electrodes, *ACS Omega*, 2017, **2**(4), 1653–1659.

51 K. Fic, M. Meller, J. Menzel and E. Frackowiak, Around the Thermodynamic Limitations of Supercapacitors Operating in Aqueous Electrolytes, *Electrochim. Acta*, 2016, **206**, 496–503.

52 E. Frackowiak and F. Beguin, Electrochemical Storage of Energy in Carbon Nanotubes and Nanostructured Carbons, *Carbon*, 2002, **40**(10), 1775–1787.

53 J. Lee, A. Tolosa, B. Krüner, N. Jäckel, S. Fleischmann, M. Zeiger, D. Kim and V. Presser, Asymmetric Tin–Vanadium Redox Electrolyte for Hybrid Energy Storage with Nanoporous Carbon Electrodes, *Sustainable Energy Fuels*, 2017, **1**, 9.

54 J. Lee, B. Krüner, A. Tolosa, S. Sathyamoorthi, D. Kim, S. Choudhury, K.-H. Seo and V. Presser, Tin/Vanadium Redox Electrolyte for Battery-like Energy Storage Capacity Combined with Supercapacitor-like Power Handling, *Energy Environ. Sci.*, 2016, **9**(11), 3392–3398.

55 N. Jäckel, D. Weingarth, M. Zeiger, M. Aslan, I. Grobelsek and V. Presser, Comparison of Carbon Onions and Carbon Blacks as Conductive Additives for Carbon Supercapacitors in Organic Electrolytes, *J. Power Sources*, 2014, **272**, 1122–1133.

56 M. Aslan, M. Zeiger, N. Jäckel, I. Grobelsek, D. Weingarth and V. Presser, Improved Capacitive Deionization Performance of Mixed Hydrophobic/Hydrophilic Activated Carbon Electrodes, *J. Phys.: Condens. Matter*, 2016, **28**(11), 114003.

57 B. Krüner, P. Srimuk, S. Fleischmann, M. Zeiger, A. Schreiber, M. Aslan, A. Quade and V. Presser, Hydrogen-treated, Sub-micrometer Carbon Beads for Fast Capacitive Deionization with High Performance Stability, *Carbon*, 2017, **117**, 46–54.

58 A. Kolodziej, K. Fic and E. Frackowiak, Towards Sustainable Power Sources: Chitin-Bound Carbon Electrodes for Electrochemical Capacitors, *J. Mater. Chemi. A*, 2015, **3**(45), 22923–22930.

59 M. Zeiger, N. Jäckel, D. Weingarth and V. Presser, Vacuum or Flowing Argon: What is the Best Synthesis Atmosphere for Nanodiamond-Derived Carbon Onions for Supercapacitor Electrodes?, *Carbon*, 2015, **94**, 507–517.

60 C. Schneidermann, N. Jäckel, S. Oswald, L. Giebeler, V. Presser and L. Borchardt, Solvent-Free Mechanochemical Synthesis of Nitrogen-Doped Nanoporous Carbon for Electrochemical Energy Storage, *ChemSusChem*, 2017, **10**(11), 2416–2424.

SUPPORTING INFORMATION

Carbide-derived carbon beads with tunable nanopores from continuously produced polysilsesquioxanes for supercapacitor electrodes

Benjamin Krüner,[1,2,†] Christina Odenwald,[3,†] Aura Tolosa,[1,2] Anna Schreiber,[1]
Mesut Aslan,[1] Guido Kickelbick,[3,*] and Volker Presser[1,2,*]

[1] *INM - Leibniz Institute for New Materials, 66123 Saarbrücken, Germany*

[2] *Department of Materials Science and Engineering, Saarland University, 66123 Saarbrücken, Germany*

[3] *Inorganic Solid State Chemistry, Saarland University, 66123 Saarbrücken, Germany*

[†] *these authors contributed equally*

* *Corresponding authors' eMails:*
guido.kickelbick@uni-saarland.de *(G. Kickelbick);* volker.presser@leibniz-inm.de *(V. Presser)*

Table S1: Properties of the PTFE-bound electrodes.

	Electrode density (mg·cm^{-3})	**Active mass of one electrode (mg)**	**Electrode disc diameter (mm)**	**Electrode thickness (µm)**
		1 M TEA-BF$_4$ in acetonitrile		
Vi-SiOC-CDC	197	1.15	8	122
Ph$_{0.25}$Vi$_{0.75}$-SiOC-CDC	372	2.33	8	131
Ph$_{0.5}$Vi$_{0.5}$-SiOC-CDC	452	2.51	8	116
Ph$_{0.75}$Vi$_{0.25}$-SiOC-CDC	438	2.41	8	115
AC	435	2.27	8	109
		Aqueous 1 M Na$_2$SO$_4$		
Vi-SiOC-CDC	206	1.47	8	150
Ph$_{0.25}$Vi$_{0.75}$-SiOC-CDC	377	2.24	8	124
Ph$_{0.5}$Vi$_{0.5}$-SiOC-CDC	450	2.51	8	117
Ph$_{0.75}$Vi$_{0.25}$-SiOC-CDC	432	2.44	8	118

Table S2: Porosity of the Vi-SiOC-CDC electrodes measured with nitrogen gas sorption.

	SSA$_{DFT}$ (m^2·g^{-1})	**SSA$_{DFT}$ loss after voltage floating (%)**	**SSA$_{BET}$ (m^2·g^{-1})**	**Total pore volume (cm^3·g^{-1})**	**Total pore volume loss after voltage floating (%)**	**Average pore size (nm)**
Vi-SiOC-CDC initial electrode	1756	-	2287	1.83	-	2.5
Vi-SiOC-CDC negative electrode	980	44	1515	1.23	34	2.6
Vi-SiOC-CDC positive electrode	897	49	1403	1.19	35	2.8

Table S3: EDX element analysis of Vinyl-SiOC-CDC electrodes before the electrochemical testing and after the voltage floating at 1.4 V for 100 h in aqueous 1 M Na$_2$SO$_4$. Values below the detection limit are denoted n.d. (not detected).

	C (mass%)	**O (mass%)**	**Si (mass%)**	**F (mass%)**	**Na (mass%)**	**S (mass%)**	**Cl (mass%)**
Vi-SiOC-CDC initial electrode	89.5±0.6	4.1±0.3	3.5±0.3	2.9±0.3	n.d.	n.d.	n.d.
Vi-SiOC-CDC positive electrode	81.3±1.3	7.4±1.0	1.6±0.3	3.5±1.1	4.6±0.6	0.7±0.2	0.9±0.2
Vi-SiOC-CDC negative electrode	81.3±0.5	4.4±0.8	2.2±0.1	6.6±1.6	4.4±0.4	0.5±0.1	0.7±0.1

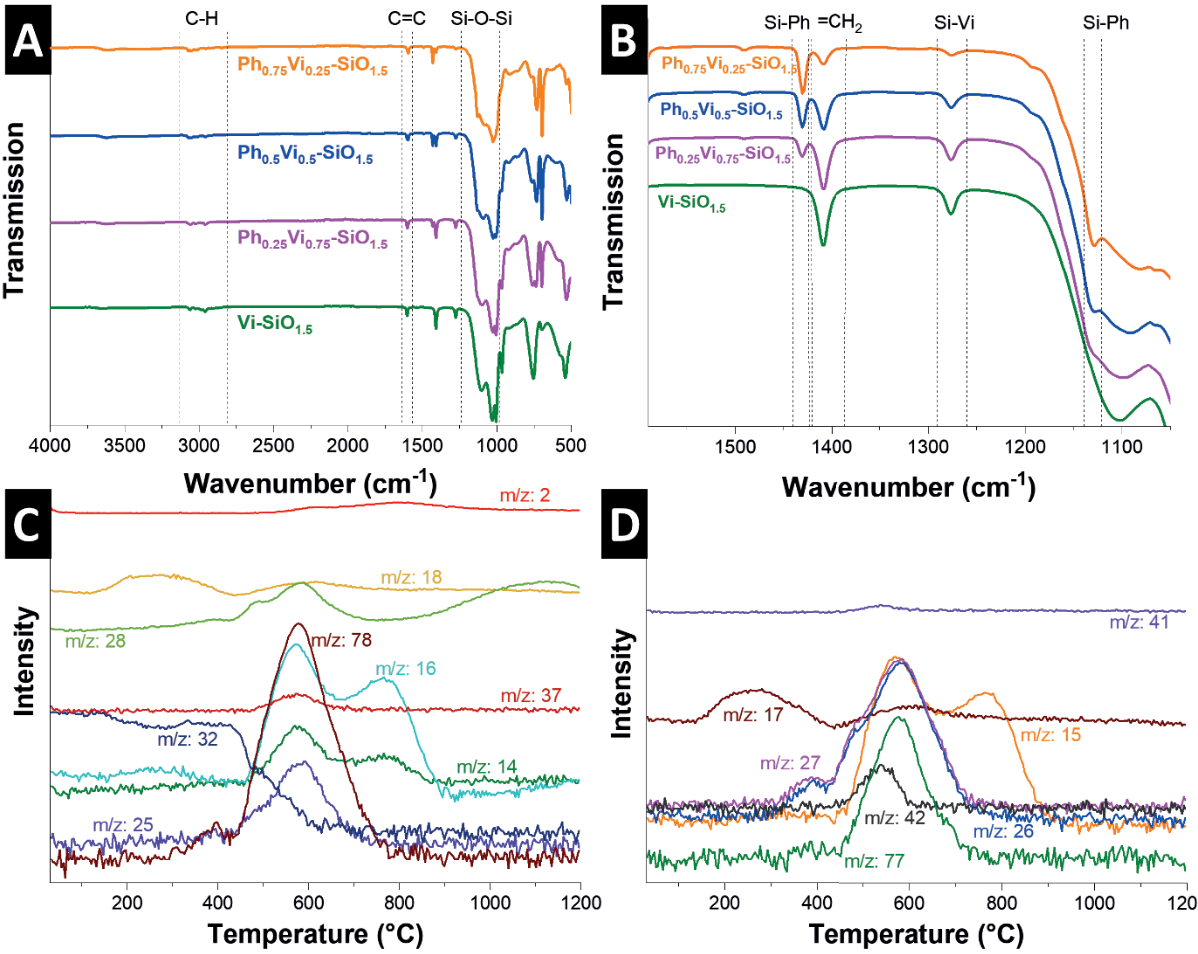

Figure S1: Overview of the FT-IR spectra of the four polymer beads (A) and detailed spectra in the range of 1000-1600 cm^{-1} (B). The corresponding mass spectra of $Ph_{0.5}Vi_{0.5}$-$SiO_{1.5}$ to the thermogram shown in Fig. 2D of relevant evolving groups (C) and (D).

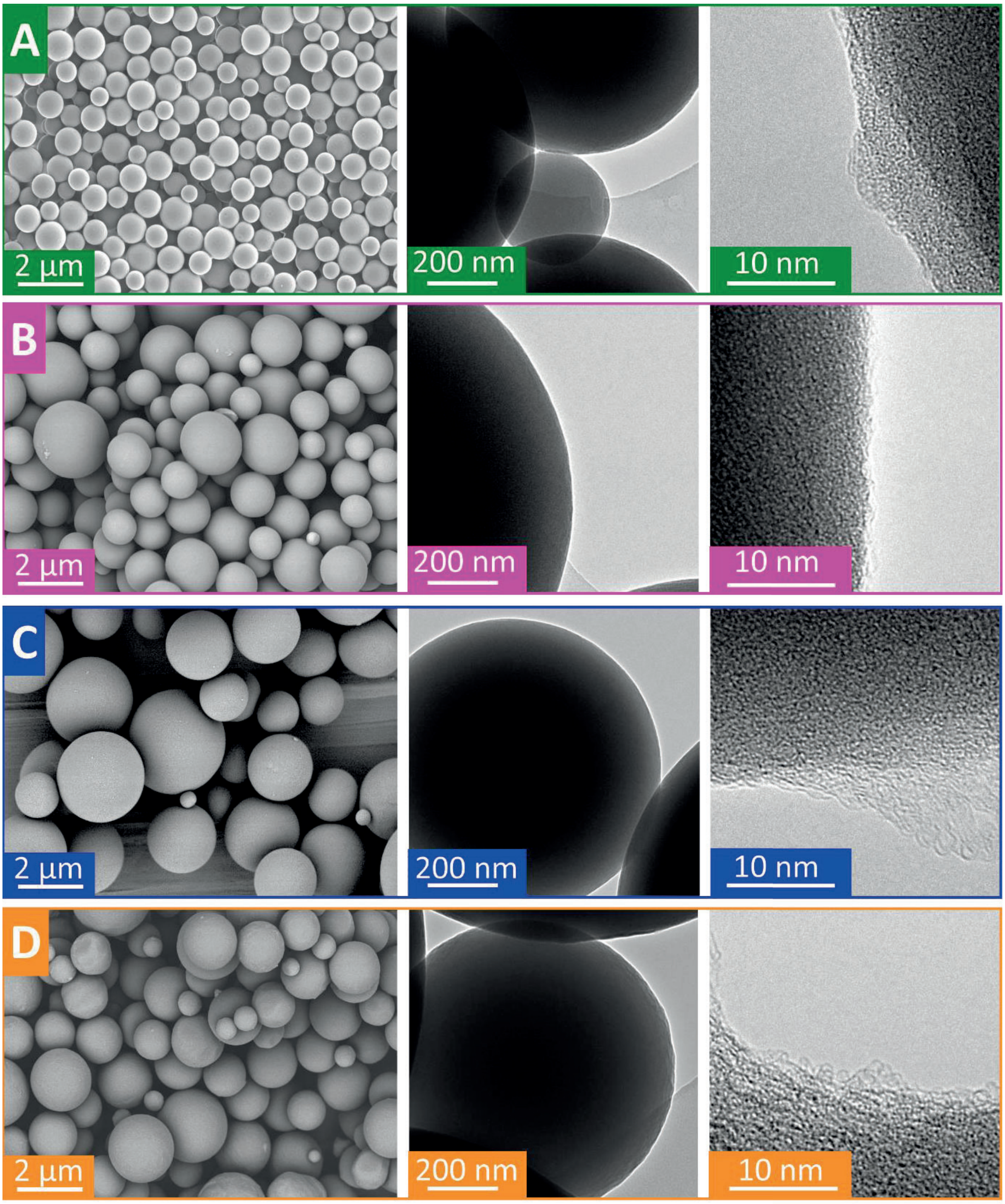

Figure S2: Scanning and transmission electron micrographs of the polymer beads Vi-$SiO_{1.5}$ (A), $Ph_{0.25}Vi_{0.75}$-$SiO_{1.5}$ (B), $Ph_{0.5}Vi_{0.5}$-$SiO_{1.5}$ (C), and $Ph_{0.75}Vi_{0.25}$-$SiO_{1.5}$ (D).

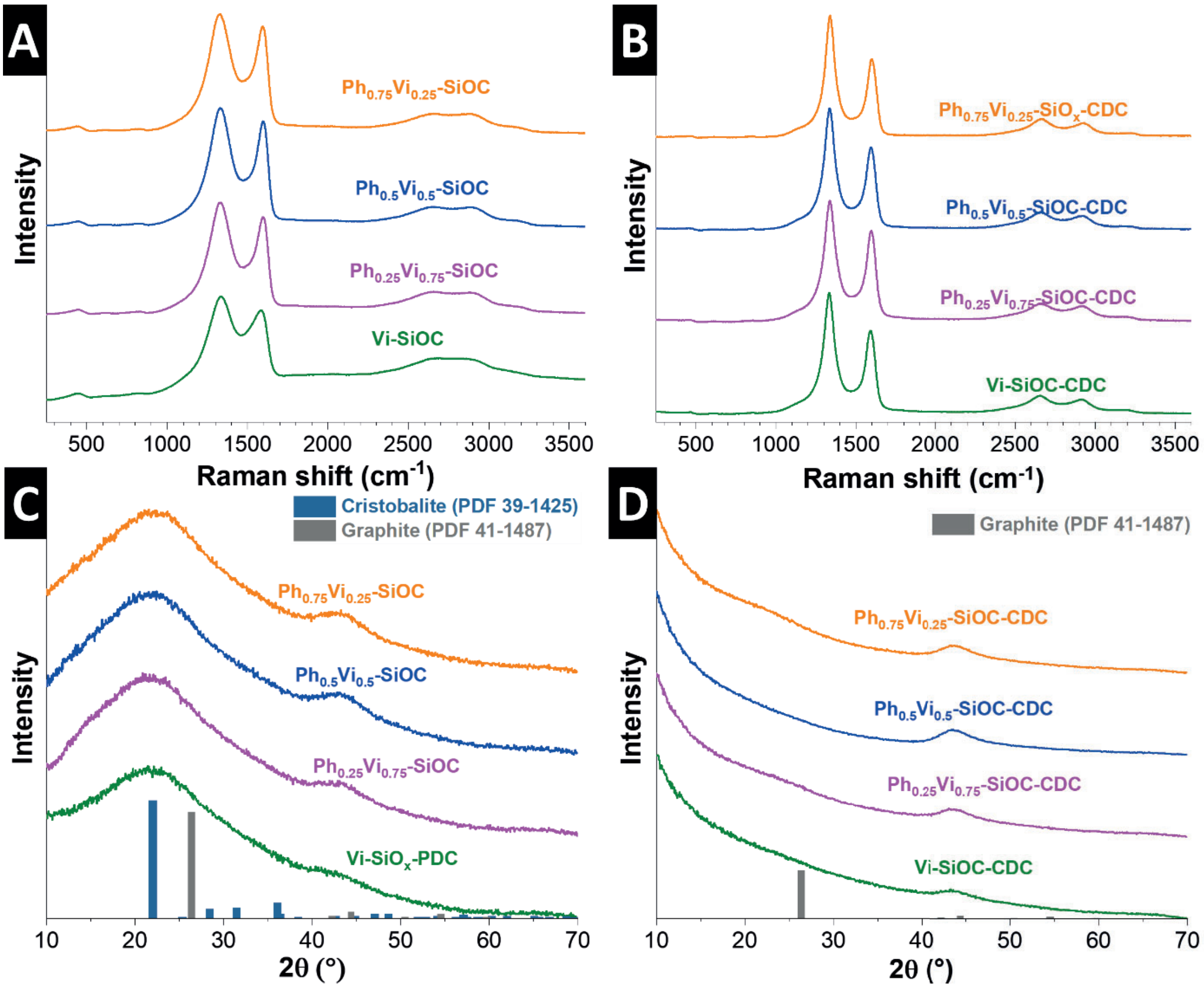

Figure S3: Raman spectra of PDCs (A) and CDCs (B). XRD pattern of PDCs (C) and CDCs (D).

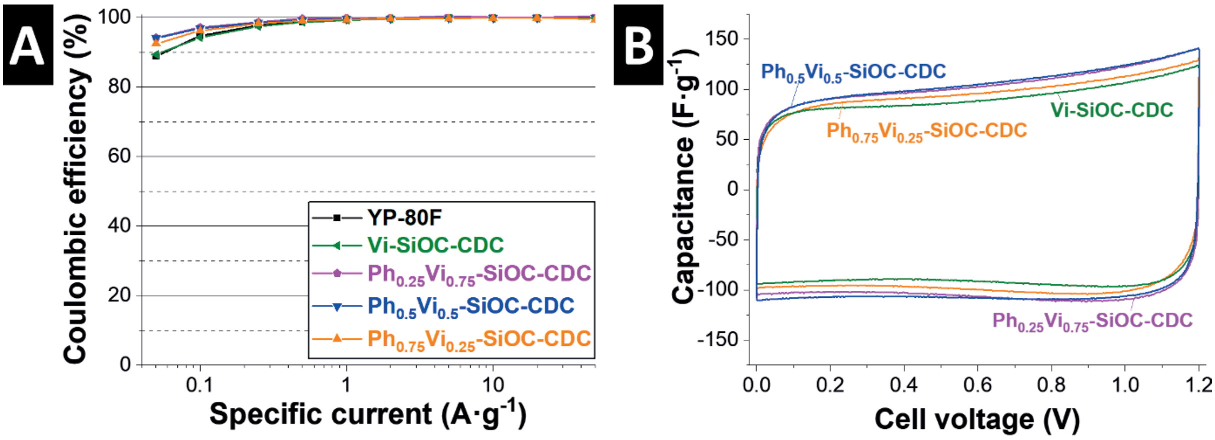

Figure S4: Coulombic efficiencies of all CDC materials including the AC in TEA-BF$_4$ in ACN (A) and cyclic voltammograms of all CDC samples in aqueous 1 M Na$_2$SO$_4$ (B) up to a cell voltage of 1.2 V.

The study confirmed the good suitability of ORMOSIL spheres for the production of energy storage materials. Especially the knowledge that the composition of ORMOSIL can influence the properties of the final product is used for the following study in which a nitrogen doping of the CDC material is aimed.

3.3.3 Influence of nitrogen-doping for carbide-derived carbons on the supercapacitor performance in an organic electrolyte and an ionic liquid

When the following study was carried out, there were different statements in the literature about the effect of nitrogen doping on the performance of the supercapacitor. The use of various materials, synthesis and measurement conditions made it difficult to compare the different studies. Therefore, a possibility was sought to produce CDC materials with similar properties (with respect to particle size, pore size distribution, surface area, etc.) that differ only in their nitrogen content.

The idea was to use a system with phenyl and vinyl groups again, however prepared from slightly modified precursors. The starting molecules 3-(phenylamino)propyl]trimethoxysilane (for N-doping) and 4-phenylbutyltrimethoxysilane (for CDCs without N-doping) turn out to be suitable for this purpose and in the following study, each of them is cocondensed with vinyltrimethoxysilane in the MicroJet reactor. The resulting ORMOSIL particles are converted into CDC beads whereby the resulting nitrogen content also depends on the temperature of the treatment. The properties of the CDC beads as electrode material are tested in different electrolytes.

Contributions:

Christina Odenwald: Planning, synthesis of the polymer particles, discussion, and revision of the manuscript. **Benjamin Krüner**: Design, planning, writing, pyrolysis, chlorine gas treatment, SEM, particle size analysis, EDX analysis, TGA coupled with MS analysis, CO_2 and N_2 sorption analysis, Raman analysis, XRD, and electrochemical analysis for double-layer capacitors. **Antje Quade:** XPS analysis, discussion, and revision of the manuscript. **Guido Kickelbick:** Discussion and revision of the manuscript. **Volker Presser:** Supervision, discussion, and revision of the manuscript.

Krüner, B.; Odenwald, C.; Quade, A.; Kickelbick, G.; Presser, V.: Influence of nitrogen-doping for carbide-derived carbons on the supercapacitor performance in an organic electrolyte and an ionic liquid. *Batteries & Supercaps,* **2018**. *1*. 135–148. https://doi.org/10.1002/batt.201800051

ChemPubSoc Europe
DOI: 10.1002/batt.201800051
BATTERIES & SUPERCAPS
Articles

Influence of Nitrogen-Doping for Carbide-Derived Carbons on the Supercapacitor Performance in an Organic Electrolyte and an Ionic Liquid

Benjamin Krüner,[a] Christina Odenwald,[b] Antje Quade,[c] Guido Kickelbick,*[b] and Volker Presser*[a]

We investigated the influence of nitrogen groups on the electrochemical performance of carbide-derived carbons by comparing materials with a similar pore structure with and without nitrogen-doping. These materials were tested in a half-cell and full-cell supercapacitor setup with a conventional organic electrolyte (1 M tetraethylammonium tetrafluoroborate in acetonitrile) and an ionic liquid (1-ethyl-3-methylimidazolium tetrafluoroborate). Varying the nitrogen content in the range of 1–7 mass% had no systematic influence on the energy storage capacity but a stronger impact on the rate handling ability. The highest specific capacitance in a half-cell supercapacitor at a negative potential was 215 F/g in EMIM-BF_4. Using the best-performing carbide-derived carbon with and without nitrogen-doping (i.e., by applying a synthesis temperature of 800 °C), the full-cell performance was 174 F/g, which results in a high specific energy of 61 Wh/kg in EMIM-BF_4. For the same materials, the corresponding specific energy was about 30 Wh/kg when using the organic electrolyte.

1. Introduction

Supercapacitors are electrochemical energy storage devices for high power applications with long cycling stability.[1–3] The most common type of supercapacitor is the electrical double-layer capacitor (EDLC) where the charge is stored by electrosorption of ions from an electrolyte on a high surface area electrode.[1] Electrodes for EDLCs are usually carbon-based, and various materials have been explored, including activated carbons,[4–6] salt-templated carbons,[7–9] graphene,[10] carbon-nanotubes,[11] carbon onions,[12,13] and carbide-derived carbons (CDC).[14,15] Especially nanoporous carbons with a high surface area are well suited to provide high specific energy and power.[3,16] One way to further increase the energy storage capacity of a porous carbon electrode is to choose an average pore size close to the diameter of the bare ion.[17–19] This effect can be explained by the partial desolvation of the ions in aqueous or organic electrolytes and the resulting more space-effective arrangement of ions within nanopores.[18–22]

Beyond the design of carbon materials with an optimized porosity, there are other ways to enhance the energy storage capacity of supercapacitors.[1,16,23] Examples include the use of ionic liquids[1,7] or redox electrolytes,[5,24–27] and the addition of a redox-active material like metal oxides[28–31] or heteroatom doping.[32] Especially the use of ionic liquids as an electrolyte for supercapacitors is promising because the significantly enhanced potential window leads to a large increase of the specific energy (the latter scales with the square of the voltage).[1] Along with this line of research, Ewert et al. reported that nitrogen-doping of CDC leads to an enhanced specific capacitance for certain ionic liquids, such as EMIM-BF_4, while there was no enhancement for organic electrolytes based on acetonitrile as the solvent.[32] Also, other groups investigated nitrogen-doped carbon materials made from different precursors and reported high specific energy of up to 64 Wh/kg (measured at a cell voltage of 3.2 V).[6,7,33,34] Yan et al. used EMIM-BF_4 as the electrolyte and different micro- and mesoporous carbons as the electrodes in symmetric full-cells.[7] The specific capacitance and rate capability of these porous carbon materials with and without nitrogen-doping (up to 6 mass%) were quite similar, but there was an improvement of the rate capability for the nitrogen-containing electrodes.[7] Yet, the comparison of half-cell and full-cell data complicates the identification of underlying energy storage mechanisms during ion electrosorption, and our understanding of the general role of nitrogen in different forms (pyridinic, graphitic, etc.) remains limited at present.

Due to the influence of the pore size distribution on the double-layer capacitance,[20] it is necessary to produce carbon materials with a similar porosity to investigate the contribution of the nitrogen groups. In a previous study, we applied the MicroJet reactor technique to produce SiOC-CDC and varied the ratio of silanes with different organic groups.[35] Thereby, it

---

[a] B. Krüner, Prof. Dr. V. Presser
INM – Leibniz Institute for New Materials
66123 Saarbrücken, Germany
Department of Materials Science and Engineering
Saarland University
66123 Saarbrücken, Germany
E-mail: volker.presser@leibniz-inm.de
[b] C. Odenwald, Prof. Dr. G. Kickelbick
Inorganic Solid State Chemistry
Saarland University
66123 Saarbrücken, Germany
E-mail: guido.kickelbick@uni-saarland.de
[c] Dr. A. Quade
Leibniz Institute for Plasma Science and Technology
Felix-Hausdorff-Straße 2
17489 Greifswald, Germany

Supporting information for this article is available on the WWW under https://doi.org/10.1002/batt.201800051

was possible to adjust the porosity of the highly porous carbon material. The continuous MicroJet technique ensures a constant quality of polysilsesquioxane beads with homogeneous particle size. In the present study, we used a similar approach but varied the organic group to introduce nitrogen via silane to the ceramic material. Nitrogen in the carbide can still be found in the CDC material after chlorine gas treatment, as we know from previous work.[32] We produced CDCs also with another silane to obtain porous carbon materials without nitrogen with a similar pore size distribution (average pore size of 1.6–1.9 nm and 94–99 % of the pore volume relates to pores smaller than 5 nm). Thereby, our materials cover the range of nitrogen concentration of 0–7 mass %. The materials were tested as electrodes for supercapacitors in half-cell and full-cell configuration in 1 M TEA-BF_4 in acetonitrile (ACN) and neat ionic liquid (EMIM-BF_4).

Experimental

Materials and Material Synthesis

Vinyltrimethoxysilane (VTMS) and 4-phenylbutyltrimethoxysilane (PBTMS) were obtained from ABCR. [3-(phenylamino)propyl]trimethoxysilane (PAPTMS) was purchased from Sigma-Aldrich. The structural formulae of the silanes precursors are shown in the *Supporting Information*, Figure S1. Ammonia was purchased from VWR International. All chemicals were used as received.

The polymer spheres were produced by mixing the precursor solutions A1/A2 and B in a microreactor. Solution A1 contained VTMS (37.04 g, 250 mmol) and PAPTMS (12.81 g, 50 mmol) dissolved in methanol (307.58 g, 9.6 mol). For the A2 solution, PBTMS (12.76 g, 50 mmol) was used instead of PAPTMS. The alkoxysilanes were partly hydrolyzed by adding aqueous HCl (150 mL of a 0.55 mmol/L solution) and stirring at room temperature for 16 h.[36] The solution B was an aqueous solution of ammonia (2.2 mol/L).

The synthesis of similar particles with the same technical setup is described in detail in previous work.[35,36] In short: two HPLC pumps (LaPrep P110 preparative HPLC pumps, VWR International) transport solution A1 or A2 and solution B at a rate of 250 mL/min (pressure of 3–4 MPa) to the MicroJet reactor (Synthesechemie Dr. Penth GmbH). The solutions enter the reactor chamber through narrow nozzles (300 μm in diameter) from opposing sites and collide inside as fine impinging jets. A fast mixing takes place before a support gas flow forces the suspension out of the microreactor in vertical direction out to a collecting vessel. The particles were separated by centrifugation (8000 rpm, 7012 G, 10 min) and dried in vacuum at room temperature. The reactor system was flushed with methanol between the production of different samples.

The pyrolysis of the polysilsesquioxane beads was carried out in a graphite heated furnace (LHTG from Carbolite Gero) in a nitrogen atmosphere with a gas flow of 150 L/h. The target temperature of 1000 °C was reached with a heating rate of 300 °C/h, and we used a holding time of 2 h. A mass of 1.5 g of the obtained polymer-derived ceramic (PDC) was transferred to a graphite crucible and placed in a quartz tube furnace from Carbolite Gero. The chlorine gas treatment to produce carbide-derived carbon (CDC) spheres was performed at 600 °C, 800 °C, or 1000 °C for 5 h with a chlorine gas flow of 10 cm^3/min. The quartz tube furnace was constantly supplied with argon (flow: 50 cm^3/min) during the chlorine gas treatment including the heating and cooling step. A hydrogen treatment at 600 °C for 3 h was conducted after the chlorination step to remove residual chlorine from the surface. We labeled the three non-doped SiOC-CDC materials as CDC-600, CDC-800, and CDC-1000, depending on the chlorination temperature. Accordingly, we labeled the nitrogen-containing CDCs as N-CDC-600, N-CDC-800, and N-CDC-1000.

Material Characterization

The carbon beads were analyzed with a field emission scanning electron microscope (SEM) Jeol JSM-7500F at 3 kV and a high-resolution transmission electron microscopy (TEM) Jeol JEM-2100F at 200 kV. We quantified the bead diameter of 150 individual particles with the image analysis software ImageJ.[37] For TEM measurements, the samples were dispersed and sonicated in ethanol to deposit them on a lacey carbon film on a copper grid from Gatan.

The porosity of the mainly microporous materials was analyzed via nitrogen gas sorption analysis (N_2 GSA) and carbon dioxide gas sorption analysis (CO_2 GSA) with an Autosorb iQ system from Quantachrome. The powder samples were outgassed before the measurement at 10 kPa at 200 °C for 1 h and at 300 °C for 20 h. To avoid any issue with the presence of the polymer binder polytetrafluoroethylene (PTFE), the electrodes were pretreated at 10 kPa first at 100 °C for 1 h and then at 150 °C for 20 h. The N_2 GSA measurements were carried out in a relative pressure range from $5\cdot10^{-6}$ to 1 at $-196\,^{\circ}C$. The measurement temperature for the CO_2 GSA was 0 °C, and the relative pressure was in the range of $7\cdot10^{-5}$ to $1\cdot10^{-2}$. The specific surface area was calculated with the Brunauer-Emmett-Teller equation in the linear regime of the N_2 isotherm.[38] We further analyzed the pore structure by applying a quenched-solid density functional theory (QSDFT) kernel assuming slit-like carbon nanopores.[39] A non-local density functional theory (NLDFT) assuming the same pore geometry was used to deconvolute the CO_2 isotherm.[40] The BET and DFT calculations were performed with the software ASiQwin from Quantachrome. The pore size distributions obtained from N_2 and CO_2 GSA measurements were combined with a cross-over point at 0.9 nm to obtain a pore size distribution in the range from 0.35 nm to 35 nm.[41] The total pore volume and the SSA_{DFT} values were obtained by combining the pore size distribution data of the CO_2 and N_2 GSA measurements; the average pore size corresponds to the pore diameter of the half of the total pore volume (d_{50}) of the cumulative pore size distribution.[41] For all GSA measurements, a sufficient time at each pressure increment was obtained so that a near-equilibrium was obtained, which is important to obtain a reliable combined pore size distribution pattern (as pointed out by Lobato et al.[42]).

The structure of the carbon materials was investigated via Raman spectroscopy. We used a Renishaw inVia Raman microscope with a wavelength of 532 nm and a grating of 2400 lines/mm. The spectral resolution was 1.2 cm^{-1}, the numeric aperture 0.75, and the incident power on the sample ~0.2 mW. The recording time was 30 s, and 10 accumulations were accomplished. Four Voigt functions were chosen to fit the D- and G-mode of the Raman spectra.

The chemical composition was quantified with a CHNS analyzer Vario Micro Cube from Elementar. The temperature for the tube was 850 °C and for the combustion tube 1150 °C. The equipment was calibrated with sulfanilamide. The oxygen content was obtained with a rapid OXY cube from Elementar. The analysis temperature was 1450 °C, and it was calibrated with benzoic acid.

The chemical composition of the materials was also quantified by use of X-ray photoelectron spectroscopy (XPS). We used an Axis Ultra DLD from Kratos Analytical with Al K_α radiation at a high voltage 15 kV and current of 10 mA to acquire survey spectra at a pass energy of 80 eV. The current was increased to 15 mA for the highly resolved measurement of the C 1s and N 1s peaks at a pass energy of 10 eV. The XPS spectra were analyzed with the software CasaXPS and charged corrected by shifting all peaks to the aliphatic C 1s spectral component set to a binding energy of 285 eV. The Shirley background was subtracted before fitting the peaks with a Gaussian-Lorentzian (GL(30)) profile function. The carbon peaks were fitted with a constant full-width-at-half-maximum (FWHM). An asymmetric line shape was used for the sp^2-hybridized carbon component, which is well-described by the Doniach-Šunjić function.[43,44]

Electrochemical Measurements

The synthesized carbon powders were mixed with 5 mass% of PTFE binder (60 mass% in water, Sigma-Aldrich) and crushed in a mortar to form a doughy paste. The carbon paste was rolled to free-standing films with a thickness of ~100 μm and we dried the electrodes at 120 °C and 2 kPa for 48 h. Discs with a diameter of 10 mm and a mass of 2–4 mg were punched from the casted electrodes for the electrochemical measurements. The electrodes were tested in a half-cell figuration with YP-80F as a counter electrode (>5 times heavier) and YP-50F from Kuraray as a reference electrode in a custom-built cell.[45] For electrochemical characterization, we used either an organic electrolyte (1 M tetraethylammonium tetrafluoroborate, TEA-BF_4, in acetonitrile, ACN) or a neat ionic liquid (1-ethyl-3-methylimidazolium tetrafluoroborate, EMIM-BF_4). The cells were loaded with the electrolyte in an argon-filled glove box (O_2, $H_2O \leq 1$ ppm) and placed in a vacuum oven (2 kPa) at 120 °C to remove adsorbed moisture for 16 h. A carbon coated aluminum foil (Zflo 2653, Coveris Advanced Coatings) was used as a current collector, and we employed a glass-fiber mat (GF/A from Whatman, GE Healthcare Life Science) as a separator for all measurements with a potentiostat/galvanostat VMP300 from Bio-Logic. The cyclic voltammetry (CV) was conducted at 10 mV/s and the galvanostatic cycling with potential limitation (GCPL) with a 10 min holding step at each potential for the half-cells. The specific capacitance was calculated following Eq. (1):

$$C_{sp} = \frac{\int_{t_0}^{t_{end}} I dt}{\Delta U \cdot m} \tag{1}$$

with specific capacitance C_{sp}, starting time of discharge t_0, end of discharge time t_{end}, applied potential difference ΔU, discharge current I and active mass of the working electrode m.

The limits for the positive and negative potential window of the samples CDC-800 and N-CDC-800 were investigated in the organic electrolyte and ionic liquid via S-value analysis in a half-cell configuration. The cyclic voltammetry was tested in a potential range of ±(0.2–2.5) V vs. carbon with intervals of 0.05 V and a scan rate of 1 mV/s. The S-values were calculated with Eq. (2).

$$S = \frac{Q_{charge}}{Q_{discharge}} - 1 \tag{2}$$

with S for S-value, Q_{charge} and $Q_{\mathrm{discharge}}$ for the charge during charge and discharge.

Was also measured the sample with the highest specific capacitance with and without nitrogen in a symmetrical full-cell supercapacitor device with YP-50F from Kuraray as a quasi-reference.[46] The capacitance from cyclic voltammograms was calculated with Eq. (3) and from GCPL cycling with Eq. (4). The IR-drop of the GCPL measurements was obtained after a resting time of 10 s.

$$C_{sp} = \frac{4 \cdot I}{\frac{dU}{dt} \cdot m} \tag{3}$$

with C_{sp} as the specific capacitance per electrode, I as the current, dU/dt as the scan rate, and m as the mass of carbon in the electrode (e.g., mass of the electrode without the polymer binder).

$$C_{sp} = \frac{4 \cdot Q_{discharge}}{U \cdot m} \tag{4}$$

with C_{sp} as the specific capacitance per electrode, $Q_{\mathrm{discharge}}$ as the charge of the discharging half-cycle, U as the IR-drop corrected cell voltage, and m as the mass of carbon in the electrode.

Stability testing via voltage floating[47] for 100 h was also conducted in a temperature-controlled environment at 25 °C at 2.7 V for the organic electrolyte and 3.2 V for the ionic liquid. These cell voltages were chosen based on the results of the S-value analysis. Every 10 h, galvanostatic cycling was performed at a cell voltage of 2.5 V (organic solvent-based electrolyte) or 3.2 V (ionic liquid).

2. Results and Discussion

2.1. Characterization of the Carbide-Derived Carbon Beads

The spherical shape of the synthesized materials after chlorine gas treatment is exemplified for CDC-800 and N-CDC-800 by scanning and transmission electron micrographs (Figure 1). SEM images of the other samples are shown in Figure S2. Transmission electron micrographs (Figure 1C,D,G,H) document the disordered nature of the carbon structure. Quantitative SEM image analysis revealed no major influence of the chlorination temperature on the volume dependent sphere diameter which all are about 1–2 μm (Table S1). All samples showed a mass loss of 24% after the pyrolysis, and 91–95% of the residual mass is lost after the chlorine gas treatment (Table S1). Thereby, when we compare the initial and final mass, there is a mass loss of 93–96%, which aligns with the low amount of aromatic groups in the precursor.[35]

We used a combination of CO_2 and N_2 gas sorption to characterize the micro- and mesopores of the samples (Figure 2, Table 1, Figure S3, S4).[20,41] All samples showed a well-developed porosity after chlorine gas treatment with a predominance of micropores, as inferred from the type I nitrogen sorption isotherms (Figure 2A,B).[48] Only the data of sample CDC-1000 shows a type IV isotherm with a large hysteresis caused by mesopores.[48] In accordance with previous works,[49,50] we see the lowest SSA_{DFT} for samples produced at 600 °C with 1740 m^2/g for CDC-600 and 1416 m^2/g for N-CDC-600. By increasing the annealing temperature to 800 °C during the chlorine gas treatment, the SSA_{DFT} of the resulting CDC material increased to 2163 m^2/g for CDC-800 and 2133 m^2/g for N-CDC-800. A further increase of the synthesis temperature increased the SSA_{DFT} to 2320 m^2/g for CDC-1000 and 2206 m^2/g for N-CDC-1000. In addition to the surface area, also the total

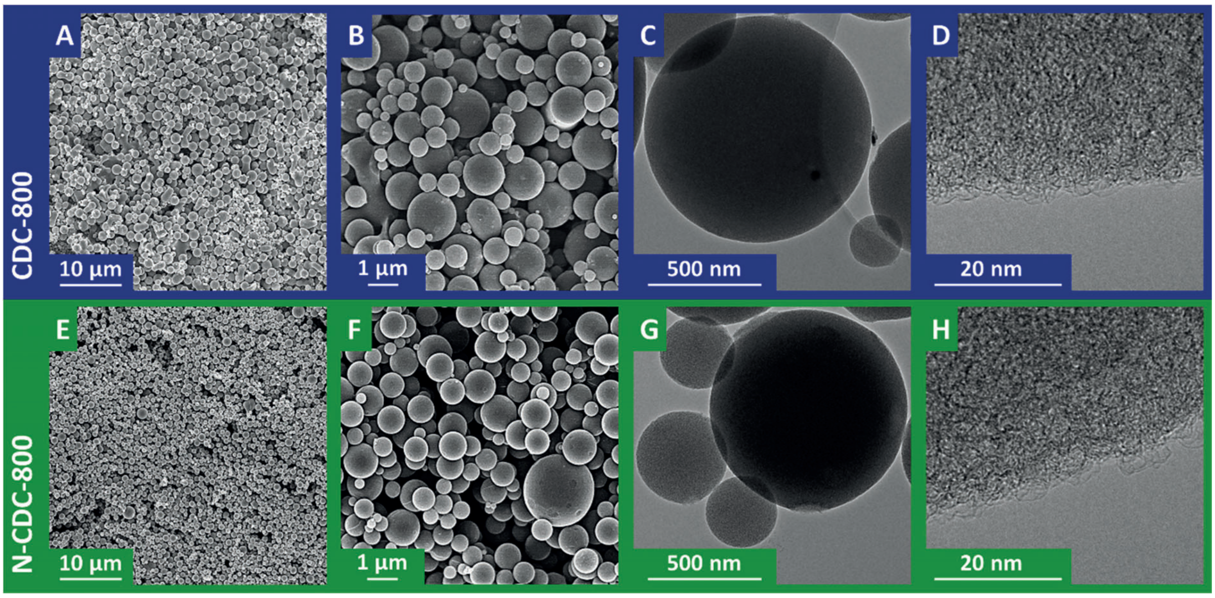

Figure 1. Scanning and transmission electron micrographs of A)-D) CDC-800 and E)-H) N-CDC-800.

Table 1. Porosity data of the powder and the electrode samples obtained by gas sorption analysis with CO_2 and N_2.

	powder				electrode					
	SSA$_{DFT}$ [m^2/g]	SSA$_{BET}$ [m^2/g]	Pore volume [cm^3/g]	Average pore size [nm]	SSA$_{DFT}$ [m^2/g]	SSA$_{BET}$ [m^2/g]	Pore volume [cm^3/g]	Cation accessible SSA$_{DFT}$ [m^2/g]	Anion accessible SSA$_{DFT}$ [m^2/g]	Average pore size [nm]
CDC-600	1740	1965	1.17	1.69	1446	1796	1.02	1095	1401	1.74
CDC-800	2163	2955	1.54	1.66	1966	2512	1.34	1555	1938	1.69
CDC-1000	2320	2430	1.73	1.85	2066	2485	1.53	1614	2030	1.90
N-CDC-600	1416	1644	0.92	1.69	1441	1432	0.89	1058	1377	1.61
N-CDC-800	2133	2771	1.57	1.86	1915	2334	1.36	1498	1886	1.84
N-CDC-1000	2206	2530	1.57	1.85	1908	2293	1.39	1498	1893	1.88

pore volume increased with the synthesis temperature in the range of 0.92–1.73 cm^3/g (Table 1) which agrees to previous works on CDC synthesis.[49,51]

Albeit some differences in total pore volume and total surface area, all samples showed a very similar pore size distribution, which can be best seen when normalizing the latter to the maximum pore volume. As seen from Figure S4, the average pore sizes of all samples range within a narrow range of 1.7–1.9 nm. When transforming the carbon powder into composite film electrodes, the presence of polymer binder reduces the overall porosity.[52,53] As seen from Table 1, about 11 % of the total pore volume and about 9 % of the total surface area are lost when comparing the dry carbon powder with the composite film electrodes. Yet, as required for this study, the average pore size is only marginally affected with values of 1.6–1.9 nm, and the pore size distribution pattern of all CDC and N-CDC samples remain highly similar.

The elemental analysis of the samples is summarized in Table 2 and was measured via chemical analysis (CHNS/O) and X-ray photoelectron spectroscopy (XPS). The carbon content of

Table 2. Chemical composition by CHNS/O analysis and XPS.

	Chemical analysis (CHNS/O)				XPS		
	C [mass %]	H [mass %]	N [mass %]	O [mass %]	C [mass %]	N [mass %]	O [mass %]
CDC-600	94.6 ± 1.3	1.1 ± 1.0	0.4 ± 0.1	3.8 ± 0.3	97.6	0.0	2.4
CDC-800	93.1 ± 1.9	0.6 ± 0.1	0.5 ± 0.2	6.2 ± 0.4	97.7	0.0	2.3
CDC-1000	93.1 ± 0.2	n.d.[a]	0.6 ± 0.1	4.4 ± 0.9	98.3	0.0	1.7
N-CDC-600	85.0 ± 0.6	1.1 ± 0.1	7.0 ± 0.1	5.0 ± 0.2	88.5	4.5	7.0
N-CDC-800	89.9 ± 1.0	0.7 ± 0.1	3.7 ± 0.1	5.5 ± 0.4	94.9	2.7	2.4
N-CDC-1000	92.1 ± 0.2	0.5 ± 0.1	1.2 ± 0.2	5.5 ± 0.1	96.5	0.9	2.5

[a] n.d.: not detectable.

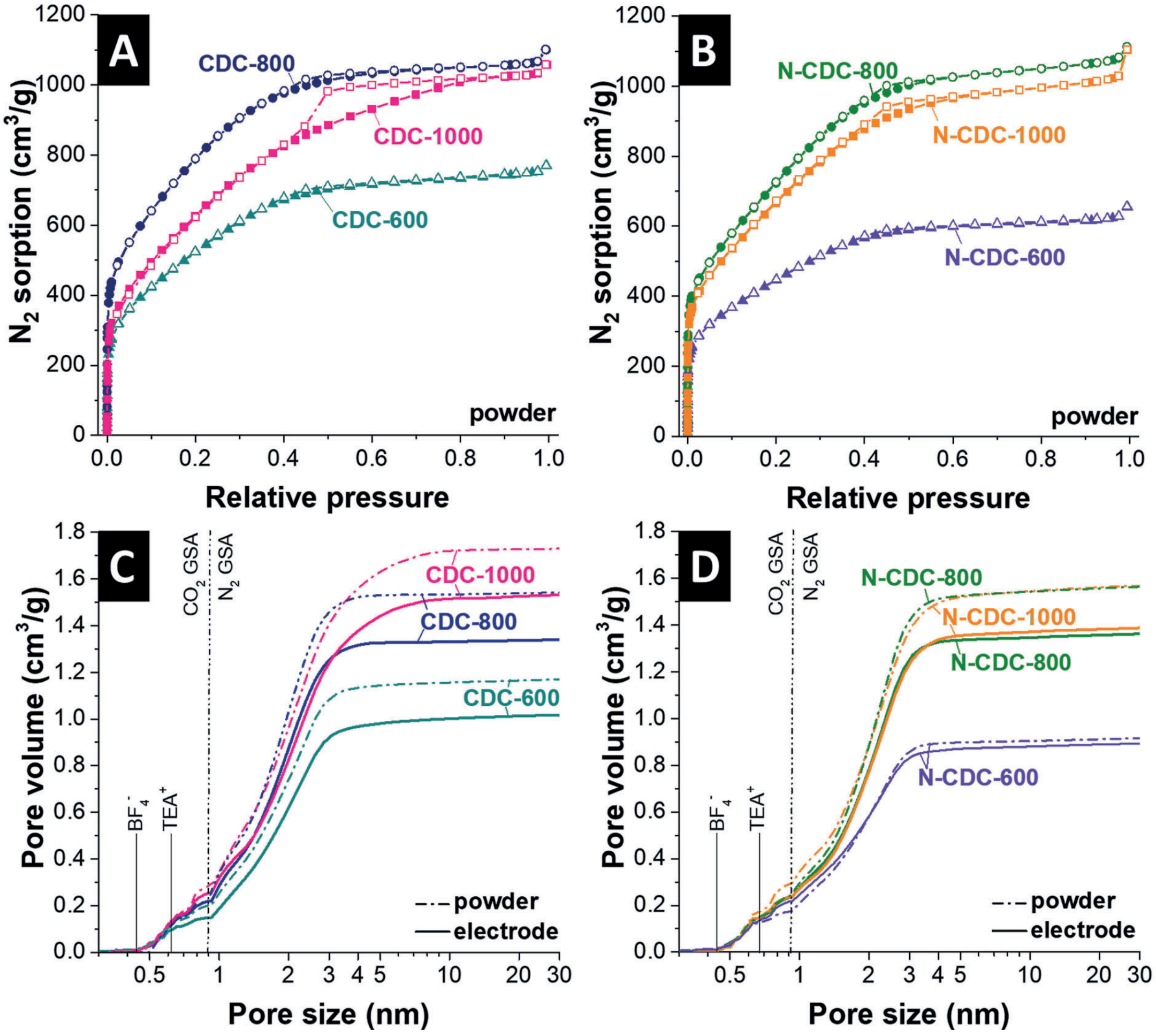

Figure 2. Pore analysis of carbide-derived carbon samples with nitrogen-doping (A,C) and without nitrogen-doping (B,D). A), B) Nitrogen sorption isotherms of the carbon powder materials recorded at $-196\,^{\circ}$C. C), D) Cumulative pore size distribution of the carbon powder materials and the electrodes (i.e., carbon plus 5 mass% polytetrafluoroethylene binder). The ionic diameter of the TEA$^+$ and BF$_4^-$ is added to the pore size distributions in (C,D).

all CDC samples exceeds 93 mass%, and the hydrogen content is lowered for increased synthesis temperature from around 1 mass% for 600 °C to a not detectable value for 1000 °C. The oxygen content of all samples is in the range of 4–6 mass%. A low amount of nitrogen (~0.5 mass%) is also detectable for the CDC samples without nitrogen in the precursor. This nitrogen could be introduced to the samples during the particle synthesis were NH$_3$ served as a catalyst or during the pyrolysis in a nitrogen atmosphere, as reported in earlier work.[54] All N-CDC samples show a nitrogen content ranging from 1–7 mass% and both the nitrogen and hydrogen content are reduced when using a higher synthesis temperature. The sample N-CDC-600 has a nitrogen content of 7 mass%, which is reduced to 4 mass% for N-CDC-800 and to 1 mass% for N-CDC-1000.

Although chemical data and XPS analysis are intrinsically different regarding the sampling depth and the overall detection sensitivity,[55] we also see a reduced nitrogen content with an increasing synthesis temperature in the XPS data. The N1s peak of the XPS spectra can be fitted to identify the nitrogen groups, and we used 4 peaks (N1, N2, N3, and N4) which can be related to different nitrogen groups (Figure 3). The N1 species has a typical binding energy of around 398 eV which indicates pyridinic nitrogen.[56,57] The binding energy of N2 is 400.7 eV and relates to pyrrolic nitrogen, amide, amine, or nitrile.[57] Nitrogen surface groups like amide, amine, or nitrile are unlikely due to the origin of nitrogen in the precursor and the absence of an additional post-synthesis treatment with nitrogen. Therefore, we can assume that N2 peaks are mainly obtained by pyrrolic nitrogen. Graphitic nitrogen (N3) shows a characteristic binding energy of 402 eV.[56,57] A fourth nitrogen peak (N4) was identified for the samples N-CDC-800 and N-CDC-1000 at approximately 404 eV, which relates to nitrogen bonded to oxygen (pyridine oxide).[57] Figure 3B displays the relative bond content of the four identified nitrogen groups. An increasing synthesis temperature reduces the amount of

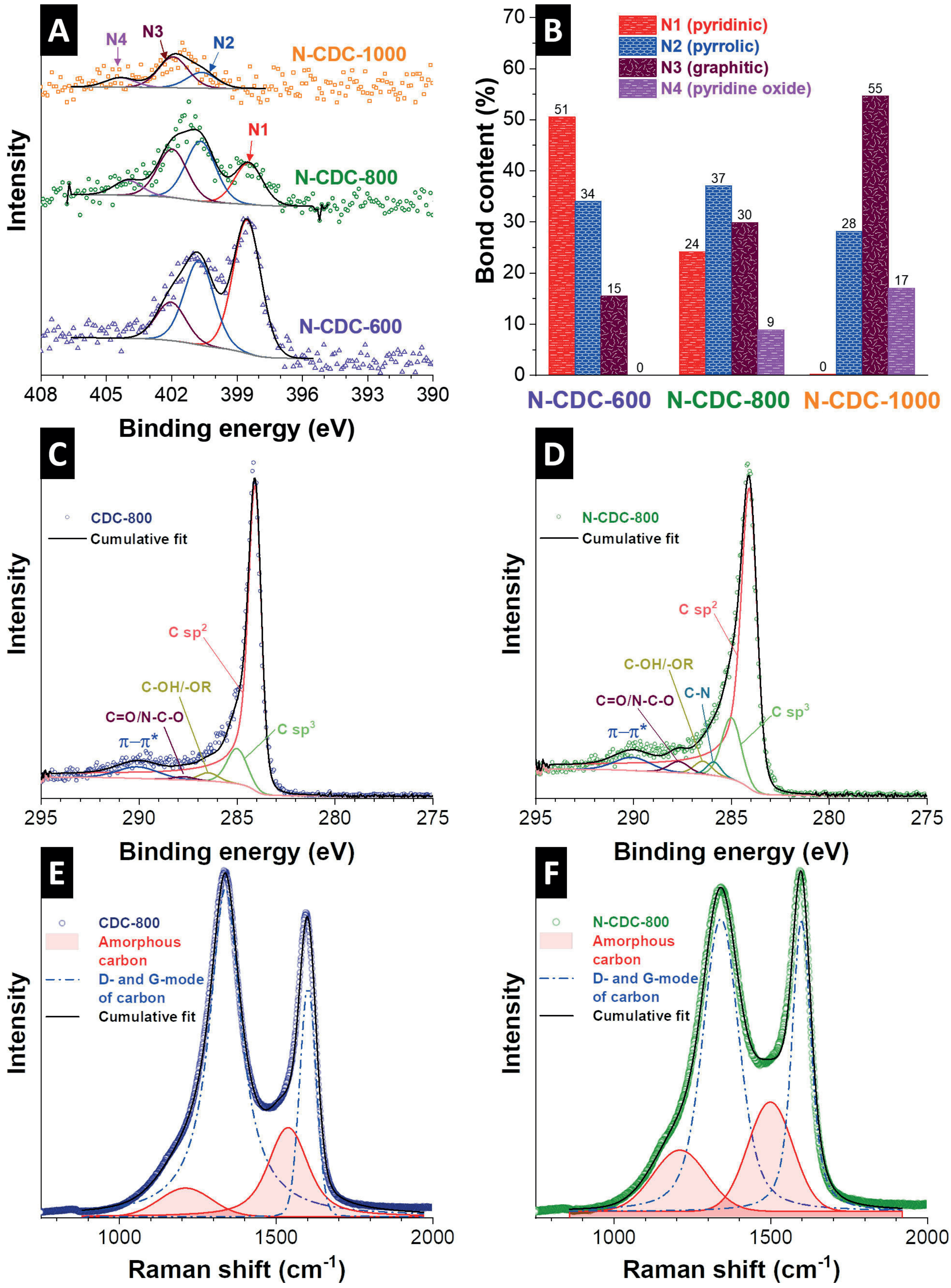

Figure 3. A) XPS N 1s spectra and peak fitting of all nitrogen-doped samples and B) bond content of the nitrogen groups. XPS C 1s spectra and peak fitting of C) CDC-800 and D) N-CDC-800. Raman spectra and peak fitting of E) CDC-800 and F) N-CDC-800.

pyridinic nitrogen from 51% to 0%, while the relative amount of graphitic nitrogen and pyridine oxide increases from 15% to 55% and from 0% to 17%. The pyridinic groups are released at lower temperatures and can be converted to graphitic nitrogen at higher temperatures, which explains the relative increase of the groups with higher binding energy.[6] The relative amount of pyrrolic nitrogen remained rather constant for all samples in the range of 28–37 %.

The carbon bonding can be characterized by analysis of the XPS C1s spectra (Figure 3C,D, and Figure S5, Table S2). Peak fitting shows that most of the carbon is sp^2-hybridized and the CDC samples have with 83–92 % a slightly higher relative amount of the latter bonding type than N-CDC samples with 78–85 %. An increase in the synthesis temperature reduces the sp^2-hybridized carbon content, while the sp^3-hybridized carbon content increases up to 9–11 %. The N-CDC samples show in addition to C–C and C–O bonds also C–N bonds due to the nitrogen-doping in the range of 1.6-2.5 % and the sample with the lowest nitrogen content N-CDC-1000 has the lowest amount of C–N bonds as well.

We further characterized the carbon structure by use of Raman spectroscopy (Figure 3E,F, and Figure S6). The D- and G-modes were fitted with Voigt functions, and the obtained values are listed in Table 3. The D-mode for the CDC is located between 1330–1338 cm^{-1}, while the G-mode is found between 1599–1602 cm^{-1}. The nitrogen-doped CDCs have a similar position of the D-mode (1339–1342 cm^{-1}) and G-mode (1596–1604 cm^{-1}). The position of the D- and G-mode indicate that the carbon of all samples is incompletely graphitic (nanocrystalline).[58] Higher synthesis temperatures lead to a higher degree of carbon ordering, as can be seen from a reduced full-width at half-maximum (FWHM) for all samples. When comparing the FWHMs of the CDC and N-CDC samples produced at the same temperature, there is an increased FWHM for the nitrogen-containing samples in alignment with previous work.[59,60]

Table 3. Fitted values of the D- and G- mode from the Raman spectroscopy of all CDC and N-CDC samples.

		Position [cm^{-1}]	FWHM [cm^{-1}]
CDC-600	D-mode	1330	130
	G-mode	1599	59
CDC-800	D-mode	1338	122
	G-mode	1602	62
CDC-1000	D-mode	1338	100
	G-mode	1600	67
N-CDC-600	D-mode	1342	159
	G-mode	1604	61
N-CDC-800	D-mode	1341	136
	G-mode	1598	72
N-CDC-1000	D-mode	1339	122
	G-mode	1596	68

2.2. Supercapacitor Performance in an Organic Electrolyte

We conducted half-cell measurements for all CDC materials with carbon as a quasi-reference electrode. The cyclic voltammograms in Figure 4A + B show the typical rectangular shape of a supercapacitor with an increased capacitance at higher potentials. This increased differential capacitance yields a characteristic butterfly-like shape and can be explained by the increased charge carrier density when the non-metallic carbon is being charged.[45,61–63] Values of the specific capacitance obtained at ±1 V vs. carbon are listed in Table 4, and we have identified the lowest specific capacitance for CDC-600 at −1 V vs. carbon with 116 F/g and 146 F/g at +1 V vs. carbon. CDC-800 and CDC-1000 have very similar specific capacitances of 143 F/g and 135 F/g, respectively, at −1 V vs. carbon and 144 F/g and 150 F/g, respectively, at +1 V vs. carbon. The specific capacitance at negative polarization is lower compared to the values obtained from positive polarization due to the larger ionic diameter of the TEA^+ ion (0.67 nm non-solvated) compared to the BF_4^- (0.45 nm non-solvated).[64] The nitrogen-containing CDCs have in general a higher specific capacitance at the negative potential vs. carbon. N-CDC-600 has a very similar specific capacitance at ±1 V vs. carbon (118 F/g and 120 F/g), and the largest specific capacitance in the organic electrolyte was obtained for N-CDC-800 with 151 F/g at −1 V vs. carbon and 143 F/g at +1 V vs. carbon (Table 4).

We determined the electrochemical stability window of N-CDC-800 and CDC-800 by using the S-value analysis (Figure 4E + F). The S-value (stability value) is the ratio of invested charge during charging and recovered charge during discharging [Eq. (2)].[65] Weingarth et al. proposed that the electrochemical stability window limit is reached when the second derivative of the S-value over the potential (d^2S/dU^2) exceeds 5 %.[65] This definition is of particular use for a system that shows an exponential increase in the non-reversible charge at a certain potential limit. Using this criterion, we have identified a potential limit of −1.75 ± 0.05 V vs. carbon for both CDC-800 and N-CDC-800 in 1 M TEA-BF_4 in ACN. This value is close to the literature value of −1.7 ± 0.1 V vs. carbon.[65] The more monotonic shape of the S-curve for positive polarization shown in

Table 4. Half-cell capacitance of the CDC materials with and without nitrogen-doping in 1 M TEA-BF_4 in ACN at ±1.0 V vs. carbon and in EMIM-BF_4 at ±1.0 V and ±1.5 V vs. carbon.

	Specific capacitance [F/g] 1 M TEA-BF_4 in ACN at −1.0 V	 at +1.0 V	 EMIM-BF_4 at −1.0 V	 at +1.0 V	 at −1.5 V	 at +1.5 V
CDC-600	116	146	127	125	158	139
CDC-800	143	144	145	157	184	155
CDC-1000	135	150	135	159	176	162
N-CDC-600	118	120	146	124	171	134
N-CDC-800	151	143	169	174	215	173
N-CDC-1000	145	138	150	168	211	172

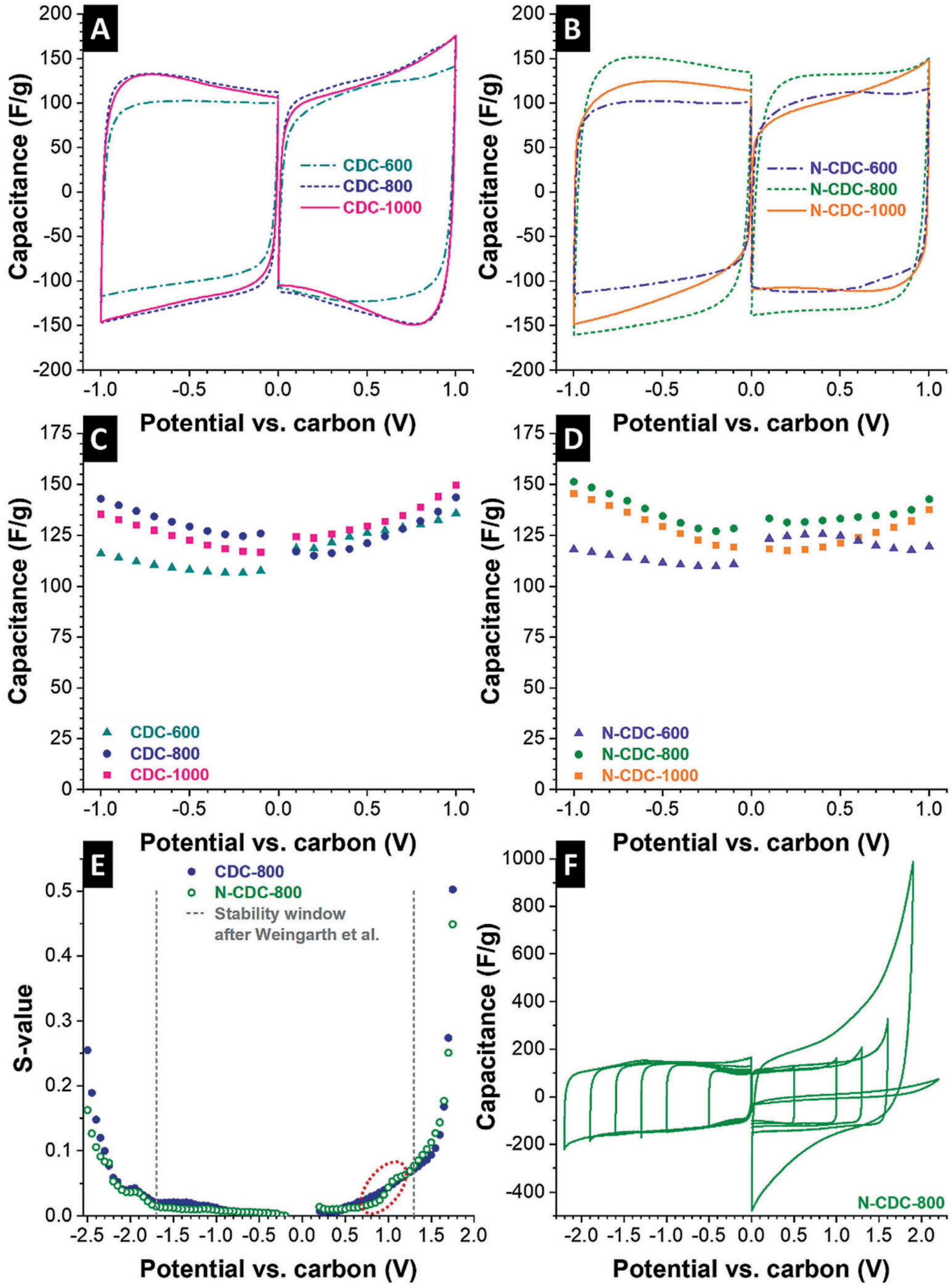

Figure 4. Electrochemical characterization of carbon materials without nitrogen-doping (A,C) and with nitrogen-doping (B,D,F) and S-value analysis of CDC-800 and N-CDC-800 (E,F) in a half-cell configuration in 1 M TEA-BF_4 in ACN. A), B) Cyclic voltammetry measured at a scan rate of 10 mV/s in the potential range of ±1.0 V vs. carbon. C)-D) Capacitance obtained by galvanostatic charge/discharge cycling at a specific current of 0.2 A/g. E) S-value analysis measured by cyclic voltammetry at a scan rate of 1 mV/s and the stability windows after Weingarth et al. (Ref.[65]). F) Selected cyclic voltammograms from the S-value analysis of N-CDC-800.

Figure 4E makes the direct application of $d^2S/dU^2 > 0.05$ more difficult; in fact, the 5% limit is reached already at around +1 V vs. carbon. An increased slope of the S-value can also be caused by (incompletely) reversible Faradaic reactions without leading immediately to escalating electrochemical degradation.[66] From the literature, we would expect the upper limit of the electrochemical stability window at +1.3 V vs. carbon.[65] For CDC-800 and N-CDC-800, we observed the onset of an escalating increase in non-reversible charge above +1.3 V to +1.5 V vs. carbon (Figure 4E). This range also coincides with the stability criterion of S > 0.1 as defined by Xu et al. (where the S-value is called the R-value; Ref.[67]). In addition, N-CDC-800 shows a first rapid increase of the S-value at around +0.95 V vs. carbon which may indicate an early onset of the electrolyte degradation aided by the presence of nitrogen, which can be observed at large potentials. Figure 4F shows selected cyclic voltammograms of N-CDC-800 recorded during the S-value analysis, where the electrolyte decomposition can be observed at large potentials. It is also noticeable that the specific capacitance is dramatically reduced at even higher potentials (+2.2 V vs. carbon).

In addition to the half-cell experiments, we conducted symmetrical full-cell measurements with the samples CDC-800 and N-CDC-800. The cyclic voltammograms show the typical rectangular shape of an electrical double-layer capacitor (Figure 5A). The specific capacitance of N-CDC-800 at a low specific current (0.05 A/g) is 139 F/g, which is slightly lower than the value obtained by the half-cell experiment. The sample CDC-800 without nitrogen has a very similar specific capacitance of 135 F/g at the same specific current. The rate capability analysis is seen in Figure 5B and reveals at a high specific current of 100 A/g a lower specific capacitance of N-CDC-800 (20 F/g) compared to CDC-800 (86 F/g). This observation aligns with the strong correlation between ion mobility and the resulting rate capability of nanoporous carbons.[7] In the case of nitrogen-doping, there is an increased interaction strength between the pore wall and ions, which reduces the ion mobility.[7,68,69] Thereby, the relaxation time of the ions in the micropores increases which leads to a lower rate capability of the nitrogen-doped CDCs.

The performance stability of the nitrogen-containing sample is also reduced (Figure 5D): while CDC-800 retained 89 % of its initial capacitance after voltage floating at 2.7 V for 100 h, the capacitance of N-CDC-800 decayed rapidly. The reduced stability seems to align with the reduced electrochemical stability window as seen from the increased slope of N-CDC-800 in the S-value analysis at around +1 V vs. carbon. The full-cell experiments show that the additional nitrogen-doping does not improve the specific capacitance in organic electrolyte TEA-BF_4 in ACN significantly and reduce the rate handling capability and performance stability.

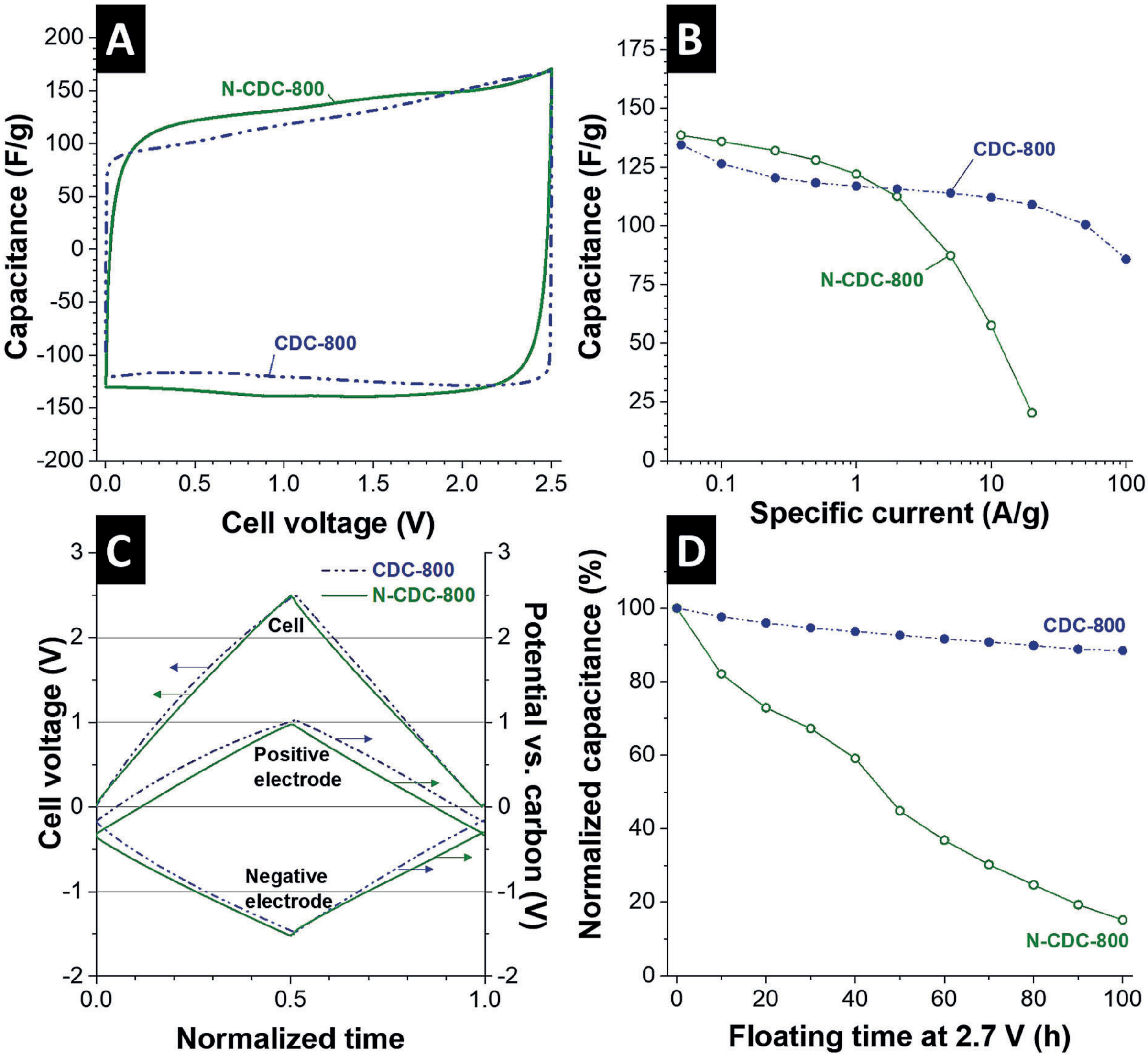

Figure 5. Results of the full-cell supercapacitor measurements with 1 M TEA-BF_4 in ACN. A) Cyclic voltammetry at a scan rate of 10 mV/s, B) galvanostatic charge/discharge rate handling measurement, C) cell voltage and electrode potential distribution during galvanostatic charge/discharge cycling at 0.1 A/g, D) performance stability characterization by floating at a cell voltage of 2.7 V.

2.3. Supercapacitor Performance in Ionic Liquid

We further characterized the CDC materials with and without nitrogen-doping as electrodes using the ionic liquid EMIM-BF_4. The results of the half-cell measurements vs. carbon are presented in Figure 6 and in Table 4. The electric response depicted in the cyclic voltammograms in the negative potential range retains the typical rectangular shape of an electrical double-layer capacitor for all samples with an increased capacitance at higher potentials.[45,61] The specific capacitance in the ionic liquid is in general for all CDCs higher at a negative polarization with an almost linear increase with the potential.

During positive polarization, we see for CDC-600 and N-CDC-600 a rectangular shape without any peaks and a linear increase of the capacitance with the potential. All other samples show to a different degree the emergence of a peak at around +1 V vs. carbon during charging and at +0.7 V vs. carbon during discharging. The area of these peaks is much larger for

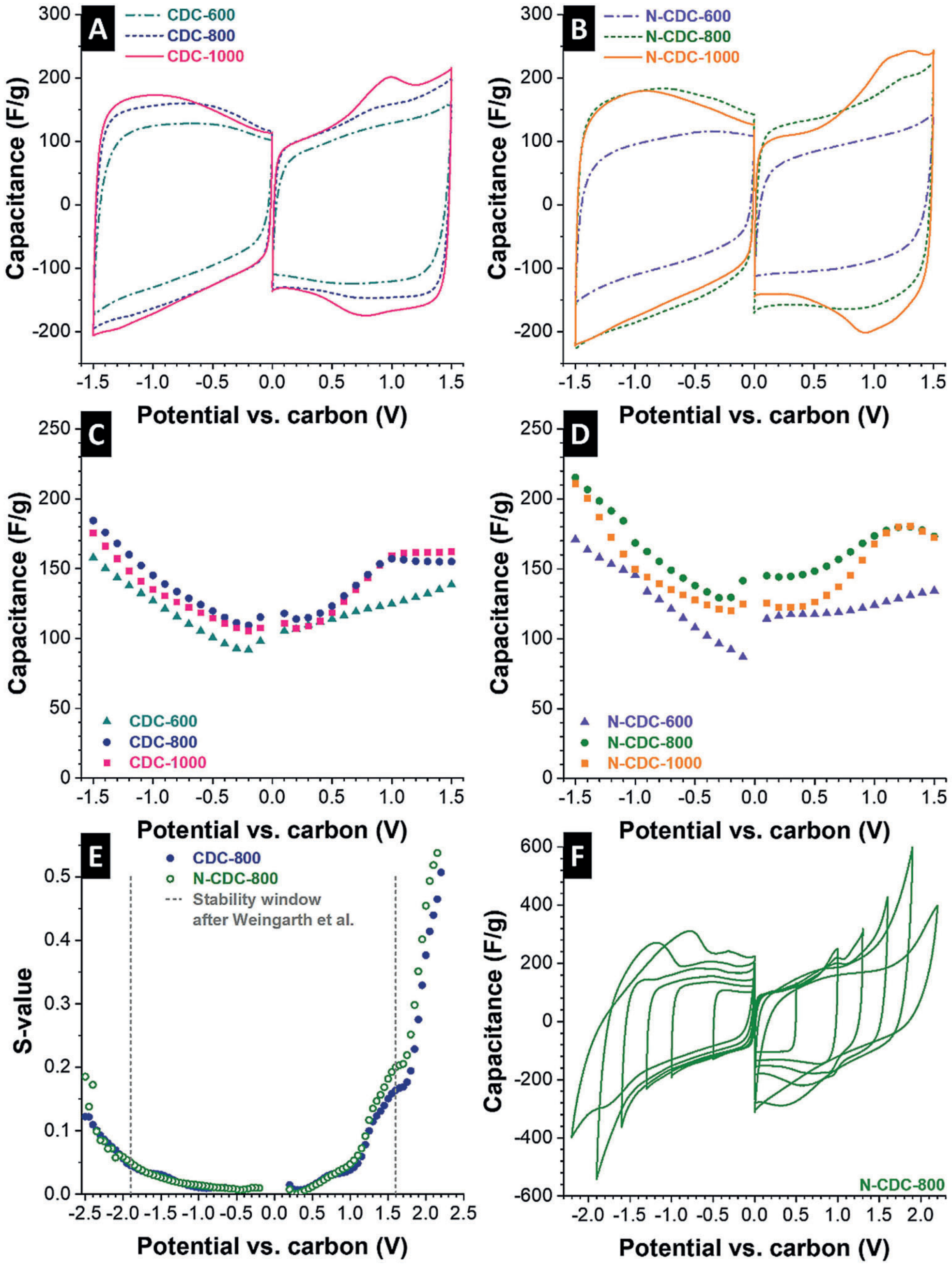

Figure 6. Electrochemical characterization of carbon materials without nitrogen-doping (A, C) and with nitrogen-doping (B,D,F) and S-value analysis of CDC-800 and N-CDC-800 (E, F) in a half-cell configuration in the ionic liquid EMIM-BF_4. A), B) Cyclic voltammetry measured at a scan rate of 10 mV/s in the potential range of ±1.5 V vs. carbon. C)-D) Capacitance obtained by galvanostatic charge/discharge cycling at a specific current of 0.2 A/g. E) S-value analysis measured by cyclic voltammetry at a scan rate of 1 mV/s and the stability windows after Weingarth et al. (Ref.[65]). F) Selected cyclic voltammograms from S-value analysis of N-CDC-800.

the samples produced at 1000 °C and very small for CDC-800 and N-CDC-800. Similar peaks have been reported for EMIM-BF_4 in the literature before, but the origin of this electrochemical signal is not often discussed.[70,71] Intercalation of the BF_4^- as the origin of these peaks is unlikely since it only occurs at much higher potentials for graphitic carbon.[72] A highly irreversible decomposition of BF_4^- can also not cause the highly reversible current peaks.[71] In less pure systems, peaks may also occur because of parasitic side-reactions, as shown by the Kötz group.[64] However, if our system were plagued by impurity-related issues, we would see this redox peak for all samples. The presence of nitrogen in the material also cannot explain the peaks because the samples with the lowest amount of nitrogen show the largest peaks.

A reasonable explanation for the peak was provided by Yan et al. by assuming conformational changes of the ionic liquid inside the micropores during electrochemical cycling.[7] Accordingly, we can relate the higher current signal relates to a better ion packing. This explanation is further supported by our previous work on the use of electrochemical dilatometry (eD) and quartz crystal microbalance measurements (EQCM) to explain the electrosorption of EMIM-BF_4 in microporous carbons.[70] The enhanced volume expansion found in the latter study aligns with highly mobile BF_4^- anions being electro-adsorbed during positive polarization while more of the less mobile $EMIM^+$ cations remain inside the pores.[70] Possibly, the larger $EMIM^+$ leave the micropore confinement more easily at high positive potential when the pore diameter is larger. The free space can be filled by electro-adsorption of additional anions, and the enhanced number of charge carriers induces the peak seen in the CVs at potentials larger than 1 V vs. carbon. This explains why we see the peak very clearly for CDC-1000 and N-CDC-1000 because these samples have a broader pore size distribution with larger average pore size. Samples synthesized at lower temperatures, however, show no visible peak (CDC-600 and N-CDC-600) or only a small peak (CDC-800 and N-CDC-800).

The specific capacitance measured by galvanostatic charge/discharge cycling shows a maximum at +1 V vs. carbon for CDC-800 (157 F/g) and at +1.5 V vs. carbon for N-CDC-800 (180 F/g), which aligns with the data obtained by cyclic voltammetry. During negative polarization, we see even higher capacitance values in EMIM-BF_4 with 184 F/g for CDC-800 and 215 F/g for N-CDC-800 (both values at −1.5 V vs. carbon). A summary of all specific capacitances measured in the half-cell with EMIM-BF_4 is provided in Table 4.

We also tested the electrochemical stability window of CDC-800 and N-CDC-800 using the ionic liquid electrolyte (Figure 6E+F). The S-value pattern for the non-doped and the nitrogen-doped materials are quite similar for both negative and positive polarization (Figure 6E). The electrochemical stability window is characterized by an exponential current increase.[65] We subtract the restored charge for the calculation of S-value. Hence, if the reaction is reversible, we do not expect the exponential S-value increase. The irreversible reaction will cause the exponential S-value increase. The stability criterion from Weingarth et al. ($d^2S/dU^2 < 0.05$) is reached for CDC-800 at −2.00 ± 0.05 V vs. carbon and for N-CDC-800 at −2.10 ± 0.05 V vs. carbon, which are close to the literature value of −1.9 ± 0.1 V vs. carbon.[65] During positive polarization, the sample N-CDC-800 exceeds a value of 0.05 for d^2S/dU^2 already at +0.5 V vs. carbon. The S-values further show a significant increase at +1.15 ± 0.05 V and +1.60 ± 0.05 V vs. carbon. The latter value is also similar to the electrochemical stability window of +1.6 ± 0.1 V vs. carbon typically found in the literature.[65] The increased S-value below +1.5 V vs. carbon may align with incompletely reversible Faradaic reactions, which were also observed in the cyclic voltammograms (Figure 6A+B+F). While the criterion of exceeding the stability window when reaching a value of 0.05 for d^2S/dU^2 is a highly useful tool, our data also show that S-value analysis may be more complex, and it is important to consider the general development of arising incompletely recoverable charge at different potentials. This is also why voltage floating experiments are important to further investigate practical limitations for the performance stability.

The materials CDC-800 and N-CDC-800 were further tested in a symmetrical full-cell setup with EMIM-BF_4 (Figure 7). We chose these two samples because of the promising electrochemical performance in half-cell configuration and for comparability with the full-cell data using 1 M TEA-BF_4 (Figure 5). The CV in Figure 7A shows at a low scan rate a higher specific capacitance for the nitrogen-doped sample compared to the non-doped sample. Galvanostatic charge/discharge cycling measurements yield for CDC-800 a specific capacitance of 164 F/g at 0.05 A/g, while the nitrogen-doped N-CDC-800 has a higher initial capacitance of 174 F/g at the same specific current. The capacitance of N-CDC-800 is being reduced more pronouncedly compared to CDC-800 when increasing the applied current. For example, at a high specific current of 10 A/g, the electrode with N-CDC-800 retains only a specific capacitance of 24 F/g (14 %) while CDC-800 still provides 102 F/g (62 %) at the same current. As seen from these data, we noticed the same trend of reduced high rate performance of nitrogen-doped CDC for operation with the ionic liquid as we did when using the organic electrolyte. Therefore, we also suspect the reduced ion mobility to be caused by an increased interaction strength between the pore walls and the ions since the pore size distribution is highly comparable for all samples.

Stability testing was performed at a floating cell voltage of 3.2 V (Figure 7D). In general, EMIM-BF_4 has a maximum potential window of 3.5 V but is limited to +1.6 V vs. carbon for the positive electrode.[65] Therefore, we chose a maximum cell voltage of 3.2 V for the full-cell measurements. Our data show a slightly better electrochemical stability of the nitrogen-doped sample: after 100 h at 3.2 V, the nitrogen-doped sample retains 78 % of the initial capacitance, while 70 % is retained for CDC-800.

3. Conclusions

The doping of SiOC-CDC beads with nitrogen can be obtained by adding nitrogen groups to the precursor. The resulting nitrogen content depends on the chlorine gas treatment

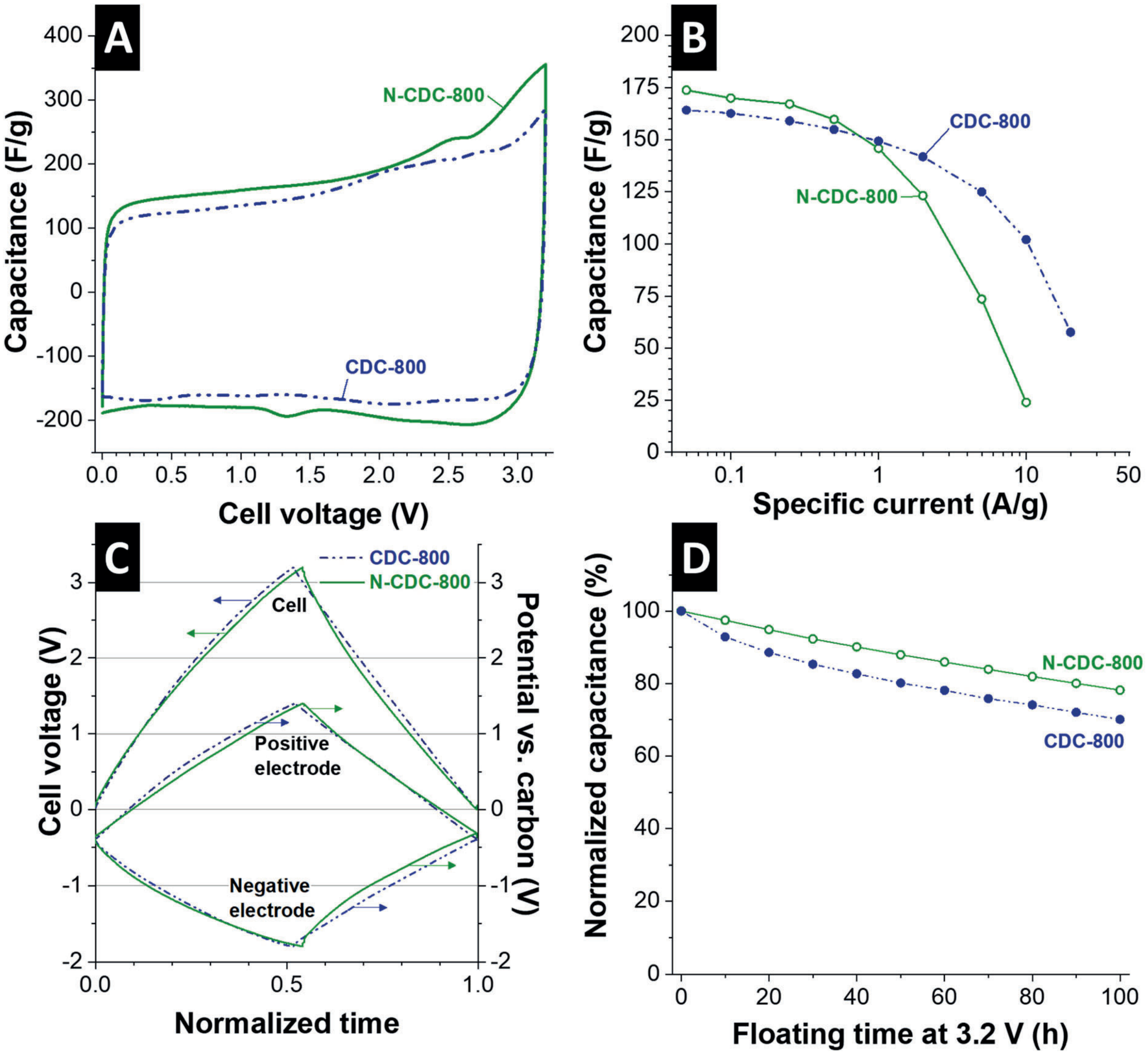

Figure 7. Results of the full-cell supercapacitor measurements with the ionic liquid EMIM-BF_4. A) Cyclic voltammetry at a scan rate of 10 mV/s, B) galvanostatic charge/discharge rate handling measurement. C) Cell voltage and electrode potential distribution during galvanostatic charge/discharge cycling at 0.1 A/g. D) Performance stability characterization by floating at a cell voltage of 3.2 V.

temperature: a low temperature of 600 °C led to a nitrogen content of 7 mass %, while the sample produced at a higher temperature only had a nitrogen content from 1–4 mass %. The nitrogen groups for the sample N-CDC-600 were mainly pyridinic, which were removed at high temperatures.

We investigated the electrochemical performance of the CDCs with a similar pore structure in an organic electrolyte (TEA-BF_4 in ACN) and an ionic liquid (EMIM-BF_4). Using a half-cell setup, we observed that the nitrogen groups did not systematically yield a higher capacitance; instead, the pore structure seemed to have a larger influence on the electrochemical performance. The measurements in a symmetrical full-cell showed that the nitrogen-doped samples have a slightly higher specific capacitance in the organic electrolyte and the ionic liquid at low specific currents. However, when increasing the charge/discharge rate, the specific capacitance decreases more pronouncedly for the nitrogen-doped samples compared to the non-doped samples. This effect may be caused by stronger interaction between the in-pore ions with the pore wall in the presence of nitrogen compared to nitrogen-free CDC.

The different electrochemical full-cell performances of the CDC and N-CDC materials produced by the MicroJet reactor technique are compared in a Ragone plot depicted in Figure 8. N-CDC-800 in EMIM-BF_4 has the highest specific energy of 62 Wh/kg, but the non-doped CDC-800 provides a higher specific power. The organic electrolyte has a lower specific energy of ~30 Wh/kg which is mostly related to the lower maximum cell voltage of 2.7 V. The lower viscosity of the organic electrolyte combined with the non-doped CDC-800 shows the highest specific energy combined with high specific powers (12 Wh/kg at 44 kW/kg).

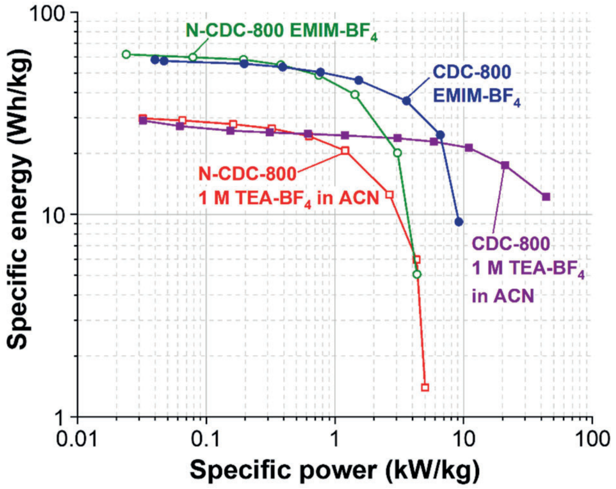

Figure 8. Ragone plot of the carbide-derived carbon materials synthesized at 800 °C with and without nitrogen-doping measured in a symmetrical full-cell supercapacitor in the organic electrolyte 1 M TEA-BF$_4$ in ACN and an ionic liquid EMIM-BF$_4$.

Acknowledgements

The INM authors kindly acknowledge the continuing support of Eduard Arzt (INM). This work was part of the Carbon Metal Oxide Nanohybrid project (CarMON) supported by the Leibniz Association (SAW-2017). We also thank Aura Tolosa, Nicolas Jäckel, and Juhan Lee (all at INM) for fruitful discussions and technical support.

Conflict of Interest

The authors declare no conflict of interest.

Keywords: carbide-derived carbon · carbon · nitrogen-doping · sol-gel processes · supercapacitors

[1] F. Beguin, V. Presser, A. Balducci, E. Frackowiak, *Adv. Mater.* **2014**, *26*, 2219–2251.
[2] P. Simon, Y. Gogotsi, B. Dunn, *Science.* **2014**, *343*, 1210–1211.
[3] P. Simon, Y. Gogotsi, *Nat. Mater.* **2008**, *7*, 845–854.
[4] D. Qu, H. Shi, *J. Power Sources.* **1998**, *74*, 99–107.
[5] B. Krüner, J. Lee, N. Jäckel, A. Tolosa, V. Presser, *ACS Appl. Mater. Interfaces.* **2016**, *8*, 9104–9115.
[6] B. Krüner, A. Schreiber, A. Tolosa, A. Quade, F. Badaczewski, T. Pfaff, B. M. Smarsly, V. Presser, *Carbon.* **2018**, *132*, 220–231.
[7] R. Yan, M. Antonietti, M. Oschatz, *Adv. Energy Mater.* **2018**, 1800026.
[8] T.-P. Fellinger, A. Thomas, J. Yuan, M. Antonietti, *Adv. Mater.* **2013**, *25*, 5838–5855.
[9] N. Fechler, T.-P. Fellinger, M. Antonietti, *Adv. Mater.* **2013**, *25*, 75–79.
[10] Y. Wang, Z. Shi, Y. Huang, Y. Ma, C. Wang, M. Chen, Y. Chen, *J. Phys. Chem. C.* **2009**, *113*, 13103–13107.
[11] K. H. An, W. S. Kim, Y. S. Park, J. M. Moon, D. J. Bae, S. C. Lim, Y. S. Lee, Y. H. Lee, *Adv. Funct. Mater.* **2001**, *11*, 387–392.
[12] D. Pech, M. Brunet, H. Durou, P. Huang, V. Mochalin, Y. Gogotsi, P. L. Taberna, P. Simon, *Nat. Nanotechnol.* **2010**, *5*, 651.
[13] M. Zeiger, N. Jäckel, D. Weingarth, V. Presser, *Carbon.* **2015**, *94*, 507–517.
[14] V. Presser, M. Heon, Y. Gogotsi, *Adv. Funct. Mater.* **2011**, *21*, 810–833.
[15] M. Oschatz, S. Boukhalfa, W. Nickel, J. P. Hofmann, C. Fischer, G. Yushin, S. Kaskel, *Carbon.* **2017**, *113*, 283–291.
[16] M. Salanne, B. Rotenberg, K. Naoi, K. Kaneko, P. L. Taberna, C. P. Grey, B. Dunn, P. Simon, *Nat. Energy.* **2016**, *1*, 16070.
[17] C. Largeot, C. Portet, J. Chmiola, P.-L. Taberna, Y. Gogotsi, P. Simon, *J. Am. Chem. Soc.* **2008**, *130*, 2730–2731.
[18] E. Raymundo-Pinero, K. Kierzek, J. Machnikowski, F. Beguin, *Carbon.* **2006**, *44*, 2498–2507.
[19] J. Chmiola, G. Yushin, Y. Gogotsi, C. Portet, P. Simon, P.-L. Taberna, *Science.* **2006**, *313*, 1760–1763.
[20] N. Jäckel, M. Rodner, A. Schreiber, J. Jeongwook, M. Zeiger, M. Aslan, D. Weingarth, V. Presser, *J. Power Sources.* **2016**, *326*, 660–671.
[21] B. Kastening, S. Spinzig, *J. Electroanal. Chem. Interfacial Electrochem.* **1986**, *214*, 295–302.
[22] N. Jäckel, P. Simon, Y. Gogotsi, V. Presser, *ACS Energy Lett.* **2016**, *1*, 1262–1265.
[23] S. Zhang, N. Pan, *Adv. Energy Mater.* **2015**, *5*, 1401401.
[24] J. Lee, B. Krüner, A. Tolosa, S. Sathyamoorthi, D. Kim, S. Choudhury, K.-H. Seo, V. Presser, *Energy Environ. Sci.* **2016**, *9*, 3392–3398.
[25] E. Frackowiak, K. Fic, M. Meller, G. Lota, *ChemSusChem.* **2012**, *5*, 1181–1185.
[26] B. Akinwolemiwa, G. Chen, *Curr. Top. Electrochem.* **2017**, *19*, 47–65.
[27] E. Frackowiak, M. Meller, J. Menzel, D. Gastol, K. Fic, *Faraday Discuss.* **2014**, *172*, 179–198.
[28] S. Fleischmann, M. Zeiger, N. Jäckel, B. Krüner, V. Lemkova, M. Widmaier, V. Presser, *J. Mater. Chem. A.* **2017**, *5*, 13039–13051.
[29] J. S. Daubert, N. P. Lewis, H. N. Gotsch, J. Z. Mundy, D. N. Monroe, E. C. Dickey, M. D. Losego, G. N. Parsons, *Chem. Mater.* **2015**, *27*, 6524–6534.
[30] M. Zeiger, S. Fleischmann, B. Krüner, A. Tolosa, S. Bechtel, M. Baltes, A. Schreiber, R. Moroni, S. Vierrath, S. Thiele, *RSC Adv.* **2016**, *6*, 107163–107179.
[31] S. Fleischmann, A. Tolosa, V. Presser, *Chem. Eur. J.* **2018**, DOI:10.1002/chem.201800772.
[32] J. K. Ewert, D. Weingarth, C. Denner, M. Friedrich, M. Zeiger, A. Schreiber, N. Jäckel, V. Presser, R. Kempe, *J. Mater. Chem. A.* **2015**, *3*, 18906–18912.
[33] C. Schneidermann, N. Jäckel, S. Oswald, L. Giebeler, V. Presser, L. Borchardt, *ChemSusChem.* **2017**, *10*, 2416–2424.
[34] J. Pu, C. Li, L. Tang, T. Li, L. Ling, K. Zhang, Y. Xu, Q. Li, Y. Yao, *Carbon.* **2015**, *94*, 650–660.
[35] B. Krüner, C. Odenwald, A. Tolosa, A. Schreiber, M. Aslan, G. Kickelbick, V. Presser, *Sustainable Energy Fuels.* **2017**, *1*, 1588–1600.
[36] C. Odenwald, G. Kickelbick *J. Sol-Gel Sci. Technol.* **2018**, DOI:10.1007/s10971-10018-14626-x.
[37] C. A. Schneider, W. S. Rasband, K. W. Eliceiri, *Nat. Methods.* **2012**, *9*, 671.
[38] S. Brunauer, P. H. Emmett, E. Teller, *J. Am. Chem. Soc.* **1938**, *60*, 309–319.
[39] G. Y. Gor, M. Thommes, K. A. Cychosz, A. V. Neimark, *Carbon.* **2012**, *50*, 1583–1590.
[40] A. Vishnyakov, P. I. Ravikovitch, A. V. Neimark, *Langmuir.* **1999**, *15*, 8736–8742.
[41] V. Presser, J. McDonough, S.-H. Yeon, Y. Gogotsi, *Energy Environ. Sci.* **2011**, *4*, 3059–3066.
[42] B. Lobato, L. Suárez, L. Guardia, T. A. Centeno, *Carbon.* **2017**, *122*, 434–445.
[43] S. Doniach, M. Sunjic, *J. Phys. C: Solid State Phys.* **1970**, *3*, 285–291.
[44] S. Evans, *Surf. Interface Anal.* **1991**, *17*, 85–93.
[45] D. Weingarth, M. Zeiger, N. Jäckel, M. Aslan, G. Feng, V. Presser, *Adv. Energy Mater.* **2014**, *4*, 1400316.
[46] D. Weingarth, A. Foelske-Schmitz, A. Wokaun, R. Kötz, *Electrochem. Commun.* **2012**, *18*, 116–118.
[47] D. Weingarth, A. Foelske-Schmitz, R. Kötz, *J. Power Sources.* **2013**, *225*, 84–88.
[48] M. Thommes, K. Kaneko, A. V. Neimark, J. P. Olivier, F. Rodriguez-Reinoso, J. Rouquerol, K. S. W. Sing, *Pure Appl. Chem.* **2015**, *87*, 1051–1069.
[49] R. Dash, J. Chmiola, G. Yushin, Y. Gogotsi, G. Laudisio, J. Singer, J. Fischer, S. Kucheyev, *Carbon.* **2006**, *44*, 2489–2497.
[50] G. Laudisio, R. K. Dash, J. P. Singer, G. Yushin, Y. Gogotsi, J. E. Fischer, *Langmuir.* **2006**, *22*, 8945–8950.
[51] Y. Gogotsi, A. Nikitin, H. Ye, W. Zhou, J. E. Fischer, B. Yi, H. C. Foley, M. W. Barsoum, *Nat. Mater.* **2003**, *2*, 591.
[52] M. Aslan, D. Weingarth, N. Jäckel, J. S. Atchison, I. Grobelsek, V. Presser, *J. Power Sources.* **2014**, *266*, 374–383.
[53] B. Dyatkin, V. Presser, M. Heon, M. R. Lukatskaya, M. Beidaghi, Y. Gogotsi, *ChemSusChem.* **2013**, *6*, 2269–2280.
[54] C. R. Perez, S.-H. Yeon, J. Segalini, V. Presser, P.-L. Taberna, P. Simon, Y. Gogotsi, *Adv. Funct. Mater.* **2013**, *23*, 1081–1089.
[55] J. Zemek, J. Zalman, A. Luches, *Appl. Surf. Sci.* **1998**, *133*, 27–32.

[56] R. Arrigo, M. Hävecker, R. Schlögl, D. S. Su, *Chem. Commun.* **2008**, 4891–4893.
[57] Y. Zhao, X. Liu, Y. Han, *RSC Adv.* **2015**, *5*, 30310–30330.
[58] A. C. Ferrari, J. Robertson, *Phys. Rev. B.* **2000**, *61*, 14095.
[59] Z. R. Ismagilov, A. E. Shalagina, O. Y. Podyacheva, A. V. Ischenko, L. S. Kibis, A. I. Boronin, Y. A. Chesalov, D. I. Kochubey, A. I. Romanenko, O. B. Anikeeva, T. I. Buryakov, E. N. Tkachev, *Carbon.* **2009**, *47*, 1922–1929.
[60] J. D. Wiggins-Camacho, K. J. Stevenson, *J. Phys. Chem. C.* **2009**, *113*, 19082–19090.
[61] P. W. Ruch, R. Kötz, A. Wokaun, *Electrochim. Acta.* **2009**, *54*, 4451–4458.
[62] H. Gerischer, R. McIntyre, D. Scherson, W. Storck, *J. Phys. Chem.* **1987**, *91*, 1930–1935.
[63] H. Gerischer, *J. Phys. Chem.* **1985**, *89*, 4249–4251.
[64] M. M. Hantel, D. Weingarth, R. Kötz, *Carbon.* **2014**, *69*, 275–286.
[65] D. Weingarth, H. Noh, A. Foelske-Schmitz, A. Wokaun, R. Kötz, *Electrochim. Acta.* **2013**, *103*, 119–124.
[66] J. Lee, P. Srimuk, K. Aristizabal, C. Kim, S. Choudhury, Y. C. Nah, F. Mücklich, V. Presser, *J. Electrochem. Soc.* **2017**, *10*, 3611–3623.
[67] K. Xu, S. P. Ding, T. R. Jow, *ChemSusChem* **1999**, *146*, 4172–4178.
[68] R. Singh, J. Monk, F. R. Hung, *J. Phys. Chem. C.* **2011**, *115*, 16544–16554.
[69] R. Singh, N. N. Rajput, X. He, J. Monk, F. R. Hung, *Phys. Chem. Chem. Phys.* **2013**, *15*, 16090–16103.
[70] N. Jäckel, S. P. Emge, B. Krüner, B. Roling, V. Presser, *J. Phys. Chem. C.* **2017**, *121*, 19120–19128.
[71] T. Romann, O. Oll, P. Pikma, H. Tamme, E. Lust, *Electrochim. Acta.* **2014**, *125*, 183–190.
[72] P. W. Ruch, M. Hahn, F. Rosciano, M. Holzapfel, H. Kaiser, W. Scheifele, B. Schmitt, P. Novák, R. Kötz, A. Wokaun, *Electrochim. Acta.* **2007**, *53*, 1074–1082.

Manuscript received: June 28, 2018
Version of record online: August 9, 2018

Supporting Information

Influence of Nitrogen-Doping for Carbide-Derived Carbons on the Supercapacitor Performance in an Organic Electrolyte and an Ionic Liquid

Benjamin Krüner, Christina Odenwald, Antje Quade, Guido Kickelbick,* and Volker Presser*

Table S1: Mass losses after the pyrolysis and the chlorine treatment together with the average diameter of the CDC beads.

	Mass loss after pyrolysis (%)	Mass loss after chlorine gas treatment (%)	Total mass loss (%)	Number-dependent average diameter (nm)	Volume-dependent average diameter (nm)
CDC-600	24	91	93	1025±445	1831±445
CDC-800	24	95	96	884±459	1625±459
CDC-1000	24	95	96	1001±458	1826±458
N-CDC-600	24	92	94	839±229	1379±229
N-CDC-800	24	93	95	707±281	1261±281
N-CDC-1000	24	94	95	832±255	1305±255

Table S2: Bonding content of the fitted C 1s peak measured with XPS.

	sp^2 C (%)	sp^3 C (%)	C-N (%)	C-OH (%)	C=O/N-C-O (%)	π-π* (%)
CDC-600	92.4	2.3	-	1.9	0.5	2.8
CDC-800	82.7	8.6	-	2.0	0.8	5.8
CDC-1000	83.0	8.9	-	1.8	0.7	5.6
N-CDC-600	85.2	7.9	2.5	0.8	1.5	2.1
N-CDC-800	77.9	11.4	1.8	2.2	2.2	4.6
N-CDC-1000	77.7	10.2	1.6	2.9	1.9	5.8

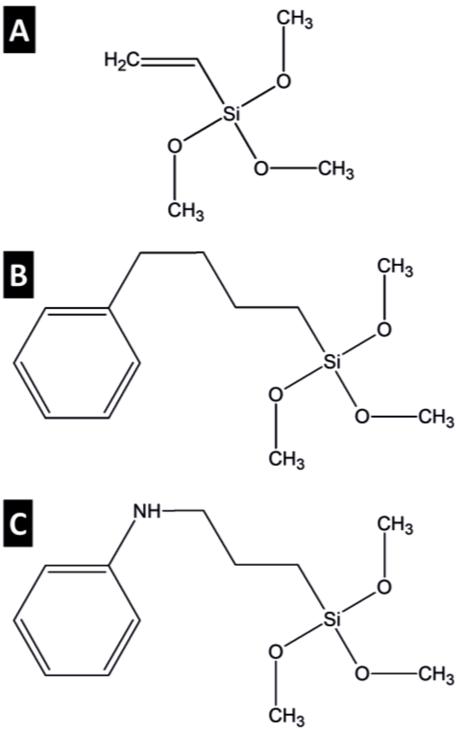

Figure S1: Structural formula of (A) vinyltrimethoxysilane (VTMS), (B) 4-phenylbutyltrimethoxysilane (PBTMS), and (C) [3-(phenylamino)propyl]trimethoxysilane (PAPTMS).

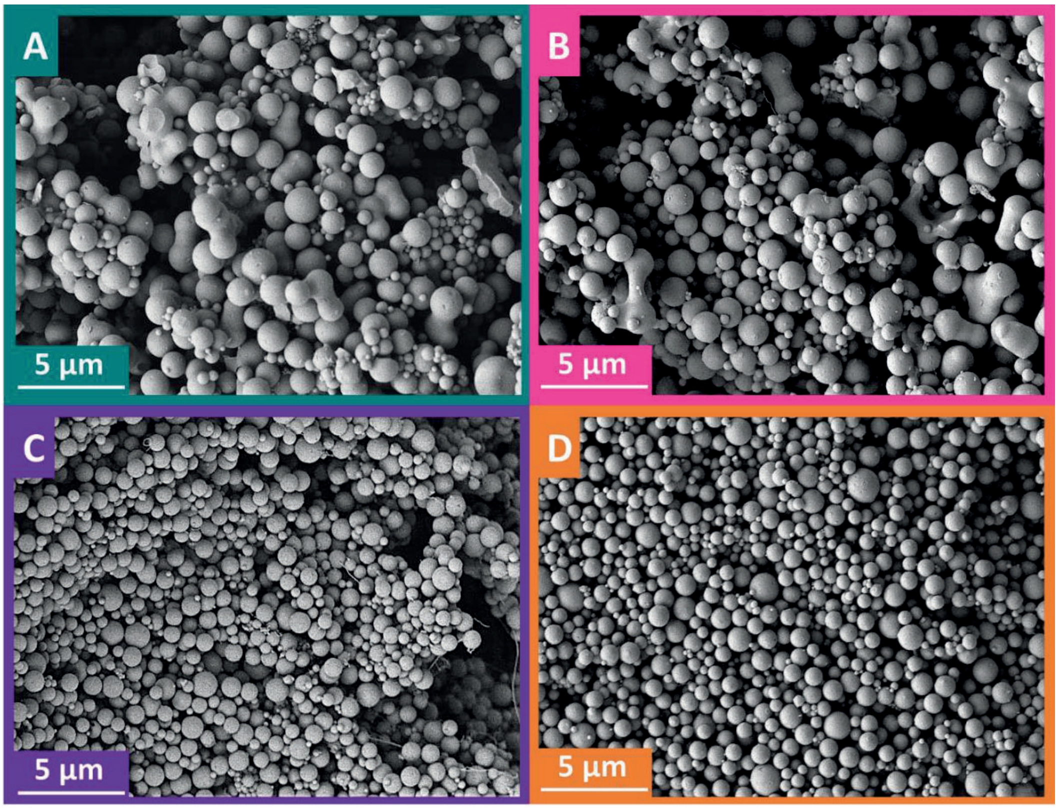

Figure S2: Scanning electron micrographs of (A) CDC-600, (B) CDC-1000, (C) N-CDC-600, and (D) N-CDC-1000.

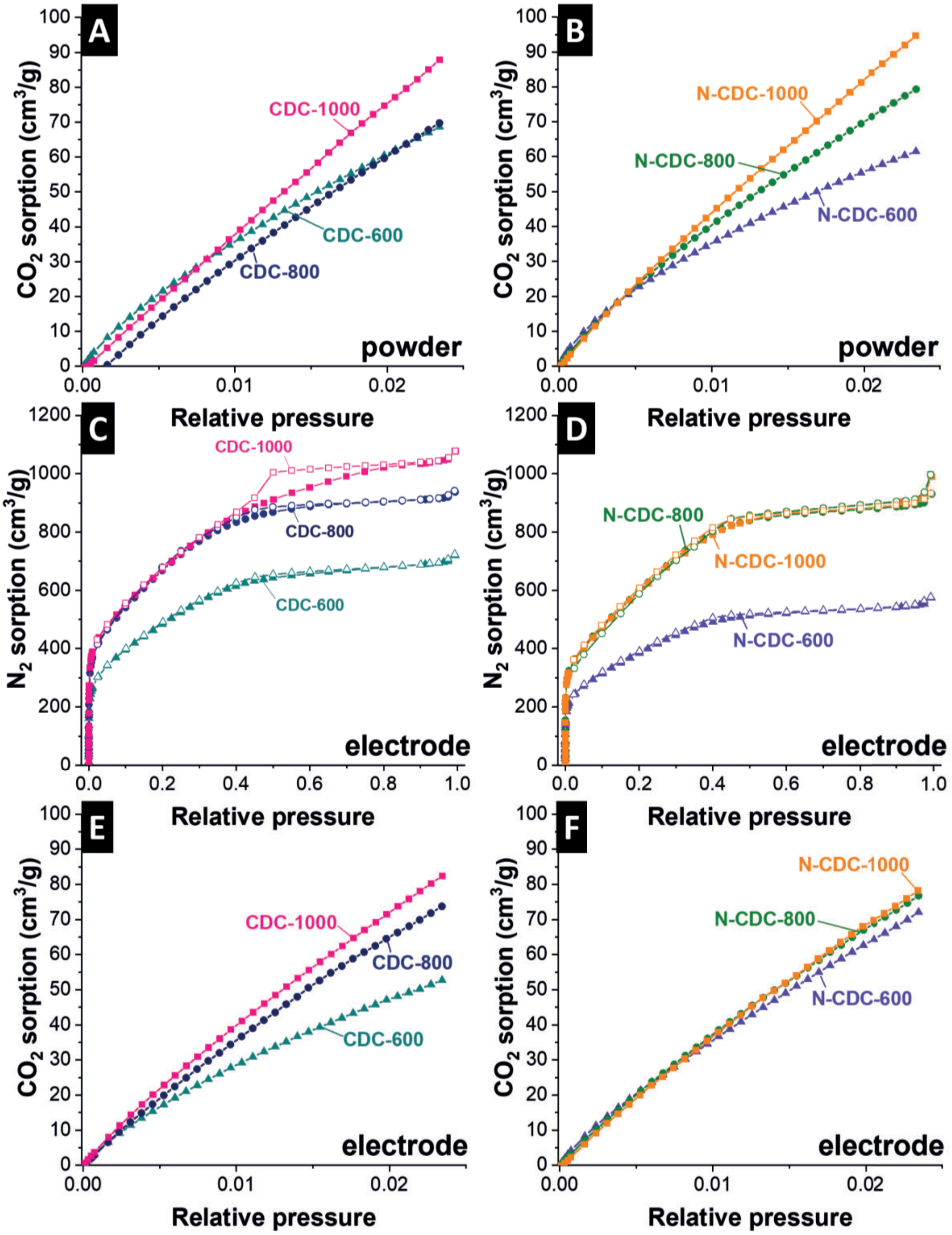

Figure S3: (A,B,E,F) CO$_2$ gas sorption isotherms recorded at 0 °C and (C,D) nitrogen gas sorption isotherms recorded at -196 °C of the carbide-derived carbons with and without nitrogen doping measured as (A,B) powder material or as (C,D,E,F) electrode (i.e., consolidated with 5 mass% of polytetrafluoroethylene).

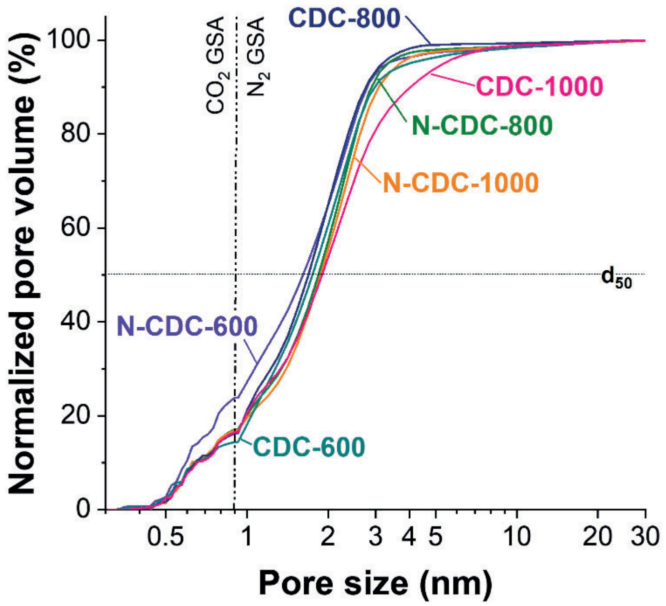

Figure S4: Comparison of the normalized pore size distribution of all materials used as electrodes. The value of d_{50} relates to the volume-weighted average pore size.

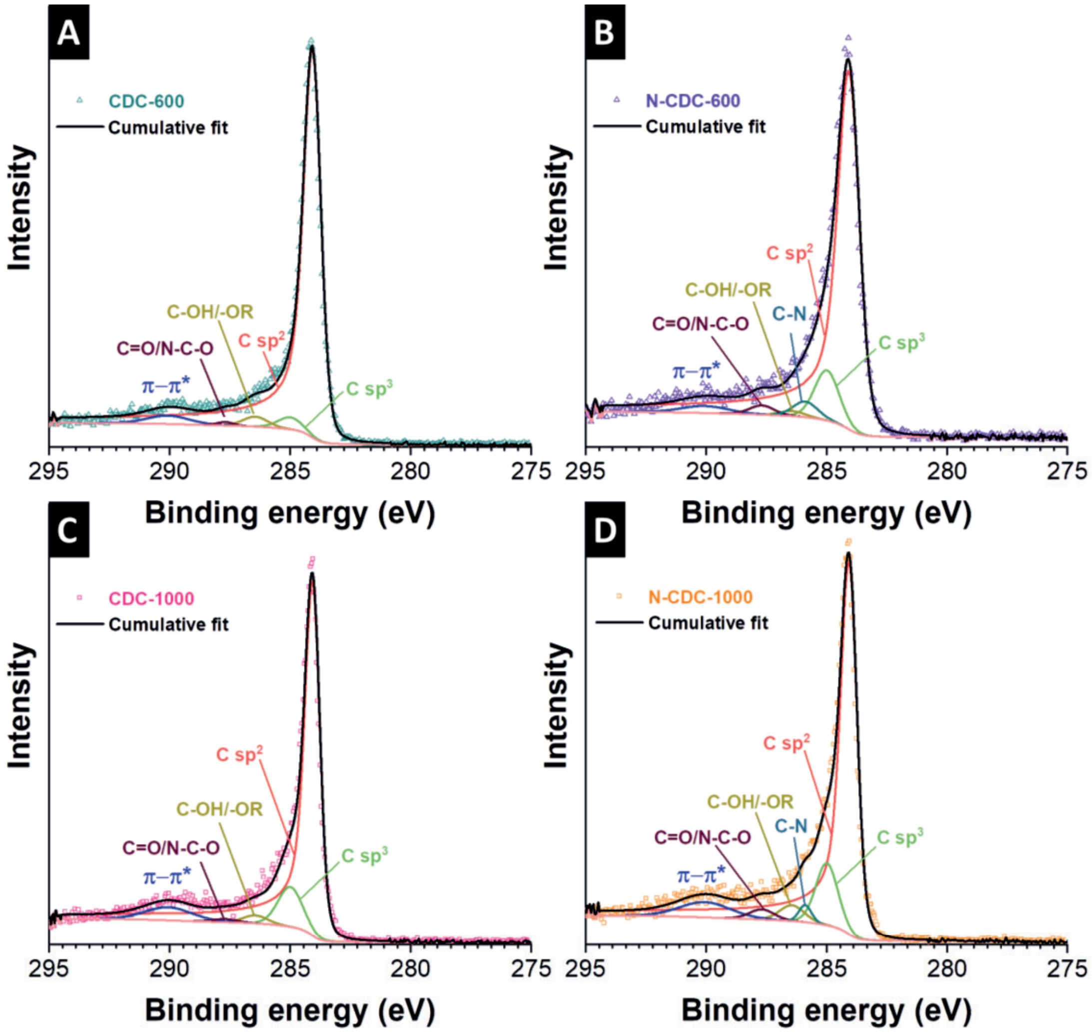

Figure S5: X-ray photoelectron spectra showing the C 1s peaks of the samples (A) CDC-600, (B) N-CDC-600, (C) CDC-1000, and (D) N-CDC-1000.

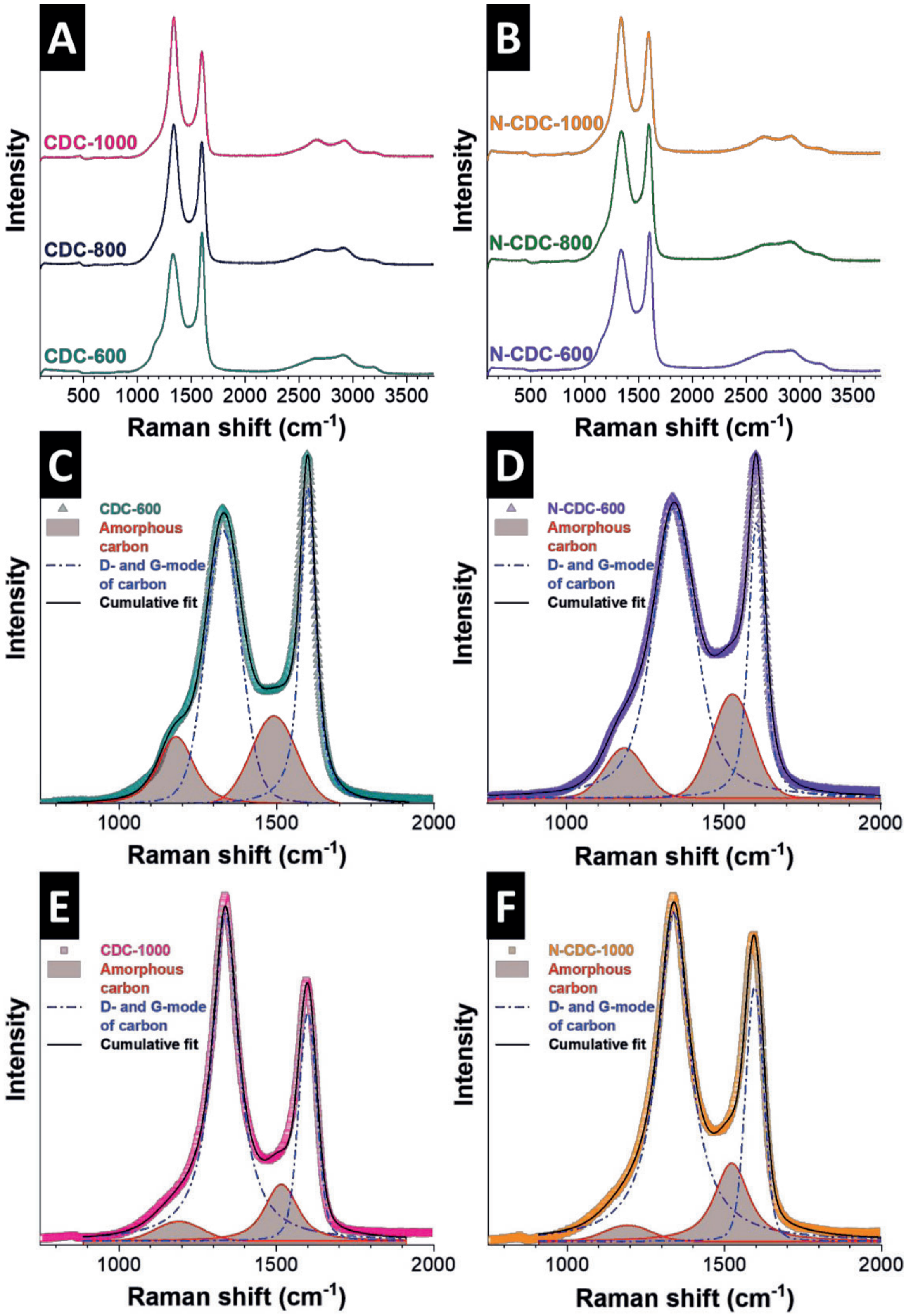

Figure S6: Raman spectra of the samples CDC-600, CDC-800, and CDC-1000 (A) and of the samples N-CDC-600, N-CDC-800, and N-CDC-1000 (B). Fitted Raman spectra of the samples (C) CDC-600, (D) N-CDC-600, (E) CDC-1000, and (F) N-CDC-1000.

3.3.4 Silicon oxycarbide beads from continuously produced polysilsesquioxane as stable anode material for lithium-ion batteries

In the following last article, another energy storage material, namely silicon oxycarbide, is produced from the ORMOSILs. This product is generated by pyrolysis of the precursor particles. By using different organic groups in the ORMOSIL, SiOC spheres can be obtained, which differ in the amount of their Si-C bonds and the amount of free carbon. The samples are used as anode material in a Li-ion battery and it is investigated how the different microstructures affect the electrochemical properties.

Through the initial extensive development and optimization of the route for the continuous production of ORMOSIL particles, described in chapter 3.3.1, a basic system was created that can now be easily adapted to the given requirements. In the following article this concept is demonstrated: Particles with methyl-, vinyl- and vinyl/phenyl mixed groups are produced, whereby the concentrations of the precursor solutions are slightly modified to adjust the particle sizes between 0.5 and 1.5 µm.

Contributions:

Christina Odenwald: Planning, synthesis of the polymer particles, discussion, and revision of the manuscript. **Benjamin Krüner:** Design, planning, writing, pyrolysis, SEM, particle size analysis, EDX analysis, N_2 sorption analysis, Raman analysis, NMR data analysis, XRD, and electrochemical analysis for Li-ion batteries. **Nicolas Jäckel:** Discussion and revision of the manuscript. **Aura Tolosa:** TEM analysis, electrochemical measurements, discussion, and revision of the manuscript. **Guido Kickelbick:** Discussion and revision of the manuscript. **Volker Presser:** Supervision, discussion, and revision of the manuscript.

The following article is reprinted with permission from Krüner, B.; Odenwald, C.; Jäckel, N.; Tolosa, A.; Kickelbick, G.; Presser, V. Silicon oxycarbide beads from continuously produced polysilsesquioxane as stable anode material for lithium-ion batteries, *ACS Applied Energy Materials* **2018,** *1* (6), 2961−2970. http://dx.doi.org/10.1021/acsaem.8b00716. Copyright 2018 American Chemical Society.

ACS APPLIED ENERGY MATERIALS
Article
Cite This: ACS Appl. Energy Mater. 2018, 1, 2961−2970
www.acsaem.org

Silicon Oxycarbide Beads from Continuously Produced Polysilsesquioxane as Stable Anode Material for Lithium-Ion Batteries

Benjamin Krüner,[†,‡] Christina Odenwald,[§] Nicolas Jäckel,[†,‡] Aura Tolosa,[†,‡] Guido Kickelbick,[*,§] and Volker Presser[*,†,‡]

[†]INM—Leibniz Institute for New Materials, 66123 Saarbrücken, Germany
[‡]Department of Materials Science and Engineering, Saarland University, 66123 Saarbrücken, Germany
[§]Inorganic Solid State Chemistry, Saarland University, 66123 Saarbrücken, Germany

Supporting Information

ABSTRACT: Silicon oxycarbides are promising anode materials for lithium-ion batteries. In this study, we used the continuous MicroJet reactor technique to produce organically modified silica (ORMOSIL) spheres which were pyrolyzed to obtain silicon oxycarbides. The continuous technique allows the production of large quantities with a constant quality. Different alkoxysilanes were used to produce the silicon oxycarbides with different compositions. Thereby, the amounts of silicon−carbon bonds, as well as the free carbon content, were modified. Electrochemical testing was carried out in 1 M $LiPF_6$ in ethylene carbonate/dimethyl carbonate. A mixture of vinyl- and phenyltrimethoxysilane was identified as the best anode material with a stable performance due to the increased carbon content. The first-cycle delithiation capacity of the most stable material was 922 mA h/g, and the capacity retention after 100 cycles was 83% (767 mA h/g).

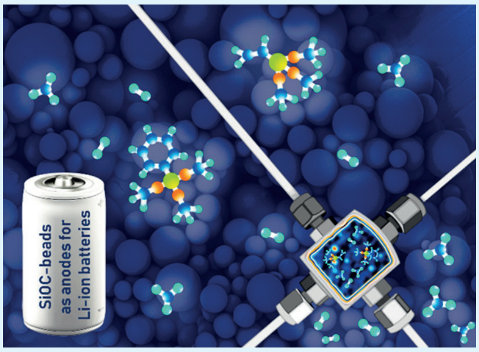

KEYWORDS: *polymer-derived ceramic, silicon oxycarbide, sol−gel, Li-ion battery, anode material, polysilsesquioxane*

1. INTRODUCTION

Lithium-ion batteries (LIBs) are a key technology for today's mobile computing and for the transition of our fleet of internal combustion vehicles to electric cars.[1,2] The constantly growing requirements for energy storage, power handling, safety, and costs are at the core of research activities on next-generation LIB electrode materials.[3,4] Graphite is a common anode material with a theoretical capacity of 372 mA h/g when fully lithiated (LiC_6).[4] A much higher theoretical capacity of 4200 mA h/g is known for silicon, which creates an alloy with lithium.[4] However, the use of silicon remains limited because of the large volume expansion during charging and discharging, causing structural deterioration and poor performance stability of the electrode material.[4−7] The use of nanoparticles and composite or hybrid materials with carbon can reduce the fast capacity fading of silicon-based Li-ion batteries,[6,8−11] but the performance stability remains unsatisfactory.

An alternative to the direct use of silicon is the use of silicon oxycarbides (SiOCs) for LIB anodes. This material can be produced on a large scale by the pyrolysis of polysilsesquioxanes.[12−15] Such SiOC materials belong to the family of polymer-derived ceramics (PDCs) and consist of nanodomains of $SiO_{4-x}C_x$ tetrahedra which are surrounded by free carbon. The encapsulating of the silica domains by graphene cages results in a viscoelastic behavior of the SiOCs, which is beneficial for the large expansion and contraction during the lithiation and delithiation.[16,17] The theoretical capacity of these SiOC materials is between 372 and 1300 mA h/g depending on the composition, which is lower than for SiO_2 (1784 mA h/g).[4,7,14,18] The alloying reaction forming Li_2O is not completely reversible; correspondingly, the Coulombic efficiency of the first cycle is in the range from about 40% to 70% and depends on the chemical composition and the structure, which is influenced by the pyrolysis conditions.[13,14,19,20] For example, Kaspar et al. investigated different pyrolysis temperatures of 900−2000 °C to produce SiOC for Li-ion batteries, and the best Coulombic efficiency was obtained for the material synthesized at 1100 °C.[13] The formation of larger graphitic domains at this temperature leads to improved electrical conductivity and is below the crystallization temperature of SiC (>1200 °C).[21] These domains of free carbon improve the electrical conductivity of the ceramic and reduce the capacity fading of the anode material.[22] The SiOC ceramics with a low amount of free carbon (~8 wt %) have a low conductivity of about 10^{-5} S/m which can increase to ~2 S/m for a high content of free carbon (~54 wt %), measured at a high pressure

Received: May 4, 2018
Accepted: June 1, 2018
Published: June 1, 2018

DOI: 10.1021/acsaem.8b00716
ACS Appl. Energy Mater. 2018, 1, 2961−2970

of 1 MPa.[22] These values are still low for use as electrodes, and it is necessary to improve the conductivity further by adding a conductive additive, such as carbon black.

The importance of silicon−carbon bonds for the electrochemical performance was shown, for example, by Graczyk-Zajac et al. using polysiloxanes pyrolyzed in an argon atmosphere or in an oxidizing CO_2 atmosphere.[19] The ^{29}Si NMR data of the oxidized sample documented the absence of silicon−carbon bonds after the pyrolysis, while the content of free carbon was about 37 wt %.[19] The sample pyrolyzed in argon contained units of C_2SiO_2, $CSiO_3$, and SiO_4, along with 47 wt % free carbon. Both electrode materials had a similar initial capacity of ∼1500 mA h/g during the cathodic sweep, but the reversible capacity was much higher for the sample treated in argon (800 mA h/g) compared to the other material (600 mA h/g). The long-time stability of the SiOC with silicon−carbon bonds was higher compared to that of the oxidized SiOC. Nevertheless, the reversible capacity after 100 cycles was only 55% of the initial capacity, and the largest capacity fade occurs already after 20 cycles. In another study, Pradeep et al. synthesized a SiOC aerogel which had a capacity retention of almost 80% after 100 cycles, but the overall specific capacity was rather low (450 mA h/g).[23] Many other publications of SiOCs as anode material for Li-ion batteries report even less than 100 cycles at low rate, by which measure it is difficult to assess the actual performance stability.[12,22,24]

In this study, we investigate three SiOC bead materials obtained from methyltrimethoxysilane, vinyltrimethoxysilane, and a mixture of vinyltrimethoxysilane with phenyltrimethoxysilane. Wilamowska-Zawlocka et al. used similar precursors for the synthesis of SiOC as LIB anodes, but they used a batch method which resulted in large particles which were ball-milled to obtain particles of around 10 μm.[20] In contrast to previous work, we produced polysilsesquioxane with a spherical shape and by use of the continuous MicroJet reactor.[25,26] The voids between the spherical particles may partially buffer the volume expansion and improve the performance stability of the LIB.[10,11] Our approach does not need any cross-linking agent to maintain the sphere morphology, and the continuous process allows the production of large amounts with constant quality. The absence of a cross-linker is expected to enhance the purity of the resulting SiOC material.[15,27]

We analyzed the SiOC beads among others with electron microscopy, X-ray diffraction, Raman spectroscopy, solid-state NMR, and Fourier-transform infrared spectroscopy. This array of analytical tools helped us to clarify the correlation between structural properties and the resulting electrochemical performance when used as an anode for Li-ion batteries. The electrochemical performance in 1 M $LiPF_6$ in ethylene carbonate/dimethyl carbonate was characterized with a focus on the long-time stability.

2. EXPERIMENTAL DESCRIPTION

2.1. Synthesis of Siloxane Beads and Pyrolysis. Methyltrimethoxysilane (MTMS; 97%), vinyltrimethoxysilane (VTMS; 99%), and phenyltrimethoxysilane (PTMS; 97%) were purchased from ABCR. The diluted ammonia (25%) was obtained from VWR. All chemicals were used as received.

The synthesis of the polysiloxane microparticles is described in detail in our previous publications.[25,26] An overview of the synthesis steps is provided in the Figure 1. In short, the silanes were dissolved in methanol and aqueous HCl and prehydrolyzed at room temperature overnight. The silane solution was mixed with an ammonia solution with a concentration of 2.2 M in a microreactor (MicroJet reactor, Synthesechemie Dr. Penth GmbH) at 20 °C. The composition of the used silane solution is listed in Table 1. Two HPLC pumps (LaPrep P110 preparative HPLC pumps, VWR; flow rate, 250 mL/min) transport the precursor solutions through opposing horizontal nozzles (300 μm in diameter) in the mixing chamber where they collide as fine impinging jets, and a fast mixing occurs. A gas flow (N_2, 0.8 MPa) orthogonal to the feeding jets supports the transfer of the product suspension out of the reactor. The suspension was collected, and the particles were centrifuged (8000 rpm, 7012*g*, 10 min) and dried in vacuum at room temperature.

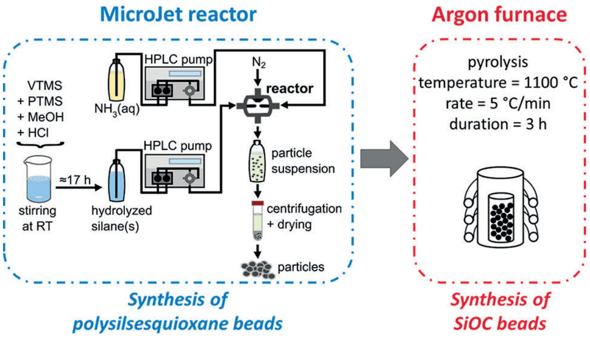

Figure 1. Schematic synthesis using the MicroJet reactor to obtain polysilsesquioxane beads which are transformed to silicon oxycarbide beads via thermal treatment in argon. The scheme was modified and is reproduced with permission.[26] Copyright 2017 Royal Society of Chemistry.

The three different types of polysiloxane particles were pyrolyzed in a graphite furnace (LHTG, Carbolite Gero) in an argon atmosphere at 1100 °C for 3 h with a heating rate of 300 °C/h. The pyrolysis temperature of 1100 °C was chosen to yield graphitic carbon which improves the conductivity, but to stay below the temperature regime of silicon carbide crystallization.[13]

2.2. Electrode Preparation. The pyrolyzed SiOC beads were mixed with 5 wt % of carbon black (CB; C-Nergy Super C65 from Imerys Graphite & Carbon). We chose 5 wt % sodium carboxymethylcellulose (NaCMC) as the binder because it is superior to polyvinylidene fluoride (PVdF) for silicon and silicon oxide electrodes, and the use of water as solvent is less hazardous than *N*-methyl-2-pyrrolidone (NMP).[28−30] A solution of NaCMC in water (1 wt %) was used to prepare a suspension of SiOC and CB which was coated with a doctor blade (layer thickness: 200 μm) on a copper foil as a current collector and dried at 80 °C for 24 h.

2.3. Material Characterization. Electron microscopy was performed with a field emission scanning electron microscopy (SEM) JSM-7500F instrument from JEOL and a high-resolution transmission electron microscopy (TEM) JEM-2100F instrument from JEOL as well. A thin platinum layer was sputtered onto the SEM samples to increase the surface conductivity, and 175 beads were analyzed with the software ImageJ to obtain the average diameter.[31] For TEM, the samples were dispersed and sonicated in ethanol to deposit them on a lacey carbon film on a copper grid from Gatan. The TEM was operated using a voltage of 200 kV under vacuum.

The chemical composition of the silicon oxycarbides was quantified with energy-dispersive X-ray spectroscopy (EDX). This X-MAX silicon detector from Oxford Instruments was attached to the SEM chamber. The electron beam for the EDX had a voltage of 5 kV, and the samples were sputtered with a thin layer of gold. A total of 20 EDX spectra were recorded, and the average composition was used to calculate the theoretical formula for the SiOCs.

Nitrogen gas sorption analysis (GSA) was carried out to measure the specific surface area (SSA) with an Autosorb iQ system from Quantachrome. The samples were outgassed at 300 °C for up to 20 h, and the measurements were performed at −196 °C in the relative pressure range from 2×10^{-4} to 1.0. The linear regime of the isotherm was analyzed with the Brunauer−Emmett−Teller equation to calculate the specific surface area.[32] The skeletal density of the silicon

Table 1. Compositions of Precursor Silane Solutions and Ammonia Solution That Were Used for the Synthesis of Polysilsesquioxane Microparticles

	silane solution						
sample	$n_{(\mathrm{MTMS})}$ (mmol)	$n_{(\mathrm{VTMS})}$ (mmol)	$n_{(\mathrm{PTMS})}$ (mmol)	$n_{(\mathrm{MeOH})}$ (mol)	$n_{(\mathrm{H_2O})}$ (mol)	$n_{(\mathrm{HCl})}$ (mmol)	ammonia solution $c_{(\mathrm{NH_3})}$ (mol/L)
Me-SiOC	69.4			2.8	2.8	0.01	2.2
Vi-SiOC		277.6		6.4	5.6	0.06	2.2
Vi-Ph-SiOC		83.3	16.7	6.4	11.1	0.01	2.2

oxycarbide beads was measured by helium pycnometry (AccuPyc 1330 pycnometer from Micromeritics; He purity, 5.0).

The solid-state NMR measurements were performed on a Bruker AV400WB spectrometer. The samples were packed in zirconia rotors that were spun at 13 kHz under nitrogen or compressed air flow. The spectra were recorded with single pulse excitation under the following conditions: ^{29}Si frequency, 79.5 MHz; $\pi/4$ pulse length, 3.8 μs; recycle delay, 10 s, >10^3 scans. ^{13}C frequency, 100.7 MHz; $\pi/4$ pulse length, 3.5 μs; recycle delay, 10 s, >10^3 scans. Adamantane (for ^{13}C) and octakis(trimethylsiloxy)silsesquioxane (for ^{29}Si) were used as the external standards. The ^{29}Si NMR spectra were fitted with 4 Voigt functions to quantify the SiO_4, $CSiO_3$, C_2SiO_2, and C_3SiO units. The Fourier-transform infrared spectroscopy (FT-IR) was measured with a diamond total attenuated reflectance crystal (ATR; Tensor 27 system from Bruker AXS). The spectra were integrated over 28 scans.

X-ray diffraction was carried out with a D8 Discover diffractometer from Bruker AXS. Cu Kα radiation was chosen with a Lynxeye detector in a Bragg−Brentano configuration. We carried out Raman spectroscopy to investigate the structure of the SiOC beads with a Renishaw inVia Raman microscope. The wavelength of the laser was 532 nm, and a grating of 2400 lines/mm was used. The spectral resolution was 1.2 cm^{-1}, the numeric aperture 0.75, and the incident power on the sample ~0.2 mW.

The conductivity of the powder was measured in a custom-built device seen in the Supporting Information, Figure S1, and the two-point-probe was operated with a Keithley 199 System DMM/scanner. The diameter of the pressure cell was 13 mm, and a powder mass of 50 mg was filled in the cell. The powder was contacted with copper foil, and a pressure of 1 MPa was applied during the measurement with a Zwick Roell Xforce HP system.

2.4. Electrochemical Measurements.

Electrode disks with a diameter of 1.42 cm were punched out and placed in a CR2032 coin cell. The electrodes had a thickness after drying of approximately 100 μm while the mass loading (SiOC with carbon black and binder) was 1.9 mg/cm^2. A glass fiber mat (GF/D from Whatman, GE Healthcare Life Science) was used as a separator, and a lithium disk (diameter: 15.6 mm) served as the counter electrode in a two-electrode setup. Lithium hexafluorophosphate ($LiPF_6$) in electrochemical grade ethylene carbonate/dimethyl carbonate (EC/DMC 1:1 by volume; LP30) with a concentration of 1 M from BASF served as the electrolyte.

An Astrol BatSmall battery analyzer was used for the galvanostatic measurements. The cell voltage was applied between +0.01 and +3.0 V versus Li/Li$^+$. For characterization of the rate handling, the first 5 cycles were conducted with a specific current of 35 mA/g, which corresponds to a C-rate of 0.05C when we assume a specific capacity of 700 mA h/g. The specific current was increased to 70 mA/g (0.1C) for 20 cycles, 140 mA/g (0.2C), 350 mA/g (0.5C), 700 mA/g (1C), and 1400 mA/g (2C) for 10 cycles each. Afterward, the specific current was reduced to 70 mA/g for the last cycles. The long-time stability test was carried out using a specific current of 70 mA/g. The specific capacity C_{sp} was calculated with eq 1 with I for the current, dt for the time per charging or discharging step, and m_{SiOC} for the active mass of the electrode (i.e., 90 wt % of SiOC).

$$C_{\mathrm{sp}} = \frac{\int_{t_0}^{t_1} I \, \mathrm{d}t}{m_{\mathrm{SiOC}}} \tag{1}$$

The cyclic voltammograms were recorded with a Squidstat Prime potentiostat from Admiral Instruments with a scan rate of 0.1 mV/s in the same potential window as the galvanostatic measurements.

3. RESULTS AND DISCUSSION

3.1. Material Characterization.

The TEM images in Figure 2 show the synthesized spherical particles after pyrolysis.

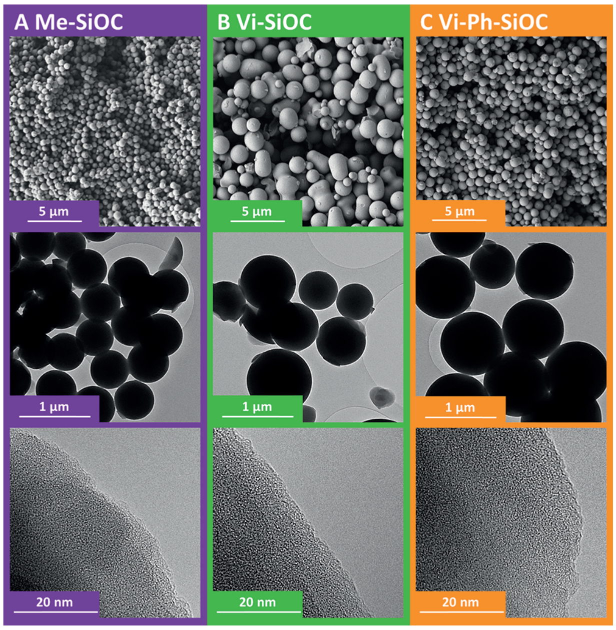

Figure 2. Scanning and transmission electron micrographs of the pyrolyzed SiOC samples. (A) Me-SiOC, (B) Vi-SiOC, and (C) Vi-Ph-SiOC.

The average volume-dependent diameter of the beads is 0.9−2.4 μm, while Me-SiOC has the smallest and Vi-SiOC the largest size within that range. The particle size distributions are plotted in the Supporting Information, Figure S2A. These values, together with the specific surface area, the skeletal density, and the mass loss during pyrolysis, are listed in Table 2. The skeletal density of the SiOCs is in the range 2.16−2.36 g/cm^3, which is similar to values for SiOC ceramics found in the literature (1.9−2.3 g/cm^3).[33,34]

The pyrolysis of the polysilsesquioxane particles leads to a mass loss of 29 wt % for Me-SiOC, 12 wt % for Vi-Ph-SiOC, and 10 wt % for Vi-SiOC. The small methyl groups tend to decompose more easily which explains the higher mass loss. The phenyl groups have a higher molar mass than the vinyl and methyl groups, and we observed correspondingly a larger mass loss for Vi-Ph-SiOC compared to Vi-SiOC.[26] The mass loss also reflects the specific surface area because the decomposition of organic components produces pores. Nitrogen gas sorption was carried out to measure the specific surface area, and the

Table 2. Mass Loss after the Pyrolysis, Average Diameter, Skeletal Density, Measured Specific Surface Area, and Calculated External Surface Area of the SiOC Beads

sample	mass loss (wt %)	number-dependent average diameter (nm)	volume-dependent average diameter (nm)	skeletal density (cm^3/g)	SSA_{BET} (m^2/g)	$SSA_{external}$ (m^2/g)
Me-SiOC	29	576 ± 77	903 ± 77	2.36	6.0	2.8
Vi-SiOC	10	1365 ± 509	2366 ± 509	2.20	3.1	1.2
Vi-Ph-SiOC	12	776 ± 156	1244 ± 156	2.16	4.7	2.2

Table 3. Chemical Composition Measured with EDX and the Theoretical Formula of the SiOC Calculated by the EDX and the Specific Conductivity of Powder of SiOC Beads and Carbon Black (C65) Compacted with 1 MPa Compression Force

sample	Si (wt %)	O (wt %)	C (wt %)	Si (atom %)	O (atom %)	C (atom %)	formula via EDX	specific conductivity (S/m)
Me-SiOC	37.9 ± 5.1	40.0 ± 1.5	22.1 ± 4.4	23.9 ± 4.1	44.0 ± 1.6	32.1 ± 5.0	$SiO_{1.84}C_{0.08} + C_{1.26}$	$<3 \times 10^{-6}$
Vi-SiOC	38.9 ± 3.0	29.6 ± 1.8	31.5 ± 1.3	23.7 ± 2.3	31.6 ± 1.4	44.8 ± 1.1	$SiO_{1.33}C_{0.33} + C_{1.56}$	$(7.3 \pm 0.1) \times 10^{-6}$
Vi-Ph-SiOC	30.6 ± 2.2	29.4 ± 0.8	40.0 ± 1.5	17.5 ± 1.5	29.4 ± 0.5	53.2 ± 1.2	$SiO_{1.68}C_{0.16} + C_{2.89}$	$(1.2 \pm 0.1) \times 10^{-2}$
carbon black			>98			>98	C	2264 ± 22

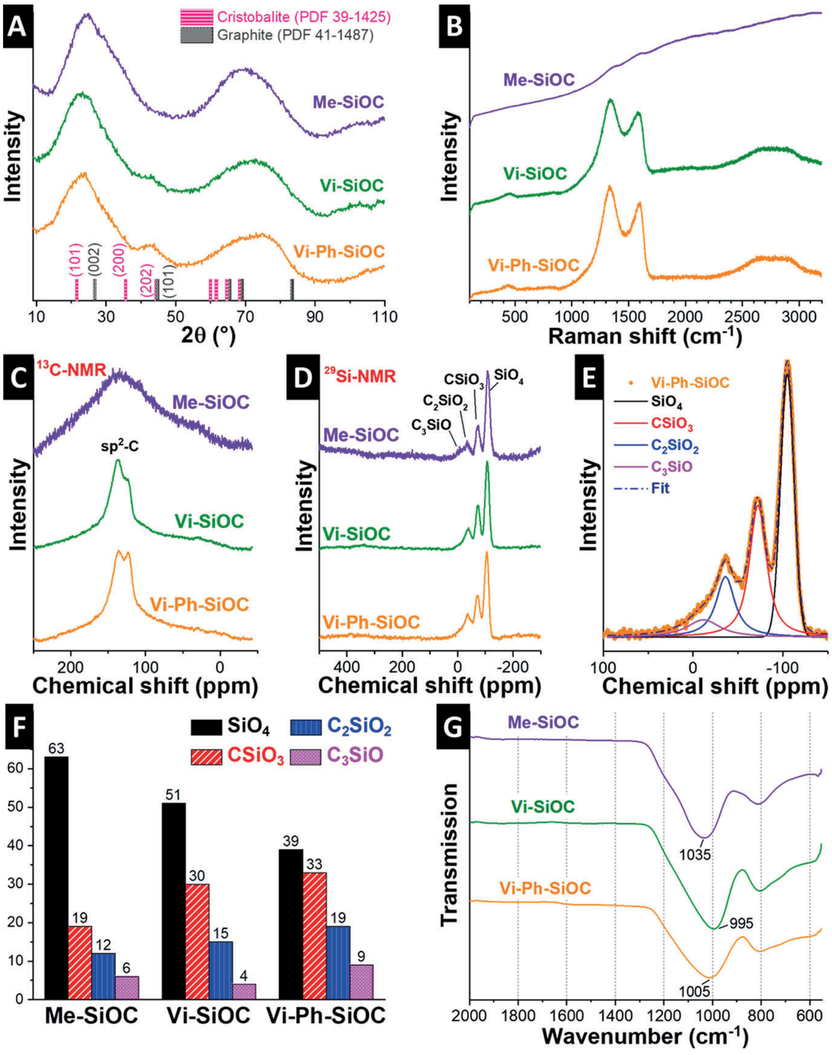

Figure 3. Material characterization of the pyrolyzed SiOC samples. (A) X-ray diffractograms. (B) Raman spectra. (C) ^{13}C NMR. (D) ^{29}Si NMR. (E) ^{29}Si NMR peak deconvolution for Vi-Ph-SiOC. (F) Contributions of the measured Si-bonds. (G) FT-IR spectra.

isotherms are plotted in the Supporting Information (Figure S2B). Me-SiOC and Vi-Ph-SiOC have an SSA_{BET} of 6 and 5 m^2/g, respectively. The sample with the lowest mass loss was Vi-SiOC which also shows the lowest surface area (3 m^2/g). While these values were obtained from gas sorption measurements, we can also calculate the external specific surface area using the volume-dependent average diameter (d) and the skeletal density (ρ) of the ceramic particles with eq 2:

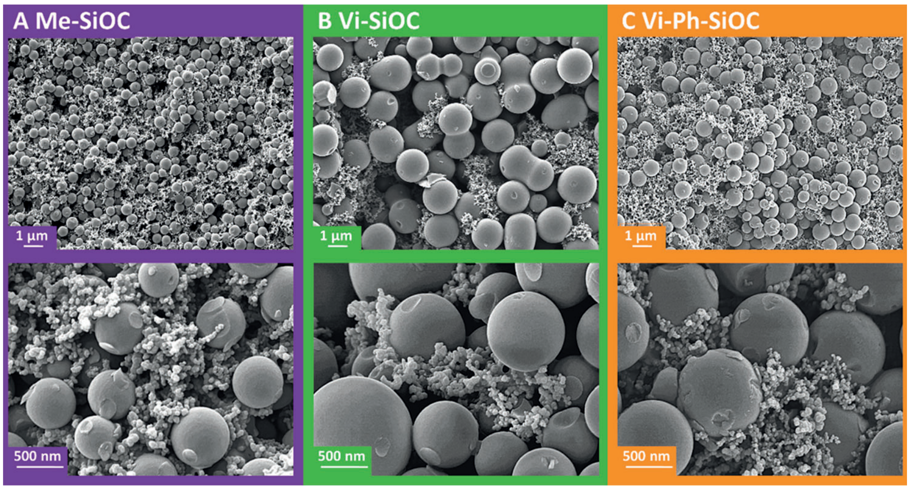

Figure 4. Scanning electron micrographs of the electrodes coated on a nickel current collector with 5 wt % NaCMC (binder) and 5 wt % carbon black (conductive additive). (A) Me-SiOC, (B) Vi-SiOC, and (C) Vi-Ph-SiOC.

$$\mathrm{SSA}_{\mathrm{external}} = \frac{\pi d^2}{\rho d^3 \frac{1}{6}\pi} = \frac{6}{\rho d} \tag{2}$$

As seen from Table 2, the external specific surface area of the particles is approximately half of the measured $\mathrm{SSA}_{\mathrm{BET}}$. Accordingly, all beads have internal pores in addition to the external surface. Overall, the specific surface area of our SiOC beads is very small compared to those of mesoporous SiOC aerogels with around 200 $\mathrm{m^2/g}$.[19,23]

The chemical composition of the SiOC materials was quantified via EDX. As can be seen from Table 3, the material with the lowest carbon amount in the precursor had also the lowest amount of carbon in the ceramic. This finding aligns with previous reports.[26,35] Me-SiOC had a carbon content of 22 wt %, while Vi-SiOC and Vi-Ph-SiOC had 32 and 40 wt % of carbon, respectively. The chemical composition also allows the calculation of the theoretical formula $\mathrm{SiO_{2-2x}C_x} + y\mathrm{C_{free}}$.[36] The samples with a higher overall carbon content also have a higher content of free carbon, which is known to surround the silica domains. Me-SiOC has 1.26 parts of $\mathrm{C_{free}}$ corresponding to one $\mathrm{SiO_{2-2x}C_x}$ unit, which increases for Vi-SiOC to 1.56 and for Vi-Ph-SiOC to 2.89.

The TEM images in Figure 2 show the morphology and the structure of the beads. At high magnifications, we see the nonordered structure of the silicon oxycarbides which were pyrolyzed at 1100 °C. This maximum temperature remains below the temperature at which the formation of crystalline carbides is expected.[13,17] The domain size was estimated from XRD data (Figure 3A) by applying the Scherrer equation and assuming a $\mathrm{SiO_2}$ and graphite phase.[37] The domain size of the $\mathrm{SiO_2}$ and graphite phase for Me-SiOC, Vi-SiOC, and Vi-Ph-SiOC is around 1 nm. Fewer than six unit cells of crystalline $\mathrm{SiO_2}$ with a volume of approximately $0.5 \times 0.5 \times 0.7$ $\mathrm{nm^3}$ can fit into a volume of 1 $\mathrm{nm^3}$ assuming a crystalline structure with $\mathrm{SiO_4}$ tetrahedrons and a Si−O distance of 0.16 nm.[38] A significant difference in the XRD pattern of Vi-SiOC and Vi-Ph-SiOC is an increased peak intensity at 43° 2θ. These two materials have a larger amount of carbon, and the observed peaks align with the (101) plane of incompletely graphitic carbon. The incompletely graphitic nature of carbon is also confirmed with Raman spectroscopy where we observed a characteristic D-mode at 1340 $\mathrm{cm^{-1}}$ and a G-mode at 1600 $\mathrm{cm^{-1}}$ (Figure 3B).[39,40] In the case of the Raman spectrum of Me-SiOC, the D-mode and the G-mode are overlaid by a large fluorescence background.

The $^{13}\mathrm{C}$ and $^{29}\mathrm{Si}$ solid-state NMR spectra give further insights into the chemical structure of the SiOC samples (Figure 3C−F). Me-SiOC has only one very broad peak for the chemical shift of $^{13}\mathrm{C}$ at +130 ppm, which indicates the formation of aromatic carbon groups.[40−43] After the pyrolysis at 1100 °C, there is no signal from the methyl group at around −5 ppm.[42,43] The data of Vi-SiOC and Vi-Ph-SiOC show a larger signal for $\mathrm{sp^2}$-conjugated carbon, which is split into two peaks at 123 and 136 ppm. These signals relate to aromatic carbon.[42,43]

The carbon/silicon and silicon/oxide bonds were further investigated with $^{29}\mathrm{Si}$ NMR (Figure 3D). The presence of $\mathrm{SiO_4}$ groups is documented by a peak at a chemical shift of −105 ppm. This signal is reduced when the silicon atoms are bound to carbon atoms as well. $\mathrm{CSiO_3}$ units have a shift of −73 ppm, $\mathrm{C_2SiO_2}$ units of −35 ppm, and $\mathrm{C_3SiO}$ units of −11 ppm.[19,44] We deconvoluted these contributions by fitting four Voigt functions (Figure 3F). $\mathrm{SiO_4}$ units are dominant in all samples, and we see the largest contributions thereof for Me-SiOC (63%), which has also the lowest amount of silicon−carbon bonds. There are fewer $\mathrm{SiO_4}$ units in Vi-SiOC (51%) and even less for Vi-Ph-SiOC (39%). The number of silicon−carbon bonds increases with the amount of carbon. Vi-Ph-SiOC has the highest amount of $\mathrm{CSiO_3}$, $\mathrm{C_2SiO_2}$, and $\mathrm{C_3SiO}$ units (in total 61%). Vi-SiOC has a similar amount of silicon atoms only bound to oxygen, as silicon atoms bound to oxygen and carbon at the same time.

The FT-IR spectra provide further information about the structure of the pyrolyzed SiOC materials. Peaks in the range 1000−1100 $\mathrm{cm^{-1}}$ relate to an antisymmetric stretching mode Si−O−Si network.[45] A shift toward lower wavenumbers of the latter occurs when carbon atoms are introduced to the structure (Figure 3G).[19,45] This mode is at 1035 $\mathrm{cm^{-1}}$ for Me-SiOC, and the downshift becomes larger for a higher amount of carbon. Accordingly, Vi-SiOC and Vi-Ph-SiOC exhibit a Si−O−Si stretching mode at 995 and 1005 $\mathrm{cm^{-1}}$, respectively. Another peak is observed at 810 $\mathrm{cm^{-1}}$ for all samples, which indicates Si−C or C−O bonds.[45,46]

The electrical conductivity of the SiOC powders was measured at a pressure of 1 MPa and is listed in Table 3.

DOI: 10.1021/acsaem.8b00716
ACS Appl. Energy Mater. 2018, 1, 2961−2970

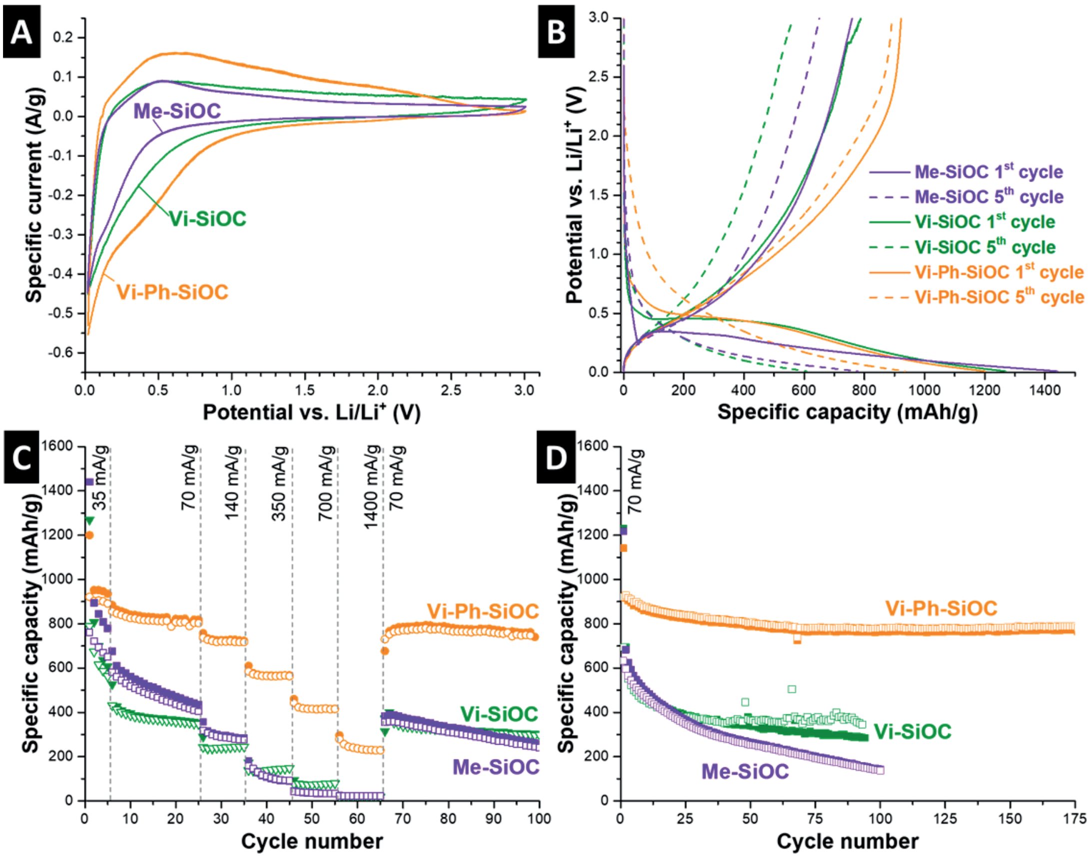

Figure 5. Electrochemical characterization of pyrolyzed Me-SiOC, Vi-SiOC, and Vi-Ph-SiO using 1 M $LiPF_6$ in EC/DMC. (A) Cyclic voltammograms of the 5th cycle at 0.1 mV/s. (B) Galvanostatic charge/discharge profiles of the 1st and 5th cycle at 35 mA/g. (C) Rate capability at 35−1400 mA/g. (D) Performance stability at 70 mA/g.

The conductivity of Me-SiOC was below the limit of detection of 3×10^{-6} S/m. Vi-SiOC had a low conductivity of $(7.3 \pm 0.1) \times 10^{-6}$ S/m, and Vi-Ph-SiOC had the value of $(1.2 \pm 0.1) \times 10^{-2}$ S/m due to the higher amount of carbon in the sample. An increase of the conductivity of SiOCs with an increasing amount of free carbon was also observed by Kasper et al. and was found beneficial for the use in LIBs.[22,47] Although the electrical conductivity of Vi-Ph-SiOC beads was much larger compared to those of the other materials, it is still low compared to those of other electrode materials; accordingly, we added carbon black (C65 with a conductivity of 2264 ± 22 S/m) to all electrodes.

3.2. Electrochemical Characterization of SiOC Beads as Anodes for Li-Ion Batteries.

For electrochemical measurements, the pyrolyzed SiOC beads were mixed with NaCMC binder and carbon black. The resulting cast electrodes show a homogeneous distribution for all three types of material (Figure 4). The carbon black particles percolate well between the SiOC beads to guarantee a sufficient electrical conductivity.[48] The specific capacity was normalized to the amount of silicon oxycarbide.[13,19,22,27]

First, we determined the possible contribution of carbon black to the measured specific capacity at 0.1 mV/s in the used potential range (from +0.01 to +3.0 V versus Li/Li$^+$). The cyclic voltammograms and the voltage profile of an electrode only composed of carbon black are provided in the Supporting Information, Figure S3. The first lithiation cycle at 35 mA/g of carbon black electrodes provides a specific capacity of 480 mA h/g, and the first delithiation capacity is about 250 mA h/g. The latter value remains stable during four subsequent charge/discharge cycles. In our SiOC electrodes, we admixed only 5 wt % of carbon black. Therefore, the contribution of carbon black to the measured specific capacity of our SiOC materials is around 13 mA h/g. This contribution is minor compared to the high specific capacity of the SiOC (>700 mA h/g).

The cyclic voltammograms for the fifth cycle were recorded at 0.1 mV/s in a potential range from +0.01 to +3.0 V versus Li/Li$^+$ and plotted in Figure 5A. The data show a cathodic lithiation peak below 1 V versus Li/Li$^+$. Vi-Ph-SiOC shows the largest specific current response and, thereby, the largest specific capacity. This is in agreement with the study of Wilamowska-Zawlocka et al. showing that a mixture of vinyl with phenyl groups with the ratio of 1:2 yielded the best performance for SiOC materials.[20] The extraction of the Li$^+$ out of the SiOC occurs at around +0.6 V versus Li/Li$^+$. Similar potentials for the lithiation (discharging) and delithiation (charging) are seen in the galvanostatic charge/discharge profiles shown in Figure 5B. As common for LIB anodes, the first-cycle lithiation capacity is much larger than the following, which is partially attributed to the reduction of the electrolyte below 1 V versus Li/Li$^+$ forming the solid−electrolyte interphase (SEI).[7] The first delithiation of the Vi-Ph-SiOC yielded a specific capacity of 922 mA h/g, which slightly reduced to 892 mA h/g for the fifth cycle. Me-SiOC and Vi-SiOC have a higher specific capacity of 1440 mA h/g and 1269 mA h/g during the first lithiation cycle (Figure 5C,D) because

Table 4. Electrochemical Performance[a] of the SiOC Beads Compared with the Literature

sample	electrode	carbon content (wt %)	potential vs Li/Li$^+$ (V)	specific capacity (mA h/g) 1st cycle L	1st cycle D	5th cycle L	5th cycle D	100th cycle L	100th cycle D	capacity retention (%)	ref
Me-SiOC	90 wt % SiOC; 5 wt % NaCMC; 5 wt % carbon black	22	0.01–3	1440	761	779	650	258	241	32	this work
Vi-SiOC	90 wt % SiOC; 5 wt % NaCMC; 5 wt % carbon black	32	0.01–3	1269	789	608	563	302	299	38	this work
Vi-Ph-SiOC	90 wt % SiOC; 5 wt % NaCMC; 5 wt % carbon black	40	0.01–3	1200	922	936	892	762	747	83	this work
carbon black (C65)	95 wt % carbon black; 5 wt % NaCMC	98	0.01–3	479	251	272	251	282	279	111	this work
PhTES:VTES 2:1 sol–gel particles	85 wt % SiOC; 10 wt % PVdF; 5 wt % carbon black	39	0.005–3	1462	900				558 (134 cycles)	62	20
electrospun Sn/SiOC fibers (0.05Sn-1200)	free-standing electrode	41	0.01–3	1075	840	804	801		509	61	15
SiOC-1100 °C microparticles	85 wt % SiOC; 10 wt % PVdF; 5 wt % carbon black	42	0.005–3	866	532						13
SiOC-1000 °C (PD2) microparticles	85 wt % SiOC; 10 wt % PVdF; 5 wt % carbon black	55	0–3	898	568						14
PR/DVB SiOC	85 wt % SiOC; 10 wt % PVdF; 5 wt % carbon black	59	0.005–3	791	504				338 (60 cycles)	67	22
PR SiOC	85 wt % SiOC; 10 wt % PVdF; 5 wt % carbon black	51	0.005–3	872	536				304 (60 cycles)	57	22
SR/RR SiOC	85 wt % SiOC; 10 wt % PVdF; 5 wt % carbon black	39	0.005–3	1178	683				90 (60 cycles)	14	22
PB-SiOC microparticles	85 wt % SiOC; 7.5 wt % PVdF; 7.5 wt % carbon black	72	0–3	867	608	~570	~560		~550 (50 cycles)	90	12
SiOC-Ar aerogels	85 wt % SiOC; 10 wt % PVdF; 5 wt % carbon black	>47	0.005–3	~1500	~780		~660		~430	55	19
SiOC aerogels	85 wt % SiOC; 10 wt % PVdF; 5 wt % carbon black	43	0.005–3	~1160	~580			~420	~450	78	23
SiOC–CNT composite	80 wt % SiOC/CNT; 10 wt % PAA; 10 wt % carbon black	>16	0.01–2.5	1255	842				686 (40 cycles)	82	24
porous Si/C	75 wt % Si/C; 5 wt % carbon black; 20 wt % NaCMC	66	0.005–3	1190	~750	636		~630		84	53

[a] L, lithiation; D, delithiation; PVdF, polyvinylidene difluoride; PAA, poly(acrylic acid). The capacity retention is calculated from the difference between the first and last reported cycle in the respective studies.

of the higher amount of silicon oxide in the silicon oxycarbide.[14,20,22] However, the higher initial lithiation capacity cannot be maintained during delithiation. Me-SiOC and Vi-SiOC have a specific capacity of only 761 and 789 mA h/g, respectively, in the first delithiation cycle. Possibly more significant Li_2O formation occurs for Me-SiOC and Vi-SiOC.[7,49] Me-SiOC has a higher initial specific capacity than Vi-SiOC, but the long-time performance stability is better for Vi-SiOC (Figure 5D). This is because of the higher amount of free carbon in the structure and more silicon−carbon bonds. The performance of Me-SiOC and Vi-SiOC in $LiPF_6$ in EC/DMC is relatively low at high rates. Both materials have a specific capacity below 200 mA h/g at a specific current of 350 mA/g (corresponds to ∼0.5C). The higher content of free carbon in Vi-SiOC improves the specific capacity at high rates (700 mA/g; ∼1C) with around 75 mA h/g compared to 35 mA h/g of Me-SiOC.[22]

Vi-Ph-SiOC shows a superior electrochemical performance at high specific currents as well as very high performance stability among all SiOC anode materials in $LiPF_6$ in EC/DMC. By increasing the specific current to 70 mA/g, the specific capacity reduces from 936 (5th lithiation) to 885 (6th lithiation) mA h/g. Vi-Ph-SiOC still provided a specific capacity of 610 mA h/g measured at 350 mA/g (36th lithiation) and at the highest measured rate of 1400 mA/g still 116 mA h/g (56th lithiation). This performance is accomplished even with the low specific surface area of only 5 m^2/g. Thereby, there is a lack of a large pore volume of intraparticle pores which would contribute toward fast ion transport kinetics. For example, Pradeep et al. synthesized a mesoporous SiOC aerogel with a specific surface area of more than 200 m^2/g.[23] They obtained a high rate capability by a porous structure with a specific capacity of 600 mA h/g at 360 mA/g (0.5C), which is similar to our results.[23] At even higher C-rates (720 mA/g; 1C), the latter material provided still a specific capacity of ∼500 mA h/g; however, the mesopores of the aerogel had a diameter of 24 nm which is much smaller than the diameter (∼1 μm) of the SiOC beads from this study. The reduction of the diffusion length for the Li through the SiOC to a nanometer range is beneficial for very high C-rates (>1C) when considering the low diffusion coefficient of Li-ions in SiOCs in the range 10^{-9}−10^{-11} cm^2/s; for comparison, the Li-ion diffusion coefficients of amorphous Si films is 10^{-10}−10^{-11} cm^2/s, of Si nanowires is 10^{-10} cm^2/s, and of nano-Si is 10^{-12}−$10^{-13}$$cm^2/s$.[47,50−52] When we returned for operation of the Vi-Ph-SiOC beads to a lower specific current (70 mA/g) after 50 cycles, a specific charge capacity of about 800 mA h/g was re-established. The specific capacity of Me-SiOC and Vi-SiOC was also reaching a similar value for the specific capacity after the rate performance test.

The coin cells were disassembled after the rate capability test to investigate the morphology of the beads with TEM (see the Supporting Information, Figure S4). As can be seen from the electron micrographs, the SiOC beads conserved their shape after 100 cycles, and the spherical carbon black particles remain well-distributed throughout the electrode. The absence of visible structural changes of the electrode material encourages further characterization of the long-time performance; accordingly, we carried out performance stability tests at 0.1C (70 mA/g). After 100 cycles (Figure 5D), Vi-Ph-SiOC still provides a lithiation capacity of 764 mA h/g and a delithiation capacity of 778 mA h/g, which corresponds to 84% compared to the first lithiation. The specific capacitance remained stable from the 100th onward until the end of the testing procedure (175th cycle) at a value of 773 mA h/g for the lithiation capacity and a delithiation capacity of 789 mA h/g. We see a similar pattern compared to the rate capability data where Me-SiOC and Vi-SiOC have lower stability compared to Vi-Ph-SiOC. The performance stability of the samples Me-SiOC and Vi-SiOC measured only at low C-rates is lower after the same number of cycles compared to the samples which were also cycled at high C-rates. The performance stability of Vi-Ph-SiOC is similar for both measurement methods because of its high reversibility. Graczyk-Zajac et al. showed that the presence of silicon−carbon bonds improves the stability of SiOC anode materials.[19] Since all of our materials have silicon−carbon bonds in different amounts we conclude that a high amount of silicon−carbon bonds combined with a higher free carbon content is beneficial for a high performance stability.

Our data on SiOC as the LIB anode in 1 M $LiPF_6$ in EC/DMC is compared to the literature data in Table 4. A direct comparison is complicated by the influence of silicon oxycarbide structure, type and amount of the binder and the conductive additive, number of charge/discharge cycles, charge/discharge rates, and the voltage window. Nevertheless, Table 4 shows that Vi-Ph-SiOC has a higher specific capacity after the long-time experiment than all other silicon oxycarbides which we found in the literature. Our material also provides a higher specific capacity than the sol−gel-produced particles from Wilamowska-Zawlocka et al. using similar precursors for their synthesis.[20] The capacity retention of Vi-Ph-SiOC after 100 cycles is 83% higher than most other materials. The high performance stability originates from the high amount of carbon (especially free carbon) and possibly with carbon/silicon bonds, which leads to a higher reversible capacity. The spherical shape of the particles may also benefit the compensation of volume expansion which occurs during the alloying reaction.

4. CONCLUSIONS

Three types of spherical SiOC materials were synthesized with a MicroJet reactor by use of methyltrimethoxysilane, vinyltrimethoxysilane, and a mixture of vinyltrimethoxysilane with phenyltrimethoxysilane. Thereby, no additional cross-linking agent, which could cause impurities, was needed to preserve the morphology of the particles. The use of the MicroJet reactor to produce beads is also beneficial because the particles have a similar size, and the volumetric changes during lithiation and delithiation are equally distributed.

By choice of the precursor, it was possible to influence the amount of silicon−carbon bonds as well as the content of free carbon. Both parameters are important for the synthesis of SiOC anode materials for Li-ion batteries with high capacity and performance stability. The mixture of vinyl and phenyl groups provided the best electrochemical performance (922 mA h/g for first delithiation) and a high specific delithiation capacity after 100 cycles of 677 mA h/g was obtained. A mixture of phenyl and vinyl groups showed for the resulting SiOC materials the best performance in our study. Future optimization of the power-handling ability of the SiOC beads may be further promoted by additional mesopores by adding a template to the silane solution which decomposes during the pyrolysis.

■ ASSOCIATED CONTENT

Ⓢ Supporting Information

The Supporting Information is available free of charge on the ACS Publications website at DOI: 10.1021/acsaem.8b00716.

> Images of the conductivity-probe setup, supplementary data on particle size distribution, nitrogen gas sorption isotherms, electrochemical characterization of carbon black (used as a conductive additive), and post-mortem TEM images of the SiOC beads after the electrochemical measurements (PDF)

■ AUTHOR INFORMATION

Corresponding Authors

*E-mail: guido.kickelbick@uni-saarland.de.
*E-mail: volker.presser@leibniz-inm.de.

ORCID

Guido Kickelbick: 0000-0001-6813-9269
Volker Presser: 0000-0003-2181-0590

Notes

The authors declare no competing financial interest.

■ ACKNOWLEDGMENTS

The INM authors kindly acknowledge the continuing support of Eduard Arzt (INM). We also thank Simon Fleischmann, Ingrid Grobelsek, Hwirim Shim, and Robert Drumm (all INM) for technical support and discussions and Michael Zimmer (Saarland University) for the NMR measurements. We also acknowledge the kind support of the INM workshop for the design and construction of the conductivity-probe setup.

■ REFERENCES

(1) Diouf, B.; Pode, R. Potential of Lithium-Ion Batteries in Renewable Energy. *Renewable Energy* **2015**, *76*, 375−380.

(2) Dunn, J. B.; Gaines, L.; Kelly, J. C.; James, C.; Gallagher, K. G. The Significance of Li-ion Batteries in Electric Vehicle Life-cycle Energy and Emissions and Recycling's Role in its Reduction. *Energy Environ. Sci.* **2015**, *8* (1), 158−168.

(3) Nitta, N.; Wu, F.; Lee, J. T.; Yushin, G. Li-ion Battery Materials: Present and Future. *Mater. Today* **2015**, *18* (5), 252−264.

(4) Li, H.; Wang, Z.; Chen, L.; Huang, X. Research on Advanced Materials for Li-Ion Batteries. *Adv. Mater.* **2009**, *21* (45), 4593−4607.

(5) Boukamp, B. A.; Lesh, G. C.; Huggins, R. A. All-Solid Lithium Electrodes with Mixed-Conductor Matrix. *J. Electrochem. Soc.* **1981**, *128* (4), 725−729.

(6) Kasavajjula, U.; Wang, C.; Appleby, A. J. Nano-and Bulk-Silicon-Based Insertion Anodes for Lithium-ion Secondary Cells. *J. Power Sources* **2007**, *163* (2), 1003−1039.

(7) Zhang, W.-J. A Review of the Electrochemical Performance of Alloy Anodes for Lithium-ion Batteries. *J. Power Sources* **2011**, *196* (1), 13−24.

(8) Dash, R.; Pannala, S. Theoretical Limits of Energy Density in Silicon-Carbon Composite Anode Based Lithium Ion Batteries. *Sci. Rep.* **2016**, *6*, 27449.

(9) Szczech, J. R.; Jin, S. Nanostructured Silicon for High Capacity Lithium Battery Anodes. *Energy Environ. Sci.* **2011**, *4* (1), 56−72.

(10) Ma, X.; Liu, M.; Gan, L.; Tripathi, P. K.; Zhao, Y.; Zhu, D.; Xu, Z.; Chen, L. Novel mesoporous Si@C microspheres as anodes for lithium-ion batteries. *Phys. Chem. Chem. Phys.* **2014**, *16* (9), 4135−4142.

(11) Liu, M.; Ma, X.; Gan, L.; Xu, Z.; Zhu, D.; Chen, L. A facile synthesis of a novel mesoporous Ge@C sphere anode with stable and high capacity for lithium ion batteries. *J. Mater. Chem. A* **2014**, *2* (40), 17107−17114.

(12) Fukui, H.; Ohsuka, H.; Hino, T.; Kanamura, K. A Si-O-C Composite Anode: High Capability and Proposed Mechanism of Lithium Storage Associated with Microstructural Characteristics. *ACS Appl. Mater. Interfaces* **2010**, *2* (4), 998−1008.

(13) Kaspar, J.; Graczyk-Zajac, M.; Riedel, R. Lithium Insertion into Carbon-rich SiOC Ceramics: Influence of Pyrolysis Temperature on Electrochemical Properties. *J. Power Sources* **2013**, *244*, 450−455.

(14) Pradeep, V. S.; Graczyk-Zajac, M.; Riedel, R.; Soraru, G. D. New Insights in to the Lithium Storage Mechanism in Polymer Derived SiOC Anode Materials. Electrochim. *Electrochim. Acta* **2014**, *119*, 78−85.

(15) Tolosa, A.; Widmaier, M.; Krüner, B.; Griffin, J. M.; Presser, V. Continuous Silicon Oxycarbide Fiber Mats with Tin Nanoparticles as a High Capacity Anode for Lithium-Ion Batteries. *Sustainable Energy Fuels* **2018**, *2* (1), 215−228.

(16) Scarmi, A.; Sorarù, G. D.; Raj, R. The Role of Carbon in Unexpected Visco (An) Elastic Behavior of Amorphous Silicon Oxycarbide Above 1273 K. *J. Non-Cryst. Solids* **2005**, *351* (27−29), 2238−2243.

(17) Kleebe, H.-J.; Blum, Y. D. SiOC Ceramic with High Excess Free Carbon. *J. Eur. Ceram. Soc.* **2008**, *28* (5), 1037−1042.

(18) Guo, B.; Shu, J.; Wang, Z.; Yang, H.; Shi, L.; Liu, Y.; Chen, L. Electrochemical Reduction of Nano-SiO_2 in Hard Carbon as Anode Material for Lithium Ion Batteries. *Electrochem. Commun.* **2008**, *10* (12), 1876−1878.

(19) Graczyk-Zajac, M.; Vrankovic, D.; Waleska, P.; Hess, C.; Sasikumar, P. V.; Lauterbach, S.; Kleebe, H.-J.; Sorarù, G. D. The Li-storage Capacity of SiOC Glasses with and without Mixed Silicon Oxycarbide Bonds. *J. Mater. Chem. A* **2018**, *6* (1), 93−103.

(20) Wilamowska-Zawlocka, M.; Puczkarski, P.; Grabowska, Z.; Kaspar, J.; Graczyk-Zajac, M.; Riedel, R.; Sorarù, G. D. Silicon Oxycarbide Ceramics as Anodes for Lithium Ion Batteries: Influence of Carbon Content on Lithium Storage Capacity. *RSC Adv.* **2016**, *6* (106), 104597−104607.

(21) Rouxel, T.; Massouras, G.; Sorarù, G.-D. High Temperature Behavior of a Gel-derived SiOC Glass: Elasticity and Viscosity. *J. Sol-Gel Sci. Technol.* **1999**, *14* (1), 87−94.

(22) Kaspar, J.; Graczyk-Zajac, M.; Choudhury, S.; Riedel, R. Impact of the Electrical Conductivity on the Lithium Capacity of Polymer-derived Silicon Oxycarbide (SiOC) Ceramics. *Electrochim. Acta* **2016**, *216*, 196−202.

(23) Pradeep, V. S.; Ayana, D. G.; Graczyk-Zajac, M.; Soraru, G. D.; Riedel, R. High Rate Capability of SiOC Ceramic Aerogels with Tailored Porosity as Anode Materials for Li-ion Batteries. *Electrochim. Acta* **2015**, *157*, 41−45.

(24) Bhandavat, R.; Singh, G. Stable and Efficient Li-ion Battery Anodes Prepared from Polymer-derived Silicon Oxycarbide−Carbon Nanotube Shell/Core Composites. *J. Phys. Chem. C* **2013**, *117* (23), 11899−11905.

(25) Odenwald, C.; Kickelbick, G. Additive-free Continuous Synthesis of Silica and ORMOSIL Micro-and Nanoparticles Applying a MicroJet Reactor. *J. Sol-Gel Sci. Technol.* **2018**, DOI: 10.1007/s10971-018-4626-x.

(26) Krüner, B.; Odenwald, C.; Tolosa, A.; Schreiber, A.; Aslan, M.; Kickelbick, G.; Presser, V. Carbide-derived Carbon Beads with Tunable Nanopores from Continuously Produced Polysilsesquioxanes for Supercapacitor Electrodes. *Sustainable Energy Fuels* **2017**, *1* (7), 1588−1600.

(27) Kaspar, J.; Terzioglu, C.; Ionescu, E.; Graczyk-Zajac, M.; Hapis, S.; Kleebe, H. J.; Riedel, R. Stable SiOC/Sn Nanocomposite Anodes for Lithium-Ion Batteries with Outstanding Cycling Stability. *Adv. Funct. Mater.* **2014**, *24* (26), 4097−4104.

(28) Magasinski, A.; Zdyrko, B.; Kovalenko, I.; Hertzberg, B.; Burtovyy, R.; Huebner, C. F.; Fuller, T. F.; Luzinov, I.; Yushin, G. Toward Efficient Binders for Li-Ion Battery Si-Based Anodes: Polyacrylic Acid. *ACS Appl. Mater. Interfaces* **2010**, *2* (11), 3004−3010.

(29) Chou, S. L.; Pan, Y.; Wang, J. Z.; Liu, H. K.; Dou, S. X. Small Things Make a Big Difference: Binder Effects on the Performance of

Li and Na Batteries. *Phys. Chem. Chem. Phys.* **2014**, *16* (38), 20347−20359.

(30) Komaba, S.; Shimomura, K.; Yabuuchi, N.; Ozeki, T.; Yui, H.; Konno, K. Study on Polymer Binders for High-Capacity SiO Negative Electrode of Li-Ion Batteries. *J. Phys. Chem. C* **2011**, *115* (27), 13487−13495.

(31) Schneider, C. A.; Rasband, W. S.; Eliceiri, K. W. NIH Image to ImageJ: 25 Years of Image Analysis. *Nat. Methods* **2012**, *9* (7), 671.

(32) Brunauer, S.; Emmett, P. H.; Teller, E. Adsorption of Gases in Multimolecular Layers. *J. Am. Chem. Soc.* **1938**, *60* (2), 309−319.

(33) Vakifahmetoglu, C.; Zeydanli, D.; Innocentini, M. D.; Ribeiro, F. D.; Lasso, P. R.; Soraru, G. D. Gradient-Hierarchic-Aligned Porosity SiOC Ceramics. *Sci. Rep.* **2017**, *7*, 41049.

(34) Zanchetta, E.; Cattaldo, M.; Franchin, G.; Schwentenwein, M.; Homa, J.; Brusatin, G.; Colombo, P. Stereolithography of SiOC Ceramic Microcomponents. *Adv. Mater.* **2016**, *28* (2), 370−376.

(35) Bujalski, D. R.; Grigoras, S.; Wieber, G. M.; Zank, G. A. Stoichiometry Control of SiOC Ceramics by Siloxane Polymer Functionality. *J. Mater. Chem.* **1998**, *8* (6), 1427−1433.

(36) Soraru, G. D.; D'Andrea, G.; Campostrini, R.; Babonneau, F.; Mariotto, G. Structural Characterization and High-Temperature Behavior of Silicon Oxycarbide Glasses Prepared from Sol-Gel Precursors Containing Si-H Bonds. *J. Am. Ceram. Soc.* **1995**, *78* (2), 379−387.

(37) Scherrer, P. Bestimmung der Größe und der inneren Struktur von Kolloidteilchen mittels Röntgenstrahlen. *Nachr. Ges. Wiss. Göttingen* **1918**, *2*, 98−100.

(38) Wright, A. F.; Leadbetter, A. J. The Structures of the *β*-Cristobalite Phases of SiO_2 and $AlPO_4$. *Philos. Mag.* **1975**, *31* (6), 1391−1401.

(39) Ferrari, A. C.; Robertson, J. Interpretation of Raman Spectra of Disordered and Amorphous Carbon. *Phys. Rev. B: Condens. Matter Mater. Phys.* **2000**, *61* (20), 14095.

(40) Kleebe, H.-J.; Gregori, G.; Babonneau, F.; Blum, Y. D.; MacQueen, D. B.; Masse, S. Evolution of C-Rich SiOC Ceramics. *Z. Metallkd.* **2006**, *97* (6), 699−709.

(41) Trimmel, G.; Badheka, R.; Babonneau, F.; Latournerie, J.; Dempsey, P.; Bahloul-Houlier, D.; Parmentier, J.; Soraru, G. D. Solid State NMR and TG/MS Study on the Transformation of Methyl Groups During Pyrolysis of Preceramic Precursors to SiOC Glasses. *J. Sol-Gel Sci. Technol.* **2003**, *26* (1−3), 279−283.

(42) Brus, J.; Kolář, F.; Machovič, V.; Svıtilová, J. Structure of Silicon Oxycarbide Glasses Derived from Poly (Methylsiloxane) and Poly [Methyl(Phenyl)siloxane] Precursors. *J. Non-Cryst. Solids* **2001**, *289* (1−3), 62−74.

(43) Sitarz, M.; Czosnek, C.; Jelen, P.; Odziomek, M.; Olejniczak, Z.; Kozanecki, M.; Janik, J. F. SiOC Glasses Produced from Silsesquioxanes by the Aerosol-assisted Vapor Synthesis Method. *Spectrochim. Acta, Part A* **2013**, *112*, 440−445.

(44) Widgeon, S. J.; Sen, S.; Mera, G.; Ionescu, E.; Riedel, R.; Navrotsky, A. ^{29}Si and ^{13}C Solid-state NMR Spectroscopic Study of Nanometer-scale Structure and Mass Fractal Characteristics of Amorphous Polymer Derived Silicon Oxycarbide Ceramics. *Chem. Mater.* **2010**, *22* (23), 6221−6228.

(45) Grill, A.; Neumayer, D. A. Structure of Low Dielectric Constant to Extreme Low Dielectric Constant SiCOH Films: Fourier Transform Infrared Spectroscopy Characterization. *J. Appl. Phys.* **2003**, *94* (10), 6697−6707.

(46) Oh, T.; Choi, C. K. Comparison Between SiOC Thin Films Fabricated by Using Plasma Enhance Chemical Vapor Deposition and SiO_2 Thin Films by Using Fourier Transform Infrared Spectroscopy. *J. Korean Phys. Soc.* **2010**, *56* (4), 1150−1155.

(47) Kaspar, J.; Graczyk-Zajac, M.; Riedel, R. Determination of the chemical diffusion coefficient of Li-ions in carbon-rich silicon oxycarbide anodes by electro-analytical methods. *Electrochim. Acta* **2014**, *115*, 665−670.

(48) Pandolfo, A. G.; Wilson, G. J.; Huynh, T. D.; Hollenkamp, A. F. The Influence of Conductive Additives and Inter-Particle Voids in Carbon EDLC Electrodes. *Fuel Cells* **2010**, *10* (5), 856−864.

(49) Miyachi, M.; Yamamoto, H.; Kawai, H.; Ohta, T.; Shirakata, M. Analysis of SiO Anodes for Lithium-ion Batteries. *J. Electrochem. Soc.* **2005**, *152* (10), A2089−A2091.

(50) Ding, N.; Xu, J.; Yao, Y. X.; Wegner, G.; Fang, X.; Chen, C. H.; Lieberwirth, I. Determination of the diffusion coefficient of lithium ions in nano-Si. *Solid State Ionics* **2009**, *180* (2), 222−225.

(51) Ruffo, R.; Hong, S. S.; Chan, C. K.; Huggins, R. A.; Cui, Y. Impedance Analysis of Silicon Nanowire Lithium Ion Battery Anodes. *J. Phys. Chem. C* **2009**, *113* (26), 11390−11398.

(52) Xie, J.; Imanishi, N.; Zhang, T.; Hirano, A.; Takeda, Y.; Yamamoto, O. Li-ion diffusion in amorphous Si films prepared by RF magnetron sputtering: A comparison of using liquid and polymer electrolytes. *Mater. Chem. Phys.* **2010**, *120* (2), 421−425.

(53) Li, X.; Yan, P.; Xiao, X.; Woo, J. H.; Wang, C.; Liu, J.; Zhang, J.-G. Design of Porous Si/C−Graphite Electrodes with Long Cycle Stability and Controlled Swelling. *Energy Environ. Sci.* **2017**, *10* (6), 1427−1434.

Supporting Information

Silicon Oxycarbide Beads from Continuously Produced Polysilsesquioxane as Stable Anode Material for Lithium-ion Batteries

Benjamin Krüner,[1,2] Christina Odenwald,[3] Nicolas Jäckel,[1,2]
Aura Tolosa,[1,2] Guido Kickelbick,[3,*] and Volker Presser[1,2,*]

[1] *INM - Leibniz Institute for New Materials, 66123 Saarbrücken, Germany*

[2] *Department of Materials Science and Engineering, Saarland University, 66123 Saarbrücken, Germany*

[3] *Inorganic Solid State Chemistry, Saarland University, 66123 Saarbrücken, Germany*

* *Corresponding authors' eMails:*

guido.kickelbick@uni-saarland.de *(G. Kickelbick);* volker.presser@leibniz-inm.de *(V. Presser)*

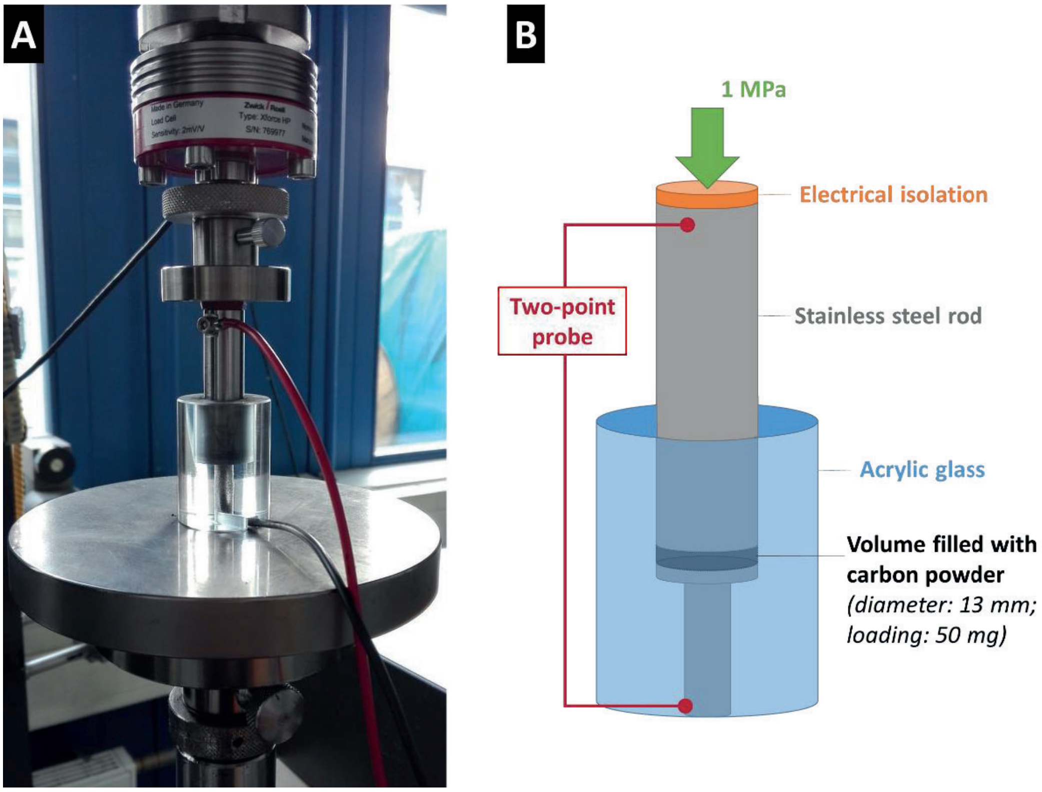

Figure S1: (A) Photograph of the custom-built conductivity probe setup and the corresponding (B) schematic setup.

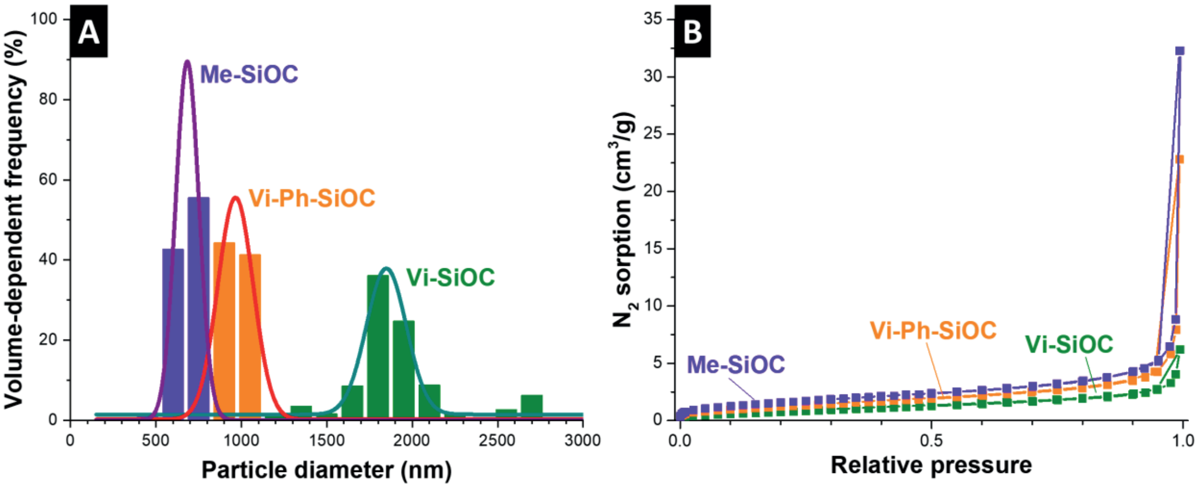

Figure S2: (A) Particle size distribution obtained by the analysis of SEM images and (B) nitrogen sorption isotherms at -196 °C of the samples Me-SiOC, Vi-SiOC, and Vi-Ph-SiOC.

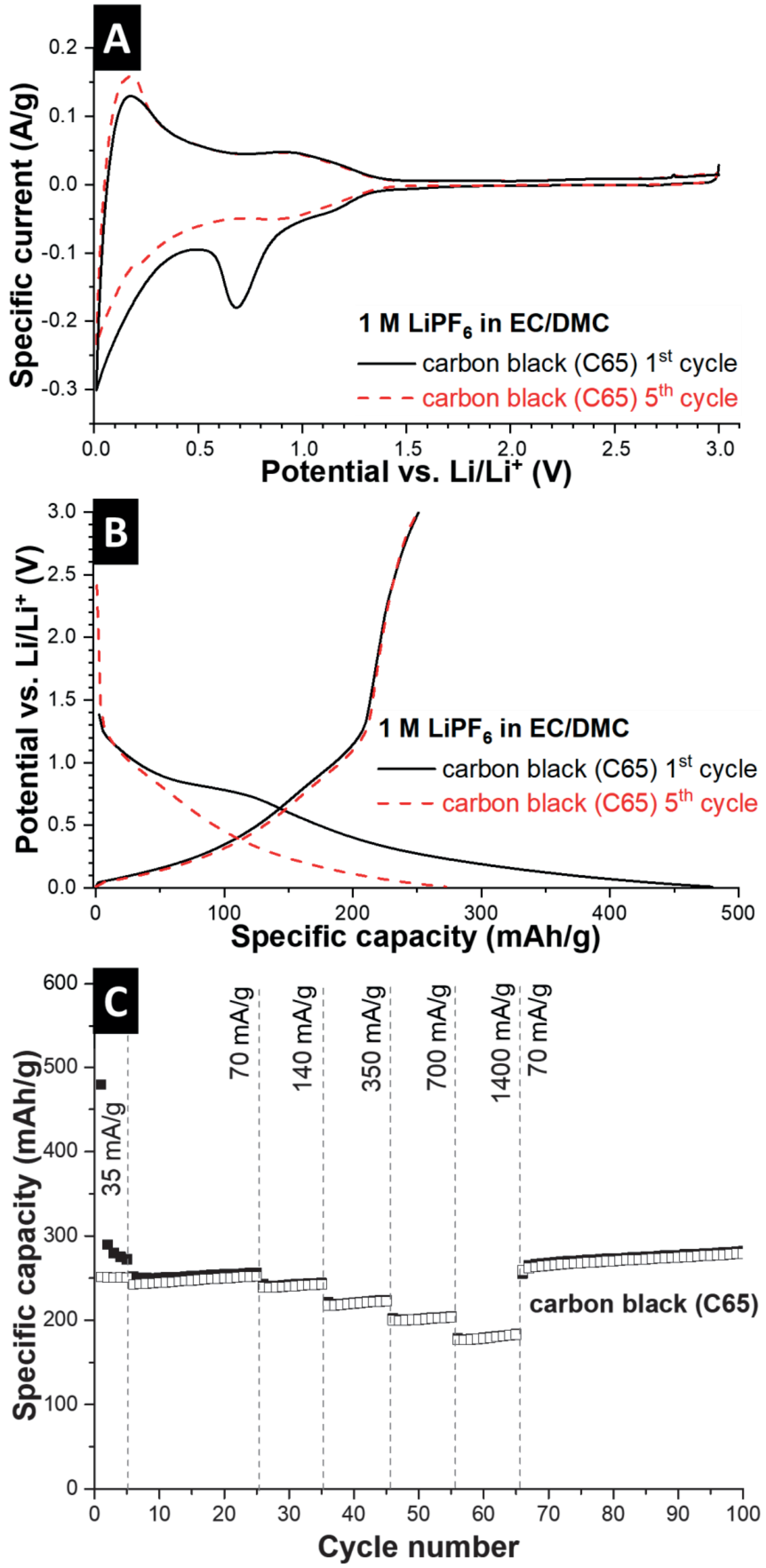

Figure S3: Electrochemical characterization of the carbon black (C65) using 1 M $LiPF_6$ in EC/DMC. (A) Cyclic voltammograms at 0.1 mV/s, (B) galvanostatic charge/discharge profiles at 35 mA/g of the 1st and 5th cycle, and (C) rate capability at 35-1400 mA/g.

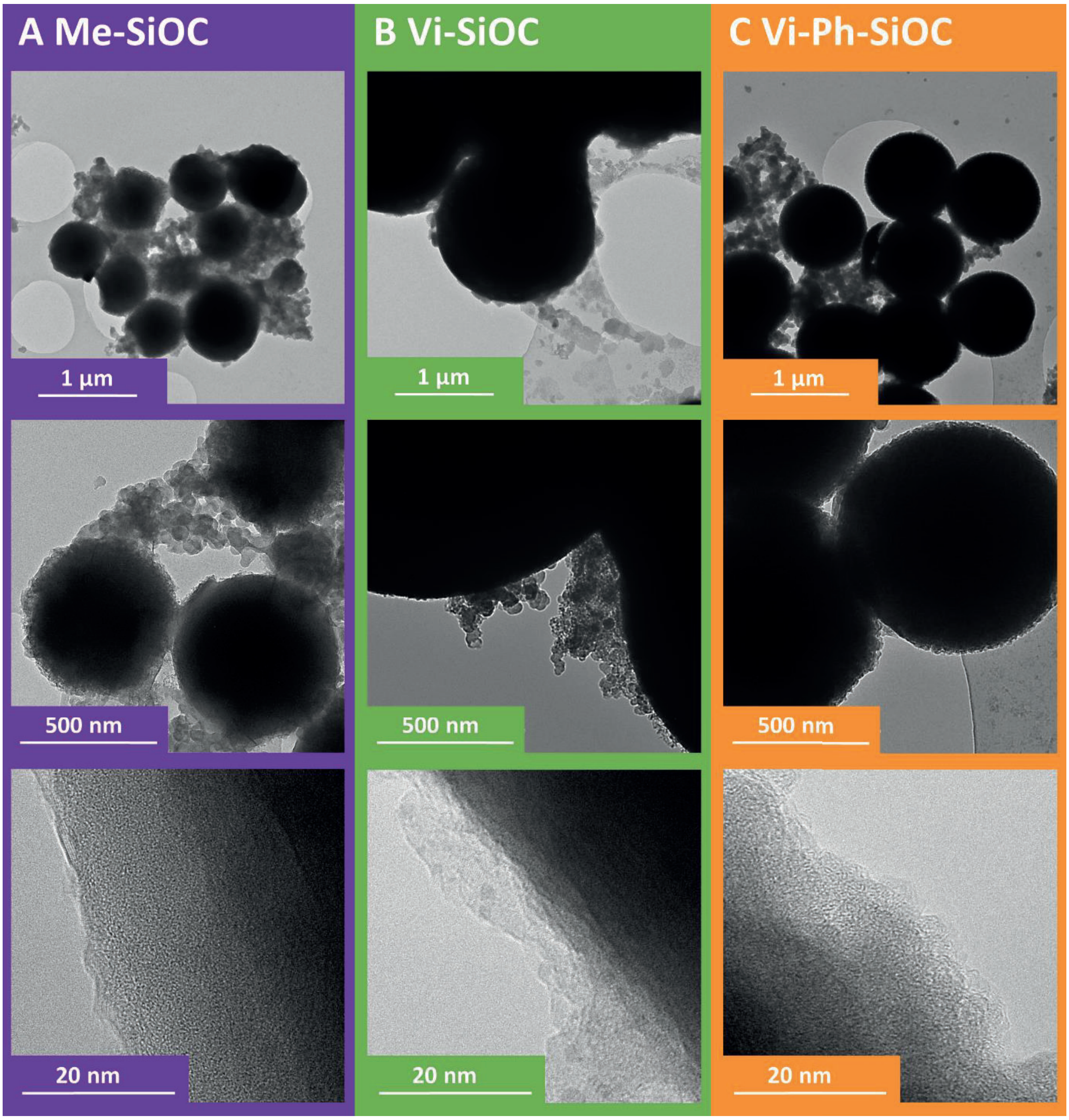

Figure S4: Post-mortem transmission electron micrographs of the SiOC electrodes after the rate capability tests. (A) Me-SiOC, (B) Vi-SiOC, and (C) Vi-Ph-SiOC.

4 SUMMARY AND OUTLOOK

This study investigated the strengths and limits of the MicroJet reactor for the continuous synthesis of nano- and microparticles. Therefore, this technique was tested for different reaction- and product groups and was also compared with other synthesis methods. A further research intent was the detailed characterization of the products and the optimization of their properties to apply them to different applications.

In the case of SnO_2 it turned out that particles with similar properties were produced by the batch as well as the continuous microreactor pathway. Particle sizes between 1.7–3.0 nm and crystallite sizes between 1.7–2.3 nm were obtained. The XRD data suggested that among the expected tetragonal phase ($P4_2/mnm$) an orthorhombic high pressure phase (*Pbcn*) is present in the products. Furthermore, different purification methods were studied to separate the particles from the formed salts. Washing the particles with ethanol achieved the best results (lowest chloride content of 0.1 wt.%) but also led to an occupation of the particles surfaces with ethoxy groups. By water washing (0.2 wt.% chloride after washing) this problem was prevented but the method suffered from high yield losses through the formation of soluble tin species. The fewest technical effort was to expose the particles to a thermal treatment (550 °C for 2 h). Thereby a crystallite growing from 1.6 to 9.4 nm (100 to 600 °C) occurred accompanied by a phase transition to a pure tetragonal structure. The results demonstrated how efficient the individual processes for removing chloride residues are and which side effects can occur. In this way, an information basis was provided to decide which purification method is most suitable for a planned application project.

The second study, which also investigated a precipitation reaction in a MicroJet reactor, was the production of CsH_2PO_4. Together with the cooperation partners, a new synthesis protocol was developed that uses CsOH as a source of cesium instead of $CsCO_3$ and therefore avoids gas evolution during the reaction with H_3PO_4. In this manner, the batch reaction could be easily transferred to the MicroJet reactor process. Furthermore, alcoholic precursor solutions were used instead of aqueous ones and a commercial dispersion reagent was added. This allowed a better particle stabilization and small particle sizes (below 200 nm). The new synthesis protocol was optimized by varying the amount of additive, the concentration of the precursors, the batch size and the type of solvent. DLS measurements showed that increasing the amount of additive (0, 2, 20, 40 wt.%), decreases the particle size (maximum intensity: 998, 278, 150, 119 nm). Furthermore, larger additive quantities resulted in an improved stability of the particle suspensions with extended sedimentation times (start of sedimentation: 10 minutes to 1 week). XRD measurements revealed that the same crystallite sizes (42 and 44 nm) were obtained for the samples with and without dispersion additive. Therefore, it can be assumed that the additive mainly influences the degree of agglomeration as already observed in the literature for the precipitation of $BaSO_4$[44]. The variation of the batch size (0.25, 1 and 4 g) led to slight differences in particle diameters, but no apparent trend. The nominal product concentration was gradually increased from 1 g/l to 50 g/l. The particles with the lowest (1 g/l) and highest product concentrations (40 and 50 g/l) sedimented faster than the other samples and showed bimodal size distributions in DLS measurements with maxima at about 200 nm and > 400 nm). In contrast, samples with medium product concentrations displayed distribution curves with only one peak at about 200 nm. The large particle diameters of the bimodal distributions could be explained on the one hand by the reduced number of nuclei (low product concentration) and on the other hand by a slower mixing due to the increased viscosity (high product concentration). In addition, agglomeration at high concentrations is favored by the reduced particle distances. The particle shape could be modified by varying the solvent. While in ethanol mainly spherical particles were obtained, the use of an ethanol/ethylene glycol mixture resulted in a slow formation of rods. The influence of the mixing speed was investigated by performing the same reaction in a microreactor. Again, a higher amount of dispersion additive caused a reduced particle size. Compared to beaker synthesis, similar particle sizes but narrower particle size distributions were obtained. It can be concluded that the improved mixing conditions in the reactor allow a more uniform particle growth and thus a more homogeneous product quality.

The experiences from the tin oxide system from the first chapter were used to accomplish a sol-gel synthesis of ORMOSIL particles in the MicroJet reactor. In order to yield high amounts of organic groups in the products, solely trialkoxysilanes without the addition of further crosslinkers were used. However, the overall kinetics of the sol-gel reaction of these trialkoxysilanes was too slow for the fast MicroJet reactor process. This problem was solved by developing a new process route, which consisted of an initial partial hydrolysis of the species and a subsequent base-catalyzed continuous condensation. After optimizing the ratios and the amounts of the different reaction species a broad variety of spherical ORMOSIL particles with different organic groups (methyl, ethyl, propyl, vinyl phenyl) as well as pure SiO_2 nanoparticles could be produced on a large scale (23 g/min). Different particles sizes were produced by varying the educt concentrations. Batch experiments that were carried out under identical conditions showed broader size distributions and partially non-spherical morphologies. In contrast, homogeneous, spherical particles were produced on the continuous path, without the use of additives for growth and stabilization. A detailed overview of the samples' properties was developed by applying different analytical methods. Solid-state NMR measurements led to the result that less bulky groups (e.g. methyl) and vinyl groups form particles with a high degree of condensation (89 and 91 %), while the incorporation of phenyl groups resulted in the lowest degree of condensation (80 %). The narrowest size distributions were obtained for pure SiO_2, methyl and ethyl modified samples. Furthermore, the temperature of thermal degradation was measured, which decreases for the alkyl-$SiO_{1.5}$ samples with increasing chain length (methyl 481 °C, ethyl 283 °C and propyl 257 °C). Phenyl-ORMOSILs showed the highest degradation temperatures (527 °C) of all samples. Knowledge of the degree of crosslinking and the thermal behavior proved to be key factors for the further application of the particles as energy storage material.

ORMOSIL particles containing a combination of phenyl and vinyl groups turned out to be excellent precursor materials for the production of CDC beads: during the high-temperature transformation process they retained their morphology and spherical CDC beads were obtained. In contrast, thermal softening followed by a loss of shape was observed in purely phenyl-modified samples. Different vinyl/phenyl ratios (phenyl content = 0.75, 0.50, 0.25, 0.00) were tested and it turned out that higher phenyl contents led to higher total yields (≈ 22 % for $Ph_{0.75}Vi_{0.25}$-$SiO_{1.5}$ compared to 2 % for Vi-$SiO_{1.5}$), whereas an increased vinyl content increased the total pore volume and the specific surface area (1.3 cm^3/g and 2014 m^2/g for $Ph_{0.75}Vi_{0.25}$-$SiO_{1.5}$ compared to 2.0 cm^3/g and 2044 m^2/g for Vinyl-$SiO_{1.5}$). In this way, a system was found that offered the possibility of a tunable pore size. In electrochemical tests, the cooperation partners confirmed the suitability of the particles as electrode material for supercapacitors and detected an improved rate handling behavior, especially for the samples with high vinyl content (the specific energy of Vi-SiOC-CDC decreased only slightly from 25 to 12 Wh/kg at high specific powers of 41 kW/kg).

The phenyl/vinyl modified ORMOSIL particles were further developed by incorporate nitrogen into the network. This was accomplished by performing a cocondensation reaction between vinyltrimethoxysilane and [3-(phenylamino)propyl]trimethoxysilane in the reactor. Depending on the later chlorine gas treatment temperatures (600, 800 and 1000 °C) different amounts of nitrogen (7, 4 and 1 mass%) could be transferred to the final CDC product. Furthermore, particles with similar sizes and pore structures (average pore size between 1.7 and 1.9 nm for all samples) but without nitrogen doping were prepared by applying 4-phenylbutyltrimethoxysilane. By comparing both materials, the effect of a nitrogen doping on the electrochemical performance of a CDC material could be tested. However, while the nitrogen-doped samples had slightly higher capacities at low specific currents than the undoped samples, their specific capacity collapsed earlier when the charge/discharge rate was increased. The results did not confirm any major advantages resulting from the introduction of nitrogen into the CDC material. However, the study showed that further elements can easily be introduced into the ORMOSIL particles via the applied production route.

The last article demonstrated that ORMOSIL particles cannot only be used for the production of porous carbons. By pyrolysis SiOCs can be obtained, which are very well suited as anode material in lithium ion batteries. For the experiments, spherical methyl, vinyl and phenyl/vinyl mixed ORMOSIL particles were produced on a large scale in the MicroJet reactor. The incorporation of various organic groups resulted in SiOC beads with different amounts of silicon-carbon bonds and free carbon. The material with the highest carbon content (Vi-Ph-SiOC, 40 wt.% carbon) proved to be the best anode material with a stable performance. Its first-cycle capacity was 922 mAh/g and the capacity retention after 100 cycles was 83 %. Compared to state of the art anodes for lithium-ion batteries, consisting of graphitic carbon (theoretical capacities of only 372 Ah/g, but no capacity decrease after 100 cycles), Si-C bonds seem to increase the capacity significantly. Comparing different SiOCs with each other, higher carbon contents are advantageous. The result that the samples produced in this work have higher capacities than similar SiOCs from other publications could be explained by the fact that no additional crosslinkers were needed during synthesis, which contaminate the product, that homogeneous particles were used, and that the spherical shape of the particles has advantages in compensating the volume expansion.

In an overall view, the MicroJet reactor technique proved to be a flexible and reliable method for the continuous, wet chemical synthesis of different products. The reactor geometry and the support gas stream showed a good suitability for the production of solid particles without clogging, up to high concentration ranges and high throughputs. The syntheses profited from the continuous proceeding and the resulting homogenous reaction conditions. In some cases, the high energy impinging jet principle can have further effects on the particle properties like the crystallography or the particle size. This behavior could not be observed for the tin oxide samples, but for CsH_2PO_4 and ORMOSIL particles, for which narrower size distributions were obtained with this method.

Prospective research studies can focus on clarifying the specific mixing conditions inside the reactor. A first attempt in this direction was the determination of the mixing time. Further investigations could aim at monitoring certain characteristic values (e.g. the educt or product concentration) during the process by means of in-situ analyses.

New preparative options arise through the arrangement of two or more reactors in series or parallel. Hereby, surface modified particles or core-shell structures could be prepared and scale-up strategies could be tested.

Referring to the synthesis and characterization of SnO_2 nanoparticles the formation of an orthorhombic phase under ambient conditions can be further investigated, e.g. by applying higher educt concentrations, increased flow rates, other bases or further preparation methods.

The preparation of SiOC and CDC materials from ORMOSIL particles was studied in detail in this thesis. In future research projects, new oxycarbides and carbides can be developed by substituting silicon with other metals that have hardly been investigated so far.

REFERENCES

1. Khan, S. A.; Günther, A.; Schmidt, M. A.; Jensen, K. F., *Microfluidic synthesis of colloidal silica. Langmuir* **2004,** *20* (20), 8604–8611. http://dx.doi.org/10.1021/la0499012

2. Jongen, N.; Donnet, M.; Bowen, P.; Lemaître, J.; Hofmann, H.; Schenk, R.; Hofmann, C.; Aoun-Habbache, M.; Guillemet-Fritsch, S.; Sarrias, J.; Rousset, A.; Viviani, M.; Buscaglia, M. T.; Buscaglia, V.; Nanni, P.; Testino, A.; Herguijuela, J. R., *Development of a continuous segmented flow tubular reactor and the "scale-out" concept - in search of perfect powders. Chem. Eng. Technol.* **2003,** *26* (3), 303–305. https://doi.org/10.1002/ceat.200390046

3. Gutmann, B.; Cantillo, D.; Kappe, C. O., *Continuous-flow technology—a tool for the safe manufacturing of active pharmaceutical ingredients. Angew. Chem. Int. Ed. Engl.* **2015,** *54* (23), 6688–6728. http://dx.doi.org/10.1002/anie.201409318

4. Yao, X.; Zhang, Y.; Du, L.; Liu, J.; Yao, J., *Review of the applications of microreactors. Renew. Sust. Energ. Rev.* **2015,** *47*, 519–539. https://doi.org/10.1016/j.rser.2015.03.078

5. Wegner, K.; Pratsinis, S. E., *Aerosol flame reactors for the synthesis of nanoparticles. KONA Powder Par. J.* **2000,** *18*, 170–182. https://doi.org/10.14356/kona.2000023

6. Gutsch, A.; Krämer, M.; Michael, G.; Mühlenweg, H.; Pridöhl, M.; Zimmermann, G., *Gas-phase production of nanoparticles. KONA Powder Par. J.* **2002,** *20*, 24–37. https://doi.org/10.14356/kona.2002008

7. Teoh, W. Y.; Amal, R.; Mädler, L., *Flame spray pyrolysis: An enabling technology for nanoparticles design and fabrication. Nanoscale* **2010,** *2* (8), 1324–1347. http://dx.doi.org/10.1039/c0nr00017e

8. Mädler, L., *Liquid-fed aerosol reactors for one-step synthesis of nano-structured particles. KONA Powder Par. J.* **2004,** *22*, 107–120. https://doi.org/10.14356/kona.2004014

9. Trommer, R. M.; Bergmann, C. P., *Flame spray technology: method for production of nanopowders.* Springer Berlin Heidelberg: 2015; pp 1–5.

10. Park, H. K.; Park, K. Y., *Control of particle morphology and size in vapor-phase synthesis of titania, silica and alumina nanoparticles. KONA Powder Par. J.* **2015,** *32*, 85–101. https://doi.org/10.14356/kona.2015018

11. Shrestha, S.; Wang, B.; Dutta, P., *Nanoparticle processing: understanding and controlling aggregation. Adv. Colloid Interface Sci.* **2020,** *279*, 1–16. https://doi.org/10.1016/j.cis.2020.102162

12. Rahman, I. A.; Padavettan, V., *Synthesis of silica nanoparticles by sol-gel: size-dependent properties, surface modification, and applications in silica-polymer nanocomposites — a review. J. Nanomater.* **2012,** *2012*, 1–15. https://doi.org/10.1155/2012/132424

13. Rahman, M. T.; Rebrov, E. V., *Microreactors for gold nanoparticles synthesis: from Faraday to flow. Processes* **2014,** *2* (2), 466–493. https://doi.org/10.3390/pr2020466

14. Nikam, A. V.; Prasad, B. L. V.; Kulkarni, A. A., *Wet chemical synthesis of metal oxide nanoparticles: a review. CrystEngComm* **2018,** *20* (35), 5091–5107. https://doi.org/10.1039/c8ce00487k

15. Boyjoo, Y.; Pareek, V. K.; Liu, J., *Synthesis of micro and nano-sized calcium carbonate particles and their applications. J. Mater. Chem. A* **2014,** *2* (35), 14270–14288. https://doi.org/10.1039/c4ta02070g

16. Sadat-Shojai, M.; Khorasani, M.-T.; Dinpanah-Khoshdargi, E.; Jamshidi, A., *Synthesis methods for nanosized hydroxyapatite with diverse structures. Acta Biomater.* **2013,** *9* (8), 7591–7621. https://www.doi.org/10.1016/j.actbio.2013.04.012

17. Navarrete, L.; Andrio, A.; Escolástico, S.; Moya, S.; Compañ, V.; Serra, J. M., *Protonic conduction of partially-substituted CsH_2PO_4 and the applicability in electrochemical devices. Membranes (Basel)* **2019,** *9* (4), 1–11. http://dx.doi.org/10.3390/membranes9040049

18. Trindade, T.; O'Brien, P.; Pickett, N. L., *Nanocrystalline semiconductors: synthesis, properties, and perspectives. Chem. Mater.* **2001,** *13* (11), 3843–3858. https://doi.org/10.1021/cm000843p

19. Bally, F.; Serra, C. A.; Hessel, V.; Hadziioannou, G., *Micromixer-assisted polymerization processes. Chem. Eng. Sci.* **2011,** *66* (7), 1449–1462. http://dx.doi.org/10.1016/j.ces.2010.07.026

20. Choi, J. Y.; Kim, C. H.; Kim, D. K., *Formation and characterization of monodisperse, spherical organo-silica powders from organo-alkoxysilane-water system. J. Am. Ceram. Soc.* **1998,** *81* (5), 1184–1188. https://doi.org/10.1111/j.1151-2916.1998.tb02466.x

21. Simeonidis, K.; Liébana-Viñas, S.; Wiedwald, U.; Ma, Z.; Li, Z.-A.; Spasova, M.; Patsia, O.; Myrovali, E.; Makridis, A.; Sakellari, D.; Tsiaoussis, I.; Vourlias, G.; Farle, M.; Angelakeris, M., *A versatile large-scale and green process for synthesizing magnetic nanoparticles with tunable magnetic hyperthermia features. RSC Adv.* **2016,** *6* (58), 53107–53117. http://dx.doi.org/10.1039/c6ra09362k

22. Virkar, P. D.; Hoare, M.; Chan, M. Y. Y.; Dunnill, P., *Kinetics of the acid precipitation of soya protein in a continuous-flow tubular reactor. Biotechnol. Bioeng.* **1982,** *24* (4), 871–887. https://doi.org/10.1002/bit.260240410

23. Jensen, K. F., *Microreaction engineering — is small better? Chem. Eng. Sci.* **2001,** *56* (2), 293–303. https://doi.org/10.1016/S0009-2509(00)00230-X

24. Löwe, H.; Ehrfeld, W., *State-of-the-art in microreaction technology: concepts, manufacturing and applications. Electrochim. Acta* **1999,** *44* (21-22), 3679–3689. https://doi.org/10.1016/S0013-4686(99)00071-7

25. Zhao, C.-X.; He, L.; Qiao, S. Z.; Middelberg, A. P. J., *Nanoparticle synthesis in microreactors. Chem. Eng. Sci.* **2011,** *66* (7), 1463–1479. http://dx.doi.org/10.1016/j.ces.2010.08.039

26. Jähnisch, K.; Hessel, V.; Löwe, H.; Baerns, M., *Chemistry in microstructured reactors. Angew. Chem. Int. Ed. Engl.* **2004,** *43* (4), 406–446. http://dx.doi.org/10.1002/anie.200300577

27. Matsuyama, K.; Mine, K.; Kubo, H.; Mae, K., *Design of micromixer for emulsification and application to conventional commercial plant for cosmetic. Chem. Eng. J.* **2011,** *167* (2–3), 727–733. http://dx.doi.org/10.1016/j.cej.2010.09.085

28. Knauer, A.; Thete, A.; Li, S.; Romanus, H.; Csáki, A.; Fritzsche, W.; Köhler, J. M., *Au/Ag/Au double shell nanoparticles with narrow size distribution obtained by continuous micro segmented flow synthesis. Chem. Eng. J.* **2011,** *166* (3), 1164–1169. http://dx.doi.org/10.1016/j.cej.2010.12.028

29. Rife, J. C.; Bell, M. I.; Horwitz, J. S.; Kabler, M. N.; Auyeung, R. C. Y.; Kim, W. J., *Miniature valveless ultrasonic pumps and mixers. Sens. Actuators, A* **2000,** *86* (1–2), 135–140. https://doi.org/10.1016/S0924-4247(00)00433-7

30. Nguyen, N.-T.; Wu, Z., *Micromixers—a review. J. Micromech. Microeng.* **2005,** *15* (2), R1–R16. http://dx.doi.org/10.1088/0960-1317/15/2/r01

31. Hessel, V.; Löwe, H.; Schönfeld, F., *Micromixers—a review on passive and active mixing principles. Chem. Eng. Sci.* **2005,** *60* (8–9), 2479–2501. http://dx.doi.org/10.1016/j.ces.2004.11.033

32. Ward, K.; Fan, Z. H., *Mixing in microfluidic devices and enhancement methods. J. Micromech. Microeng.* **2015,** *25* (9), 1–33. http://dx.doi.org/10.1088/0960-1317/25/9/094001

33. Abgrall, P.; Gué, A.-M., *Lab-on-chip technologies: making a microfluidic network and coupling it into a complete microsystem—a review. J. Micromech. Microeng.* **2007,** *17* (5), R15–R49. http://dx.doi.org/10.1088/0960-1317/17/5/r01

34. Mengeaud, V.; Josserand, J.; Girault, H. H., *Mixing processes in a zigzag microchannel: Finite element simulations and optical study. Anal. Chem.* **2002,** *74* (16), 4279–4286. https://doi.org/10.1021/ac025642e

35. Liu, R. H.; Stremler, M. A.; Sharp, K. V.; Olsen, M. G.; Santiago, J. G.; Adrian, R. J.; Aref, H.; Beebe, D. J., *Passive mixing in a three-dimensional serpentine microchannel. J. Microelectromech. S.* **2000,** *9* (2), 190–197. http://dx.doi.org/10.1109/84.846699

36. Lin, B.; Basuray, S., *Microfluidics: Technologies and applications.* Springer: 2011; pp 30–35.

37. Lee, C. Y.; Chang, C. L.; Wang, Y. N.; Fu, L. M., *Microfluidic mixing: a review. Int. J. Mol. Sci.* **2011,** *12* (5), 3263–3287. http://dx.doi.org/10.3390/ijms12053263

38. Lee, C.-Y.; Wang, W.-T.; Liu, C.-C.; Fu, L.-M., *Passive mixers in microfluidic systems: A review. Chem. Eng. J.* **2016,** *288*, 146–160. http://dx.doi.org/10.1016/j.cej.2015.10.122

39. Penth, B., *(K)ein Fall für die Fällung. Chemie Technik* **2004,** *33* (3), 18–20.

40. Nayak, P. S.; Arakha, M.; Kumar, A.; Asthana, S.; Mallick, B. C.; Jha, S., *An approach towards continuous production of silver nanoparticles using Bacillus thuringiensis. RSC Adv.* **2016,** *6* (10), 8232–8242. http://dx.doi.org/10.1039/c5ra21281b

41. Lince, F.; Marchisio, D. L.; Barresi, A. A., *A comparative study for nanoparticle production with passive mixers via solvent-displacement: Use of CFD models for optimization and design. Chem. Eng. Process. Process Intensif.* **2011,** *50* (4), 356–368. http://dx.doi.org/10.1016/j.cep.2011.02.015

42. Penth, B. Method and device for carrying out chemical and physical processes. Patent WO 00/61275 (A2), October 19, 2000.

43. Wille, C.; Gabski, H.-P.; Haller, T.; Kim, H.; Unverdorben, L.; Winter, R., *Synthesis of pigments in a three-stage microreactor pilot plant—an experimental technical report. Chem. Eng. J.* **2004,** *101* (1–3), 179–185. http://dx.doi.org/10.1016/j.cej.2003.11.007

44. Rüfer, A.; Räuchle, K.; Krahl, F.; Reschetilowski, W., *Kontinuierliche Darstellung von Bariumsulfat-Nanopartikeln im MicroJet-Reaktor. Chem. Ing. Tech.* **2009,** *81* (12), 1949–1954. http://dx.doi.org/10.1002/cite.200900108

45. Dittert, B.; Gavrilović, A.; Schwarz, S.; Angerer, P.; Steiner, H.; Schöftner, R., *Phase content controlled TiO_2 nanoparticles using the MicroJetReactor technology. J. Eur. Ceram. Soc.* **2011,** *31* (14), 2475–2480. http://dx.doi.org/10.1016/j.jeurceramsoc.2011.01.015

46. Betke, A.; Kickelbick, G., *Bottom-up, wet chemical technique for the continuous synthesis of inorganic nanoparticles. Inorganics* **2014,** *2* (1), 1–15. http://dx.doi.org/10.3390/inorganics2010001

47. Reichelt, L.; Bertau, M., *Production of ferrihydrite and schwertmannite using a microjet mixer device. Chem. Eng. Res. Des.* **2015,** *98*, 70–80. http://dx.doi.org/10.1016/j.cherd.2015.04.008

48. Türeli, N. G.; Torge, A.; Juntke, J.; Schwarz, B. C.; Schneider-Daum, N.; Türeli, A. E.; Lehr, C.-M.; Schneider, M., *Ciprofloxacin-loaded PLGA nanoparticles against cystic fibrosis P. aeruginosa lung infections. Eur. J. Pharm. Biopharm.* **2017,** *117*, 363–371. http://dx.doi.org/10.1016/j.ejpb.2017.04.032

49. Krüner, B.; Odenwald, C.; Tolosa, A.; Schreiber, A.; Aslan, M.; Kickelbick, G.; Presser, V., *Carbide-derived carbon beads with tunable nanopores from continuously produced polysilsesquioxanes for supercapacitor electrodes. Sustain. Energ. Fuels* **2017,** *1* (7), 1588–1600. http://dx.doi.org/10.1039/c7se00265c

50. Volk, C.; Kratz, N.; Werner, J., *Synthese und Herstellung von hochreinen Yttriumvanadat-Keramiken für optische Anwendungen. Keram. Z.* **2017,** *69* (6), 156–159. https://doi.org/10.1007/BF03400332

51. Odenwald, C.; Kickelbick, G., *Additive-free continuous synthesis of silica and ORMOSIL micro- and nanoparticles applying a microjet reactor. J. Sol-Gel Sci. Technol.* **2018,** *89* (1), 343–353. http://dx.doi.org/10.1007/s10971-018-4626-x

52. Beyer, S.; Xie, L.; Gräfe, S.; Vogel, V.; Dietrich, K.; Wiehe, A.; Albrecht, V.; Mäntele, W.; Wacker, M. G., *Bridging laboratory and large scale production: preparation and in vitro-evaluation of photosensitizer-loaded nanocarrier devices for targeted drug delivery. Pharm. Res.* **2015,** *32* (5), 1714–1726. http://dx.doi.org/10.1007/s11095-014-1569-y

53. Lohmann-Richters, F. P.; Odenwald, C.; Kickelbick, G.; Abel, B.; Varga, Á., *Facile and scalable synthesis of sub-micrometer electrolyte particles for solid acid fuel cells. RSC Adv.* **2018,** *8* (39), 21806–21815. http://dx.doi.org/10.1039/c8ra03293a

54. Krüner, B.; Odenwald, C.; Jäckel, N.; Tolosa, A.; Kickelbick, G.; Presser, V., *Silicon oxycarbide beads from continuously produced polysilsesquioxane as stable anode material for lithium-ion batteries. ACS Appl. Energy Mater.* **2018,** *1* (6), 2961–2970. http://dx.doi.org/10.1021/acsaem.8b00716

55. Türeli, A. E. *Nanoparticle preparation process using novel microjet reactor technology for enhancing dissolution rates of poorly water soluble drugs.* Dissertation, Mainz, 2015.

56. Krüner, B.; Odenwald, C.; Quade, A.; Kickelbick, G.; Presser, V., *Influence of nitrogen-doping for carbide-derived carbons on the supercapacitor performance in an organic electrolyte and an ionic liquid. Batteries & Supercaps* **2018,** *1* (4), 135–148. http://dx.doi.org/10.1002/batt.201800051

57. Türeli, N. G.; Türeli, A. E.; Schneider, M., *Counter-ion complexes for enhanced drug loading in nanocarriers: proof-of-concept and beyond. Int. J. Pharm.* **2016,** *511* (2), 994–1001. http://dx.doi.org/10.1016/j.ijpharm.2016.08.004

58. Hiemer, J.; Clausing, A.; Schwarz, T.; Stöwe, K., *MicroJet reactor technology: An automated, continuous approach for nanoparticle syntheses. Chem. Eng. Technol.* **2019,** *42*, 2018–2027. http://dx.doi.org/10.1002/ceat.201900083

59. Türeli, N. G.; Türeli, A. E.; Schneider, M., *Optimization of ciprofloxacin complex loaded PLGA nanoparticles for pulmonary treatment of cystic fibrosis infections: design of experiments approach. Int. J. Pharm.* **2016,** *515* (1-2), 343–351. http://dx.doi.org/10.1016/j.ijpharm.2016.10.025

60. Schwarzer, H.-C.; Peukert, W., *Combined experimental/numerical study on the precipitation of nanoparticles. AIChE J.* **2004,** *50* (12), 3234–3247. https://doi.org/s10.1002/aic.10277

61. Marchisio, D. L.; Rivautella, L.; Barresi, A. A., *Design and scale-up of chemical reactors for nanoparticle precipitation. AIChE J.* **2006,** *52* (5), 1877–1887. https://doi.org/10.1002/aic.10786

62. Pohl, B.; Özyilmaz, N.; Brenner, G.; Peuker, U. A., *Charakterisierung einer konischen Geometrie für einen Ultraschalldurchflussreaktor. Chem. Ing. Tech.* **2009,** *81* (10), 1613–1622. https://doi.org/10.1002/cite.200900077

63. Kucher, M. *Vom Keim zum Kristall – Über die Partikelbildung bei der Fällung schwerlöslicher Feststoffe.* Dissertation, Universität Karlsruhe (TH), 2008; pp 23–26, 69–73.

64. Grigull, U.; Staub, J.; Schiebener, P., *Steam Tables in SI-Units - Wasserdampftafeln.* Springer-Verlagdima gmbh: 1990.

65. Hirschberg, H. G., *Handbuch Verfahrenstechnik und Anlagenbau: Chemie, Technik und Wirtschaftlichkeit.* Springer Berlin Heidelberg: 2013; p 350.

66. Wong, S. H.; Ward, M. C. L.; Wharton, C. W., *Micro T-mixer as a rapid mixing micromixer. Sens. Actuators, B* **2004,** *100* (3), 359–379. http://dx.doi.org/10.1016/j.snb.2004.02.008

67. Stroock, A. D.; Dertinger, S. K. W.; Ajdari, A.; Mezic´, I.; Stone, H. A.; Whitesides, G. M., *Chaotic mixer for microchannels. Science* **2002,** *295* (5555), 647–651. https://doi.org/10.1126/science.1066238

68. Cha, J.; Kim, J.; Ryu, S.-K.; Park, J.; Jeong, Y.; Park, S.; Park, S.; Kim, H. C.; Chun, K., *A highly efficient 3D micromixer using soft PDMS bonding. J. Micromech. Microeng.* **2006,** *16* (9), 1778–1782. https://doi.org/10.1088/0960-1317/16/9/004

69. Kim, D. S.; Lee, I. H.; Kwon, T. H.; Cho, D.-W., *A barrier embedded Kenics micromixer. J. Micromech. Microeng.* **2004,** *14* (10), 1294–1301. https://doi.org/10.1088/0960-1317/14/10/002

70. Roessler, A.; Rys, P., *Selektivität mischungsmaskierter Reaktionen. Wenn die Rührgeschwindigkeit die Produktverteilung bestimmt. Chem. unserer Zeit* **2001,** *35* (5), 314–323. https://doi/10.1002/1521-3781(200110)35:5<314::AID-CIUZ314>3.0.CO;2-D

71. Fournier, M.-C.; Falk, L.; Villermaux, J., *A new parallel competing reaction system for assessing micromixing efficiency – experimental approach. Chem. Eng. Sci.* **1996,** *51* (22), 5053–5064. https://doi.org/10.1016/0009-2509(96)00270-9

72. Dushman, S., *The Rate of the reaction between iodic and hydriodic acids. J. Phys. Chem.* **1904,** *8* (7), 453–482. https://doi.org/10.1021/j150061a001

73. Commenge, J.-M.; Falk, L., *Villermaux–Dushman protocol for experimental characterization of micromixers. Chem. Eng. Process.* **2011,** *50* (10), 979–990. http://dx.doi.org/10.1016/j.cep.2011.06.006

74. Masca, S. I.; Rodriguez-Mendieta, I. R.; Friel, C. T.; Radford, S. E.; Smith, D. A., *Detailed evaluation of the performance of microfluidic T mixers using fluorescence and ultraviolet resonance Raman spectroscopy. Rev. Sci. Instrum.* **2006,** *77* (5), 1–9. http://dx.doi.org/10.1063/1.2198800

75. Aubin, J.; Ferrando, M.; Jiricny, V., *Current methods for characterising mixing and flow in microchannels. Chem. Eng. Sci.* **2010,** *65* (6), 2065–2093. https://doi.org/10.1016/j.ces.2009.12.001

76. Watanabe, S.; Ohsaki, S.; Fukuta, A.; Hanafusa, T.; Takada, K.; Tanaka, H.; Maki, T.; Mae, K.; Miyahara, M. T., *Characterization of mixing performance in a microreactor and its application to the synthesis of porous coordination polymer particles. Adv. Powder Technol.* **2017,** *28* (11), 3104–3110. http://dx.doi.org/10.1016/j.apt.2017.09.005, Creative Commons user license: https://creativecommons.org/licenses/by-nc-nd/4.0/

77. Marre, S.; Jensen, K. F., *Synthesis of micro and nanostructures in microfluidic systems. Chem. Soc. Rev.* **2010,** *39* (3), 1183–1202. https://doi.org/10.1039/b821324k

78. Karnik, R.; Gu, F.; Basto, P.; Cannizzaro, C.; Dean, L.; Kyei-Manu, W.; Langer, R.; Farokhzad, O. C., *Microfluidic platform for controlled synthesis of polymeric nanoparticles. Nano Lett.* **2008,** *8* (9), 2906–2912. https://doi.org/10.1021/nl801736q

79. D'Addio, S. M.; Prud'homme, R. K., *Controlling drug nanoparticle formation by rapid precipitation. Adv. Drug Del. Rev.* **2011,** *63*, 417–426. https://doi.org/10.1016/j.addr.2011.04.005

80. Gogotsi, Y., *Nanomaterials Handbook.* CRC Press: 2006; pp 22–27.

81. Cushing, B. L.; Kolesnichenko, V. L.; O'Connor, C. J., *Recent advances in the liquid-phase syntheses of inorganic nanoparticles. Chem. Rev.* **2004,** *104* (9), 3893–3946. https://doi.org/10.1021/cr030027b

82. Karpinski, P. H.; Wey, J. S., 6 - Precipitation processes. In *Handbook of Industrial Crystallization (Second Edition)*, Myerson, A. S., Ed. Butterworth-Heinemann: Woburn, 2002; pp 141–160.

83. Dirksen, J. A.; Ring, T. A., *Fundamentals of crystallization: Kinetic effects on particle size distributions and morphology. Chem. Eng. Sci.* **1991,** *46* (10), 2389–2427. https://doi.org/10.1016/0009-2509(91)80035-W

84. Ted, J. Particle size prediction in reactive precipitation processes. In *Retrospective Theses and Dissertations*, University, I. S. Ed. 2004; pp 1–20.

85. Volmer, M.; Weber, A., *Keimbildung in übersättigten Gebilden. Z. Phys. Chem.* **1926,** *119U* (1), 277–301. https://doi.org/10.1515/zpch-1926-11927

86. Farkas, L., *Keimbildungsgeschwindigkeit in übersättigten Dämpfen. Z. Phys. Chem.* **1927,** *125U* (1), 236–242. https://doi.org/10.1515/zpch-1927-12513

87. Becker, R.; Döring, W., *Kinetische Behandlung der Keimbildung in übersättigten Dämpfen. Ann. Phys.* **1935,** *416*, 719–752. https://doi.org/10.1002/andp.19354160806

88. Frenkel, J., *A general theory of heterophase fluctuations and pretransition phenomena. J. Chem. Phys.* **1939,** *7*, 538–547. https://doi.org/10.1063/1.1750484

89. Karthika, S.; Radhakrishnan, T. K.; Kalaichelvi, P., *A review of classical and nonclassical nucleation theories. Cryst. Growth Des.* **2016,** *16* (11), 6663–6681. http://dx.doi.org/10.1021/acs.cgd.6b00794

90. Polte, J., *Fundamental growth principles of colloidal metal nanoparticles – a new perspective. CrystEngComm* **2015,** *17* (36), 6809–6830. https://doi.org/10.1039/c5ce01014d

91. Debenedetti, P. G., *Metastable liquids: concepts and principles.* Princeton University Press: 1996; pp 148–150.

92. Thanh, N. T.; Maclean, N.; Mahiddine, S., *Mechanisms of nucleation and growth of nanoparticles in solution. Chem. Rev.* **2014,** *114* (15), 7610–7630. https://doi.org/10.1021/cr400544s

93. Horn, D.; Rieger, J., *Organische Nanopartikel in wässriger Phase –Theorie, Experiment und Anwendung. Angew. Chem.* **2001,** *113*, 4460–4492. https://doi.org/10.1002/1521-3757(20011203)113:23<4460::AID-ANGE4460>3.0.CO;2-1

94. LaMer, V. K.; Dinegar, R. H., *Theory, production and mechanism of formation of monodispersed hydrosols. J. Am. Chem. Soc.* **1950,** *72* (11), 4847–4854. https://doi.org/10.1021/ja01167a001

95. Mullin, J. W., *Crystallization.* Elsevier Science: 2001; pp 184–185.

96. La Mer, V. K., *Nucleation in phase transitions. Engineering Chemistry* **1952,** *44* (6), 1270–1277. https://doi.org/10.1021/ie50510a027

97. Shen, V. K.; Debenedetti, P. G., *A computational study of homogeneous liquid–vapor nucleation in the Lennard-Jones fluid. J. Chem. Phys.* **1999,** *111* (8), 3581–3589. https://doi.org/10.1063/1.479639

98. Yau, S.; Vekilov, P., *Quasi-planar nucleus structure in apoferritin crystallization. Nature* **2000,** *406* (6795), 494–497. https://doi.org/10.1038/35020035

99. Schmelzer, J. W. P.; Gutzow, I.; Schmelzer Jr., J., *Curvature-dependent surface tension and nucleation theory. J. Colloid Interface Sci.* **1996,** *178* (2), 657–665. https://doi.org/10.1006/jcis.1996.0163

100. Stávek, J., Ulrich, J. , *A possible new approach to the better understanding of crystallization kinetics. Cryst. Res. Technol.* **1994,** *29* (4), 465–484. https://doi.org/10.1002/crat.2170290403

101. Clarke, A. S.; Kapral, R.; Patey, G. N., *Structure of two-component clusters. J. Chem. Phys.* **1994,** *101* (3), 2432–2445. https://doi.org/10.1063/1.467683

102. Kumar, A.; Yadav, N.; Bhatt, M.; Mishra, N. K.; Chaudhary, P.; Singh, R., *Sol-gel derived nanomaterials and it's applications: A review. Res. J. Chem. Sci.* **2015,** *5* (12), 98–105.

103. Sakka, S.; Almeida, R. M., *Handbook of sol-gel science and technology. 2. Characterization and properties of sol-gel materials and products.* Kluwer Academic Publishers: 2005; p 394.

104. Levy, D.; Zayat, M., *The Sol-Gel Handbook, 3 Volume Set: Synthesis, characterization, and applications.* Wiley: 2015; pp 202–209.

105. Schubert, U., *Sol-Gel-Chemie: Einfach und doch kompliziert. Chem. unserer Zeit* **2018,** *52* (1), 18–25. https://doi.org/10.1002/ciuz.201700792

106. Schmidt, H. K., *Das Sol-Gel-Verfahren: Anorganische Synthesemethoden. Chem. unserer Zeit* **2001,** *35* (3), 176–184. https://doi.org/10.1002/1521-3781(200106)35:3<176::AID-CIUZ176>3.0.CO;2-B

107. Stöber, W.; Fink, A.; Bohn, E., *Controlled growth of monodisperse silica spheres in the micron size range. J. Colloid Interface Sci.* **1968,** *26* (1), 62–69. https://doi.org/10.1016/0021-9797(68)90272-5

108. Loy, D. A.; Baugher, B. M.; Baugher, C. R.; Schneider, D. A.; Rahimian, K., *Substituent effects on the sol–gel chemistry of organotrialkoxysilanes. Chem. Mater.* **2000,** *12* (12), 3624–3632. https://doi.org/10.1021/cm000451i

109. Moriones, P.; Arzamendi, G.; Cornejo, A.; Garrido, J. J.; Echeverria, J. C., *Comprehensive kinetics of hydrolysis of organotriethoxysilanes by* ^{29}*Si NMR. J. Phys. Chem. A* **2019,** *123* (48), 10364–10371. https://doi.org/10.1021/acs.jpca.9b08910

110. Osterholtz, F. D.; Pohl, E. R., *Kinetics of the hydrolysis and condensation of organofunctional alkoxysilanes: a review. J. Adhes. Sci. Technol.* **1992,** *6* (1), 127–149. https://doi.org/10.1163/156856192x00106

111. Schubert, U., *Organically modified transition metal alkoxides: Chemical problems and structural issues on the way to materials syntheses. Acc. Chem. Res.* **2007,** *40*, 730–737. https://doi.org/10.1021/ar600036x

112. Schubert, U., Chemistry and Fundamentals of the Sol–Gel Process. In *The Sol-Gel Handbook*, Levy, D.; Zayat, M., Eds. Wiley-VCH Verlag GmbH & Co. KGaA: 2015; pp 1–28.

113. Chandler, C. D.; Caruso, J.; Hampden-Smith, M. J., *Structural investigation of tin(IV) alkoxide compounds-II. Polyhedron* **1995,** *14* (17-18), 2491–2497. https://doi.org/10.1016/0277-5387(95)00059-2

114. Hampden-Smith, M. J.; Wark, T. A.; Rheingold, A.; Huffman, J. C., *Solid state and solution structural investigation of homoleptic tin(IV) alkoxide compounds. Part I. Can. J. Chem.* **1991,** *69*, 121–129. https://doi.org/10.1139/v91-020

115. Hampden-Smith, M. J.; Wark, T. A.; Brinker, C. J., *The solid state and solution structures of tin(IV) alkoxide compounds and their use as precursors to form tin oxie ceramics via sol-gel-type hydrolysis and condensation. Coord. Chem. Rev.* **1992,** *112*, 81–116.

116. Hou, X.; Hu, Y.; Jiang, H.; Huo, J.; Li, Y.; Li, C., *In situ Au-catalyzed fabrication of branch-type SnO_2 nanowires by a continuous gas-phase route for dye-sensitized solar cells. J. Mater. Chem. A* **2013,** *1* (44), 13814–13820. http://dx.doi.org/10.1039/c3ta12533e

117. Kim, J.-Y.; Kim, E.-R.; Han, Y.-K.; Nam, K.-H.; Ihm, D.-W., *Highly transparent tin oxide films prepared by DC magnetron sputtering and its liquid crystal display application. Jpn. J. Appl. Phys.* **2002,** *41* (1), 237–240. http://dx.doi.org/10.1143/jjap.41.237

118. Gotlib-Vainstein, K.; Gouzman, I.; Girshevitz, O.; Bolker, A.; Atar, N.; Grossman, E.; Sukenik, C. N., *Liquid phase deposition of a space-durable, antistatic SnO_2 coating on Kapton. ACS Appl. Mater. Interfaces* **2015,** *7* (6), 3539–3546. http://dx.doi.org/10.1021/am5072817

119. Rizzato, A. P.; Broussous, L.; Santilli, C. V.; Pulcinelli, S. H.; Craievich, A. F., *Structure of SnO_2 alcosols and films prepared by sol-gel dip coating. J. Non-Cryst. Solids* **2001,** *284*, 61–67. https://doi.org/10.1016/S0022-3093(01)00380-5

120. Yin, M.; Xu, J.; Li, Q.; Jensen, J. O.; Huang, Y.; Cleemann, L. N.; Bjerrum, N. J.; Xing, W., *Highly active and stable Pt electrocatalysts promoted by antimony-doped SnO_2 supports for oxygen reduction reactions. Appl. Catal., B* **2014,** *144*, 112–120. http://dx.doi.org/10.1016/j.apcatb.2013.07.007

121. Santos, L. R. B.; Pulcinelli, S. H.; Santilli, C. V., *Preparation of SnO_2 supported membranes with ultrafine pores. J. Membrane Sci.* **1997,** *127*, 77–86. https://doi.org/10.1016/S0376-7388(96)00309-2

122. Dattoli, E. N.; Wan, Q.; Guo, W.; Chen, Y.; Pan, X.; Lu, W., *Fully transparent thin-film transistor devices based on SnO_2 nanowires. Nano Lett.* **2007,** *7* (8), 2463–2469. https://doi.org/10.1021/nl0712217

123. Idota, Y.; Kubota, T.; Matsufuji, A.; Maekawa, Y.; Miyasaka, T., *Tin-based amorphous oxide: A high-capacity lithium-ion–storage material. Science* **1997,** *276*, 1395–1397. http://dx.doi.org/10.1126/science.276.5317.1395

124. Göpel, W.; Schierbaum, K. D., *SnO_2 sensors: current status and future prospects. Sens. Actuators, B* **1995,** *26* (1–3), 1–12. https://doi.org/10.1016/0925-4005(94)01546-T

125. Schleife, A.; Varley, J. B.; Fuchs, F.; Rödl, C.; Bechstedt, F.; Rinke, P.; Janotti, A.; Van de Walle, C. G., *Tin dioxide from first principles: quasiparticle electronic states and optical properties. Phy. Rev. B* **2011,** *83* (3), 1–9. http://dx.doi.org/10.1103/PhysRevB.83.035116

126. Reimann, K.; Steube, M., *Experimental determination of the electronic band structure of SnO_2. Solid State Commun.* **1998,** *105* (10), 649–652. https://doi.org/10.1016/S0038-1098(97)10151-X

127. Rumyantseva, M. N.; Safonova, O. V.; Boulova, M. N.; Ryabova, L. I.; Gas´kov, A. M., *Dopants in nanocrystalline tin dioxide. Russ. Chem. Bull.* **2003,** *52* (6), 1217–1238. https://doi.org/10.1023/A:1024916020690

128. Das, S.; Jayaraman, V., *SnO_2: A comprehensive review on structures and gas sensors. Prog. Mater Sci.* **2014,** *66*, 112–255. http://dx.doi.org/10.1016/j.pmatsci.2014.06.003

129. Gracia, L.; Beltrán, A.; Andrés, J., *Characterization of the high-pressure structures and phase transformations in SnO_2. A density functional theory study. J. Phys. Chem. B* **2007,** *111* (23), 6479–6485. http://dx.doi.org/10.1021/jp067443v

130. Tiginyanu, I. M.; Lupan, O.; Ursaki, V. V.; Chow, L.; Enachi, M., 3.11 - Nanostructures of metal oxides. In *Comprehensive Semiconductor Science and Technology*, Bhattacharya, P.; Fornari, R.; Kamimura, H., Eds. Elsevier: Amsterdam, 2011; pp 449–456.

131. Jensen, K. M. Ø.; Christensen, M.; Juhas, P.; Tyrsted, C.; Bøjesen, E. D.; Lock, N.; Billinge, S. J. L.; Iversen, B. B., *Revealing the mechanisms behind SnO_2 nanoparticle formation and growth during hydrothermal synthesis: an in situ total scattering study. J. Am. Chem. Soc.* **2012,** *134* (15), 6785–6792. http://dx.doi.org/10.1021/ja300978f

132. Carvalho, M. H.; Pereira, E. C.; de Oliveira, A. J. A., *Orthorhombic SnO_2 phase observed composite $(Sn_{1-x}Ce_x)O_2$ synthesized by sol–gel route. RSC Adv.* **2018,** *8* (8), 3958–3963. http://dx.doi.org/10.1039/c7ra12727h

133. Grinblat, F.; Ferrari, S.; Pampillo, L. G.; Saccone, F. D.; Errandonea, D.; Santamaria-Perez, D.; Segura, A.; Vilaplana, R.; Popescu, C., *Compressibility and structural behavior of pure and Fe-doped SnO_2 nanocrystals. Solid State Sci.* **2017,** *64*, 91–98. http://dx.doi.org/10.1016/j.solidstatesciences.2016.12.015

134. Kumar, M.; Kumar, A.; Abhyankar, A. C., *Occurrence of non-equilibrium orthorhombic SnO_2 phase and its effect in preferentially grown SnO_2 nanowires for CO detection. RSC Adv.* **2015,** *5* (45), 35704–35708. http://dx.doi.org/10.1039/c4ra15539d

135. Bhardwaj, N.; Pandey, A.; Mohapatra, S., *Effects of MeV heavy ion irradiation on structural, morphological and optical properties of nanostructured SnO_2 thin films prepared by thermal evaporation. J. Alloys Compd.* **2016,** *656*, 647–653. http://dx.doi.org/10.1016/j.jallcom.2015.09.275

136. Munoz-Espí, R.; Dolcet, P.; Rossow, T.; Wagner, M.; Landfester, K.; Crespy, D., *Tin(IV) oxide coatings from hybrid organotin/polymer nanoparticles. ACS Appl. Mater. Interfaces* **2011,** *3* (11), 4292–4298. http://dx.doi.org/10.1021/am200954e

137. Davar, F.; Mohandes, F.; Salavati-Niasari, M., *A novel chelating acid-assisted thermolysis procedure for preparation of tin oxide nanoparticles. Polyhedron* **2010,** *29* (16), 3132–3136. http://dx.doi.org/10.1016/j.poly.2010.08.022

138. Tian, S.; Gao, Y.; Zeng, D.; Xie, C., *Effect of zinc doping on microstructures and gas-sensing properties of SnO_2 nanocrystals. J. Am. Ceram. Soc.* **2012,** *95* (1), 436–442. http://dx.doi.org/10.1111/j.1551-2916.2011.04957.x

139. Rai, R., *Study of structural and electrical properties of pure and Zn-Cu doped SnO_2. Adv. Mat. Lett.* **2010,** *1* (1), 55–58. http://dx.doi.org/10.5185/amlett.2010.3101

140. Ali, S. M.; Muhammad, J.; Hussain, S. T.; Ali, S. D.; Rehman, N. U.; Aziz, M. H., *Annealing effect on structural, optical and electrical properties of pure and Mg doped tin oxide thin films. J. Mater. Sci. - Mater. Electron.* **2013,** *24* (12), 4925–4931. http://dx.doi.org/10.1007/s10854-013-1499-1

141. Li, Q.; Zhao, H.; Sun, H.; Zhao, X.; Fan, W., *Doubling the photocatalytic performance of SnO_2 by carbon coating mixed-phase particles. RSC Adv.* **2018,** *8* (53), 30366–30373. http://dx.doi.org/10.1039/c8ra03794a

142. Sabarilakshmi, M.; Janaki, K., *Effect of Mg concentration on structural, optical and humidity sensing performance of SnO_2 nanoparticles prepared by one step facile route. J. Mater. Sci. - Mater. Electron.* **2017,** *28* (11), 8101–8107. http://dx.doi.org/10.1007/s10854-017-6516-3

143. Ahmad, T.; Khatoon, S.; Coolahan, K., *Structural, optical, and magnetic properties of nickel-doped tin dioxide nanoparticles synthesized by solvothermal method. J. Am. Ceram. Soc.* **2016,** *99* (4), 1207–1211. http://dx.doi.org/10.1111/jace.14088

144. Klinbumrung, A.; Thongtem, T.; Phuruangrat, A.; Thongtem, S., *Optical and ammonia-sensing properties of SnO_2 nanoparticles synthesized using a 900 W microwave. Jpn. J. Appl. Phys.* **2016,** *55* (8), 1–7. http://dx.doi.org/10.7567/jjap.55.085001

145. Srivastava, D. N.; Chappel, S.; Palchik, O.; Zaban, A.; Gedanken, A., *Sonochemical synthesis of mesoporous tin oxide. Langmuir* **2002,** *18* (10), 4160–4164. http://dx.doi.org/10.1021/la015761+

146. Soltan, W. B.; Nasri, S.; Lassoued, M. S.; Ammar, S., *Structural, optical properties, impedance spectroscopy studies and electrical conductivity of SnO_2 nanoparticles prepared by polyol method. J. Mater. Sci. - Mater. Electron.* **2017,** *28* (9), 6649–6656. http://dx.doi.org/10.1007/s10854-017-6356-1

147. Xiang, X.; Zhu, D.; Wang, D., *Enhanced formaldehyde gas sensing properties of La-doped SnO_2 nanoparticles prepared by ball-milling solid chemical reaction method. J. Mater. Sci. - Mater. Electron.* **2016,** *27* (7), 7425–7432. http://dx.doi.org/s10.1007/s10854-016-4718-8

148. Liu, G.; Sun, W.-j.; Tang, S.-s.; Liang, S.-q.; Liu, J., *Synthesis of α-Fe_2O_3@SnO_2 core-shell nanoparticles via low-temperature molten salt reaction route. Trans. Nonferrous Met. Soc. China* **2015,** *25* (11), 3651–3656. http://dx.doi.org/10.1016/s1003-6326(15)64076-6

149. Zhang, J.; Gao, L., *Synthesis and characterization of nanocrystalline tin oxide by sol–gel method. J. Solid State Chem.* **2004,** *177* (4–5), 1425–1430. http://dx.doi.org/10.1016/j.jssc.2003.11.024

150. Shaikh, F. I.; Chikhale, L. P.; Mulla, I. S.; Suryavanshi, S. S., *Synthesis, characterization and enhanced acetone sensing performance of Pd loaded Sm doped SnO_2 nanoparticles. Ceram. Int.* **2017,** *43* (13), 10307–10315. http://dx.doi.org/10.1016/j.ceramint.2017.05.060

151. Wang, J.; Wu, W.; Wang, W.-H.; Bao, M., *Expeditious synthesis of SnO_2 nanoparticles through controlled hydrolysis and condensation of tin alkoxide in reverse microemulsion. Ceram. Int.* **2017,** *43* (5), 4702–4705. http://dx.doi.org/10.1016/j.ceramint.2017.01.002

152. Turova, N. Y.; Turevskaya, E. P.; Kessler, V. G.; Yanovskaya, M. I., *The chemistry of metal alkoxides.* 1 ed.; Springer US: 2002; pp 114–115, 297–309

153. Toupance, T.; Babot, O.; Jousseaume, B.; Vilaça, G., *Nanocrystalline mesoporous tin dioxide prepared by the sol-gel route from a dialkoxydi(ß-diketonato)tin complex. Chem. Mater.* **2003,** *15* (24), 4691–4697. http://dx.doi.org/10.1021/cm0344459

154. Jaumier, P.; Jousscaume, B.; Lahcini, M.; Ribotc, F.; Sanchez, C., *New route to monoorganotin oxides and alkoxides from trialkynylorganotins. Chem. Commun.* **1998**, 369–370. https://doi.org/10.1039/A707298H

155. Elhamzaoui, H.; Jousseaume, B.; Riague, H.; Toupance, T.; Dieudonné, P.; Zakri, C.; Maugey, M.; Allouchi, H., *Self-assembled tin-based bridged hybrid materials. J. Am. Chem. Soc.* **2004,** *126* (26), 8130–8131. http://dx.doi.org/10.1021/ja048272f

156. Molloy, K. C., *Precursors for the formation of tin(IV) oxide and related materials. J. Chem. Res.* **2008,** *2008* (10), 549–554. https://doi.org/10.3184/030823408X356846

157. Chu, G.-w.; Zeng, Q.-h.; Shen, Z.-g.; Zou, H.-k.; Chen, J.-f., *Preparation of SnO_2 nanoparticles using a helical tube reactor via continuous hydrothermal route. Chem. Eng. J.* **2014,** *253*, 78–83. http://dx.doi.org/10.1016/j.cej.2014.05.016

158. Hellstern, H. L.; Becker, J.; Hald, P.; Bremholm, M.; Mamakhel, A.; Iversen, B. B., *Development of a dual-stage continuous flow reactor for hydrothermal synthesis of hybrid nanoparticles. Ind. Eng. Chem. Res.* **2015,** *54* (34), 8500–8508. http://dx.doi.org/10.1021/acs.iecr.5b02899

159. Hellstern, H. L.; Bremholm, M.; Mamakhel, A.; Becker, J.; Iversen, B. B., *Hydrothermal synthesis of TiO_2@SnO_2 hybrid nanoparticles in a continuous-flow dual-stage reactor. ChemSusChem* **2016,** *9* (5), 532–539. https://doi.org/10.1002/cssc.201501199

160. Fang, Z.; Assaaoudi, H.; Guthrie, R. I. L.; Kozinski, J. A.; Butler, I. S., *Continuous synthesis of tin and indium oxide nanoparticles in sub- and supercritical water. J. Am. Ceram. Soc.* **2007,** *90* (8), 2367–2371. https://doi.org/10.1111/j.1551-2916.2007.01773.x

161. NaderiNasrabadi, M.; Mortazavi, Y.; Khodadadi, A. A., *Highly sensitive and selective Gd_2O_3-doped SnO_2 ethanol sensors synthesized by a high temperature and pressure solvothermal method in a microreactor. Sensors Actuators B: Chem.* **2016,** *230*, 130–139. https://doi.org/10.1016/j.snb.2016.02.045

162. Hong, Y. J.; Son, M. Y.; Kang, Y. C., *One-pot facile synthesis of double-shelled SnO_2 yolk-shell-structured powders by continuous process as anode materials for Li-ion batteries. Adv. Mater.* **2013,** *25* (16), 2279–2283. http://dx.doi.org/10.1002/adma.201204506

163. Rikka, V. R.; Sameera, I.; Bhatia, R.; Prasad, V., *Synthesis, characterization and field emission properties of tin oxide nanowires. Mater. Chem. Phys.* **2015,** *166*, 26–30. https://doi.org/10.1016/j.matchemphys.2015.09.035

164. Hwang, I.-S.; Kim, S.-J.; Choi, J.-K.; Choi, J.; Ji, H.; Kim, G.-T.; Cao, G.; Lee, J.-H., *Synthesis and gas sensing characteristics of highly crystalline ZnO–SnO_2 core–shell nanowires. Sensors Actuators B: Chem.* **2010,** *148* (2), 595–600. https://doi.org/10.1016/j.snb.2010.05.052

165. Hossain, M. A.; Yang, G.; Parameswaran, M.; Jennings, J. R.; Wang, Q., *Mesoporous SnO_2 spheres synthesized by electrochemical anodization and their application in CdSe-sensitized solar cells. J. Phys. Chem. C* **2010,** *114*, 21878–21884. https://doi.org/10.1021/jp109083k

166. Akram, M.; Alshemary, A. Z.; Butt, F. K.; Goh, Y.-F.; Ibrahim, W. A. W.; Hussain, R., *Continuous microwave flow synthesis and characterization of nanosized tin oxide. Mater. Lett.* **2015,** *160*, 146–149. https://doi.org/10.1016/j.matlet.2015.07.088

167. Akram, M.; Saleh, A. T.; Ibrahim, W. A. W.; Awan, A. S.; Hussain, R., *Continuous microwave flow synthesis (CMFS) of nano-sized tin oxide: Effect of precursor concentration. Ceram. Int.* **2016,** *42* (7), 8613–8619. https://doi.org/10.1016/j.ceramint.2016.02.092

168. Haile, S. M.; Boysen, D. A.; Chisholm, C. R. I.; Merle, R. B., *Solid acids as fuel cell electrolytes. Nature* **2001,** *410*, 910–913. https://doi.org/10.1038/35073536

169. Mohammad, N.; Mohamad, A. B.; Kadhum, A. A. H.; Loh, K. S., *A review on synthesis and characterization of solid acid materials for fuel cell applications. J. Power Sources* **2016,** *322*, 77–92. https://doi.org/10.1016/j.jpowsour.2016.05.021

170. Haile, S. M.; Chisholm, C. R.; Sasaki, K.; Boysen, D. A.; Uda, T., *Solid acid proton conductors: from laboratory curiosities to fuel cell electrolytes. Faraday Discuss.* **2007,** *134*, 17–39. https://doi.org/10.1039/b604311a

171. Lee, K.-S., *Hidden nature of the high-temperature phase transitions in crystals of KH_2PO_4-type: Is it a physical change ? J. Phys. Chem. Solids* **1996,** *57* (3), 333–342. https://doi.org/10.1016/0022-3697(95)00233-2

172. Ortiz, E.; Vargas, R. A.; Mellander, B.-E., *On the high-temperature phase transitions of CsH_2PO_4: A polymorphic transition? A transition to a superprotonic conducting phase? J. Chem. Phys.* **1999,** *110*, 4847–4853. https://doi.org/10.1063/1.478371

173. Taninouchi, Y.-k.; Uda, T.; Awakura, Y.; Ikeda, A.; Haile, S. M., *Dehydration behavior of the superprotonic conductor CsH_2PO_4 at moderate temperatures: 230 to 260 °C. J. Mater. Chem.* **2007,** *17* (30), 3182–3189. https://doi.org/10.1039/b704558c

174. Kreuer, K.-D., *Proton conductivity: Materials and applications. Chem. Mater.* **1996,** *8* (3), 610–641. https://doi.org/10.1021/cm950192a

175. Baranov, A. I.; Khiznichenko, V. P.; Shuvalov, L. A., *High temperature phase transitions and proton conductivity in some kdp-family crystals. Ferroelectrics* **1989,** *100* (1), 135–141. https://doi.org/10.1080/00150198908007907

176. Romain, F.; Novak, A., *Raman study of the high-temperature phase transition in CsH_2PO_4. J. Mol. Struct.* **1991,** *263* (2), 69–74. https://doi.org/10.1016/0022-2860(91)80056-A

177. Preisinger, A.; Mereiter, K.; Bronowska, W., *The phase transition of CsH_2PO_4 (CDP) at 505 K. Mater. Sci. Forum* **1994,** *166-169*, 511–516. https://doi.org/10.4028/www.scientific.net/MSF.166-169.511

178. Boysen, D. A.; Haile, S. M.; Liu, H.; Secco, R. A., *High-temperature behavior of CsH_2PO_4 under both ambient and high pressure conditions. Chem. Mater.* **2003,** *15* (3), 727–736. https://doi.org/10.1021/cm020138b

179. Hosseini, S.; Daud, W. R. W.; Badiei, M.; Kadhum, A. A. H.; Mohammad, A. B., *Effect of surfactants in synthesis of CsH_2PO_4 as protonic conductive membrane. Bull. Mater. Sci.* **2011,** *34* (4), 759–765. https://doi.org/10.1007/s12034-011-0192-3

180. Li, Z.; Tang, T., *High-temperature thermal behaviors of XH_2PO_4 (X=Cs, Rb, K, Na) and LiH_2PO_3. Thermochim. Acta* **2010,** *501* (1–2), 59–64. https://doi.org/10.1016/j.tca.2010.01.010

181. Suryaprakash, R. C.; Lohmann, F. P.; Wagner, M.; Abel, B.; Varga, A., *Spray drying as a novel and scalable fabrication method for nanostructured CsH_2PO_4, Pt-thin-film composite electrodes for solid acid fuel cells. RSC Adv.* **2014,** *4*, 60429–60436. https://doi.org/10.1039/C4RA10259B

182. Peighambardoust, S. J.; Rowshanzamir, S.; Amjadi, M., *Review of the proton exchange membranes for fuel cell applications. Int. J. Hydrogen Energy* **2010,** *35* (17), 9349–9384. https://doi.org/10.1016/j.ijhydene.2010.05.017

183. Ponomareva, V.; Shutova, E., *High-temperature behavior of CsH_2PO_4 and CsH_2PO_4–SiO_2 composites. Solid State Ion.* **2007,** *178* (7-10), 729–734. https://doi.org/10.1016/j.ssi.2007.02.035

184. Bondarenko, A. S.; Zhou, W.; Bouwmeester, H. J. M., *Superprotonic $KH(PO_3H)$–SiO_2 composite electrolyte for intermediate temperature fuel cells. J. Power Sources* **2009,** *194* (2), 843–846. https://doi.org/10.1016/j.jpowsour.2009.06.001

185. Chisholm, C. R. I.; Boysen, D. A.; Papandrew, A. B.; Zecevic, S.; Cha, S.; Sasaki, K. A.; Varga, Á.; Giapis, K. P.; Haile, S. M., *From laboratory breakthrough to technological realization: the development path for solid acid fuel cells. Electrochem. Soc. Interface* **2009,** *18* (3), 53–59. https://resolver.caltech.edu/CaltechAUTHORS:20131113-161625630

186. Lohmann, F. P.; Schulze, P. S. C.; Wagner, M.; Naumov, O.; Lotnyk, A.; Abel, B.; Varga, Á., *The next generation solid acid fuel cell electrodes: stable, high performance with minimized catalyst loading. J. Mater. Chem. A* **2017,** *5* (29), 15021–15025. https://doi.org/10.1039/c7ta03690f

187. Gao, F.; Blunier, B.; Miraoui, A., *Proton Exchange Membrane Fuel Cells Modeling*. Wiley: 2013; pp 3–12.

188. Otomo, J.; Minagawa, N.; Wen, C.-j.; Eguchi, K.; Takahashi, H., *Protonic conduction of* CsH_2PO_4 *and its composite with silica in dry and humid atmospheres. Solid State Ion.* **2003,** *156* (3-4), 357–369. https://doi.org/10.1016/S0167-2738(02)00746-4

189. Xie, Q.; Li, Y.; Hu, J.; Chen, X.; Li, H., *A* CsH_2PO_4 *-based composite electrolyte membrane for intermediate temperature fuel cells. J. Membr. Sci.* **2015,** *489*, 98–105. http://dx.doi.org/10.1016/j.memsci.2015.03.083

190. Schmidt, H., *New type of non-crystalline solids between inorganic and organic materials. J. Non-Cryst. Solids* **1985,** *73*, 681–691. http://dx.doi.org/10.22028/D291-24311

191. Sharma, R. K.; Das, S.; Maitra, A., *Surface modified ormosil nanoparticles. J. Colloid Interface Sci.* **2004,** *277* (2), 342–346. https://doi.org/10.1016/j.jcis.2004.04.019

192. Peled, A.; Naddaka, M.; Lellouche, J.-P., *Smartly designed photoreactive silica nanoparticles and their reactivity. J. Mater. Chem.* **2011,** *21* (31), 11511–11517. https://doi.org/10.1039/c1jm00055a

193. Baney, R. H.; Itoh, M.; Sakakibara, A.; Suzuki, T., *Silsesquioxanes. Chem. Rev.* **1995,** *95* (5), 1409–1430. https://doi.org/10.1021/cr00037a012,

194. Kim, S.; Pudavar, H. E.; Prasad, P. N., *Dye-concentrated organically modified silica nanoparticles as a ratiometric fluorescent pH probe by one- and two-photon excitation. Chem. Commun.* **2006,** (19), 2071–2073. https://doi.org/10.1039/b600926c

195. Baù, L.; Tecilla, P.; Mancin, F., *Sensing with fluorescent nanoparticles. Nanoscale* **2011,** *3* (1), 121–133. https://doi.org/10.1016/S0928-4931(98)00039-310.1039/c0nr00405g

196. Bescher, E.; Mackenzie, J. D., *Hybrid organic-inorganic sensors. Mater. Sci. Eng., C* **1998,** *6*, 145–154. https://doi.org/10.1016/S0928-4931(98)00039-3

197. Mori, H., *Design and synthesis of functional silsesquioxane-based hybrids by hydrolytic condensation of bulky triethoxysilanes. Int. J. Polym. Sci.* **2012,** *2012*, 1–17. https://doi.org/10.1155/2012/173624

198. Kashio, M.; Tamada, T. Adhesive mainly composed of polyorganosiloxane compond. Patent US 8,357.261 B2, January 22, 2013.

199. Macan, J.; Tadanaga, K.; Tatsumisago, M., *Softening of octyl-modified phenylsilsesquioxanes. Polimeri* **2011,** *32* (3–4), 112–118.

200. Mackenzie, J. D.; Bescher, E. P., *Structures, properties and potential applications of ormosils. J. Sol-Gel Sci. Technol.* **1998,** *13*, 371–377. https://doi.org/10.1023/A:1008600723220

201. Budunoglu, H.; Yildirim, A.; Guler, M. O.; Bayindir, M., *Highly transparent, flexible, and thermally stable superhydrophobic ORMOSIL aerogel thin films. ACS Appl. Mater. Interfaces* **2011,** *3* (2), 539–545. https://doi.org/10.1021/am101116b

202. Palmisano, G.; Le Bourhis, E.; Ciriminna, R.; Tranchida, D.; Pagliaro, M., *ORMOSIL thin films: tuning mechanical properties via a nanochemistry approach. Langmuir* **2006,** *22* (26), 11158–11162. https://doi.org/10.1021/la061520w

203. Lu, X.; Yin, Q.; Xin, Z.; Li, Y.; Han, T., *Synthesis of poly(aminopropyl/methyl)silsesquioxane particles as effective Cu(II) and Pb(II) adsorbents. J. Hazard. Mater.* **2011,** *196*, 234–241. https://doi.org/10.1016/j.jhazmat.2011.09.020

204. Miller, C. R.; Vogel, R.; Surawski, P. P. T.; Jack, K. S.; Corrie, S. R.; Trau, M., *Functionalized organosilica microspheres via a novel emulsion-based route. Langmuir* **2005,** *21* (21), 9733–9740. https://doi.org/10.1021/la0514112

205. Loy, D. A.; Baugher, B. M.; Baugher, C. R.; Schneider, D. A.; Rahimian, K., *Substituent effects on the sol–gel chemistry of organotrialkoxysilanes. Chem. Mater.* **2000,** *12* (12), 3624–3632. https://doi.org/10.1021/cm000451i

206. Van Blaaderen, A.; Vrij, A., *Synthesis and characterization of monodisperse colloidal organo-silica spheres J. Colloid Interface Sci.* **1993,** *156*, 1–18. https://doi.org/10.1006/jcis.1993.1073

207. Arkhireeva, A.; Hay, J. N., *Synthesis of sub-200 nm silsesquioxane particles using a modified Stöber sol–gel route. J. Mater. Chem.* **2003,** *13* (12), 3122–3127. https://doi.org/10.1039/b306994j

208. Etienne, M.; Lebeau, B.; Walcarius, A., *Organically-modified mesoporous silica spheres with MCM-41 architecture. New J. Chem.* **2002,** *26* (4), 384–386. https://doi.org/10.1039/b110741k

209. Arkhireeva, A.; Hay, J. N.; Oware, W., *A versatile route to silsesquioxane nanoparticles from organically modified silane precursors. J. Non-Cryst. Solids* **2005,** *351* (19–20), 1688–1695. https://doi.org/10.1016/j.jnoncrysol.2005.04.063

210. Sankaraiah, S.; Lee, J. M.; Kim, J. H.; Choi, S. W., *Preparation and characterization of surface-functionalized polysilsesquioxane hard spheres in aqueous medium. Macromolecules* **2008,** *41*, 6195–6204. https://doi.org/10.1021/ma8003345

211. Ottenbrite, R. M.; Wall, J. S., *Self-catalyzed synthesis of organo-silica nanoparticles. J. Am. Ceram. Soc.* **2000,** *83* (12), 3214–3215. https://doi.org/10.1111/j.1151-2916.2000.tb01709.x

212. Lee, Y.-G.; Park, J.-H.; Oh, C.; Oh, S.-G.; Kim, Y. C., *Preparation of highly monodispersed hybrid silica spheres using a one-step sol-gel reaction in aqueous solution. Langmuir* **2007,** *23* (22), 10875–10878. https://doi.org/10.1021/la702462b

213. Jung, C. Y.; Kim, J. S.; Kim, H. S.; Ha, J. M.; Kim, S. T.; Lim, H. J.; Koo, S. M., *Selective surface reactions for Janus ORMOSIL particles with multiple functional groups using an ordered monolayer film at liquid-liquid interface. J. Colloid Interface Sci.* **2012,** *367* (1), 257–263. https://doi.org/10.1016/j.jcis.2011.09.079

214. Katagiri, K.; Hasegawa, K.; Matsuda, A.; Tatsumisago, M.; Minami, T., *Preparation of transparent thick films by electrophoretic sol-gel deposition using phenyltriethoxysilane-derived particles. J. Am. Ceram. Soc.* **1998,** *81* (9), 2501–2503. https://doi.org/10.1111/j.1151-2916.1998.tb02653.x

215. Matsuda, A.; Sasaki, T.; Hasegawa, K.; Tatsumisago, M.; Minami, T., *Thermal softening behavior and application to transparent thick films of poly(benzylsilsesquioxane) particles prepared by the sol–gel process. J. Am. Ceram. Soc.* **2001,** *84* (4), 775–780. https://doi.org/10.1111/j.1151-2916.2001.tb00740.x

216. Matsuda, A.; Sasaki, T.; Tanaka, T.; Tatsumisago, M.; Minami, T., *Preparation of copolymerized phenylsilsesquioxane-benzylsilsesquioxane particles. J. Sol-Gel Sci. Technol.* **2002,** *23* (3), 247–252. https://doi.org/10.1023/A:1013979032037

217. Macan, J.; Tadanaga, K.; Tatsumisago, M., *Influence of copolymerization with alkyltrialkoxysilanes on condensation and thermal behaviour of poly(phenylsilsesquioxane) particles. J. Sol-Gel Sci. Technol.* **2010,** *53* (1), 31–37. https://doi.org/10.1007/s10971-009-2051-x

218. Takahashi, K.; Tadanaga, K.; Hayashi, A.; Matsuda, A.; Tatsumisago, M., *Glass transition and thermal softening of poly(phenylsilsesquioxane) particles prepared using two-step acid–base catalyzed sol–gel process. J. Non-Cryst. Solids* **2008,** *354* (2–9), 700–704. https://doi.org/10.1016/j.jnoncrysol.2007.07.073

219. Jung, G. I.; Kim, E. H.; Lim, M. H.; Koo, S. M., *Size control of monodisperse hollow ORMOSIL particles using a self-emulsion process. J. Ind. Eng. Chem.* **2017,** *46*, 386–396. https://doi.org/10.1016/j.jiec.2016.11.008

220. Park, T. J.; Jung, G. I.; Kim, E. H.; Koo, S. M., *Development of mesoporous structures of composite silica particles with various organic functional groups in the presence and absence of ammonia catalyst. J. Nanopart. Res.* **2017,** *19* (226), 1–11. https://doi.org/10.1007/s11051-017-3928-1

221. Park, J. W.; Kim, J. S.; Park, T. J.; Kim, E. H.; Koo, S. M., *Facile synthesis of tailored nanostructured ORMOSIL particles by a selective dissolution process. J. Colloid Interface Sci.* **2015,** *438*, 220–226. https://doi.org/10.1016/j.jcis.2014.10.002

222. Chevalier, P. M.; Ou, D. L., *Nanoporous silica particles prepared by chemical reactivity of ORMOSILs. J. Mater. Chem.* **2002,** *12* (10), 3003–3009. https://doi.org/10.1039/b203373a

223. Kim, J. S.; Jung, G. I.; Kim, S. J.; Koo, S. M., *Ten-gram-scale preparation of PTMS-based monodisperse ORMOSIL nano- and microparticles and conversion to silica particles. J. Nanopart. Res.* **2018,** *20* (73), 1–11. https://doi.org/10.1007/s11051-018-4186-6

224. Abass, M. A.; Syed, A. A.; Gervais, C.; Singh, G., *Synthesis and electrochemical performance of a polymer-derived silicon oxycarbide/boron nitride nanotube composite. RSC Adv.* **2017,** *7* (35), 21576–21584. https://doi.org/10.1039/C7RA01545C

225. Oschatz, M.; Boukhalfa, S.; Nickel, W.; Hofmann, J. P.; Fischer, C.; Yushin, G.; Kaskel, S., *Carbide-derived carbon aerogels with tunable pore structure as versatile electrode material in high power supercapacitors. Carbon* **2017,** *113*, 283–291. http://dx.doi.org/10.1016/j.carbon.2016.11.050

226. Bhandavat, R.; Pei, Z.; Singh, G., *Polymer-derived ceramics as anode material for rechargeable Li-ion batteries: a review. Nanomaterials and Energy* **2012,** *1* (6), 324–337. https://doi.org/10.1680/nme.12.00030

227. Meier, A.; Weinberger, M.; Pinkert, K.; Oschatz, M.; Paasch, S.; Giebeler, L.; Althues, H.; Brunner, E.; Eckert, J.; Kaskel, S., *Silicon oxycarbide-derived carbons from a polyphenylsilsequioxane precursor for supercapacitor applications. Microporous Mesoporous Mater.* **2014,** *188*, 140–148. https://doi.org/10.1016/j.micromeso.2013.12.022

228. Presser, V.; Heon, M.; Gogotsi, Y., *Carbide-derived carbons – from porous networks to nanotubes and graphene. Adv. Funct. Mater.* **2011,** *21* (5), 810–833. https://doi.org/10.1002/adfm.201002094

229. Stabler, C.; Ionescu, E.; Graczyk-Zajac, M.; Gonzalo-Juan, I.; Riedel, R., *Silicon oxycarbide glasses and glass-ceramics: "All-Rounder" materials for advanced structural and functional applications. J. Am. Ceram. Soc.* **2018,** *101* (11), 4817–4856. https://doi.org/10.1111/jace.15932

230. Widgeon, S. J.; Sen, S.; Mera, G.; Ionescu, E.; Riedel, R.; Navrotsky, A., *^{29}Si and ^{13}C solid-state NMR spectroscopic study of nanometer-scale structure and mass fractal characteristics of amorphous polymer derived silicon oxycarbide ceramics. Chem. Mater.* **2010,** *22* (23), 6221–6228. https://doi.org/10.1021/cm1021432

231. Saha, A.; Raj, R.; Williamson, D. L., *A model for the nanodomains in polymer-derived SiCO. J. Am. Ceram. Soc.* **2006,** *89* (7), 2188–2195. https://doi.org/10.1111/j.1551-2916.2006.00920.x

232. Kleebe, H.-J.; Blum, Y. D., *SiOC ceramic with high excess free carbon. J. Eur. Ceram. Soc.* **2008,** *28* (5), 1037–1042. https://doi.org/10.1016/j.jeurceramsoc.2007.09.024

233. Vakifahmetoglu, C.; Presser, V.; Yeon, S.-H.; Colombo, P.; Gogotsi, Y., *Enhanced hydrogen and methane gas storage of silicon oxycarbide derived carbon. Microporous Mesoporous Mater.* **2011,** *144* (1–3), 105–112. https://doi.org/10.1016/j.micromeso.2011.03.042

234. Bakumov, V.; Schwarz, M.; Kroke, E., *Emulsion processing and size control of polymer-derived spherical Si/C/O ceramic particles. Soft Mater.* **2007,** *4* (2–4), 287–299. https://doi.org/10.1080/15394450701310251

235. Maheswari, C. S.; Shanmugapriya, C.; Revathy, K.; Lalitha, A., *SnO_2 nanoparticles as an efficient heterogeneous catalyst for the synthesis of 2H-indazolo[2,1-b]phthalazine-triones. J. Nanostruct. Chem.* **2017,** *7* (3), 283–291. http://dx.doi.org/10.1007/s40097-017-0238-1

236. Li, N.; Martin, C. R.; Scrosati, B., *A high-rate, high-capacity, nanostructured tin oxide electrode. Electrochem. Solid-State Lett.* **2000,** *3* (7), 316–318. https://doi.org/10.1149/1.1391134

237. Feng, L.; Xuan, Z.; Ji, S.; Min, W.; Zhao, H.; Gao, H., *Preparation of SnO_2 nanoparticle and performance as lithiumion battery anode. Int. J. Electrochem. Sci.* **2015,** *10*, 2370–2376.

238. Tuan, P. V.; Hieu, L. T.; Nga, L. Q.; Dung, N. D.; Ha, N. N.; Khiem, T. N., *Hydrothermal synthesis and characteristic photoluminescence of Er-doped SnO_2 nanoparticles. Physica B: Condensed Matter* **2016,** *501*, 34–37. http://dx.doi.org/10.1016/j.physb.2016.08.009

239. Huang, H.; Ng, M.; Wu, Y.; Kong, L., *Solvothermal synthesis of Sb:SnO_2 nanoparticles and IR shielding coating for smart window. Mater. Des.* **2015,** *88*, 384–389. http://dx.doi.org/10.1016/j.matdes.2015.09.013

240. Bhuvana, S.; Ramalingam, H. B.; Vadivel, K.; Ranjith Kumar, E.; Ayesh, A. I., *Effect of Zn and Ni substitution on structural, morphological and magnetic properties of tin oxide nanoparticles. J. Magn. Magn. Mater.* **2016,** *419*, 429–434. http://dx.doi.org/10.1016/j.jmmm.2016.07.004

241. Hassanzadeh, A.; Moazzez, B.; Haghgooie, H.; Nasseri, M.; Golzan, M.; Sedghi, H., *Synthesis of SnO_2 nanopowders by a sol-gel process using propanol-isopropanol mixture. Cent. Eur. J. Chem.* **2008,** *6* (4), 651–656. http://dx.doi.org/10.2478/s11532-008-0072-x

242. Zhou, J. X.; Zhang, M. S.; Hong, J. M.; Fang, J. L.; Yin, Z., *Structural and spectral properties of SnO_2 nanocrystal prepared by microemulsion technique. Appl. Phys. A* **2005,** *81* (1), 177–182. https://doi.org/10.1007/s00339-004-2742-7

243. Dujardin, R.; Delorme, F.; Pintault, B.; Belleville, P.; Autret, C.; Monot-Laffez, I.; Giovannelli, F., *A high yield one-pot aqueous synthesis of crystalline SnO_2 nanoparticles. Mater. Lett.* **2017,** *187*, 151–153. https://doi.org/10.1016/j.matlet.2016.10.074

244. Toledo-Antonio, J. A.; Gutiérrez-Baez, R.; Sebastian, P. J.; Vázquez, A., *Thermal stability and structural deformation of rutile SnO_2 nanoparticles. J. Solid State Chem.* **2003,** *174* (2), 241–248. https://doi.org/10.1016/s0022-4596(03)00181-6

245. Majumdar, S.; Devi, P. S., *Synthesis of SnO_2 nanoparticles using ultrasonication. AIP Conference Proceedings* **2010,** *1276* (1), 1–7. https://doi.org/10.1063/1.3504298

246. Abrari, M.; Ghanaatshoar, M.; Hosseiny Davarani, S. S.; Moazami, H. R.; Kazeminezhad, I., *Synthesis of SnO_2 nanoparticles by electrooxidation of tin in quaternary ammonium salt for*

application in dye-sensitized solar cells. Appl. Phys. A **2017,** *123* (5), 1–9. http://dx.doi.org/10.1007/s00339-017-0941-2

247. Chan, H. K.; Kwok, P. C., *Production methods for nanodrug particles using the bottom-up approach. Adv. Drug Deliv. Rev.* **2011,** *63* (6), 406–416. http://dx.doi.org/10.1016/j.addr.2011.03.011

248. Liu, J.; Gu, F.; Hu, Y.; Li, C., *Flame synthesis of tin oxide nanorods: a continuous and scalable approach. J. Phys. Chem. C* **2010,** *114* (13), 5867–5870. https://doi.org/10.1021/jp911628r

249. Bakrania, S. D.; Perez, C.; Wooldridge, M. S., *Methane-assisted combustion synthesis of nanocomposite tin dioxide materials. Proc. Combust. Inst.* **2007,** *31* (2), 1797–1804. https://doi.org/10.1016/j.proci.2006.08.020

250. Ibarguen, C. A.; Mosquera, A.; Parra, R.; Castro, M. S.; Rodríguez-Páez, J. E., *Synthesis of SnO_2 nanoparticles through the controlled precipitation route. Mater. Chem. Phys.* **2007,** *101* (2-3), 433–440. https://doi.org/10.1016/j.matchemphys.2006.08.003

251. Devi, G. S.; Masthan, S. K.; Shakuntala, M.; Rao, V. J., *Correlation between structural properties and gas sensing characteristics of SnO_2 based gas sensors. J. Mater. Sci. - Mater. El.* **1999,** *10*, 545–549. https://doi.org/10.1023/A:1008900706941

252. Pavelko, R. G.; Vasiliev, A. A.; Llobet, E.; Vilanova, X.; Barrabés, N.; Medina, F.; Sevastyanov, V. G., *Comparative study of nanocrystalline SnO_2 materials for gas sensor application: thermal stability and catalytic activity. Sensors Actuators B: Chem.* **2009,** *137* (2), 637–643. http://dx.doi.org/10.1016/j.snb.2008.12.025

253. Chen, D.; Gao, L., *Novel synthesis of well-dispersed crystalline SnO_2 nanoparticles by water-in-oil microemulsion-assisted hydrothermal process. J. Colloid Interface Sci.* **2004,** *279* (1), 137–142. http://dx.doi.org/10.1016/j.jcis.2004.06.052

254. Xi, L.; Qian, D.; Tang, X.; Chen, C., *High surface area SnO_2 nanoparticles: synthesis and gas sensing properties. Mater. Chem. Phys.* **2008,** *108* (2–3), 232–236. http://dx.doi.org/10.1016/j.matchemphys.2007.09.023

255. Fujihara, S.; Maeda, T.; Ohgi, H.; Hosono, E.; Imai, H.; Kim, S.-H., *Hydrothermal routes to prepare nanocrystalline mesoporous SnO_2 having high thermal stability. Langmuir* **2004,** *20*, 6476–6481. http://dx.doi.org/10.1021/la0493060

256. Siciliano, P., *Preparation, characterisation and applications of thin films for gas sensors prepared by cheap chemical method. Sensors Actuators B: Chem.* **2000,** *70*, 153–164. https://doi.org/10.1016/S0925-4005(00)00585-2

257. Chiu, H.-C.; Yeh, C.-S., *Hydrothermal synthesis of SnO_2 nanoparticles and their gas-sensing of alcohol. J. Phys. Chem. C* **2007,** *111* (20), 7256–7259. http://dx.doi.org/10.1021/jp0688355

258. Thomas, I. M. Method for producing stannic tertiary alkoxide. Patent 3,946,056, March 23, 1974.

259. Chandler, C. D.; Fallon, G. D.; Koplick, A. J.; West, B. O., *The structures of mono and bis β-diketonate tin(IV) alkoxide complexes. Aust. J. Chem.* **1987,** *40* (8), 1427–1439 https://doi.org/10.1071/CH9871427

260. Bergerhoff, G.; Brown, I. D. Crystallographic databases. F.H. Allen et al.: 1987.

261. Cheary, R. W.; Coelho, A. A.; Cline, J. P., *Fundamental parameters line profile fitting in laboratory diffractometers. J. Res. Natl. Inst. Stand. Technol.* **2004,** *109* (1), 1–25. https://doi.org/10.6028/jres.109.002

262. Schneider, C. A.; Rasband, W. S.; Eliceiri, K. W., *NIH Image to ImageJ: 25 years of image analysis. Nat. Methods* **2012,** *9* (7), 671–675. https://doi.org/10.1038/nmeth.2089

263. Harrison, P. G.; Guest, A., *Tin oxide surfaces. J. Chem. Soc., Faraday Trans.* **1987,** *83* (11), 3383–3397. https://doi.org/10.1039/F19878303383

264. Zhu, J.-J.; Zhu, J.-M.; Liao, X.-H.; Fang, J.-L.; Zhou, M.-G.; Chen, H.-Y., *Rapid synthesis of nanocrystalline* SnO_2 *powders by microwave heating method. Mater. Lett.* **2002,** *53*, 12–19. https://doi.org/10.1016/S0167-577X(01)00445-1

265. Amalric-Popescu, D.; Bozon-Verduraz, F., *Infrared studies on* SnO_2 *and Pd/*SnO_2*. Catal. Today* **2001,** *70*, 139–154. https://doi.org/10.1016/S0920-5861(01)00414-X

266. Ory, H. A., *Infrared absorption frequencies of the tert-butoxy group. Anal. Chem.* **1960,** *32* (4), 509–511. https://doi.org/10.1021/ac60160a014s

267. Tazikeh, S.; Akbari, A.; Talebi, A.; Talebi, E., *Synthesis and characterization of tin oxide nanoparticles via the Co-precipitation method. Mater. Sci.-Pol.* **2014,** *32* (1), 98–101. https://doi.org/10.2478/s13536-013-0164-y

268. Sakurai, T.; Takizawa, T., *Thermal expansion of* SnO_2 *at high temperatures. High Temp. - High Press.* **1971,** *3* (3), 325–331.

269. Bartlett, G.; Langmuir, I., *The crystal stuctures of the ammonium halides above and below the transition temperatures. J. Am. Chem. Soc.* **1921,** *43* (1), 84–91. https://doi.org/10.1021/ja01434a010

270. Sedghi, S. M.; Mortazavi, Y.; Khodadadi, A.; Sahraei, O. A.; Naseh, M. V., *Sonochemically prepared* SnO_2 *quantum dots as a selective and low temperature CO sensor. Intern. J. Chem. and Biol. Eng.* **2009,** *2* (2), 69–73. http://dx.doi.org/10.5281/zenodo.1329539

271. Gaber, A.; Abdel-Rahim, M. A.; Abdel-Latief, A. Y.; Abdel-Salam, M. N., *Influence of calcination temperature on the structure and porosity of nanocrystalline* SnO_2 *synthesized by a conventional precipitation method. Int. J. Electrochem. Sci.* **2014,** *9*, 81–95. https://doi.org/10.3390/nano8040250

272. Sidorak, A. V.; Ivanov, V. V.; Shubin, A. A., *Cadmium stannates synthesis via thermal treatment of coprecipitated salts. Mater. Sci. Appl.* **2011,** *02* (09), 1219–1224. https://doi.org/10.4236/msa.2011.29165

273. Pilkenton, S.; Raftery, D., *Solid-state NMR studies of the adsorption and photooxidation of ethanol on mixed* TiO_2*–*SnO_2 *photocatalysts. Solid State Nucl. Magn. Reson.* **2003,** *24*, 236–253. https://doi.org/10.1016/S0926-2040(03)00030-4

274. Brito, G. E. S.; Briois, V.; Pulcinelli, S. H.; Santilli, C. V., *EXAFS and XRD study of the structural evolution during isothermal sintering of* SnO_2 *xerogels. J. Sol-Gel Sci. Technol.* **1997,** *8*, 269–274. https://doi.org/10.1007/BF02436851

The MicroJet reactor is an improvement of traditional T-shape and impinging jet reactors and is particularly suitable for the production of nanoscale precipitates. The aim of this work is to evaluate the strengths as well as the limitations of this method for the synthesis of inorganic and hybrid particles and to optimize the properties of the particles regarding to their intended application. In the first part tin(IV) oxide particles are produced continuously by applying tin(IV) chloride pentahydrate or tin(IV) t-butoxide as precursors. The same reactions are accomplished as beaker syntheses, some of them ultrasonic-assisted, to compare the results with those from the continuous process. In the second part, the influence of the mixing efficiency on the synthesis of cesium dihydrogen phosphate particles is investigated. The third part is about the synthesis of organically modified silica (ORMOSIL) particles. A prehydrolyzation of the alkoxysilane precursors turns out as a solution to adjust their reaction velocity to the fast MicroJet reactor process and to produce a broad variety of spherical ORMOSIL particles continuously in large scale (23 g/min). The particles can then be converted into silicon oxycarbides or carbide-derived carbons. It becomes apparent that the properties of these energy storage materials highly depend on the kind and amount of the organic groups of the precursor particles.